

2011

PHOTON FACTORY ACTIVITY REPORT

PART A : HIGHLIGHT AND FACILITY REPORT #29

Editorial Board

H. Abe
S. Adachi
L. Chavas
K. Harada
A. Hirata
K. Ito
T. Kikegawa
T. Kosuge
Y. Misumi
F. Mori
H. Nakao*
S. Nozawa
K. Ono
H. Sugiyama
R. Takai
N. Usami
T. Yamasaki
Y. Yamasaki

* editor in chief

KEK Progress Report 2012-3

© High Energy Accelerator Research Organization (KEK), 2012

KEK Reports are available from:

Library and Archives
High Energy Accelerator Research Organization (KEK)
1-1 Oho, Tsukuba, Ibaraki, 305-0801
JAPAN

E-mail: irdlib@mail.kek.jp

URL: <http://www.kek.jp/>

#29

PHOTON FACTORY ACTIVITY REPORT

2011

April 2011 to March 2012





- | | | | | |
|-------------------|------------------|------------------|-----------------|--------------------|
| 1 J. Okamoto | 21 M. Sakamaki | 41 J. Adachi | 61 N. Nakamura | 81 R. Sukegawa |
| 2 Yu. Takahashi | 22 Y. Uchida | 42 K. Hyodo | 62 Y. Uemura | 82 T. Aoki |
| 3 S. Adachi | 23 K. Nigorikawa | 43 T. Kubota | 63 S. Takano | 83 F. Mori |
| 4 Y. Murakami | 24 Y. Yamada | 44 S. Toyoda | 64 H. Toyama | 84 A. Tase |
| 5 S. Wakatsuki | 25 S. Watanabe | 45 K. Inoue | 65 N. Nagata | 85 H. Nitani |
| 6 K. Ito | 26 J. Nishino | 46 M. Hiraki | 66 T. Takahashi | 86 Y. Kitajima |
| 7 H. Kawata | 27 S. Naito | 47 L. Chavas | 67 K. Wada | 87 T. Honda |
| 8 Y. Kobayashi | 28 T. Miyajima | 48 K. Haga | 68 T. Mizuno | 88 K. Tsuchiya |
| 9 W. Voegeli | 29 H. Sagehashi | 49 A. Toyoshima | 69 N. Usami | 89 H. Makio |
| 10 S. Hinokuma | 30 T. Obina | 50 T. Yamasaki | 70 A. Ueda | 90 A. Kikuchi |
| 11 Y. Wakisaka | 31 H. Abe | 51 Y. Misumi | 71 R. Takai | 91 T. Tahara |
| 12 H. Kumigashira | 32 Y. Takeichi | 52 G. Ishikawa | 72 S. Gayen | 92 T. Koide |
| 13 K. Ono | 33 N. Inami | 53 Yo. Takahashi | 73 S. Maiti | 93 T. Sudayama |
| 14 T. Nogami | 34 M. Kawasaki | 54 R. Kato | 74 S. Velaga | 94 T. Kikuchi |
| 15 H. Nakao | 35 S. Miller | 55 T. Uchiyama | 75 S. Nagahashi | 95 Y. Yamasaki |
| 16 K. Amemiya | 36 E. Sakai | 56 Y. Tanimoto | 76 N. Shimizu | 96 H. Miyauchi |
| 17 S. Nozawa | 37 K. Takemura | 57 K. Demura | 77 K. Harada | 97 M. Mukhopadhyay |
| 18 N. Igarashi | 38 M. Shimada | 58 H. Tanaka | 78 T. Zeniya | 98 R. Kumai |
| 19 N. Sakabe | 39 T. Hyodo | 59 M. Yamamoto | 79 A. Hirata | 99 N. Matsugaki |
| 20 S. Yamamoto | 40 M. Komuro | 60 H. Uehara | 80 Y. Watanabe | 100 A. Koyama |

Editorial

This is the 29th volume of the Photon Factory (PF) Activity Report, and covers scientific activities for the Japanese fiscal year 2011 (April 2011 to March 2012). The report is divided into two parts. PART A summarizes scientific highlights achieved by users, newly developed experimental facilities including beamlines and experimental apparatuses, topical in-house research activities, research and development of light sources, reports of public events, and a description of the outline and organization of the PF. PART B presents a number of users' short reports and a list of research proposals. In this year, we have started to accept users' reports in Japanese, and the number of users' reports increased. Thank you very much for the cooperation.

For the past several editions we have promoted the electronic distribution of the PF Activity Report. Awards, Theses and Publication List in Appendices of PART A and all content including PART B is published on the PF's website at <http://pfwww.kek.jp/pfacr/index.html>.

Finally, we would like to express our sincere gratitude to all of those who have contributed to this volume.

Hironori Nakao, Editor-in-Chief

CONTENTS

INTRODUCTION	1
MEMORIALS 2011	3
HIGHLIGHTS	
1. Atomic and Molecular Science	12
2. Materials Science	14
3. Chemical and Environmental Science	32
4. Earth and Planetary Science	40
5. Life Science	44
6. Imaging and Optics	56
7. Instrumentation and Methodology	58
8. Accelerators	62
EXPERIMENTAL FACILITIES	
1. Newly Developed Experimental Facilities	67
2. Structural Biology Research Center	70
3. Condensed Matter Research Center	76
4. The Slow Positron Facility	80
5. IMSS Instrument R&D Team	83
6. Summary of Experimental Stations	84
ACCELERATORS	
1. Outline of the Accelerators	97
2. PF Ring	100
3. PF-AR.....	108
FUTURE LIGHT SOURCE	
1. ERL Project Overview	113
2. 3-GeV ERL	116
3. cERL	119
USERS PROGRAM & OUTREACH ACTIVITIES	
1. Experimental Proposals	131
2. Workshops and Seminars	134
3. Graduate School Education.....	135
4. International Collaboration	136
5. Photon Factory Science Advisory Committee (PF-SAC)	138
APPENDICES	
1. Site and Organization	140
2. Awards	148
3. Theses	150
4. Publication List	152

Introduction

We are pleased to present Photon Factory Activity Report 2011. This report covers the research activities carried out at the Photon Factory (PF) facility in fiscal 2011 (April 2011 – March 2012). I was appointed Director of the Photon Factory in April 2012, and as is the custom, it is my pleasure to write this introduction of the report. First of all, on behalf of the staff of the PF I would like to express our deepest appreciation to the staff of both domestic and overseas synchrotron facilities, who supported us and offered our users beamtime after the Great East Japan Earthquake on March 11th, 2011. In particular, SPring-8 kindly assisted us by setting aside their beamtime for more than 100 PF users' experiments. Other domestic and overseas facilities also thoughtfully accepted PF users. In the end, 122 experiments were carried out in domestic facilities and 10 experiments in overseas facilities. The PF facility has been restored to its former state very quickly; the electron beam was accumulated in the PF and PF-AR rings on May and then test runs were carried out at both the PF and PF-AR for 6 weeks. During the summer shutdown, repairs to the PF, PF-AR rings and their beamlines were carried out and the user program was resumed in October. Although we are still in the process of recovering from the disaster, the user program began to run smoothly in 2012. Once again, we sincerely thank everyone who sent us letters and emails of consolation and support.

In fiscal 2011 we organized two PF symposiums, one in July and the other in March, because the 28th PF symposium in March 2011 had to be postponed because of the earthquake. At the PF symposium in July, the situation of reconstruction after the disaster and the recovery plans were reported, and the role of our research institute amid the difficult situation was discussed with many PF users. About 380 users got together to discuss the restoration after the disaster and how to continue their ongoing studies. One of the scientific topics in this symposium was the mineralogical characteristics of Itokawa particles recovered by the spacecraft Hayabusa; the fine particles were analyzed by diffraction and fluorescence measured at beamline 3A of the PF.

The Photon Factory (PF) started operation in 1982 as the first dedicated facility for synchrotron radiation in Japan, handling photons from VUV to X-rays. The inter-university research program also started in the same year. Thus, 2011 was the 30th anniversary of the PF. To mark the occasion, a ceremony was held at the PF symposium in March 2012. Professor Kora, who was the first director of the PF, talked about the background of the formation of the PF and interesting anecdotes from the early days. Everyone was impressed by the dedication



Youichi Murakami

of the PF staff and users for synchrotron radiation at the beginning of the PF project. Next, Professor Sasaki, who was the second director of the PF, delivered a lecture on the first work of insertion devices in Japan. He explained the importance of close collaboration between users and accelerator staff for the progress of synchrotron science. Finally Professor Hodgson, who was the first chairperson of the PF Scientific Advisory Committee, gave a lecture titled "The Photon Factory – Building on a Rich History for a Bright Future of Innovation and Discovery" in which he talked about the long collaboration between SSRL and PF.

The High Energy Accelerator Research Organization (KEK) has promoted the Energy Recovery Linac (ERL) project over the past decade. The ERL is the future X-ray light source designed based on state-of-the-art superconducting linear accelerator technology, which has been developed at KEK over many years. The high repetition rate, short pulse, high spatial coherence and high brightness of the ERL will enable the filming of ultrafast atomic-scale movies and determination of the structure of heterogeneous systems on the nano-scale. KEK is planning to construct the ERL in the latter part of this decade, and expects it to enter operation in the early 2020s. In addition, it is proposed that an X-ray free-electron laser oscillator (XFEL-O) with full coherence will be feasible by taking advantage of the unprecedented quality of the electron beam of the ERL. Construction of the XFEL-O is planned for the second phase of the ERL project. The conceptual design report (CDR) of the ERL was published in collaboration with many people from universities and national laboratories. The CDR includes enabling methodologies by the ERL, many science cases, and accelerator technology related to the ERL. The superb beam quality of the ERL will open up a new era of X-ray science by extending the capabilities of existing synchrotron X-ray sciences, and will also provide an opportunity for a paradigm shift from static homogeneous systems to dynamic heterogeneous systems to many users.

During the year we held many conferences on the ERL to examine the feasibility of various technical aspects of the accelerator such as the electron gun, superconducting cavity for the injector and main linac. The ERL Science Workshop II was held at KEK on April 2011 to discuss many scientific issues and to enable the ERL to help create a sustainable society. The first ERL symposium was convened in July to discuss the relationship between synchrotron science and society. The key theme of the symposium was “a step toward realizing a sustainable society”. The second ERL symposium was held in March 2012, at which Professor Negishi, Nobel laureate for Chemistry in 2010, gave a lecture on d-Block transition metals, which have great importance for our lives today. In October 2011 the international workshop ERL2011 was held at KEK as one of the Advanced Beam Dynamics Workshops of the 50th International Committee for Future Accelerators (ICFA) to promote international collaboration on high-energy accelerators and study the related problems.

The IMSS Symposium 2011 was held in December at Tsukuba International Congress Center. The Institute of Materials Structure Science (IMSS) is studying material and life sciences through the comprehensive use of multi-probes such as synchrotron radiation, neutrons, muons, and slow positrons. Every year, we organize the IMSS symposium focusing on cutting-edge quantum beam science, and this year's symposium examined the prospects for quantum beam facilities and its sciences. The first half of the symposium was dedicated to ERL sciences: Professor Gruner presented science at the hard X-ray diffraction limit as a summary of the XDL2011 workshop and Professor Chen talked about solar energy research using X-ray transient absorption spectroscopy. In the second half of the symposium, presentations were made on recent studies on strongly correlated electron systems, focusing on electronic degrees of freedom (charge, spin, and orbital), electron correlation at surfaces and interfaces, organic electronic devices, and order and disorder in soft matter and bio-matter. These topics are being studied at the Condensed Matter Research Center (CMRC) of the IMSS, and CMRC researchers sparked vigorous discussion on the topics.

The 6th PF Science Advisory Committee (PF-SAC) meeting was held in October 2011 and discussed the following: 1) Earthquake recovery and refurbishment

processes, 2) Relation between PF operation and KEK-B upgrade, 3) The second phase of the plan to refurbish the PF, 4) The two subcommittees: Condensed Matter and Materials Chemistry, 5) Transformation from PF-Kondankai to PF User Association, 6) The 3-GeV ERL, and so on. The SAC appreciated the management and staff of KEK and the PF for their efforts in recovering from the disaster and supporting our refurbishment plan, and made useful suggestions for the above issues. In particular, the SAC strongly endorsed KEK's strategy of designing, building and operating the 3-GeV ERL as a future next-generation light source serving the broad scientific community and appreciates the rationale behind the decision to change the energy from 5 GeV to 3 GeV. As part of the PF-SAC activities, a subcommittee meeting on time-resolved science was held in February 2012. This was the first meeting of the subcommittee, which greatly evaluated and appreciated the scientific activities of PF-AR NW14A and provided important suggestions. The committee also strongly supports the scope and strategy of the beamline.

Finally, I would like to mention the PF User Organization, “PF-Kondankai”. The PF-Kondankai has a long history and has worked in cooperation with the PF. PF-Kondankai members are all power users of the PF and have worked together to achieve scientific results in a variety of academic disciplines and industrial fields. However, the percentage of PF-Kondankai members among all PF users was only 20%. The PF-SAC suggested that the PF-Kondankai should raise this proportion to become more effective in assisting the PF and its future projects. The PF-Kondankai extensively discussed its transformation to the PF User Association (PF-UA) in which all PF users become members automatically in order to represent the entire PF user community. This transformation took place in April 2012. The SAC welcomed the proposal for a major change of the users' organization and fully supported a more independent user association with the broad membership of all PF Users. The SAC commended the PF management for this change which will make the PF user organization more in line with similar organizations at many international and domestic facilities.



Youichi Murakami

Memorials 2011

April 27-28, 2011 ERL Science Workshop II

After the massive earthquake, we began to work again towards the future. Participants actively discussed the future science, although the electric power was limited.



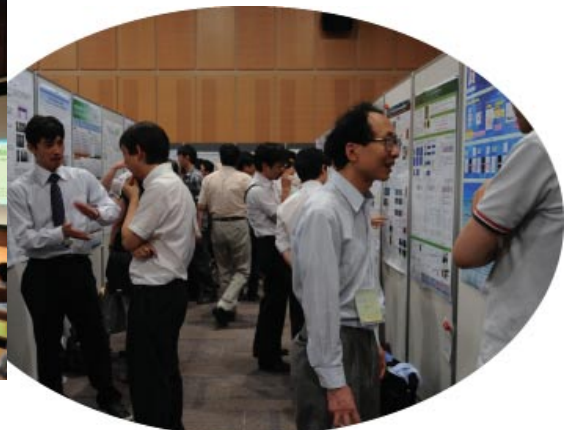
July 11, 2011 ERL Symposium

The sub-title of the ERL symposium was “Synchrotron radiation to realize a sustainable society”, and Dr. Hiroshi Komiyama, former president of the University of Tokyo, gave a special plenary talk.



July 12-13, 2011 28th PF Symposium

The 28th PF Symposium, which is the annual users' meeting, was held on July 12-13, 2011 at EPOCHAL Tsukuba. This meeting was originally scheduled to be held on March 14-15, but was postponed because of the earthquake on March 11.



 **August 19-27, 2011**
Summer Challenge



A summer school on “particle and nuclear physics” and “materials and biological science” was organized at KEK for a period of nine days. Some 88 undergraduate students from all over Japan attended this school, which included basic lectures, facility tours of the Tsukuba and Tokai campuses, and experimental courses.



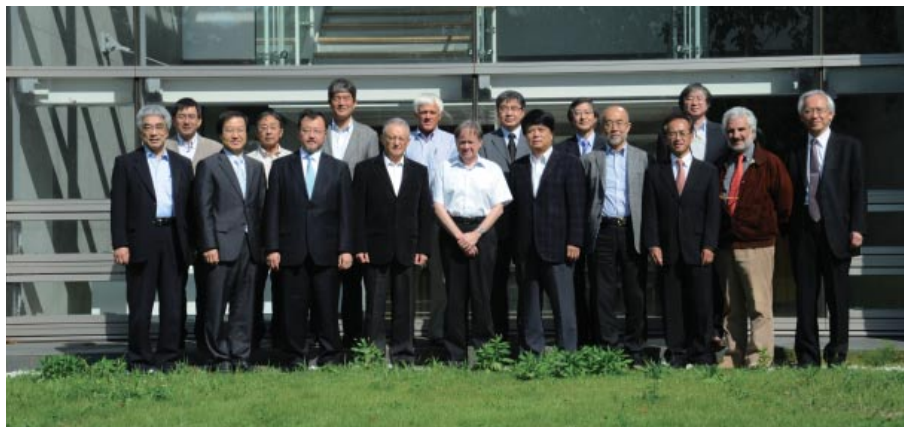
 **September 4, 2011**
Open House

There were a total of 3500 visitors to KEK on the day. All visitors enjoyed the pioneering world of modern materials, biological and accelerator science.



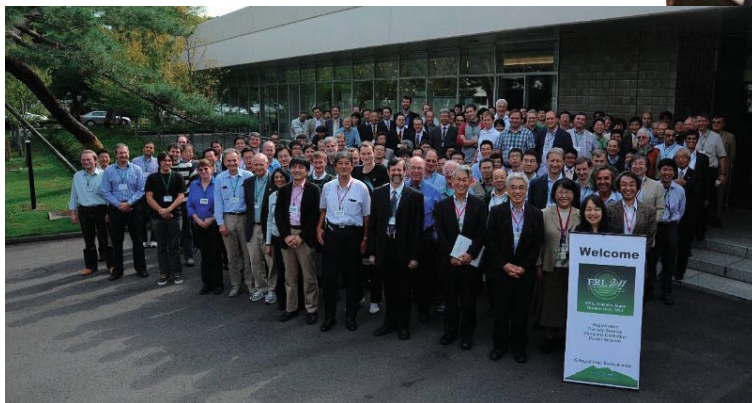
 **October 6-7, 2011**
PF-SAC

The 6th Photon Factory SAC meeting chaired by I. Lindau (Stanford Univ.) was held at KEK.



*October 16-21, 2011
ERL2011*

ERL2011, which was the 50th ICFA Advanced Beam Dynamics Workshop on Energy Recovery Linacs, was held and, accelerator technologies and applications based on the ERL was discussed.



*November 26-27, 2011
Summer Challenge in autumn*

The students who participated in the summer challenge in August performed actual experiments using synchrotron x-rays in the PF and PF-AR. This was the first trial, and was an excellent opportunity for the students.



*December 6-7, 2011
IMSS Symposium*

The 4th IMSS Symposium was held at EP-OCHAL TSUKUBA. The main theme of the symposium was "Prospects of Quantum Beam Sciences at IMSS-Strongly Correlated Systems and Future ERL Sciences".



 *March 14, 2012
ERL Symposium*

Prof. Ei-ichi Negishi of Purdue University, who won the Nobel Prize for Chemistry in 2010, gave a special plenary talk at the symposium.



 *March 15-16, 2012
29th PF Symposium*

This was a special symposium to celebrate the 30th anniversary of the PF. We had special lectures from Prof. K. Kohra (center), Prof. T. Sasaki (left), and Prof. K. Hodgson (right).



International Collaboration

 *November 14-16, 2011
SESAME School in Jordan*

The SESAME–JSPS School was held in Amman, Jordan. This school brought together world experts working in various synchrotron application fields along with students and young researchers who have the potential to become SESAME users. About 50 young scientists from seven different countries/regions (Egypt, Iran, Jordan, Morocco, Pakistan, Turkey, and the Palestinian Authority) attended the school.



 *January 23, 2012
MOU signed to promote research
collaboration with India*

An Indian delegation comprising five high-level officials visited KEK to participate in a joint meeting between the Department of Atomic Energy (DAE) and KEK. A memorandum of understanding was signed at the DAE-KEK meeting. The Indian delegation visited the Indian beamline (BL-18B) at the Photon Factory.



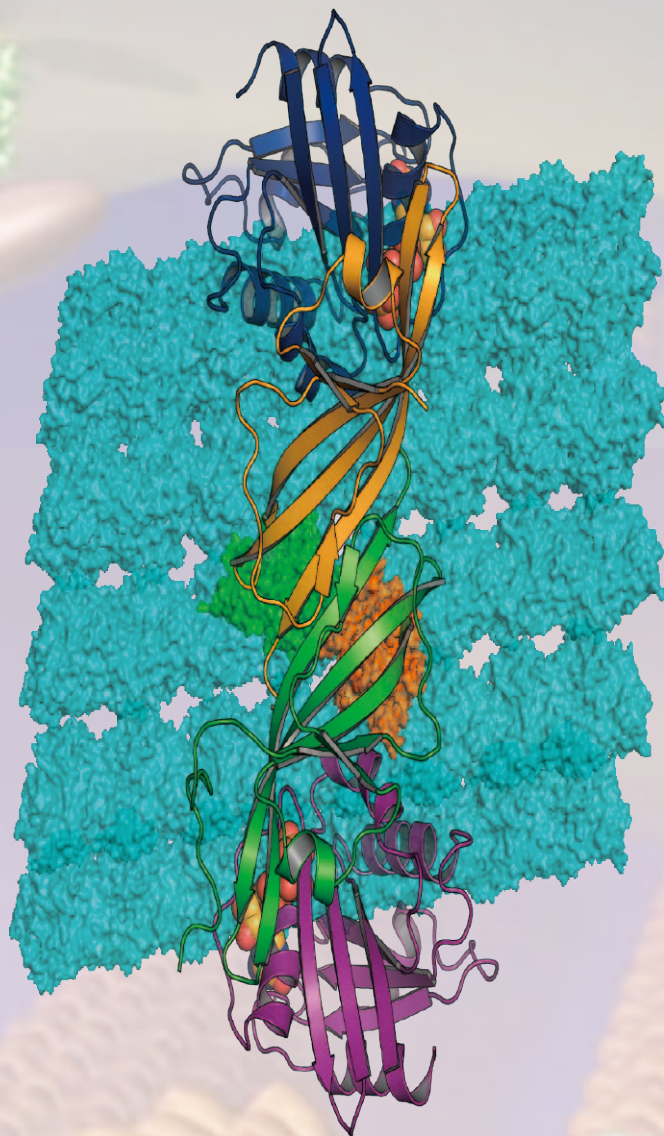


March 10, 2012
KEK-TRIUMF ERL workshop

The KEK-TRIUMF ERL Technology Workshop took place on March 10 at TRIUMF. The present status and future collaborations were discussed.



Highlights



HIGHLIGHTS

1. Atomic and Molecular Science	12
1-1 Evidence of Single-Photon Two-Site Core Double Ionization of C_2H_2 Molecules	
2. Materials Science	14
2-1 Inkjet Printing of Single-Crystal Organic Semiconductors	
2-2 Confinement of Strongly Correlated Electrons in Oxide Artificial Structures	
2-3 Chemically Homogeneous and Thermally Reversible Oxidation of Epitaxial Graphene: A Step Towards Better Performance Graphene-Based Electronics	
2-4 Origin of the Large Electric Polarization in Multiferroic Orthorhombic $YMnO_3$ Thin Films Revealed by Soft and Hard X-Ray Diffraction	
2-5 Key to the Metallic Conduction Found in an Insulator-Insulator Interface	
2-6 Magnetic-Field Control of Ferroelastic Domains in $FeCr_2O_4$	
2-7 Unconventional Mass Acquisition of Surface Dirac Fermions in a Topological Insulator	
2-8 Structural Study of the Unique Ferromagnetic Metal-Insulator Transition in Hollandite $K_2Cr_8O_{16}$	
2-9 Study of Structural Phase Transition of Pt-Induced Nanowire on Ge(001) Surface using Reflection High-Energy Positron Diffraction	
3. Chemical and Environmental Science	32
3-1 Quantum Effect and Anharmonicity in an Invar Alloy Studied by EXAFS Spectroscopy	
3-2 Combined in Situ QXAFS and FTIR Observation of a Ni Phosphide Catalyst - Determination of Active Species for a Hydrodesulfurization Reaction -	
3-3 Structural Basis for the Single Active Site to Catalyze Two Distinct Reactions in a Primitive Enzyme FBPA/P	
3-4 Observation of Structural Change upon Photoinduced Electron Transfer of 9-Mesityl-10-methylacridinium Ion by Pump-Probe X-Ray Crystal Structure Analysis	

4. Earth and Planetary Science	40
4-1 Synchrotron-Radiation X-Ray Analysis of HayabusaReturned Asteroidal Samples	
4-2 Observation of the Structure of Adsorbed Water on a Mica Surface to Understand the Mechanism of Creeping Faults	
5. Life Science	44
5-1 Discovery of Flowering Hormone (Florigen) Receptor and Its Crystal Structure	
5-2 Crystal Structure of Channelrhodopsin, a Light-Gated Cation Channel: All Cations Lead through the Monomer	
5-3 Structural Analysis of the Mammalian Cell Polarity Protein Complex mInsc and LGN	
5-4 Structural Basis of Measles Virus Entry and Effective Measles Vaccine	
5-5 Structural Basis of Arf6-MKLP1 Complex Formation on the Flemming Body Responsible for Cytokinesis	
5-6 Crystal Structure of the Rotor from V-ATPase Molecular Motor	
6. Imaging and Optics	56
6-1 Refraction-Contrast Tomosynthesis for a Breast Specimen	
7. Instrumentation and Methodology	58
7-1 Homogeneity Characterization of Lattice Spacing of Silicon Single Crystals by a Self-Referenced Lattice Comparator at BL-3C	
7-2 Production of an Energy-Tunable Positronium Beam	
8. Accerelators	62
8-1 Evaluation of Emittance Characteristics of Negative Electron Affinity GaAs-Based Photocathode	

Evidence of Single-Photon Two-Site Core Double Ionization of C_2H_2 Molecules

We present the first experimental evidence of molecular $K^{-1}K^{-1}$ states, where two K shell electrons are removed from two different atoms of the molecule. These states were produced by single photon double ionization, an extremely weak process that relies on electron correlation and is reasonably well described by an internal collision process. This proof-of-principle experiment opens up the way to establishing the spectroscopy of double core hole states (DCHs), which would overcome some limitations of the traditional ESCA technique (Electron Spectroscopy for Chemical Analysis), as discussed previously from a theoretical point of view.

Interest in DCHs was expressed 26 years ago by Cederbaum et al. [1], who predicted that $K^{-1}K^{-1}$ spectroscopy would distinguish the C_2H_{2n} series ($n = 1, 2$ and 3), while it was impossible to determine the nature of the C-C bond from traditional ESCA (K^{-1} spectroscopy). Theoretical interest revived recently [2] with the advent of X-ray free electron lasers (XFELs), which offer the possibility of creating DCHs in a two-photon process. Theory showed that DCHs spectroscopy gives direct access to the relaxation energy, a property of the final state. K^2 states, where two K shell electrons are missing from the same atom, have recently been observed both on XFELs [3] and on synchrotrons [4]. We present here the first evidence of $K^{-1}K^{-1}$ states formed by synchrotron radiation [5].

The experiments were carried out at the undulator beamline BL-16A in a single bunch top-up mode and used the magnetic bottle analyzer developed by the group of Professor K. Ito.

The process under study is shown schematically in Fig. 1: $K^{-1}K^{-1}$ states are populated by single photon core

double ionization. These excited states then decay by the sequential Auger decay of each core hole, releasing two Auger electrons of close energies, in the 200–250 eV range. Because of the dead time of our detector, these two Auger electrons are not distinguished in our experiment, and we searched for the weak $K^{-1}K^{-1}$ signal in the three-electron coincidence events which include detection of one such Auger electron. Figure 2(a) shows the energy correlation between the two other coincident electrons. It reveals a weak diagonal line associated with the formation of $K^{-1}K^{-1}$ states (red arrow), together with the more intense diagonal lines (green arrow) due to the formation of K^2 states. The projection in Fig. 2(b) of the two-dimensional map onto the $x=y$ diagonal reveals clearly the peaks associated with the $K^{-1}K^{-1}$ and K^2 states, from which their binding energies can be retrieved. As shown in Fig. 2(c), the K^2 states are more clearly revealed in four-electron coincidences where both released Auger electrons with well separated energies are detected. This part is similar to our previous work on the isoelectronic N_2 molecule [4].

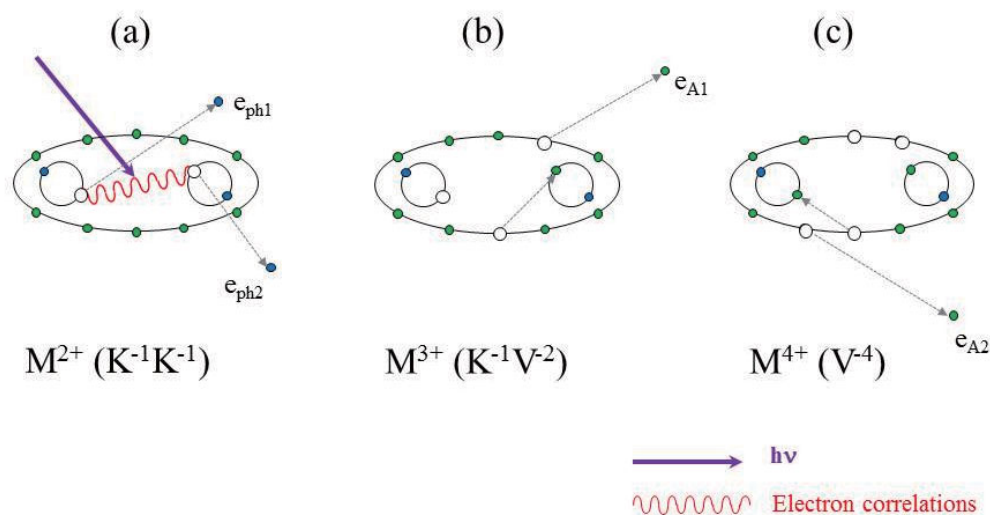


Figure 1

Schematic representation of the process studied here: single photon core double ionization creates a $K^{-1}K^{-1}$ state (a). This is followed by the sequential Auger decay of each core hole, populating first a $K^{-1}V^{-2}$ state (b) and then a V^{-4} one (c) (where V designates a valence shell).

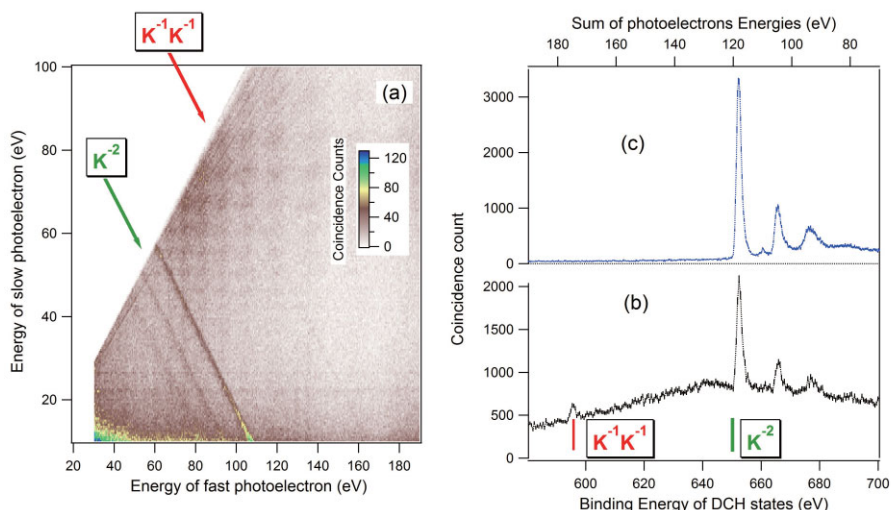


Figure 2

(a) Energy correlation map for the two photoelectrons emitted upon core double photoionization of the C_2H_2 molecule. All events considered here imply the coincidence detection of three electrons, one of them having an energy in the 230–250 eV range. (b) Histogram of the sum of the energies of the two photoelectrons, deduced from (a) integration along the diagonal lines. (c) Similar to (b), but the coincidence events imply here detection of four electrons, of which two each are in the 200–270 eV and 270–320 eV ranges. A photon energy of 770.5 eV was used.

From the number of coincidence events and taking into account the measured detection efficiencies, we estimated the relative probability P to create $K^{-1}K^{-1}$ states rather than K^{-2} states, that is, the ratio of the probability of extracting two K-shell electrons each from a different C atom to the probability that they are extracted from the same C atom. One obtains $P = 1.6 \pm 0.4\%$. The two-site K-shell double ionization process is reasonably well described by a simple internal collision model (knock-out) in which an initially ionized K shell electron collides and ejects a second K-shell electron from the neighboring atom. The model for the single-site K-shell double ionization process includes also the contribution from the shake-off mechanism. The resulting prediction of $P = 3.2\%$ [5] is in reasonable agreement with experiments.

Our work demonstrates that, in spite of the very low single-photon core double ionization probabilities, it is possible by this method to establish the spectroscopy of DCHs states, and even of the potentially more interesting $K^{-1}K^{-1}$ ones; we are currently exploring this subject. Our approach is also a relatively cheap alternative way of obtaining DCHs spectroscopic data without relying on two-photon absorption processes triggered by a XFEL source [6]. Our method seems also to be more precise and more selective, due to the multi-coincidence techniques that we use.

REFERENCES

- [1] L.S. Cederbaum, F. Tarantelli, A. Sgamellotti and J. Schirmer, *J. Chem. Phys.*, **85** (1986) 6513.
- [2] T. Darrah Thomas, *J. Phys. Chem. A*, **116** (2012) 3856 and references included.
- [3] L. Fang, M. Hoener, O. Gessner, F. Tarantelli, S.T. Pratt, O. Kornilov, C. Buth, M. Gühr, E.P. Kanter, C. Bostedt, J.D. Bozek, P.H. Bucksbaum, M. Chen, R. Coffee, J. Cryan, M. Glowina, E. Kukk, S.R. Leone and N. Berrah, *Phys. Rev. Lett.*, **105** (2010) 083005.
- [4] P. Lablanquie, F. Penent, J. Palaudoux, L. Andric, P. Selles, S. Carniato, K. Bučar, M. Žitnik, M. Huttula, J.H.D. Eland, E. Shigemasa, K. Soejima, Y. Hikosaka, I.H. Suzuki, M. Nakano and K. Ito, *Phys. Rev. Lett.*, **106** (2011) 063003.
- [5] P. Lablanquie, T.P. Grozdanov, M. Žitnik, S. Carniato, P. Selles, L. Andric, J. Palaudoux, F. Penent, H. Iwayama, E. Shigemasa, Y. Hikosaka, K. Soejima, M. Nakano, I.H. Suzuki and K. Ito, *Phys. Rev. Lett.*, **107** (2011) 193004.
- [6] P. Salén, P. van der Meulen, H.T. Schmidt, R.D. Thomas, M. Larsson, R. Feifel, M.N. Piancastelli, L. Fang, B. Murphy, T. Osipov, N. Berrah, E. Kukk, K. Ueda, J.D. Bozek, C. Bostedt, S. Wada, R. Richter, V. Feyer and K.C. Prince, *Phys. Rev. Lett.*, **108** (2012) 153003.

BEAMLINER

16A

P. Lablanquie¹, T. P. Grozdanov², M. Žitnik³, S. Carniato¹, P. Selles¹, L. Andric¹, J. Palaudoux¹, F. Penent¹, H. Iwayama⁴, E. Shigemasa⁴, Y. Hikosaka⁵, K. Soejima⁵, M. Nakano⁶, I.H. Suzuki⁶ and K. Ito⁶
¹LCP-MR, ²IP-Belgrade, ³JSI, ⁴IMS, ⁵Niigata Univ., ⁶KEK-PF)

Inkjet Printing of Single-Crystal Organic Semiconductors

We have developed a printing technology to manufacture single-crystalline organic semiconductor films. This “double-shot inkjet printing” method introduces a technique of antisolvent crystallization into the microfluidic inkjet printing processes. We found that the sequential deposition of an antisolvent and a semiconductor solution can trigger the controlled formation of exceptionally uniform thin films. The observed out-of-plane and in-plane Bragg diffractions clearly demonstrated the single crystal nature of the films. Using this approach, we obtained printed single-crystal organic transistors with very high carrier mobility.

Printing technology is usually used to reproduce characters or pictures such as photographs on paper by the patterned deposition of inks. However, the technology has recently attracted considerable attention in the field of electronics as a new way of manufacturing electronic products: fine electronic circuits could be produced, or printed, with micrometer resolution on a plastic sheet, and the technology would make electricity-hungry vacuum facilities unnecessary. In addition, the use of plastic sheets should lead to “flexible electronic” products which are light-weight, thin, and impact-resistant, revolutionizing the electronics industry. In order to realize such “printed electronics”, the most important challenge is to produce high-performance thin-film transistors (TFTs), indispensable building blocks for large-area electronics products such as active-matrix flat panel displays, by a printing method.

In 2011, a new printing technology was successfully developed to produce single-crystal thin films of organic semiconductors with molecularly flat surfaces under ambient conditions [1]. The novel “double-shot inkjet printing” technique involves the alternating print

deposition of microliquid droplets both of ink composed of a dissolved organic semiconductor and of another ink that prompts crystallization of the organic semiconductor. Figure 1 presents a schematic of this printing technique. The crystallization ink is first deposited from an inkjet head, and the semiconductor ink is then overprinted from another inkjet head to form an intermingled microliquid droplet. Here, C_8 -BTBT (2,7-dioctyl[1]benzothieno[3,2-b][1]benzothiophene) [2] was used as the organic semiconductor. A supersaturated state of the organic semiconductor is immediately formed in the intermingled droplet, which results in the slow film growth of the organic semiconductor at the liquid-air interface of the droplet. Particularly, it was found that by appropriately designing the deposited pattern on the sheets, the growth direction of the semiconductor layer could be controlled. Thus the technique allows the production of semiconductor thin films with highly uniform thickness at arbitrary positions reproducibly, which is extremely difficult to achieve by conventional printing techniques.

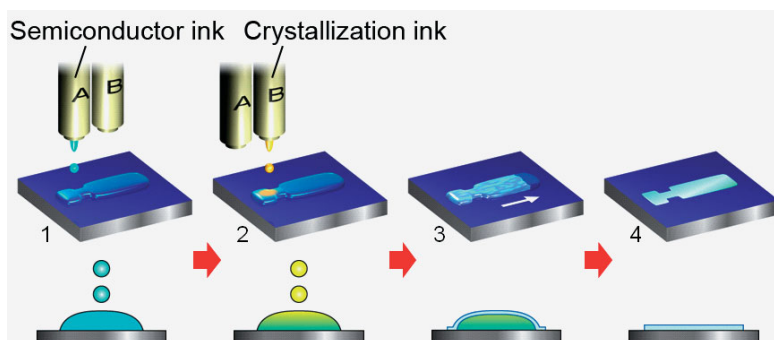


Figure 1 Schematic for producing semiconductor single-crystal thin films by the double-shot inkjet printing technique [1].

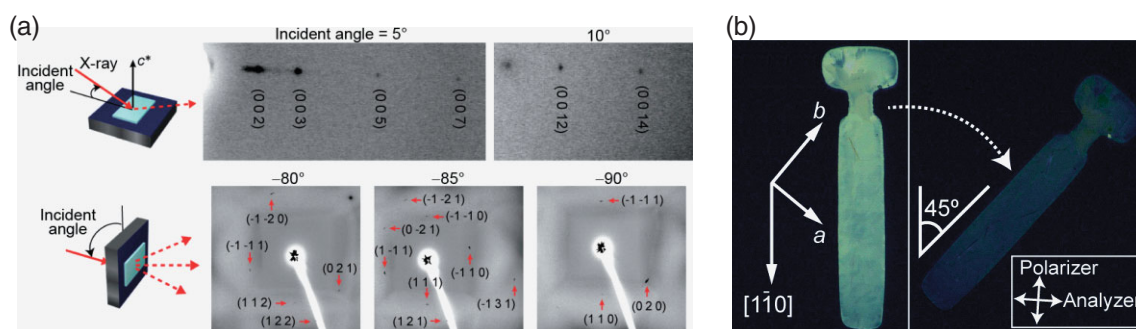


Figure 2

(a) Synchrotron X-ray oscillation photographs of the organic semiconductor single-crystal thin films. Out-of-plane (upper) and in-plane diffractions (lower), (b) Crossed-Nicols polarized micrographs for the organic semiconductor single-crystal thin films [1].

The single crystal nature of the films was investigated by synchrotron X-ray diffraction at the Photon Factory of KEK. It was found that all the diffractions were observed as clear spots [Fig. 2(a)]. The observation of Bragg reflections up to the 14th order indicates that the films have a highly crystalline nature. At high incident angles of the X-rays, we observed 16 Bragg reflections including an in-plane component. The refined unit cell based on the analyses of the observed diffractions is consistent with that of C_8 -BTBT. The films were also investigated by a crossed-Nicols microscope. It was found that the color of almost the entire film uniformly changes from bright to dark when the film was rotated around an axis perpendicular to the film surface [Fig. 2(b)]. This indicates that the whole film is uniformly optically anisotropic. From these results we conclude that the inkjet-printed semiconductor thin films are composed of single-domain crystals. Organic TFTs composed of the inkjet-printed C_8 -BTBT single crystal films exhibit high mobility reaching as high as $16.4 \text{ cm}^2/\text{Vs}$ on average. The on/off current ratio is larger than 10^5 , and the sub-threshold slope is about 2 V per decade. The mobility value is more than 10 times higher than that of amorphous sili-

con TFTs which are used in conventional liquid-crystal displays, and 100 times as high as that of organic TFTs produced by the conventional printing methods.

The newly-developed double-shot inkjet printing technique will be useful for manufacturing organic semiconductor thin films with high uniformity and for improving the performance of the TFTs, which have been major challenges in the printed electronics technology. This technology will greatly accelerate the research and development of flexible electronic devices.

REFERENCES

- [1] H. Minemawari, T. Yamada, H. Matsui, J. Tsutsumi, S. Haas, R. Chiba, R. Kumai and T. Hasegawa, *Nature*, **475** (2011) 364.
- [2] H. Ebata, T. Izawa, E. Miyazaki, K. Takimiya, M. Ikeda, H. Kuwabara and T. Yui, *J. Am. Chem. Soc.*, **129** (2007) 15732.

BEAMLINER

8A

H. Minemawari¹, T. Yamada¹, H. Matsui¹, J. Tsutsumi¹, R. Kumai² and T. Hasegawa¹ (¹AIST, ²KEK-PF)

Confinement of Strongly Correlated Electrons in Oxide Artificial Structures

The quantum confinement of strongly correlated electrons in artificial structures provides an ideal platform for studying the behavior of correlated Fermi-liquid states in reduced dimensions. We have succeeded in creating a quantum well structure using a strongly correlated oxide of SrVO₃, and have for the first time observed the quantized states that demonstrate the confinement of strongly correlated electrons in the artificial oxide structure. By means of *in situ* angle-resolved photoemission spectroscopy, the unique behavior of the corralling strongly correlated electrons in two-dimensional space was revealed.

Depending on the number of conductive layers, layered strongly correlated oxides often exhibit unusual physical properties, such as high-temperature superconductivity in cuprates [1]. The properties originate from the stacked conductive layers sandwiched by block insulating layers, where strongly correlated electrons are confined in the two-dimensional space. The lowering of the dimensionality changes the interaction among the spin, charge, and orbital degrees of freedom. Thus, the close structural similarities of layered oxides to metallic quantum well (QW) structures have motivated researchers to create low-dimensional systems using artificial structures of a strongly correlated oxide. However, metallic QW states exhibiting dimensional controllability have not yet been achieved in oxide artificial structures.

We have for the first time succeeded in confining strongly correlated electrons in the artificial oxide structure based on SrVO₃ [2]. The critical factors for success with the quantum confinement were (1) precise growth control of a conductive oxide on an atomic scale using laser molecular beam epitaxy and (2) state-of-the-art angle-resolved photoemission (ARPES) spectroscopy using the synchrotron radiation available at the Photon Factory. Utilizing these growth and characterization techniques, we confirmed that strongly correlated electrons were confined in the quantum well of an artificial oxide structure.

Figure 1 shows the ARPES spectra for SrVO₃ ultrathin films varying in overlayer thickness obtained at the Γ and X points. The energy positions of the several quasi-periodic peaks evolved as a function of the overlayer thickness: with increasing thickness, one additional peak appears after another in the ARPES spectra at the

Fermi level (E_F), and their peak positions shift to higher binding energies. The peak shift apparently converges at around 500 meV. The experimental data were adequately described by the usual phase-shift quantization rule [3], indicating the successful creation and control of metallic QW states in artificial oxide structures.

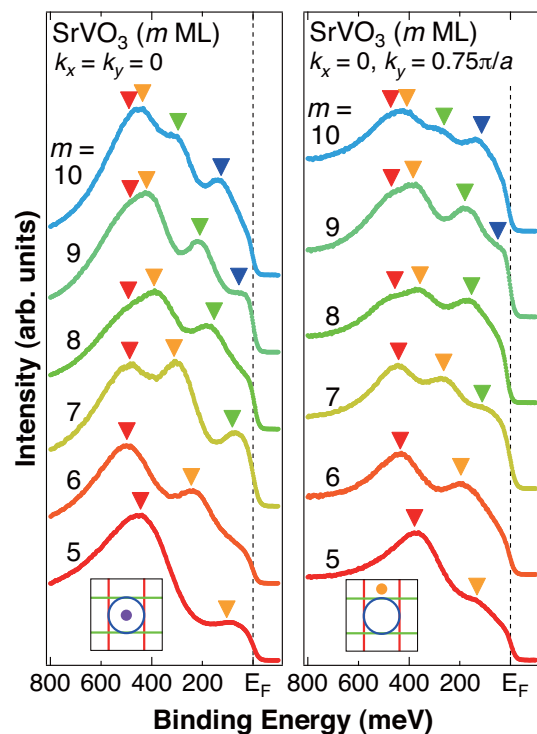


Figure 1 Thickness dependent ARPES spectra of SrVO₃ ultrathin films obtained at the Γ (left) and X (right) points. The peak structures derived from metallic QW states are marked by the triangle.

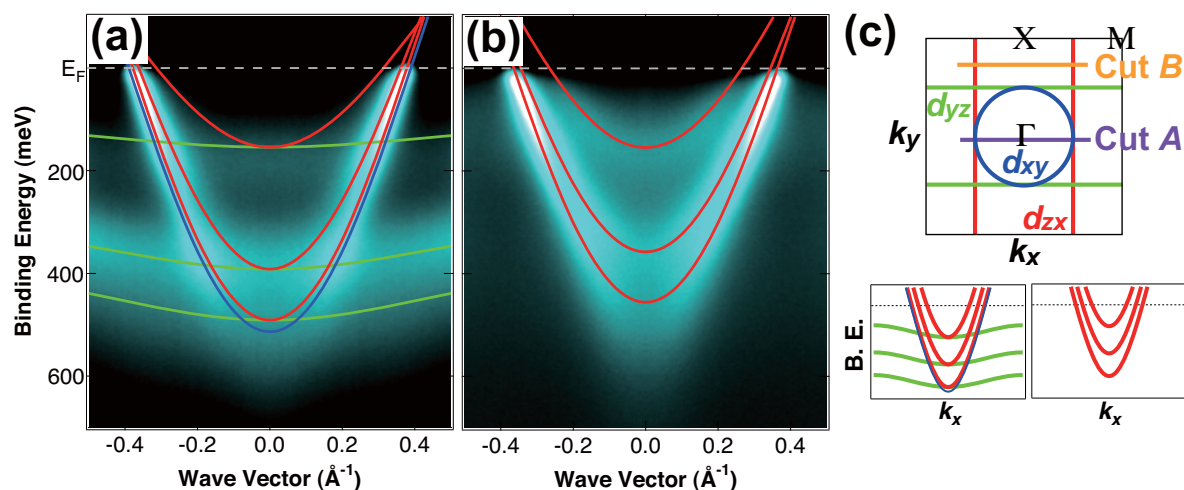


Figure 2 In-plane band dispersion of SrVO₃ (8 ML) ultrathin films along (a) Cut A and (b) Cut B. (c) Fermi surface cross section in Γ X-M plane of bulk SrVO₃ and expected subband dispersions of SrVO₃ ultrathin films.

Furthermore, additional investigation revealed the existence of other interesting phenomena in the QW states (Fig. 2): 1) orbital-selective quantization originating from the anisotropic orbital character of the V 3d states and 2) unusual enhancement of the effective mass of the quantized electrons, reflecting complex interactions in the quantum well, neither of which has previously been reported in the conventional quantum well states in noble metals [3].

The orbital-selective quantization of the QW states is clearly observed in the in-plane band dispersion determined by ARPES. As can be seen in Fig. 2, a set of subbands is clearly observed corresponding to the different V 3d orbitals. Two types of subbands were observed for the band dispersion along cut A [Fig. 2(a)]; one is the parabolic band, which approaches and eventually crosses E_F with increasing distance from the Γ point, whereas the other is the nearly flat band. These two bands degenerate at the Γ point. In contrast, only parabolic subbands were observed along cut B [Fig. 2(b)]. In comparison to the tight-binding calculation, the flat bands seen only in Fig. 2(a) and the parabolic band seen in both cases originate from the quantized d_{yz} and d_{zx} states, respectively. On the other hand, the d_{xy} state remains unchanged because of its 2D character in the xy plane.

The unusual band renormalization is also seen in the in-plane band dispersion. The subband dispersion becomes considerably narrower (the effective mass of the subbands is considerably enhanced) as its bottom energy approaches E_F . The mass enhancement in the subbands is associated with strong interaction among V 3d electrons confined in the QW structures [2].

This successful creation and control of the metallic quantum well states in artificial structures of a strongly correlated oxide is a significant first step toward creating new physical phenomena and controlling the novel physical properties of strongly correlated oxides. The present results pave the way to a new world of “strongly correlated electronics”.

REFERENCES

- [1] M. Imada, A. Fujimori and Y. Tokura, *Rev. Mod. Phys.*, **70** (1998) 1039.
- [2] K. Yoshimatsu, K. Horiba, H. Kumigashira, T. Yoshida, A. Fujimori and M. Oshima, *Science*, **333** (2011) 319.
- [3] T.-C. Chiang, *Surf. Sci. Rep.*, **39** (2000) 181.

BEAMLINES

28A and 2C

K. Yoshimatsu¹, K. Horiba^{1,2}, T. Yoshida¹, A. Fujimori¹, M. Oshima¹ and H. Kumigashira^{1,3,4} (¹The Univ. of Tokyo, ²UT-SRRO, ³KEK-PF&CMRC and ⁴PREST-JST)

Chemically Homogeneous and Thermally Reversible Oxidation of Epitaxial Graphene: A Step Towards Better Performance Graphene-Based Electronics

Graphene, a one-atom thick, honeycomb-shaped lattice of carbon atoms with exceptional physical and electronic properties, is promising for next-generation electronics applications. Many researchers and engineers consider that graphene could be a rival to silicon in creating faster, thinner and flexible electronic devices. However, a major challenge in realizing graphene-based electronics is to make the electronic properties of graphene tunable. Unlike semiconductors such as silicon, pure graphene is a zero band-gap material, making it difficult to electrically ‘turn-off’ the flow of current through it. Therefore, pristine graphene is not suitable for the digital circuitry that comprises the vast majority of integrated circuits.

In an attempt to control its properties and make graphene more functional, many researchers have been investigating methods for chemically altering graphene. The most widely used strategy is ‘‘Hummer’s method’’ which oxidizes graphene [1]. However, the chemical inhomogeneity and irreversibility of the resulting graphene oxide surface arise because of the use of aggressive oxidizing agents [2, 3]. Collaborative work between US and Japanese researchers of different institutes including Northwestern University, Gunma University, The University of Tokyo, and RIKEN has recently led to the development of a new method to oxidize graphene that overcomes the collateral damage encountered in Hummer’s method.

Chemical modification of graphene is very difficult because of the bonding nature of the carbon atoms forming hexagonal networks. Typically, researchers employ strong acidic conditions, such as those used in Hummer’s method [1], but these damage the honeycomb-shaped lattice and result in a material that is difficult to control. Here, we present an alternative approach for oxidizing epitaxial graphene using atomic oxygen in ultrahigh vacuum. In our method, we introduced oxygen gas (O_2) into an ultra-high vacuum chamber, which housed a hot tungsten filament ($\sim 1500^\circ\text{C}$) that caused the oxygen molecules to dissociate into atomic oxygen.

The highly reactive oxygen atoms then uniformly bonded to the graphene lattice.

The graphene oxide thus formed in ultra-high vacuum is chemically homogeneous and thermally reversible, which can lead to well-controlled properties and can be exploited in high-performance electronics. The chemical homogeneity and reversibility of the oxidized graphene were characterized by various surface probe techniques including scanning tunneling microscopy (STM) and high-resolution X-ray photoelectron spectroscopy (HR-XPS) [4]. HR-XPS measurements were performed using a Scienta SES-200 at the Photon Factory BL-13A (KEK-PF PAC 2009S2 007), Japan. The incident and emission angles with respect to the surface normal for the photon and photoelectron beams were 65° and 0° , respectively. The total energy resolution was ~ 70 meV.

Typical STM images of pristine and oxidized graphene on the SiC(0001) substrate are shown in Fig. 1. Careful inspection reveals that each oxygen feature has a uniform appearance in STM images, which suggests a chemically uniform binding state for atomic oxygen on epitaxial graphene. Chemical homogeneity is further confirmed by HR-XPS. Although the chemisorbed oxygen is stable at room temperature, it can be reversibly removed by annealing the oxidized surface at 260°C .

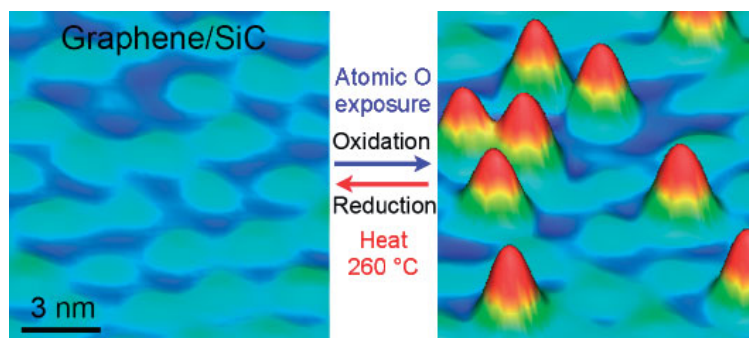


Figure 1 Scanning tunneling microscope (STM) images of before (left) and after (right) oxidation of graphene on a silicon carbide (SiC) substrate. Pyramidal-shaped protrusions in the right image are the individual oxygen atoms bonded to the graphene lattice. STM images were acquired at a sample bias of $+2.4$ V and a tunneling current of 50 pA.

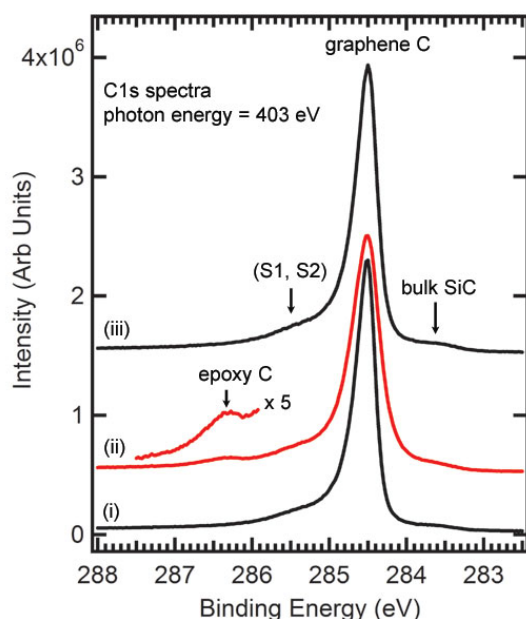


Figure 2. C1s X-ray photoelectron spectra measured at KEK-PF BL13A (PF-PAC: 2009S2 007). (i) Pristine epitaxial graphene on an SiC substrate. (ii) Oxidized graphene using atomic oxygen in UHV (red). (iii) The clean graphene was recovered after heating at 260°C. S1 and S2 peaks are ascribed to the buffer layer C atoms. $h\nu = 403$ eV.

Figure 2 shows a series of C 1s XPS spectra of (i) pristine graphene on an SiC substrate, (ii) graphene oxidized by atomic oxygen in UHV and (iii) annealed graphene at 260°C. In the HR-XPS spectrum of Fig. 2(ii), the C1s peak at 286.3 eV, which is located at 1.8 eV higher binding energy than the sp^2 C1s peak of graphene, is ascribed to the epoxy species on the epitaxial graphene surface [5]. Note that S1 is ascribed to the carbon atoms in the $(6\sqrt{3} \times 6\sqrt{3})R30^\circ$ structure bound

to one Si atom of the SiC(0001) surface and to three C atoms in the sp^2 -bonded layer, and S2 is the component emitted from the remaining sp^2 -bonded carbon atoms in the buffer layer. After annealing at 260°C, the C1s peak corresponding to the epoxy species completely disappears, and the spectrum of pristine epitaxial graphene is reestablished [Fig. 2 (iii)].

These results clearly indicate that the original pristine epitaxial graphene surface can be recovered by thermal reduction of the oxidized surface; the UHV oxidation–reduction process is fully reversible, in stark contrast to the highly defective and partially oxidized surface that results from the reduction of Hummers-method graphene oxide. We think that this is an important step towards realizing new classes of two-dimensional nanomaterials by chemical modification of graphene.

REFERENCES

- [1] W.S. Hummers and R.E. Offeman, *J. Am. Chem. Soc.*, **80** (1958) 1339.
- [2] C.G. -Navarro, J.C. Meyer, R.S. Sundaram, A. Chuvilin, S. Kurasch, M. Burghard, K. Kern and U. Kaiser, *Nano Lett.*, **10** (2010) 1144.
- [3] A. Bagri, C. Mattevi, M. Acik, Y.J. Chabal, M. Chhowall and V.B. Shenoy, *Nature Chem.*, **2** (2010) 581.
- [4] Md.Z. Hossain, J.E. Johns, K.H. Bevan, H.J. Karmel, Y.T. Liang, S. Yoshimoto, K. Mukai, T. Koitaya, J. Yoshinobu, M. Kawai, A.M. Lear, L.L. Kesmodel, S.L. Tait and M.C. Hersam, *Nature Chem.*, **4** (2012) 305.
- [5] N.A. Vinogradov, K. Schulte, M.L. Ng, A. Mikkelsen, E. Lundgren, N. Mårtensson and A.B. Preobrajenski, *J. Phys. Chem. C*, **115** (2011) 9568.

BEAMLIN

13A

Md. Zakir Hossain¹ and J. Yoshinobu² (¹Gunma Univ., ²The Univ. of Tokyo).

Origin of the Large Electric Polarization in Multiferroic Orthorhombic YMnO_3 Thin Films Revealed by Soft and Hard X-Ray Diffraction

We investigated the magnetic structure of a multiferroic orthorhombic YMnO_3 thin film by resonant soft X-ray and hard X-ray diffraction. We observed a temperature-dependent incommensurate magnetic reflection below 45 K and a commensurate lattice-distortion reflection below 35 K. These results demonstrate that the ground state is composed of coexisting E -type and cycloidal antiferromagnetic states. Their different ordering temperatures confirm that the origin of the large polarization is the E -type antiferromagnetic states in the orthorhombic YMnO_3 thin film.

Recently, there has been a lot of interest in multiferroic materials displaying both ferroelectric and magnetic orders [1-3]. It is of particular importance to control magnetization (electric polarization) by an electric (magnetic) field. Orthorhombic (o) RMnO_3 (R denotes rare earth metal) with perovskite structure belongs to this category and can be viewed as a prototypical multiferroic material. The fabrication of o - RMnO_3 thin films is especially important for the application of multiferroic materials in devices. Recently, Nakamura et al. reported the fabrication of o - YMnO_3 thin films on a YAIO_3 (010) substrate [4]. Their thin film showed a ferroelectric transition at 40 K with a large saturation electric polarization of $0.8 \mu\text{C}/\text{cm}^2$. The ferroelectric polarization could be controlled by a magnetic field, demonstrating magnetoelectric behavior. In this work, we investigated the magnetic structure of a multiferroic orthorhombic YMnO_3 thin film by resonant soft X-ray and hard X-ray diffraction to clarify the exact magnetic structure [5].

A thin film (40 nm) of YMnO_3 was grown on a YAIO_3 (010) substrate by pulsed-laser deposition. The details

of the sample fabrication were described elsewhere [4]. Resonant soft X-ray diffraction experiments were performed on the RESOXS end station at the surface-interface microscopy (SIM) beamline of the Swiss Light Source of the Paul Scherrer Institut, Switzerland. Hard X-ray diffraction experiments were performed on beamlines 3A and 4C at the Photon Factory, KEK, Japan. The photon energy of the incident X-ray was 12 keV.

Figure 1 shows the temperature dependence of the $(0 q_b 0)$ ($q_b \sim 0.5$) peak with π incident X-ray polarizations. Here, the diffraction data were taken at $h\nu = 643.1$ eV ($\text{Mn } 2p_{3/2} \rightarrow 3d$ absorption edge). This peak, which is indicated by vertical bars, appears at 45 K, which coincides with the antiferromagnetic transition temperature T_N determined from magnetization measurements [4]. Weaker peaks are observed on both sides of the reflection. These are antiferromagnetic Kiessig fringes, and describe the limited thickness of the magnetic contrast of the film. The intensity of the peaks increases monotonically with cooling. The peak position deviates from the commensurate $q_b = 1/2$ position for all temperatures.

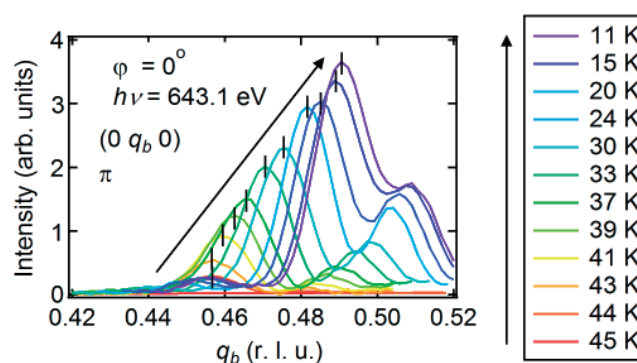


Figure 1

Temperature dependence of the $(0 q_b 0)$ ($q_b \sim 0.5$) peak in π incident X-ray polarizations. The intensity of the peaks increases monotonically with cooling. The data were taken at $h\nu = 643.1$ eV ($\text{Mn } 2p_{3/2} \rightarrow 3d$ absorption edge).

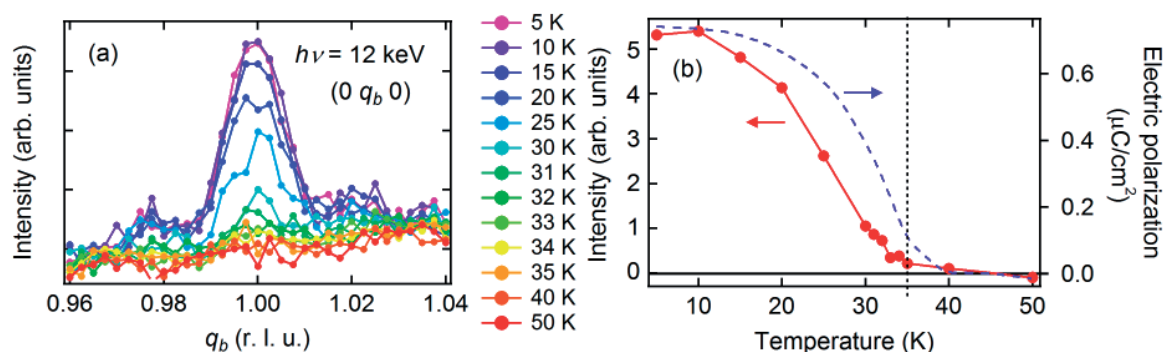


Figure 2
Temperature dependence of the (0 1 0) peak taken at $h\nu = 12$ keV. In panel (b), peak intensities are plotted as a function of temperature together with the electric polarization (broken lines) taken from Ref. [4]. The temperature of 35 K is also indicated as the onset of the (0 1 0) peak and the step onset of the spontaneous electric polarization.

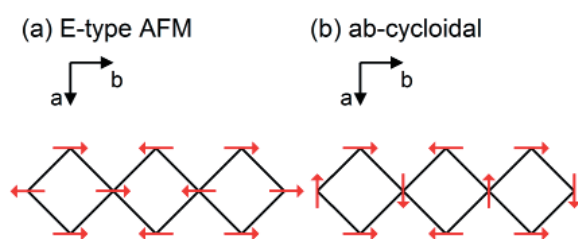


Figure 3
Spin structures in the *E*-type (a) and the *ab*-cycloidal (b) antiferromagnetic states. (a) Spins align antiparallel to each other, resulting in a large lattice strain and large electric polarization. (b) Spins align helically along the *b*-axis, resulting in small electric polarization.

In order to investigate the lattice distortions associated with magnetic order and electric polarization, we performed hard X-ray diffraction measurements of the YMnO_3 thin film. The commensurate (0 1 0) reflection appears below 35 K as shown in Fig. 2. This reflection is structurally forbidden in the chemical high-temperature structure (space group: Pbnm) and is caused by the lattice distortion accompanying ferroelectricity. Interestingly, no incommensurability of this reflection is observed by hard X-ray diffraction, in clear contrast to the observed magnetic reflection. Moreover, this reflection does appear below 35 K, at lower temperatures than the onset of the magnetic reflection, in accordance with the step onset of the spontaneous electric polarization [4], as can be seen from the temperature-dependent integrated intensity shown in Fig. 2 (b).

We can obtain a full picture of the magnetic states of the epitaxial YMnO_3 thin film by combining the above re-

sults with the macroscopic measurements of magnetization and electric polarization [4]. The ground state of the YMnO_3 thin film can be explained by the coexistence of the cycloidal and the *E*-type states as shown in Fig. 3 and as theoretically predicted [6]. In this coexistence region, magnetic reflection is incommensurate and lattice peaks are commensurate because the *E*-type phase has a much larger lattice distortion than the cycloidal phase. The existence of the *E*-type phase causes the large electric polarization of $0.8 \mu\text{C}/\text{cm}^2$ due to the symmetric exchange striction.

REFERENCES

- [1] Y. Tokura, *Science*, **312** (2006) 1481.
- [2] S.-W. Cheong and M. Mostovoy, *Nature Mater.*, **6** (2007) 13.
- [3] Y. Tokura and S. Seki, *Adv. Mater.*, **22** (2010) 1554.
- [4] M. Nakamura, Y. Tokunaga, M. Kawasaki and Y. Tokura, *Appl. Phys. Lett.*, **98** (2011) 082902.
- [5] H. Wadati, J. Okamoto, M. Garganourakis, V. Scagnoli, U. Staub, Y. Yamasaki, H. Nakao, Y. Murakami, M. Mochizuki, M. Nakamura, M. Kawasaki and Y. Tokura, *Phys. Rev. Lett.*, **108** (2012) 047203.
- [6] M. Mochizuki, N. Furukawa and N. Nagaosa, *Phys. Rev. Lett.*, **105** (2010) 037205.

BEAMLINES

3A and 4C

H. Wadati¹, J. Okamoto², M. Garganourakis³, V. Scagnoli³, U. Staub³, Y. Yamasaki², H. Nakao², Y. Murakami², M. Mochizuki¹, M. Nakamura⁴, M. Kawasaki^{1,4} and Y. Tokura^{1,4} (¹The Univ. of Tokyo, ²KEK-PF, ³Swiss Light Source, ⁴RIKEN)

Key to the Metallic Conduction Found in an Insulator-Insulator Interface

Two kinds of transition metal oxide ultrathin film, one which exhibits anomalous conductivity and another which is insulating, were examined by the crystal truncation rod scattering technique combined with holographic analysis. Successive least squares structure refinements revealed the difference in atomic intermixing at the interface as well as the local polarization. The conductive interface has a wide polarized region, whereas the insulating interface has a small polarized region. This difference in polarization gives different amounts of band bending, which accounts for the conductive properties.

Physical properties that emerge only at interfaces have long been the focus of great interest. A classic example is the semiconductor diode, and a modern example is metal oxide heterostructures. The interfaces between transition metal oxides appear to be promising for device application because of the wide variety of properties of metal oxides and the availability of highly precise film fabrication techniques.

Interfaces between LaAlO_3 (LAO) and SrTiO_3 (STO) show anomalous conductivity. Although both LAO and STO are band insulators, the interface between TiO_2 -terminated STO and LAO (n-type interface) shows metallic conductivity [1]. Interestingly, the anomalous conductivity disappears when the substrate is changed to SrO-terminated STO (p-type interface). This fact was first reported in 2004 [1], and attracted great interest. Within a few years, the sample growth technique had matured and various groups reported consistent trans-

port properties: for example, the carriers are distributed in STO within ~ 10 nm from the interface [2]. It is now clear that the difference in structure, n-type and p-type, causes the difference in conductivity. Therefore, the key to conduction is likely to be found in the structure. The detailed structures of both types of interface were analyzed by surface X-ray diffraction experiments performed at BL-3A [3].

Five-unit-cell thick LAO ultrathin films were fabricated by means of pulsed laser deposition (PLD). Four inequivalent crystal truncation rods (CTRs) were measured for each sample with 12-keV X-ray at room temperature in air. Examples of the observed CTRs for the n-type and the p-type samples are shown in Fig. 1 [3]. Other than the substrate Bragg reflections, broad undulations reflecting the thin LAO structures are clearly seen. The total scattering amplitude reflects the Fourier transform of the electron density near the surface.

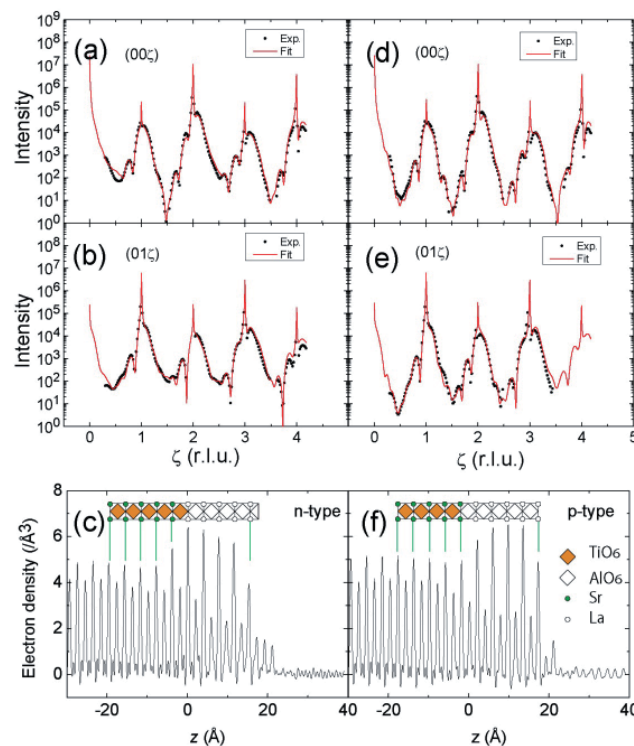


Figure 1 X-ray scattering intensity profiles along (a) the (00ζ) -line and (b) the (01ζ) -line for the n-type sample. The depth profile of the electron density, obtained from the electron density analysis performed on the (00ζ) rod, is shown in (c). Panels (d)-(f) show those for the p-type sample. Figure taken from [3], copyright (2011) by the American Physical Society.

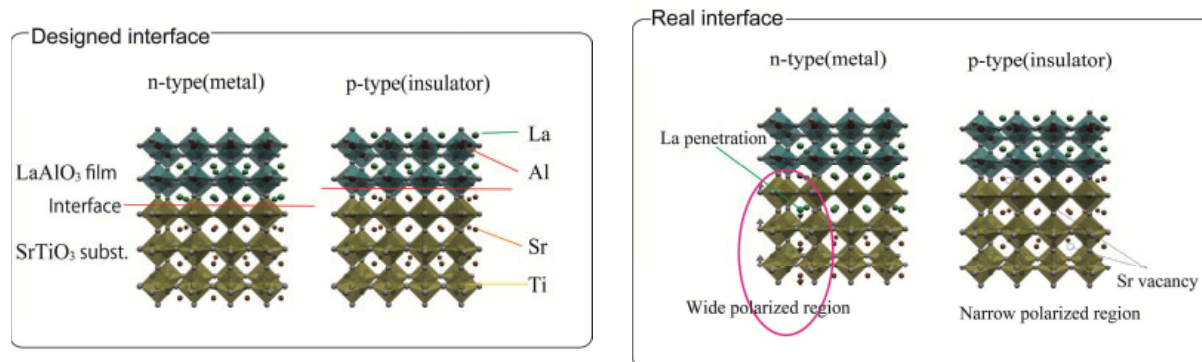


Figure 2
Schematic view of the designed and the observed structures of n-type and p-type interfaces.

The electron density profiles obtained by a holographic analysis applied to 00ζ profiles are shown in Figs. 1 (c) and (f). The structural parameters were refined by a least squares fitting using the peak positions and areas in Figs. 1 (c) and (f) as the starting models. Note that the number of structural parameters of an ultrathin film is large, and the holographic analysis played a significant role to obtain a physically reasonable structure. As a result, we found a structure difference between the two types of interface as shown in Fig. 2. The observed interfacial structure was different from the designed structure in some aspects, particularly in the degree of La inter-diffusion and the polarization. The former corresponds to the formation of the conductive $(\text{La,Sr})\text{TiO}_3$ for one monolayer only in the n-type interface [4]. While it appears to be the origin of the anomalous conduction, the formation of one monolayer $(\text{La,Sr})\text{TiO}_3$ cannot account for the thickness of the carrier distribution [2]. The latter feature is more important. Significant polarization was found only in STO in the n-type sample. This polarization causes large band bending, which can make the interface conductive. In the insulating p-type interface, by contrast, detectable polariza-

tion was suppressed within 1 nm. This screening of the polarization caused by the cation deficiency makes the band bending small, resulting in the difference in conductivity.

REFERENCES

- [1] A. Ohtomo and H.Y. Hwang, *Nature*, **427** (2004) 423.
- [2] M. Basletic, J.-L. Maurice, C. Carretero, G. Herranz, O. Copie, M. Bibes, E. Jacquet, K. Bouzehouane, S. Fusil and A. Barthelemy, *Nature Materials*, **7** (2008) 621; C. Bell, S. Harashima, Y. Kozuka, M. Kim, B.G. Kim, Y. Hikita and H.Y. Hwang, *Phys. Rev. Lett.*, **103** (2009) 226802.
- [3] R. Yamamoto, C. Bell, Y. Hikita, H.Y. Hwang, H. Nakamura, T. Kimura and Y. Wakabayashi, *Phys. Rev. Lett.*, **107** (2011) 036104.
- [4] P.R. Willmott, S.A. Pauli, R. Herger, C.M. Schlepütz, D. Martoccia, B.D. Patterson, B. Delley, R. Clarke, D. Kumah, C. Cionca and Y. Yacoby, *Phys. Rev. Lett.*, **99** (2007) 155502.

BEAMLINe

3A

Y. Wakabayashi¹, R. Yamamoto¹, C. Bell², Y. Hikita², H.Y. Hwang², H. Nakamura¹ and T. Kimura¹ (¹ Osaka Univ., ²Stanford Univ.)

Magnetic-Field Control of Ferroelastic Domains in FeCr_2O_4

The magnetic field response of Jahn-Teller distortion associated with the e orbital was investigated by synchrotron X-ray diffraction in FeCr_2O_4 . This compound exhibits successive phase transitions associated with the spin and orbital degrees of freedom of Fe^{2+} ions with six $3d$ electrons ($S=2$) on the tetrahedral sites. Structural domains exhibit two-step rearrangements when a magnetic field is applied along the c -axis in the orthorhombic phase of FeCr_2O_4 . The domain rearrangements result in large magnetostriction, which approaches 0.28%. The $c//\mathbf{H}$ domain does not reappear even after the magnetic field is removed, resulting in residual striction of about 0.1%.

Materials with large magnetostriction show promise for the design of actuation devices with large stroke. The orbital degree of freedom in strongly correlated electron systems influences physical properties such as magnetic anisotropy, lattice elasticity, and electric conductivity. If the occupied $3d$ orbital state is coupled to electron spin, the Jahn-Teller distortion can be changed by applying a magnetic field, and consequently large magnetostriction arises in such materials. In this work, we investigated the response of Jahn-Teller distortion to an external magnetic field in FeCr_2O_4 [1].

X-ray diffraction measurements were performed on BL-3A. The photon energy of the incident X-ray beam was 14 keV. A single-crystalline sample was mounted in a split-type superconducting magnet. The magnetic field direction was set parallel to the $[001]_c$ axis in the cubic setting. The X-ray diffraction profile of $(660)_c$ reflection was measured by using a CCD camera to investigate domain alignment. Note that the (066) , (606) , and (660) reflections correspond to domains in which the a , b , and c axes orient parallel to the external magnetic field, respectively, since the magnetic field is perpendicular to the scattering plane.

Figure 1 shows X-ray diffraction profiles of a single crystal of FeCr_2O_4 in several magnetic fields at 7 K, where the chromite is in the conical spin phase. After zero-field cooling, the (660) reflection is clearly split into three peaks because of orthorhombic distortion [2]. The (606) reflection disappears at 0.4 T and the intensity of the (066) reflection increases, indicating that the b axis is interchanged with the a axis in the domain where the b axis initially orients parallel to the magnetic field ($b//\mathbf{H}$). Increasing the magnetic field to 4 T, the (660) reflection also disappears, indicating that the c and a axes are swapped in the $c//\mathbf{H}$ domain. As a consequence, only $a//\mathbf{H}$ domains remain. The relation between magnetization direction and Jahn-Teller distortion strongly indicates that the occupied $3d$ orbital should tend to extend vertical to the spin direction. When the magnetic field is removed, the (606) reflection reappears, suggesting that 75% of the $b//\mathbf{H}$ domain is restored. On the other hand, the (660) reflection corresponding to the $c//\mathbf{H}$ domain does not reappear, as shown in Fig. 1.

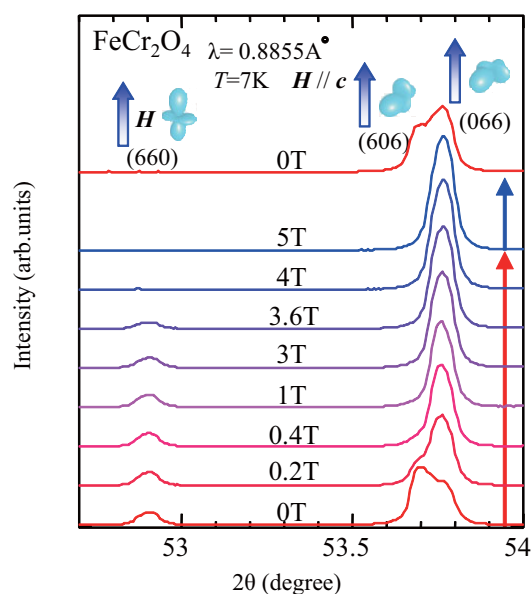


Figure 1 X-ray diffraction profiles of (660) , (606) , and (066) reflections of FeCr_2O_4 in several magnetic fields at 7 K [1].

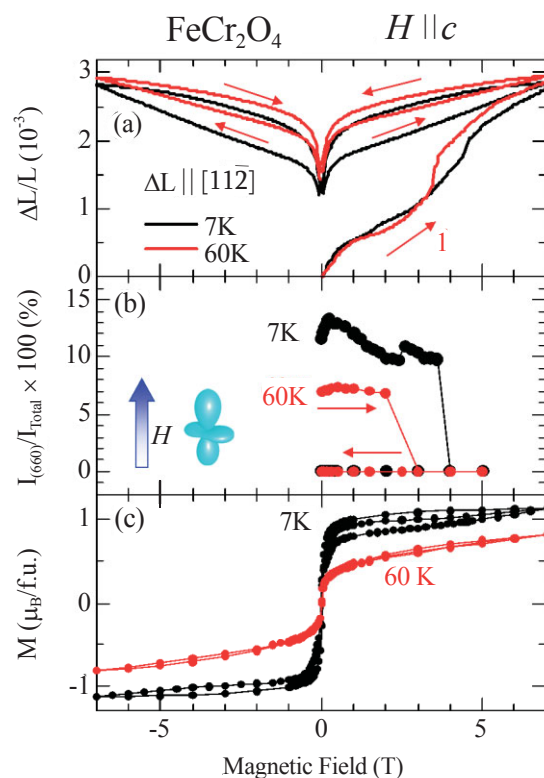


Figure 2 Magnetic field dependence of (a) relative strain observed using a strain gauge, (b) intensity of X-ray (660) diffraction, and (c) magnetizations of FeCr₂O₄ at 7 K and 60 K. All the measurements were performed after a zero-field cooling process [1].

Rearrangement of the domain structure causes magnetostriction. If the six types of domains are generated at random in zero-field cooling, the magnetic-field-induced strain $\Delta L/L$ along the $[001]_c$ axis is expected to approach 10×10^{-3} . Figure 2 (a) shows $\Delta L/L$ along $[11\bar{2}]_c$ as a function of the magnetic field along the $[001]_c$ axis at 7 K measured by a strain gauge. Rapid growths of $\Delta L/L$ are observed at around 0 T and 4.5 T in the first field-increasing run, corresponding to the domain rearrangements, as shown in Fig. 2 (b). One can also see residual strain of 1.2×10^{-3} , which is attributed to non-reversible domain switching. Hysteresis in the magnetization process shown in Fig. 2 (c) also originates from the domain rearrangements. Similar striction is observed also in the collinear ferrimagnetic phase.

REFERENCES

- [1] H. Sagayama, S. Ohtani, M. Saito, N. Abe, K. Taniguchi and T. Arima, *Appl. Phys. Lett.*, **99** (2011) 082506.
- [2] S. Ohtani, Y. Watanabe, M. Saito, N. Abe, K. Taniguchi, H. Sagayama, T. Arima, M. Watanabe and Y. Noda, *J. Phys.: Condens. Matter*, **22** (2010) 176003.

BEAMLINER

3A

H. SAGAYAMA^{1,2}, S. OHTANI², M. SAITO², N. ABE^{1,2}, K. TANIGUCHI^{1,2} and T. ARIMA^{1,2} (¹The Univ. of Tokyo ²Tohoku Univ.)

Unconventional Mass Acquisition of Surface Dirac Fermions in a Topological Insulator

A topological insulator is a novel quantum state of matter where an insulating bulk hosts a linearly dispersing surface or edge state, which can be viewed as a sea of massless Dirac fermions protected by time-reversal symmetry. By tracing the surface and bulk electronic states using angle-resolved photoemission spectroscopy, we found that the solid solution system $\text{TIBi}(\text{S}_{1-x}\text{Se}_x)_2$ goes through a quantum phase transition from the topological to the non-topological insulator. Furthermore, we observed that the massless Dirac state in TIBiSe_2 switches to a massive state before it disappears in the non-topological phase. This result suggests that Dirac particles at surfaces acquire mass without explicitly breaking time-reversal symmetry.

In three-dimensional (3D) topological insulators, insulating bulk hosts gapless topological surface states with a Dirac-cone energy dispersion [1, 2] which appear within the bulk excitation gap generated by the large spin-orbit coupling. In topological insulators, time-reversal symmetry and spin-orbit coupling characterize the spin-helical Dirac fermions which are immune to backward scattering by nonmagnetic impurities or disorder and which carry dissipationless spin current, holding promise for exploring fundamental physics, spintronics, and quantum computing [1, 2]. Strong spin-orbit coupling can lead to an inversion of the character of valence- and conduction-band wave functions, resulting in an odd Z_2 invariant that characterizes the topological insulator. All known topological insulators are based on this band-inversion mechanism, but the successive evolution of electronic states across the quantum phase transition from trivial to topological has not been well studied in 3D topological insulators due to the lack of suitable materials. $\text{TIBi}(\text{S}_{1-x}\text{Se}_x)_2$ is the first system

where one can investigate the topological quantum phase transition in 3D topological insulators. The advantage of this system is that it always maintains the same crystal structure irrespective of the S/Se ratio.

To elucidate the evolution of the surface and bulk electronic states in $\text{TIBi}(\text{S}_{1-x}\text{Se}_x)_2$, we performed high-resolution angle-resolved photoemission spectroscopy (ARPES) at BL-28A and Tohoku University [3, 4].

Figure 1(a) shows the near- E_F ARPES intensity around the Brillouin-zone center for a series of x values including TIBiSe_2 ($x = 1.0$) and TIBiS_2 ($x = 0.0$). One can immediately see that the surface state is seen for $x \geq 0.6$, whereas it is absent for $x \leq 0.4$, which points to the topological quantum phase transition occurring at $x_c \approx 0.5$. In fact, the bulk band gap estimated from our data approaches zero on both sides of the phase transition, suggesting that a band inversion takes place across the phase transition, in accordance with the natural expectation.

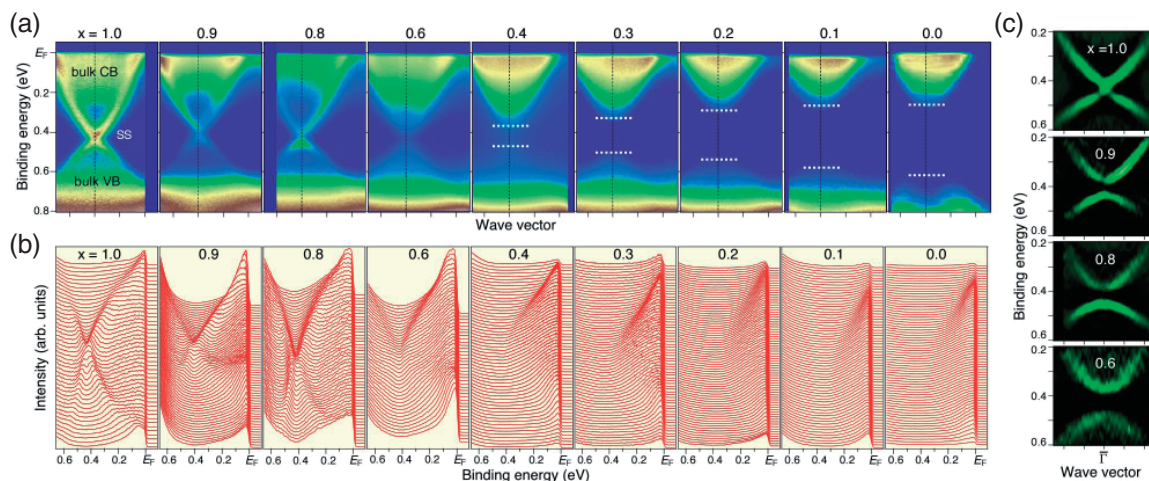


Figure 1 (a) ARPES intensity and (b) corresponding energy distribution curves of $\text{TIBi}(\text{S}_{1-x}\text{Se}_x)_2$ showing the mass acquisition of surface Dirac fermions. (c) Second-derivative intensity for $x = 1.0$ – 0.6 .

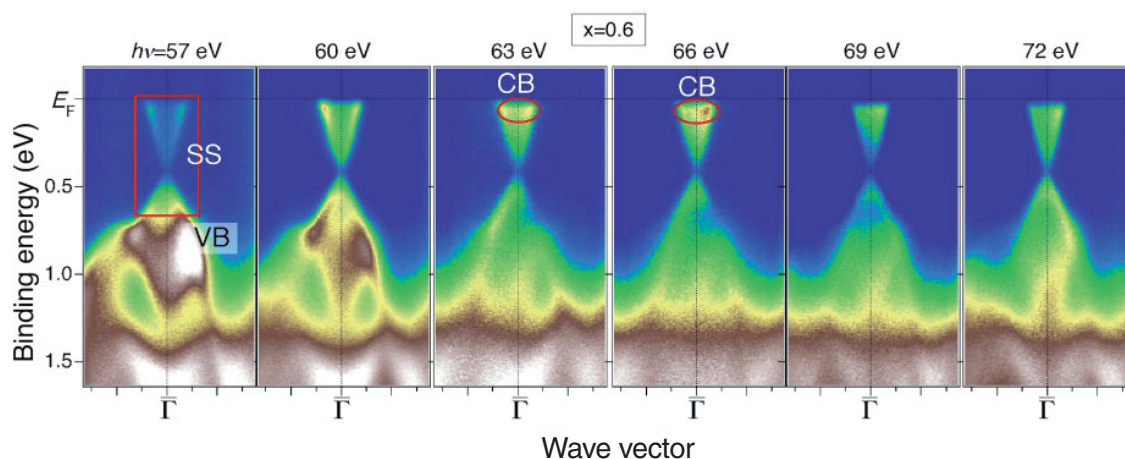


Figure 2
Photon-energy dependence of the ARPES intensity for $\text{TIBi}(\text{S}_{0.4}\text{Se}_{0.6})_2$.

The unexpected physics manifests itself at the Dirac point. The bright intensity peak at ~ 0.4 eV at $x = 1.0$ is a fingerprint of the Kramers degeneracy at the Dirac point, but it is no longer visible at $x = 0.9$ and is markedly suppressed at $x = 0.6$, suggesting that the Kramers degeneracy is lifted upon S substitution while the surface state is still present. The surface-state nature of this band was confirmed by its stationary nature of the energy position with respect to the photon energy as shown in Fig. 2, so this band evidently represents the massive Dirac fermions on the surface. Interestingly, the surface band gap, called here the Dirac gap, grows as x decreases (less than 0.1 eV at $x = 0.9$ and 0.8, and larger than 0.1 eV at $x = 0.6$), indicating that the S content is closely related to the magnitude of the Dirac gap. Taking into account that all the elements contained in $\text{TIBi}(\text{S}_{1-x}\text{Se}_x)_2$ are nonmagnetic and also that the sample shows no obvious magnetic order, our result strongly suggests that the substitution of Se with S in $\text{TIBi}(\text{S}_{1-x}\text{Se}_x)_2$ leads to an unconventional mass acquisition of the surface Dirac fermions *without* explicitly breaking the time-reversal symmetry. The present Dirac gap can be much larger than that of the magnetically-doped topological insulator Bi_2Se_3 [5] and is tunable with the S/Se ratio, making the

$\text{TIBi}(\text{S}_{1-x}\text{Se}_x)_2$ system a prime candidate for device applications of topological insulators that require a gapped surface state.

REFERENCES

- [1] M.Z. Hasan and C.L. Kane, *Rev. Mod. Phys.*, **82** (2010) 3045.
- [2] X.-L. Qi and S.-C. Zhang, *Rev. Mod. Phys.*, **83** (2011) 1057.
- [3] T. Sato, K. Segawa, K. Kosaka, S. Souma, K. Nakayama, K. Eto, T. Minami, Y. Ando and T. Takahashi, *Nature Phys.*, **7** (2011) 840.
- [4] S. Souma, K. Kosaka, T. Sato, M. Komatsu, A. Takayama, T. Takahashi, M. Kriener, K. Segawa and Y. Ando, *Phys. Rev. Lett.*, **106** (2011) 216803.
- [5] Y.-L. Chen, J.-H. Chu, J.G. Analytis, Z.K. Liu, K. Igarashi, H.-H. Kuo, X.L. Qi, S.K. Mo, R.G. Moore, D.H. Lu, M. Hashimoto, T. Sasagawa, S.-C. Zhang, I.R. Fisher, Z. Hussain and Z.-X. Shen, *Science*, **329** (2010) 659.

BEAMLINER

28A

S. Souma¹, T. Sato¹, K. Kosaka¹, M. Komatsu¹, A. Takayama¹, K. Nakayama¹, T. Takahashi¹, K. Eto², T. Minami², M. Kriener², K. Segawa² and Y. Ando² (Tohoku Univ., ²Osaka Univ.)

Structural Study of the Unique Ferromagnetic Metal-Insulator Transition in Hollandite $K_2Cr_8O_{16}$

We have studied the ferromagnetic metal-insulator transition occurring in hollandite $K_2Cr_8O_{16}$ by single crystal X-ray structure analysis. The transition is accompanied by structural distortion from a tetragonal $I4/m$ structure to a monoclinic $P2_1/a$ (or $P2_1/b$) structure with $\sqrt{2} \times \sqrt{2} \times 1$ unit cell. In the low temperature phase, Cr-O bond alternations occur in the rectangular column formed by the four CrO_6 chains (four-chain column), indicating a lattice dimerization with the formation of Cr-tetramer. The spatial arrangement of Cr-tetramer along the c -direction is of the stripe type. Such an arrangement would result from the competition between lattice distortion and coulomb repulsion.

Ferromagnetic insulator (FI) is extremely rare in transition-metal oxides; usually it is found in metallic systems and is caused by double exchange. Insulating ferromagnets are definitely not common among these materials. All the more surprising was the recent discovery [1] that chromium hollandite $K_2Cr_8O_{16}$ first becomes ferromagnetic at $T_c = 180$ K and with decreasing temperature, it experiences a metal-insulator transition (MIT) at $T_{MI} = 95$ K, and remains ferromagnetic at low temperature. $K_2Cr_8O_{16}$ is a mixed-valence oxide with $Cr^{3+}/Cr^{4+} = 1/3$ (an average valence of $Cr^{3.75+}$). In this study, we undertook a structural determination to elucidate this unique ferromagnetic MIT. Synchrotron X-ray diffraction experiments for the single crystal [2] were performed at BL-8A and 8B.

We first confirmed that the structure of the ferromagnetic metallic (FM) phase is isomorphous to that in the paramagnetic metallic (PM) phase, where all the Cr sites are crystallographically equivalent [Fig. 2 (a)]. Next, the structural change at T_{MI} was explored by oscillation photographs. Superlattice reflections with $q = (a^*/2, b^*/2, c^*)$ were clearly observed at 20 K ($< T_{MI}$), indicating that the unit cell becomes $\sqrt{2}a \times \sqrt{2}b \times c$ in the FI phase, where a , b and c are the lattice parameters in the PM and FM phases (Fig. 1). The intensity of superlattice reflections was 10^{-3} times weaker than that of fundamental reflections. Although peak splittings were not observed, the equivalent/inequivalent superlattice reflections showed $I(hkl) = I(\bar{h}\bar{k}l) \neq I(khl) = I(\bar{k}\bar{h}l)$, which agrees with

the condition of the Laue class $2/m$, indicating a monoclinic structure. Finally, from a detailed analysis of the reflection conditions we concluded that the space group of the FI phase is $P112_1/a$. The transition is accompanied by symmetry breaking with the loss of the four-fold axis and the mirror plane perpendicular to the c axis.

The structure analysis was performed taking the twinning structure which includes domains (a, b, c) and $(b, -a, c)$. When the ratio of the twin volume fraction was 0.608(1) : 0.392, we obtained good reliability factors (R -factor = 0.025, $R_w = 0.085$). In the FI phase, four Cr sites, two K sites and eight O sites become crystallographically inequivalent in contrast to unique Cr and K sites and two O sites in FM and PM phases. The Cr valences estimated via bond valence sum are the same within experimental error (≤ 0.03 electrons/Cr); the MI transition is accompanied by no charge separation/order. The four Cr sites form three kinds of double chains by sharing octahedral edges Cr1-Cr3, Cr2-Cr2 and Cr4-Cr4, respectively. Three kinds of double chains (A, B and C) are arranged such that the four Cr sites form a rectangular four-chain column by sharing corner oxygen atoms (Fig. 1)

At the same time the four-chain column has Cr-O bond alternations. This structural distortion can be understood as the formation of tetramers of Cr ions in c -direction in each of the four-chain columns; the lattice dimerization occurs in these four-chain columns [Fig. 2(b)].

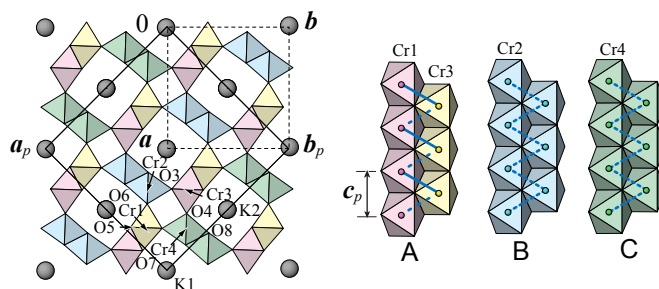


Figure 1 (left) Crystal structure of the ferromagnetic insulator phase in $K_2Cr_8O_{16}$ viewed from the c -axis. (right) Three kinds of double chains. In the structure, there are four Cr sites (Cr1 - Cr4).

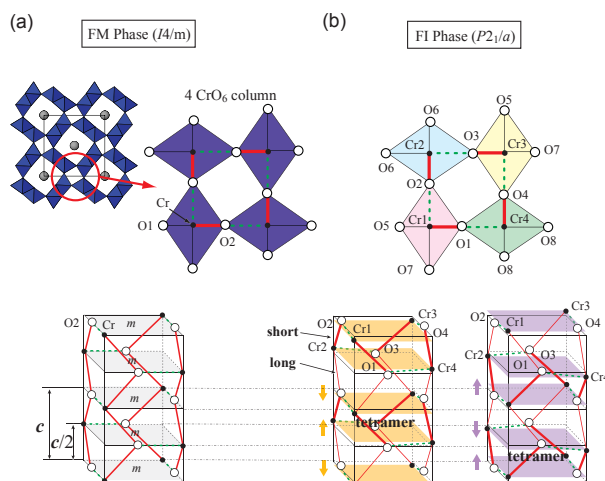


Figure 2

(a) Schematic illustrations of the four-chain columns for (a) the FM phase and (b) the FI phase. In the FI phase, the four-chain columns have Cr-O (Cr-Cr) bond alternations, indicating lattice dimerization with the formation of Cr-tetramers.

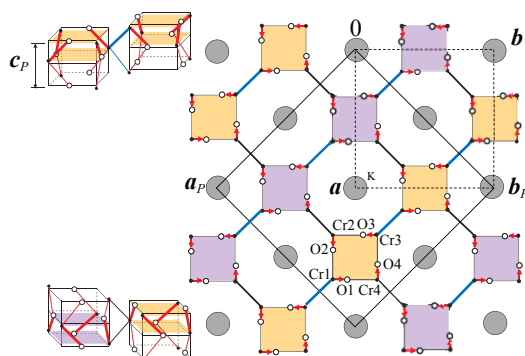


Figure 3

Schematic illustrations of structure with stripe-type arrangement.

In each of the four-chain columns short Cr-O bonds occur either at the upper or lower part of the unit cell along the c -direction. The monoclinic structure with $\sqrt{2} \times \sqrt{2} \times 1$ cell is realized as a stripe-like arrangement of these up and down four-chain columns along the diagonal direction (Fig. 3). As a consequence the double chain A has a Cr-Cr bond alternation, while the double chains B and C have no Cr-Cr bond alternation (see Fig. 1).

The observed structural characteristics well coincide with a Peierls mechanism for the metal-insulator transition proposed from electronic structure calculations [3]; one extra electron is weakly localized in the tetramer of Cr1-Cr4 due to a Peierls instability inherent in a one-dimensional electron system characterized by the rectangular four-chain column.

REFERENCES

- [1] K. Hasegawa, M. Isobe, T. Yamauchi, H. Ueda, J. Yamaura, H. Gotou, T. Yagi, H. Sato and Y. Ueda, *Phys. Rev. Lett.*, **103** (2009)146403.
- [2] A. Nakao, Y. Yamaki, H. Nakao, Y. Murakami, K. Hasegawa, M. Isobe and Y. Ueda, *J. Phys. Soc. Jpn.*, **81** (2012) 054710.
- [3] T. Toriyama, A. Nakao, Y. Yamaki, H. Nakao, Y. Murakami, K. Hasegawa, M. Isobe, Y. Ueda, A.V. Ushakov, D.I. Khomskii, S.V. Streltsov, T. Konishi and Y. Ohta, *Phys. Rev. Lett.*, **107** (2011) 266402.

BEAMLINES

8A and 8B

A. Nakao¹, Y. Yamaki², H. Nakao¹, Y. Murakami¹, T. Konishi³, Y. Ohta³, M. Isobe⁴ and Y. Ueda⁴. (¹KEK-PF, ²Tohoku Univ., ³Chiba Univ., ⁴The Univ of Tokyo)

Study of Structural Phase Transition of Pt-Induced Nanowire on Ge(001) Surface using Reflection High-Energy Positron Diffraction

The atomic configuration and the structural phase transition of Pt-induced nanowires on a Ge(001) surface are investigated using reflection high-energy positron diffraction (RHEPD). A previously proposed theoretical model, composed of Ge dimers on the top layer and buried Pt arrays in the second and fourth layers [1], is confirmed to be the fundamental structure of the nanowires. Analysis of the temperature-dependent RHEPD intensities suggests that the structural phase transition is very similar to a new type of phase transition [2]. That is, the precursory order-disorder behavior for the thermal-fluctuating low-temperature phases triggers the displacive transition to the high-temperature phase.

Self-assembled nanowires have attracted a great deal of interest not only for their potential applications in nano-devices, but also for providing a fundamental understanding of one-dimensional properties. Recently, Gürlü *et al.* [3] found that well-ordered and defectless nanowires are formed on Ge(001) surfaces by depositing Pt atoms. They first proposed a structural model of the Pt-induced nanowires based on their scanning tunneling microscopy (STM) observations, called the Pt-dimer (PD) model [Fig. 1(a)]. van Houselt *et al.* [4] reported that the nanowires undergo a Peierls transition at around 80 K. However, recent theoretical calculations suggested different structural models to explain those STM studies. The tetramer-dimer-chain (TDC) model [Fig. 1(b)] and the nanowire (NW) model [Fig. 1(c)] were suggested by Stekolnikov *et al.* [5] and Vanpoucke *et al.* [1], respectively. Despite extensive studies using STM and *ab initio* calculations, the atomic configuration and the phase transition mechanism of the nanowires are still controversial.

Reflection high-energy positron diffraction (RHEPD) is a surface-sensitive tool owing to the positive charge of the positron. Positrons are repelled by a positive crystal potential so that they cannot enter crystals at low-angle grazing incidences (total reflection). Therefore, RHEPD is very sensitive to the topmost layer of crystals. Recently, we developed a new RHEPD apparatus [6] on beamline SPF-B1 of a linac-based intense positron beam at the Slow Positron Facility (SPF). In this study,

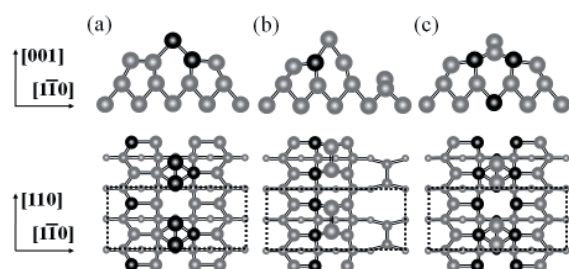


Figure 1 Schematic illustrations of Ge(001)-p(4×2)-Pt structures; (a) PD, (b) TDC and (c) NW models. The black and gray spheres represent Pt and Ge atoms, respectively. The dotted rectangles represent p(4×2) unit cells.

we investigated highly ordered Pt-induced nanowires on Ge(001) surfaces by using the RHEPD apparatus.

Pt was deposited on a clean Ge(001) surface kept at 720 K under ultra-high vacuum condition. The Pt coverage was 1.2 monolayer (ML), where 1 ML corresponds to $\sim 6.3 \times 10^{14}$ atoms/cm². RHEPD experiments were performed using a 10 keV positron beam generated from a ²²Na source at the JAEA and the intense positron beam at the SPF. The incident azimuth was 22.5° away from the [1 $\bar{1}$ 0] direction (one-beam condition). The glancing angle (θ) for total reflection is approximately 2.2°.

Figure 2 shows the RHEPD rocking curve of the specular spot at 35 K [7]. The solid and broken lines are calculated rocking curves assuming the PD, the TDC, and the NW models, respectively. Under the assumptions of the PD and the TDC models, the calculated curves exhibit dips in the total reflection region due to the interference effects of the positron waves reflected by the first and second surface layers [8]. The features do not appear in the experimental curve. On the contrary, the calculated curve for the NW model (thick solid line) is in good agreement with the experimental data. We also examined other structural models with the Pt

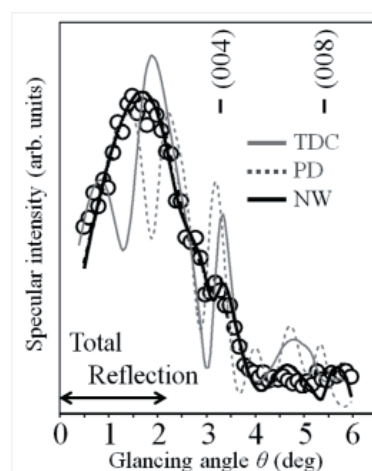


Figure 2 RHEPD rocking curves measured from Pt-induced nanowires under the one-beam condition at 35 K. The open circles denote experimental data. The solid gray, broken gray, and solid black line are the calculated curves for the TDC, PD and NW models, respectively.

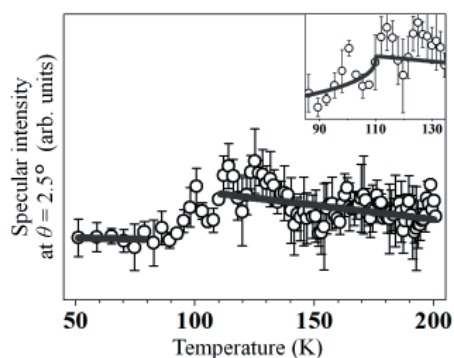


Figure 3

The temperature-dependent one-beam specular spot intensity at $\theta = 2.5^\circ$ for the temperature range 50-200 K. The solid lines indicate the calculated temperature dependence assuming Debye temperatures of 210 and 130 K. The inset shows a close-up of the temperature dependence around T_c . The solid curve and solid line indicate the optimum temperature dependence below and above T_c , respectively

coverage ranging from 0.25 to 1 ML [7]. Among these examined models, the NW model exhibits the best reliability factor. Thus, the fundamental structure of the Pt-induced nanowires is explained by the NW model.

Figure 3 shows the temperature dependence of the specular spot intensity at $\theta = 2.5^\circ$ in the temperature range from 50 to 200 K. The intensity gradually increases from 80 to 110 K, indicating the progress of the displacive transition for the topmost Ge dimers [7], and thereafter, a conventional Debye-Waller-like temperature dependence is observed within experimental error. From the slopes of the relation between specular intensity and temperature, the surface Debye temperatures are determined to be 210 ± 80 K for the low-temperature phase and 130 ± 40 K for the high-temperature phase. The amplitudes of the surface-normal vibrations of the topmost Ge dimers are 0.06 \AA at 50 K and 0.15 \AA at 120 K. The temperature dependence of the intensity between 80 and 110 K is somewhat continuous and would be reproduced by a power-law, as shown by the inset in Fig. 3. The order parameter is proportional to $|1 - T/T_c|^\beta$ with $\beta = 0.36 \pm 0.15$ and $T_c = 111 \pm 10$ K. The

value of β is smaller than that anticipated for the mean field approximation ($\beta = 0.5$). This is probably due to the coexistence and fluctuations of the low-temperature phases and the high-temperature phase as observed by using STM [7].

From the ARPES measurements, we observed the change in electronic band dispersions due to the atomic displacements of the topmost Ge dimers [7]. The results are also consistent with the scenario of the phase transition with the precursory order-disorder behaviors.

In the present results, the structural phase transition is very similar to a new type of phase transition [2]. That is, the order-disorder behavior for thermal-fluctuating low-temperature phases triggers the displacive transition from the low-temperature phases to the high-temperature phase.

REFERENCES

- [1] D.E.P. Vanpoucke and G. Brocks, *Phys. Rev. B*, **77** (2008) 241308 (R).
- [2] T. Aruga, *Surf. Sci. Rep.*, **61** (2006) 283.
- [3] O. Gurlu, O.A.O. Adam, H.J.W. Zandvliet and B. Poelsema, *Appl. Phys. Lett.*, **83** (2003) 4610.
- [4] A. van Houselt, T. Gnielka, J.M.J. Aan de Brugh, N. Oncel, D. Kockmann, R. Heid, K.-P. Bohnen, B. Poelsema and H.J.W. Zandvliet, *Surf. Sci.*, **602** (2008) 1731.
- [5] A.A. Stekolnikov, F. Bechstedt, M. Wisniewski, J. Schäfer and R. Claessen, *Phys. Rev. Lett.*, **100** (2008) 196101.
- [6] K. Wada, T. Hyodo, A. Yagishita, M. Ikeda, S. Ohsawa, T. Shidara, K. Michishio, T. Tachibana, Y. Nagashima, Y. Fukaya, M. Maekawa and A. Kawasuso, *Eur. Phys. J. D*, **66** (2012) 37.
- [7] I. Mochizuki, Y. Fukaya, A. Kawasuso, K. Yaji, A. Harasawa, I. Matsuda, K. Wada and T. Hodo, *Phys. Rev. B*, **85** (2012) 245438.
- [8] A. Kawasuso and S. Okada, *Phys. Rev. Lett.*, **81** (1998) 2695.

BEAMLINER

SPF-B1

**I. Mochizuki¹, Y. Fukaya¹, A. Kawasuso¹, K. Yaji²,
A. Harasawa², I. Matsuda², K. Wada³ and T. Hyodo³**
(¹JAEA, ²The Univ. of Tokyo, ³KEK-PF)

Quantum Effect and Anharmonicity in an Invar Alloy Studied by EXAFS Spectroscopy

We have investigated the vibrational anharmonicity and quantum effects in the Invar alloy $\text{Fe}_{64.6}\text{Ni}_{35.4}$ which shows anomalously small thermal expansion. We have performed Fe and Ni *K*-edge EXAFS spectroscopic measurements and computational simulations based on the path-integral effective-classical-potential theory. The first nearest-neighbor (NN) shells around Fe showed almost no thermal expansion, while those around Ni exhibited significant but smaller expansion than that of fcc Ni. At low temperature (<100 K), the vibrational quantum effect was found to play an essential role. This was confirmed by comparing the quantum mechanical simulations to the classical ones: the latter exhibited large (normal) thermal expansion at low temperature. It was also revealed that thermal expansion of the Ni-Ni and Ni-Fe pairs was noticeably suppressed, even though the Ni electronic state may not vary with temperature.

Anomalously small thermal expansion over a wide temperature range in an iron-nickel alloy with a nickel concentration of around 35% was discovered by Guillaume [1] in 1897. The effect is well known as the Invar effect and has been used in various kinds of industrial products. The effect is known to originate from magnetism, and many papers have still been published on the origins of the Invar effect, implying a lack of full understanding of the effect. The basic concept of the Invar effect is that there exist at least two types of electronic states in Fe, typically high-spin (HS) and low-spin (LS) states [2]. In this two-state model, the equilibrium potential energy is lower in the HS state than in the LS one, while the equilibrium atomic radius is larger in the former. This results in the compensation of thermal expansion due to increasing density of the LS state at higher temperature. In the present work [3], we conducted an experimental study on the local thermal expansion and anharmonic behavior around Fe and Ni by measuring Fe and Ni *K*-edge EXAFS of the Invar alloy. EXAFS is a very powerful tool for the characterization of local thermodynamic properties and has been extensively applied to various kinds of thermodynamic systems. We also performed Monte-Carlo (MC) simulations of thermal expansion and vibrational anharmonicity obtained by the path-integral effective-classical-potential (PIECP) theory within the simple two-state (HS+LS) model.

The Fe and Ni *K*-edge EXAFS spectra of an Invar foil (8 μm thick) were recorded at Beamline 9C in transmission mode over the temperature range of 12.5–300 K. The EXAFS oscillation functions $k^3\chi(k)$ were analyzed by the *k*-space curve-fitting method for the Fourier-filtered $k^3\chi(k)$. Note that the neighboring atoms of surrounding Fe or Ni were not distinguished because there is only a small difference in the backscattering amplitudes between Fe and Ni, and therefore the resultant values obtained experimentally are the average one for each X-ray absorbing atom. The average bond distance R , the mean square relative displacements $C_2 = \langle (r-R)^2 \rangle$, and the mean cubic relative displacements $C_3 = \langle (r-R)^3 \rangle$ were obtained. C_2 and C_3 correspond to the thermal and static variance of the bond distance and

the asymmetry of the pair distribution function, respectively. PIECP MC simulations within the low coupling approximation were performed under constant number of particles, pressure, and temperature (*NPT*) conditions. Details of the computational method are given in the literature [3].

Figure 1 shows the experimental and simulated bond distances around Fe (a) and Ni (b) and the lattice constants (c). Almost no thermal expansion is seen in the local structure around Fe, while it is clearly observed around Ni. The magnitude of thermal expansion around Ni is, however, significantly smaller than that of fcc Ni, indicating the suppression of thermal expansion around Ni as well as Fe. As we expected from the two-state model, the almost complete lack of thermal expansion around Fe can be ascribed to the direct effect of the increasing population of the LS state in Fe with increasing

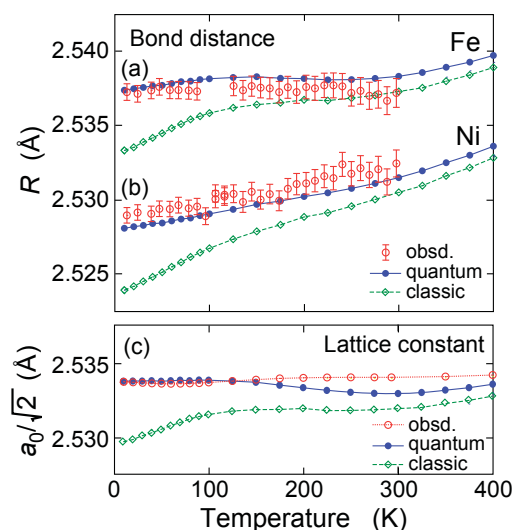


Figure 1 (a, b) Experimentally obtained 1st NN bond distance around Fe (a) and Ni (b) (red open circles with an error bar), together with the simulated results by the PIECP (blue circles and solid line, quantum) and the classical MC (green diamonds and dashed line, classic) methods. (c) Lattice constant scaled for the 1st NN distance ($a_0/\sqrt{2}$) given by the X-ray diffraction data in the literature (red circles and dotted line) and the PIECP and classical MC simulations.

temperature. On the other hand, the behavior around Ni may be attributed to the indirect effect in the two-state model. Although Ni is likely to expand normally with increasing temperature, this is also suppressed by the almost fixed lattice constant. In Fig. 1, the agreement between the PIECP and experiments is good: almost no thermal expansion around Fe and significant thermal expansion around Ni. On the contrary, the classical method is found to give fatal discrepancies at low temperature below ~ 100 K; the bond and lattice distances significantly increase with increasing temperature. These findings imply the importance of the vibrational quantum effect, which is recognized as a zero-point vibration.

To get further insights into local thermal expansion, the bond distance of each component (Fe-Fe, Ni-Ni and Ni-Fe) pair is shown in Fig. 2. In this plot, the PIECP MC results by using only the HS Fe state are also depicted to determine the hypothetical normal thermal expansion in this system. As expected, the Fe-Fe pair shows the largest discrepancies between the two-state (HS+LS) and the HS-only models. This is caused by the increasing population of the Fe LS state with higher temperature, yielding compensation of the thermal expansion with the one originating from anharmonic vibration. The most important finding in Fig. 2 is that even Ni-Ni and Ni-Fe pairs exhibit significant suppression of thermal expansion compared to the results by the HS-only model. This is consistent with the above experimental finding that thermal expansion around Ni is noticeably suppressed compared to that of fcc Ni. Although Ni does not change its electronic configuration depending on temperature and tends to expand because of anharmonic vibration, the Ni-Ni or Ni-Fe bond expansion is significantly suppressed due to the anomalously small expansion of the lattice. Interestingly, the suppression of thermal expansion seems to be more significant in the Ni-Fe bond than in the Ni-Ni bond. This can be explained by the fact that the Fe atom surrounded by many Ni atoms tends to maintain the HS state. Furthermore, the Ni-Ni bond is noticeably softer than the Ni-Fe bond and is more likely to match the lattice parameter. These effects yield smaller thermal expansion in the Ni-Ni bond than the Ni-Fe one.

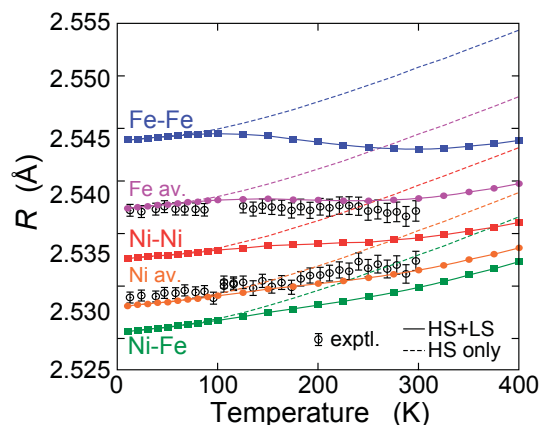


Figure 2

Simulated bond distances of Fe-Fe (blue squares and solid line), Ni-Ni (red squares and solid line), and Ni-Fe (green squares and solid line) pairs, together with the average ones around Fe (pink circles and solid line) and Ni (orange circles and solid line). The experimental data for the average one around Fe and Ni are again shown. The dashed lines are the PIECP results by using only the HS state in Fe.

Clear and significant third-order anharmonicity C_3 in the Invar alloy was confirmed not only by experiments but also by simulations in spite of almost no thermal expansion. The simulated values for the LS and HS states exhibit essentially the same C_3 values, implying no suppression of C_3 due to the contribution of the LS state, as observed in the thermal expansion. Since the asymmetric radial distribution for the 1st NN shell almost exclusively originates from the anharmonic interatomic potential, the present result implies that the third-order anharmonicity clearly exists even in the case of no thermal expansion.

REFERENCES

- [1] C.E. Guillaume, *CR Acad. Sci.*, **125** (1897) 235.
- [2] R.J. Weiss, *Proc. R. Soc. Lond. A*, **82** (1963) 281.
- [3] T. Yokoyama and K. Eguchi, *Phys. Rev. Lett.*, **107** (2011) 065901.

BEAMLINER

9C

T. Yokoyama¹ and K. Eguchi² (¹IMS, ²The Grad. Univ. for Adv. Stud.)

Combined in Situ QXAFS and FTIR Observation of a Ni Phosphide Catalyst - Determination of Active Species for a Hydrodesulfurization Reaction -

Supported Ni_2P catalysts have been studied as a new class of catalysts for hydrodesulfurization (HDS) of petroleum feedstocks. In order to determine the reaction mechanism of thiophene HDS over $\text{Ni}_2\text{P}/\text{MCM-41}$, we have developed a new technique, which conducts simultaneous time-resolved analysis of in situ X-ray absorption fine structure (XAFS) spectroscopy and Fourier transform infrared (FTIR) spectroscopy together with product analysis. The formation of a nickel phosphosulfide phase (NiPS) was observed by XAFS prior to the emergence of tetrahydrothiophene (THT) in FTIR, which was accompanied by the HDS product. It is concluded that NiPS acted as the active phase and THT as a reaction intermediate for the HDS reaction.

Over the past decade, nickel phosphide has attracted much attention as a promising catalyst for hydrodesulfurization (HDS) of petroleum feedstocks. Preliminary characterization of the active phase revealed that it had a Ni_2P composition and that Ni_2P showed a high performance due to its high resistance to sulfur [1]. However, in situ X-ray absorption fine structure (XAFS) spectroscopy under reaction conditions indicated the presence of sulfur on Ni_2P during the HDS reaction, which seemed to work as a promoter rather than as a poison [2].

In order to determine the role of this sulfur in the HDS reaction, a new simultaneous time-resolved (STR) analysis technique was developed and applied to the study of a supported Ni_2P catalyst under thiophene

HDS conditions [3]. In this STR analysis, in situ quick X-ray absorption fine structure (QXAFS) spectra were obtained simultaneously with in situ Fourier transform infrared (FTIR, JASCO VIR-9500) spectra, using a cross-shaped cell as shown in Fig. 1. The catalyst was pressed into a self-supporting pellet and set in the center of the cell positioned at 45° to both the X-ray and IR beams, and both spectra were obtained in a transmittance mode. On-line HDS product analysis was also conducted with a quadrupole mass spectrometer (QMS, Hyden Analytical HAL301). The experiments were conducted at BL-9C. The QXAFS of Ni K-edge from 8080 eV to 8900 eV was collected every 20 s with a scan time of 10 s, while the IR data were obtained with an accumulation time of 60 s. The XAFS data were analyzed by the software program REX2000 (Rigaku Co.). Curve-fitting analysis was carried out with parameters obtained with FEFF8 (Univ. of Washington).

The supported Ni_2P catalyst was prepared with a siliceous mesoporous material, MCM-41, as a support. Prior to the HDS reaction, the catalyst was pretreated under hydrogen at 723 K or 803 K to complete the formation of the active Ni_2P phase [4]. Then, a reactant mixture composed of thiophene (0.1 vol.%), He (1.8 vol.%) and H_2 (98 vol.%) was introduced at a total flow rate of 102 cm^3 (NTP)/min under atmospheric pressure. As mentioned above, due to its high tolerance to sulfur, the bulk structure of Ni_2P was retained during HDS as shown in Fig. 2 (a). However, a close examination of the X-ray absorption near-edge structure (XANES) in-

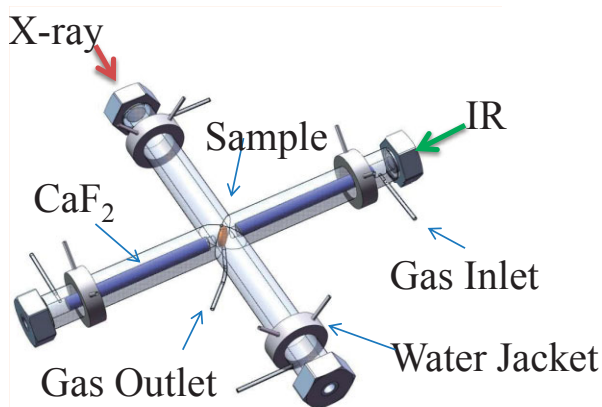


Figure 1
Diagram of a cell for the STR analysis.

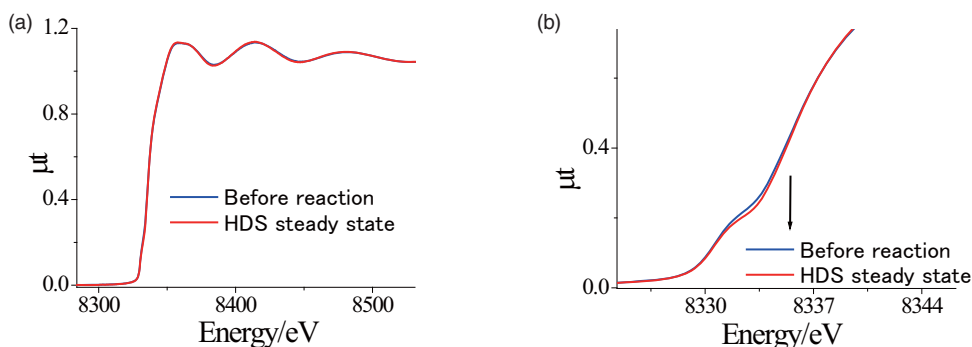


Figure 2
XAFS spectra before and during the HDS reaction. (a) All area, (b) XANES area.

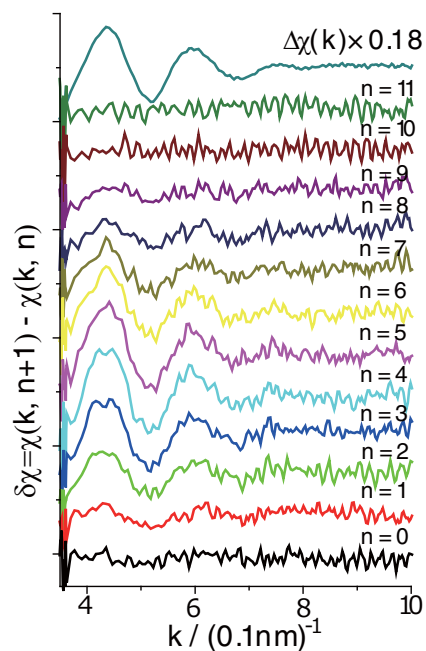


Figure 3
Difference spectra between consecutive scans. The difference spectrum between the ones before the reaction and under the steady state ($\Delta\chi(k) = \chi(k, n) - \chi(k, 0)$) is given at the top.

indicated a decrease in intensity at 8333.3 eV as shown in Fig. 2 (b), which was assigned to the formation of a nickel phosphosulfide phase, since the presence of a Ni-S bond was also confirmed by the extended X-ray absorption fine structure (EXAFS) under the steady state condition [2]. Further investigation of EXAFS spectra in the transient process to the steady state was carried out with difference spectra between consecutive scans as depicted in Fig. 3 [5]. The transient difference spectra were found to consist of one component that was proportional to the EXAFS difference spectrum obtained for the steady state, in other words, the species that evolved during the transient process was the Ni-S bond in the NiPS phase. In addition, it was confirmed that the change in XANES properly corresponded to the evolution of the NiPS phase in EXAFS.

The STR study was applied to the structural analysis of Ni_2P during the HDS reaction. As shown in Fig. 4 [3], immediately after the reaction started, a rapid decrease in XANES was observed, which was assigned to the formation of NiPS, as mentioned above. After the NiPS formation was saturated, adsorbed tetrahydrothiophene

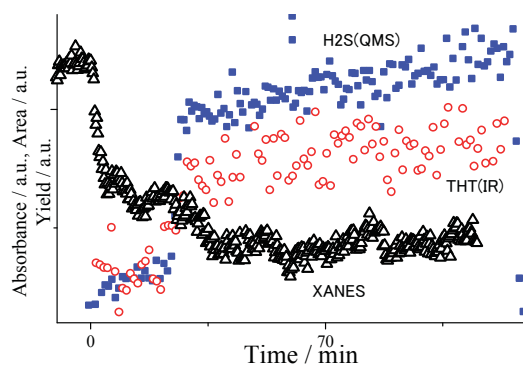


Figure 4
Change in XANES at 8333.3 eV (triangles) compared with that of IR band in the aliphatic $\nu(\text{CH})$ region (open circles) and the formation of H_2S detected by QMS ($m/z = 34$) (squares) during HDS at 513 K.

(THT) started developing in FTIR, which coincided with the detection of HDS products by QMS. All these experimental data indicated that NiPS acted as the active phase and identified THT as a reaction intermediate for the HDS reaction. The STR study proved to be a powerful tool for the precise study of reaction intermediates.

REFERENCES

- [1] T. Kawai, S. Sato, S. Suzuki, W.-J. Chun, K. Asakura, K.K. Bando, T. Matsui, Y. Yoshimura, T. Kubota, Y. Okamoto, Y.-K. Lee and S.T. Oyama, *Chem. Lett.*, **32** (2003) 956.
- [2] T. Kawai, K.K. Bando, Y.-K. Lee, S.T. Oyama, W.-J. Chun and K. Asakura, *J. Catal.*, **241** (2006) 20.
- [3] K.K. Bando, T. Wada, T. Miyamoto, K. Miyazaki, S. Takakusagi, Y. Koike, Y. Inada, M. Nomura, A. Yamaguchi, T. Gott, S.T. Oyama and K. Asakura, *J. Catal.*, **286** (2012) 165.
- [4] K.K. Bando, Y. Koike, T. Kawai, G. Tateno, S.T. Oyama, Y. Inada, M. Nomura and K. Asakura, *J. Phy. Chem., C* **115** (2011) 7466.
- [5] T. Wada, K.K. Bando, T. Miyamoto, S. Takakusagi, S.T. Oyama and K. Asakura, *J. Synchrotron Rad.*, **19** (2012) 205.

BEAMLIN

9C

K.K. Bando¹, T. Wada², T. Miyamoto², K. Miyazaki², S. Takakisagi², Y. Koike³, Y. Inada⁴, M. Nomura³, A. Yamaguchi¹, T. Gott⁵, S.T. Oyama^{5, 6} and K. Asakura² (¹AIST, ²Hokkaido Univ., ³KEK-PF, ⁴Ritsumeikan Univ., ⁵Virginia Polytechnic Inst. and State Univ., ⁶The Univ. of Tokyo)

Structural Basis for the Single Active Site to Catalyze Two Distinct Reactions in a Primitive Enzyme FBPA/P

The bifunctional enzyme fructose 1,6-bisphosphate aldolase/phosphatase (FBPA/P) is distributed among primordial organisms such as hyperthermophiles and catalyzes two consecutive reactions of gluconeogenesis: the aldol condensation of dihydroxyacetone phosphate and glyceraldehyde-3-phosphate to fructose 1,6-bisphosphate, and the hydrolysis of FBP to fructose-6-phosphate. X-ray crystallographic analysis revealed that conversion between aldolase and phosphatase forms of the enzyme is based on the toggle switch-like motions of three mobile loops in the active site. This is the first example of an enzyme that catalyzes two different reactions in a single active site.

An enzyme called fructose 1,6-bisphosphate aldolase/phosphatase (FBPA/P) catalyzes two consecutive reactions of gluconeogenesis: (1) the aldol condensation (aldolase reaction) of dihydroxyacetone phosphate (DHAP) and glyceraldehyde-3-phosphate to fructose 1,6-bisphosphate (FBP), and (2) the hydrolysis (phosphatase reaction) of FBP to fructose-6-phosphate and phosphate. FBPA/P is distributed among hyperthermophilic archaea and deeply branched bacteria [1].

FBPA/P was initially identified as a novel class of fructose 1,6-bisphosphatase (class V FBPAse), essential for gluconeogenesis of thermophilic organisms [2, 3]. In 2004, the first structure of class V FBPAse (ST0318) from a hyperthermophilic archaeon *Sulfolobus tokodaii* was determined as a complex with FBP (PDB ID: 1UMG) [4].

In 2010, the discovery that archaeal FBPA aldolase is identical with class V FBPAse, thereby designated as a

bifunctional enzyme FBPA/P, raised the serious question as to how Class V FBPAse can act as FBPA aldolase, because Lys232 (K232) essential for the aldolase reaction is far away (~17Å) from the substrate binding site in the 1UMG structure [1]. In 2011, the crystal structure of the ST0318 protein in complex with DHAP was determined (PDB ID: 3R1M) [5], using the AR-NW12A beamline.

The overall structures of both 1UMG and 3R1M are similar, with eight subunits stacking back-to-back, and the active site is located at the subunit interface within the ring-shaped tetramer (Fig. 1). Detailed structural comparison revealed a conformational difference in the active site arising from the toggle switch-like motions of three mobile loops termed lid (blue), Schiff-base (yellow), and C-terminal (pink) loops. The structures 1UMG and 3R1M represent 'phosphatase form' and 'aldolase form', respectively.

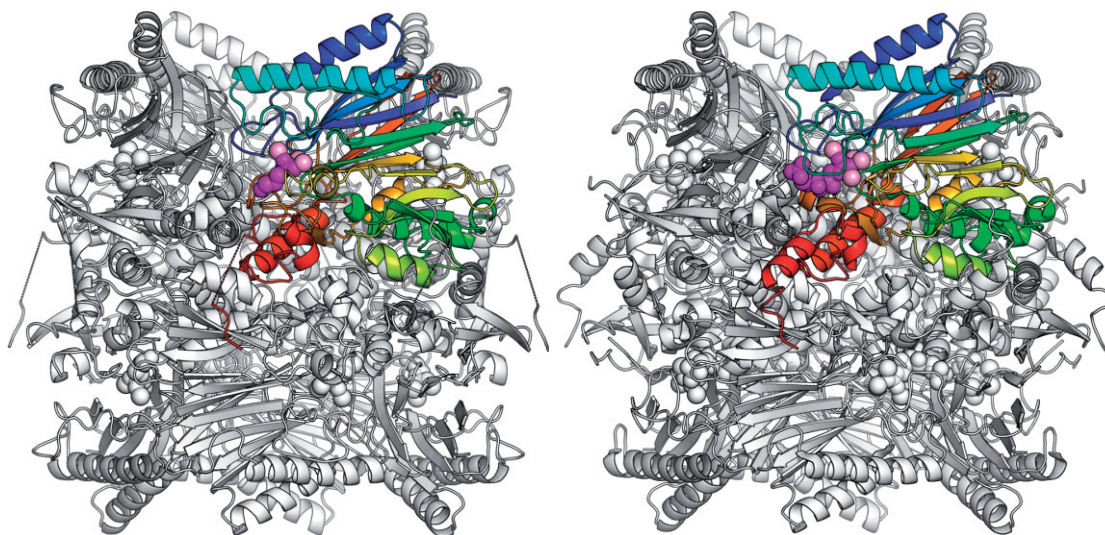


Figure 1 Octameric structure of aldolase (left) and phosphatase (right) forms of FBPA/P. One subunit is shown in rainbow colors. Ligands at one active site are shown as purple (DHAP and FBP) and pink (Mg^{2+}) spheres.

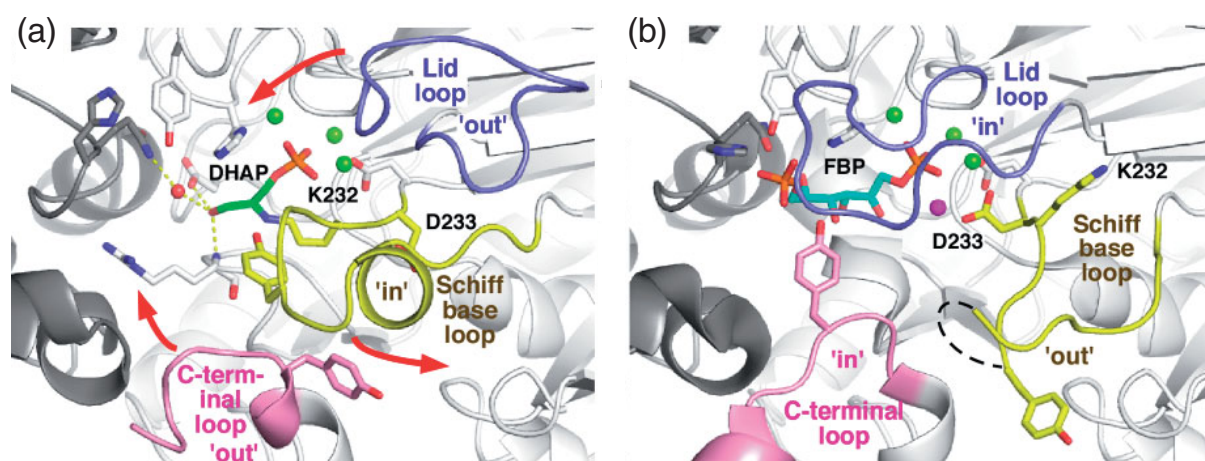


Figure 2
Active site of FBPA/P. (a) Aldolase form and (b) phosphatase form.

Figure 2 compares the active site of the two forms. A large structural change is observed at the three mobile loops. In the aldolase form [Fig. 2(a)], a critical lysine residue (K232) forms a covalent Schiff base with DHAP (green). Three Mg^{2+} ions (green) are also bound. During the structural change from the aldolase to phosphatase form, the Schiff-base loop moves from 'in' to 'out' conformation. In contrast, the lid and C-terminal loops move from 'out' to 'in'. In the phosphatase form [Fig. 2(b)], a FBP molecule (cyan) is bound in an open-keto (linear) form. An additional Mg^{2+} ion (magenta) is bound in this form, and this fourth Mg^{2+} ion is essential for the phosphatase reaction. The 'in' to 'out' conformational change in the Schiff-base loop flips the D233 side chain, thereby creating the binding site for the fourth Mg^{2+} . An independent group also reported a similar result, using another FBPA/P enzyme from a hyperthermophilic archaeon, *Thermoproteus neutrophilus* [6].

The organisms that possess FBPA/P occupy the closest branches to the root of the phylogenetic tree of life, and they thus may retain some of the physiological features of early life forms. FBPA/P may represent an ancestral, simple gluconeogenic system that was pres-

ent in primordial chemolithoautotrophic organisms. This study is the first to elucidate the molecular mechanism of a "true" bifunctional enzyme. Our findings suggest the possible existence of undiscovered enzymes that also catalyze multiple chemical reactions at a single site.

REFERENCES

- [1] R.F. Say and G. Fuchs, *Nature*, **464** (2010) 1077.
- [2] N. Rashid, H. Imanaka, T. Kanai, T. Fukui, H. Atomi and T. Imanaka, *J. Biol. Chem.*, **277** (2002) 30649.
- [3] T. Sato, H. Imanaka, N. Rashid, T. Fukui, H. Atomi and T. Imanaka, *J. Bacteriol.*, **186** (2004) 5799.
- [4] H. Nishimasu, S. Fushinobu, H. Shoun and T. Wakagi, *Structure*, **12** (2004) 949.
- [5] S. Fushinobu, H. Nishimasu, D. Hattori, H.-J. Song and T. Wakagi, *Nature*, **478** (2011) 538.
- [6] J. Du, R.F. Say, W. Lü, G. Fuchs and O. Einsle, *Nature*, **478** (2011) 534.

BEAMLIN

AR-NW12A

T. Wakagi, H. Nishimasu and S. Fushinobu (The Univ. of Tokyo)

Observation of Structural Change upon Photoinduced Electron Transfer of 9-Mesityl-10-methylacridinium Ion by Pump-Probe X-Ray Crystal Structure Analysis

The molecular structure of 9-mesityl-10-methylacridinium ion ($\text{Acr}^+\text{-Mes}$) at the photoinduced electron-transfer (ET) state was determined by pump-probe single crystal X-ray structure analysis. Precise crystallographic analysis of the photoinduced structural change of $[\text{Acr}^+\text{-Mes}]\text{ClO}_4$ clearly indicated the bending of the *N*-methyl group by reduction of Acr^+ and the movement of the counter anion, ClO_4^- , by the electrostatic attraction from the oxidized Mes. This allowed the ET state of $\text{Acr}^+\text{-Mes}$ to be established with its three-dimensional structural features for the first time.

The utilization of sunlight as a renewable and clean energy source by an artificial photosynthetic system is a promising way to solve global energy problems. Many photosynthetic reaction center model compounds have been developed as donor–acceptor linked and supramolecular systems based on the crystal structure of the photosynthetic reaction center. However, crystallographic determination of the photoinduced structural change of these compounds remains a formidable challenge. In this study, we determined the structural change upon photoinduced electron transfer in a simple donor–acceptor-like dyad as a photosynthetic reaction center model compound, $\text{Acr}^+\text{-Mes}$, for the first time by pump-probe single crystal X-ray structure analysis [1].

$\text{Acr}^+\text{-Mes}$ is designed to mimic the charge separation in the natural photosynthesis reaction center [2]. The electron donor (Mes) and acceptor (Acr^+) are directly connected by a covalent bond. There is no π conjugation between them because the dihedral angle between them is approximately perpendicular. The photoinduced ET state of $\text{Acr}^+\text{-Mes}$ ($\text{Acr}^+\text{-Mes}^{*+}$) is generated via the singlet excited state of the Acr^+ moiety by visible light irradiation [Fig. 1(a)]. The energy of the ET state lies deep within the Marcus-inverted region, so its lifetime is significantly long (e.g., 2 h at 203 K) [1]. Furthermore, $\text{Acr}^+\text{-Mes}^{*+}$ also has very high energy (2.37 eV), which is useful in photocatalyzed reactions [3, 4].

The structural change of $\text{Acr}^+\text{-Mes}$ by ET was determined by pump-probe single crystal X-ray structure analysis. A femtosecond laser was used as an excitation light source. The laser pulse and the X-ray pulses were synchronized at a frequency of 946 Hz [5]. The single crystal of $[\text{Acr}^+\text{-Mes}]\text{ClO}_4$ was cooled at 90 K by a cold nitrogen stream. Photoinduced bending of the *N*-methyl group in $\text{Acr}^+\text{-Mes}$ and movement of ClO_4^- with its rotation were observed in the Fourier map using the

difference of the observed structural factors in the light-on and -off stages [$F_{\alpha(\text{on})} - F_{\alpha(\text{off})}$] as a coefficient [Fig. 1(b)].

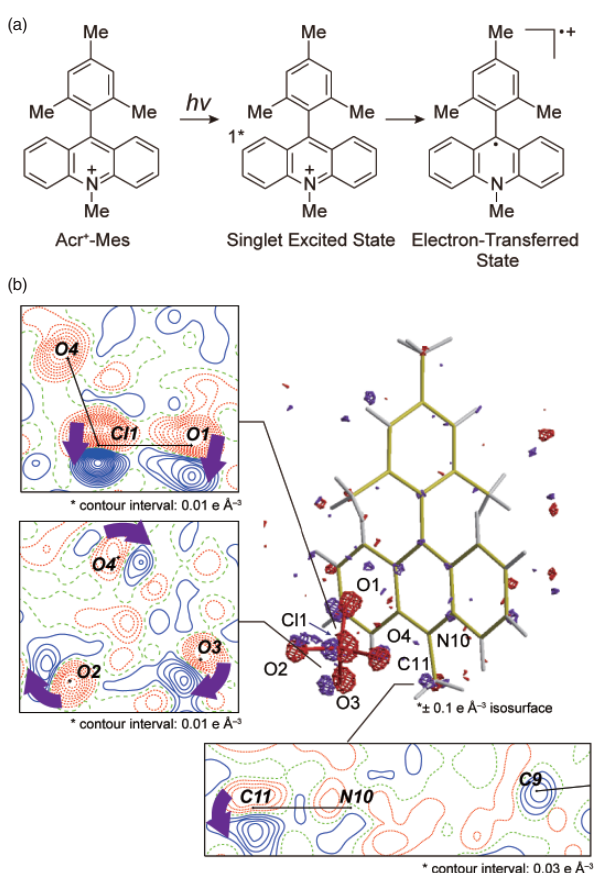


Figure 1 (a) Generation process of photoinduced electron-transfer state of $\text{Acr}^+\text{-Mes}$. (b) The $F_{\alpha(\text{on})} - F_{\alpha(\text{off})}$ difference Fourier map of $[\text{Acr}^+\text{-Mes}]\text{ClO}_4$. Blue and red contours (isosurfaces) represent negative and positive electron density in the 2D (3D) map. Blue bold arrows indicate the structural change upon photoinduced electron transfer.

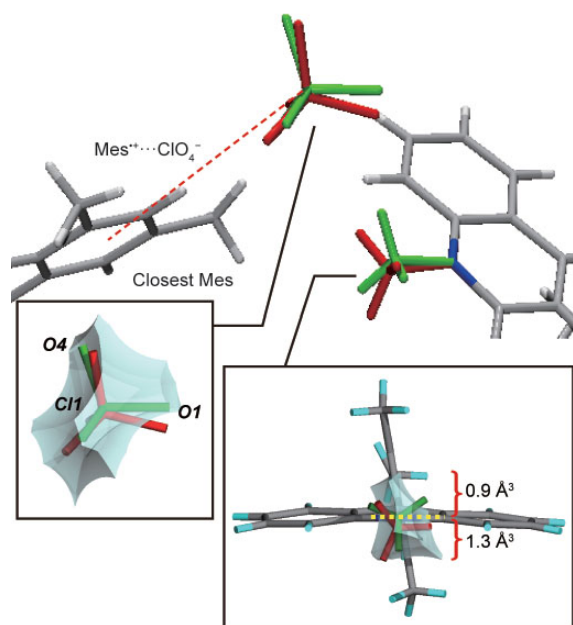


Figure 2
The photoinduced cooperative geometrical rearrangement in $[\text{Acr}^+-\text{Mes}]\text{ClO}_4^-$. Green and red fragments indicate the ground and photoinduced electron-transfer state geometries. The suggested electrostatic interaction between the oxidized Mes and ClO_4^- is indicated by the red dashed line. The reaction cavities around the *N*-methyl group and ClO_4^- are shown as a greenish-blue area in insets. The volumes of the divided cavity formed by the yellow dotted line are added on the side of it.

The photoinduced bending of the *N*-methyl group clearly indicates the reduction of Acr^+ by ET, because the sp^3 hybrid orbital character of the nitrogen atom is enhanced by reduction. Indeed, natural population analysis by theoretical calculation showed that the lone pair orbital of the nitrogen atom is filled by reduction. The reaction cavity drawing, which indicates the free space for an atom and a functional group to move in a crystal [6], shows that the direction of the photoinduced bending of the *N*-methyl group was toward the larger (i.e., sterically favorable) space (Fig. 2).

Oxidation of Mes by ET was reflected by the photoinduced movement of the counter anion, ClO_4^- . ClO_4^- moves toward the closest Mes in the crystal (Fig. 2), showing that ClO_4^- was attracted by the electrostatic interaction between the oxidized Mes and ClO_4^- ($\text{Mes}^+\cdots\text{ClO}_4^-$). The reaction cavity around ClO_4^- indicates that one of the oxygen atoms in ClO_4^- (O1) moved

out of the reaction cavity (Fig. 2). This sterically unfavorable geometrical change is due to the cooperative geometrical rearrangement in the crystal; the bending of the *N*-methyl group enlarged the space for the movement of O1, and ClO_4^- moved and filled that space by the $\text{Mes}^+\cdots\text{ClO}_4^-$ electrostatic interaction. This cooperative geometrical rearrangement suggests the generation of domains of $\text{Acr}^+-\text{Mes}^+$ (ClO_4^-). Domain generation indicates that the intramolecular back-ET is so slow that intermolecular back-ET becomes a dominant deactivation process.

Additionally, there was no intramolecular twisting between Acr^+ and Mes in the generation of the ET state, indicating that intramolecular back-ET by electronic coupling between Acr^+ and Mes^+ is restricted in the ET state.

In conclusion, the structural features of $\text{Acr}^+-\text{Mes}^+$ were determined by pump-probe single crystal X-ray structure analysis, definitively proving the formation of a long-lived ET state. This work provides a solid basis for developing efficient artificial photosynthetic systems.

REFERENCES

- [1] M. Hoshino, H. Uekusa, A. Tomita, S. Koshihara, T. Sato, S. Nozawa, S. Adachi, K. Ohkubo, H. Kotani and S. Fukuzumi, *J. Am. Chem. Soc.*, **134** (2012) 4569.
- [2] S. Fukuzumi, H. Kotani, K. Ohkubo, S. Ogo, N.V. Tkachenko and H. Lemmetyinen, *J. Am. Chem. Soc.*, **126** (2004) 1600.
- [3] H. Kotani, K. Ohkubo and S. Fukuzumi, *J. Am. Chem. Soc.*, **126** (2004) 15999.
- [4] S. Fukuzumi, K. Doi, A. Itoh, T. Suenobu, K. Ohkubo, Y. Yamada and K.D. Karlin, *Proc. Natl. Acad. Sci. U.S.A.*, **109** (2012) 15572.
- [5] S. Nozawa, S. Adachi, J. Takahashi, R. Tazaki, L. Guerin, M. Daimon, A. Tomita, T. Sato, M. Chollet, E. Collet, H. Cailleau, S. Yamamoto, K. Tsuchiya, T. Shioya, H. sasaki, T. Mori, K. Ichiyanagi, H. Sawa, H. Kawata and S. Koshihara, *J. Synchrotron. Rad.*, **14** (2007) 313.
- [6] Y. Ohashi, K. Yanagi, T. Kurihara, Y. Sasada and Y. Ohgo, *J. Am. Chem. Soc.*, **103** (1981) 5805.

BEAMLINER

AR-NW14A

M. Hoshino^{1,2}, H. Uekusa¹, A. Tomita¹, S. Koshihara^{1,2}, T. Sato³, S. Nozawa³, S. Adachi³, K. Ohkubo^{4,5}, H. Kotani^{4,5}, S. Fukuzumi^{4,5,6} (Tokyo Inst. of Tech., ²JST-CREST, ³KEK-PF, ⁴Osaka Univ., ⁵JST-ALCA, ⁶Ewha Womans Univ.)

Synchrotron-Radiation X-Ray Analysis of Hayabusa-Returned Asteroidal Samples

The Hayabusa spacecraft successfully captured dust particles on the Muses C Regio of asteroid 24153 Itokawa. Synchrotron-radiation X-ray diffraction analysis indicates that the mineralogy of the Itokawa dust particles is identical to that of the most primitive solar system material, chondrites, and dissimilar to that of terrestrial rocks. Chondrites were meteorites that formed 4.5 billion years ago and have a chemical composition close to that of the Sun. The similarity of Itokawa particles to chondrites proves that asteroids are the most primitive solar-system bodies formed in the early solar system. Further transmission and scanning electron microscope analyses indicate that most particles have experienced long-term thermal annealing, suggesting that Itokawa is an asteroid made of broken pieces of an inner part of a larger asteroid [1]. Computer simulations suggest that the original Itokawa asteroid was at least 20 km in radius and formed approximately 150 million years after the birth of the solar system.

Approximately 40 particles ranging in size from 30 to 180 microns that were collected during the first and second touchdowns on the surface of Itokawa were analyzed by various analytical methods. First we used synchrotron X-ray diffraction at BL-3A by applying high-intensity X-rays to identify crystal species in the Itokawa dust particles. Unfortunately the particles are very small (Fig. 1), but we must extract the maximum information from the particles. For this purpose, synchrotron radiation X-ray is the most powerful tool, because it enables us to identify crystal species in such a small particle without any destructive treatment. A variety of destructive analyses can then be performed after non-destructive X-ray analysis.

The X-ray diffraction analysis of individual particles indicates that most abundant mineral is highly crystalline olivine, and the next most abundant minerals are low-

and high-Ca pyroxene. Plagioclase is also abundant, but crystallinity differs between particles.

Major and minor element concentrations in all constituent minerals in all dust particles were determined by electron-probe analysis. Chemical compositions of olivine, low-Ca pyroxene, and Co and Ni concentrations of FeNi metals in Itokawa particles are within the range of LL chondrites, indicating that the surface of the Itokawa asteroid is covered with LL-chondrite dust particles. Olivine, pyroxene, and plagioclase in the Itokawa dust particles show homogeneous chemical compositions, indicating that these crystals have undergone intense thermal metamorphism. The metamorphic temperatures experienced by highly equilibrated particles are estimated based on two-pyroxene geothermometry to be approximately 800°C.

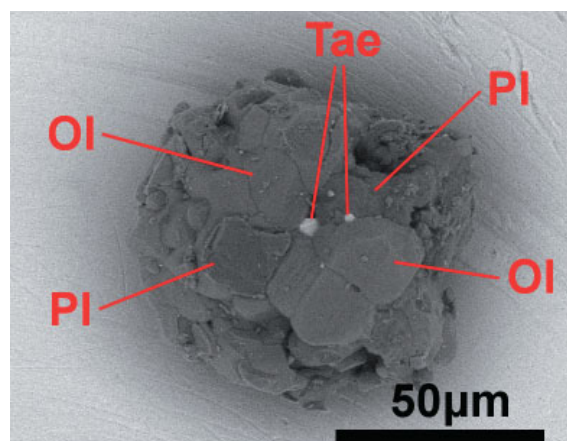


Figure 1 Itokawa dust particle returned by the Hayabusa mission. The particle consists of olivine (OI), plagioclase (PI) and FeNi metal taenite (Tae). It shows a smooth surface that was likely formed by sputtering due to solar wind radiation [1].

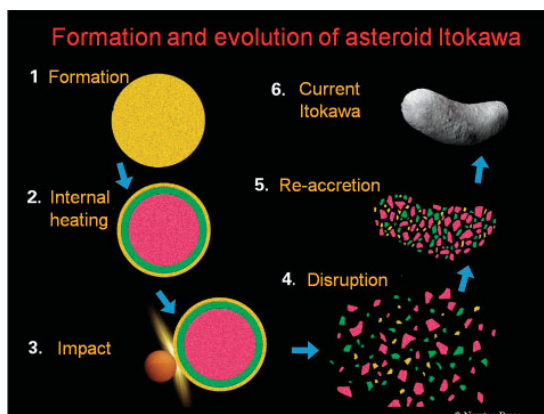


Figure 2
Model of formation of the Itokawa asteroid. (A modified figure appeared in Newton Magazine, 2011).

During thermal metamorphism, temperatures increase with depth and the high petrologic type lay deeper in the parent body than the lower type, assuming internal heating due to decay energy of the short-lived radioisotope ^{26}Al . The metamorphic temperature of 800°C experienced by the Itokawa particles requires the asteroid to have been larger than 20 km in radius and formed approximately 150 million years after the birth of the solar system, i.e., after the formation of the oldest solar system material called CAIs (Ca- and Al-rich inclusions). The current size of Itokawa (approximately 0.5 km in diameter) is much smaller than the initial size, suggesting that the parent Itokawa asteroid was much larger than the current Itokawa. The high abundance of thermally metamorphosed particles, which formed in

the interior of the asteroid, on the surface of the asteroid suggests that Itokawa is an asteroid made of broken pieces of an inner part of a larger asteroid (Fig. 2).

REFERENCE

- [1] T. Nakamura, T. Noguchi, M. Tanaka, M.E. Zolensky, M. Kimura, A. Tsuchiyama, A. Nakato, T. Ogami, H. Ishida, M. Uesugi, T. Yada, K. Shirai, A. Fujimura, R. Okazaki, S.A. Sandford, Y. Ishibashi, M. Abe, T. Okada, M. Ueno, T. Mukai, M. Yoshikawa and J. Kawaguchi, *Science*, **333** (2011) 1113 .

BEAMLINER

3A

T. Nakamura (Tohoku Univ.)

Observation of the Structure of Adsorbed Water on a Mica Surface to Understand the Mechanism of Creeping Faults

Creeping faults are characterized by continuous slip without large earthquakes. One of the famous creeping faults is the central zone of the San Andreas Fault. Although the mechanism of creeping faults is not yet clear, the most plausible hypothesis is lubrication due to layered-structure minerals and adsorbed water on the mineral surfaces. We have tried to understand the mechanism of low friction due to adsorbed water. Since the mechanism should be closely related to the structure of the water/mineral interfaces, we have conducted X-ray surface scattering measurements for the mica/saltwater interface and revealed the presence of adsorbed hydrated sodium ions on the mica surface. The water molecules around the sodium ions would act like ball-bearings and result in low friction between mica surfaces.

Rock fracture and fault slip are triggered by the movement of tectonic plates and cause earthquakes. However, there is a “creeping fault” type of slipping which occurs continuously without large earthquakes. One possible explanation for the continuous slip is the low frictional strength of the faults due to the presence of layered clay minerals and adsorbed water molecules on these mineral surfaces [1-3]. We have experimentally demonstrated that saltwater can be a good lubricant between muscovite (mica) surfaces even when compressed to a thickness of 1 nm [4]. Mica is ubiquitous in igneous rocks and the structure is similar to clay minerals. The thickness of 1 nm corresponds roughly to a layer of three water molecules. However, the mechanism of this lubrication is not well understood, so we have tried to understand the electronic states of the mica/NaCl solution interface because the structure should be closely related to the mechanism of water lubrication [5].

The electron density of the interface between mica and saltwater was measured by the X-ray crystal truncation rod (CTR) scattering technique. Although this technique can reveal the electron density profiles of solid/liquid interfaces with sub-nanometer resolution, on its own it cannot directly provide information about the elements. Therefore, the distribution of chemical elements at the interface was discussed by comparing the results of X-ray CTR scattering with those of molecular dynamics (MD) simulations. The X-ray CTR scattering experiments were conducted at the BL-4C. The interatomic potential model used in the MD simulations was originally developed. These experiments and simulations revealed the structure of the muscovite/NaCl solution interface, the main features of which are as follows. (1) Oscillation of the electron density profile in the saltwater was observed within 1.2 nm of the mica surface (Fig. 1).

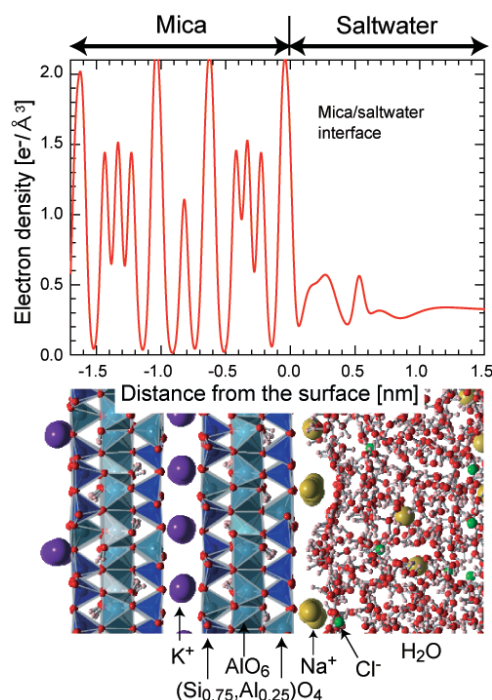


Figure 1 The electron density profile (top) and a plausible snapshot (bottom) of the mica/saltwater interface.

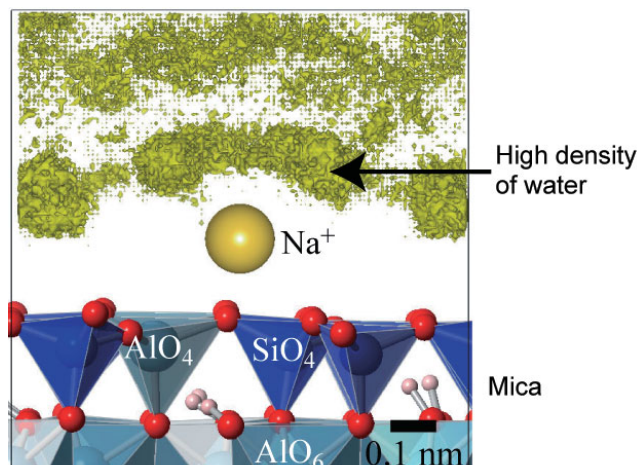


Figure 2

The iso-density surface of water on a mica surface. The yellow surface shows the positions where the density of water is six times higher than that in the bulk.

(2) Hydrated sodium ions adsorbed on the negatively charged mica surface were present as the inner sphere complexes (Fig. 2).

(3) The radii of the first hydration shell of the adsorbed sodium ions were approximately 0.5 nm.

These results provide a plausible mechanism for the high lubrication between mica surfaces due to the presence of saltwater. When saltwater is compressed to a thickness of 1 nm between opposite-facing mica surfaces, the first hydration shells of the sodium ions adsorbed onto the mica surface contact each other between both sides of the mica surfaces. The water in the first hydration shell has strong attractive interaction with the Na^+ and therefore the water should remain, even under the compressed condition, between the mica surfaces. These water molecules would act like ball-bearings between mica surfaces and result in low friction between the surfaces.

A systematic understanding of the effects of adsorbed water on the lubrication between minerals present at faults is important to establish the fundamental physics of faults. The mechanism proposed here to ex-

plain the low friction between mica surfaces due to the adsorbed water molecules provides a new perspective for the development of studies in this field.

REFERENCES

- [1] C.H. Scholz and T.C. Hanks, *Rheology and deformation of the lithosphere at continental margins*, edited by G.D. Karner, B. Taylor, N.W. Driscoll and D.L. Kohlstedt (Columbia Univ. Press, New York, 2004). Chap. 9.
- [2] D.A. Lockner, C. Morrow, D. Moore and S. Hickman, *Nature*, **472** (2011) 82.
- [3] C.A. Morrow, D.E. Moore and D.A. Lockner, *Geophys. Res. Lett.*, **27** (2000) 815.
- [4] H. Sakuma, K. Otsuki and K. Kurihara, *Phys. Rev. Lett.*, **96** (2006) 046104.
- [5] H. Sakuma, T. Kondo, H. Nakao, K. Shiraki and K. Kawamura, *J. Phys. Chem. C*, **115** (2011) 15959.

BEAMLINER

4C

H. Sakuma¹, T. Kondo², H. Nakao³ and K. Kawamura⁴
 (¹Tokyo Inst. of Tech., ²Ochanomizu Univ., ³KEK-PF, ⁴Okayama Univ.)

Discovery of Flowering Hormone (Florigen) Receptor and Its Crystal Structure

Florigen, a mobile floral induction protein, initiates the flowering process of activating floral identity genes. Many details of the molecular function of florigen remain unclear. In the present study, we found that the rice florigen Hd3a directly interacts with 14-3-3 (GF14) proteins, but not with the transcription factor OsFD1. We further determined the 2.4-Å crystal structure of a tripartite Hd3a-14-3-3-OsFD1 complex [1]. The determined crystal structure offers biological insights into 14-3-3 proteins and how they play a key role in mediating an indirect interaction between Hd3a and OsFD1. Our biochemical, biophysical, and physiological experiments using rice cultured cells and transgenic rice plants revealed that 14-3-3 proteins are intracellular receptors of florigen to activate floral identity genes.

Florigen is produced in leaves and transmitted through the phloem to the shoot apex, where it induces flowering. A number of recent reports have provided evidence that Arabidopsis FT protein (Hd3a in rice) is a key component of florigen [2]. In the shoot apical meristem, FT activates floral identity genes such as *AP1* transcription and induces flowering by interacting with the bZIP transcription factor FD, although the details of the interaction between FT and FD have not yet been clarified. In rice, the closest homolog of FD, OsFD1, has been identified based on its function and homology with maize DLF1 [1]. The FT-FD interaction is required for flowering, and phosphorylation of residue T282 in the C-terminal region of FD may be critical for this interaction and for the floral initiation.

In the present study, a direct interaction between highly purified Hd3a and OsFD1 was tested using three different methods, but none was detected. On the other hand, a direct interaction between Hd3a and rice 14-3-3 protein GF14 was observed by GST pull-down and

NMR experiments. One consensus sequence among the bZIP transcription factors, including OsFD1, that reportedly bind FT and its homologs, was found to be R-x-x-(S/T)-A-P-F, which resembles the 14-3-3 protein-binding motif R-S-x-(pS/pT)-x-P. The presence of this sequence in OsFD1 raises the possibility that the interaction between Hd3a and OsFD1 is indirect and is mediated by 14-3-3 proteins.

To elucidate the structural basis of the interactions between these three proteins, the crystal structure of a tripartite Hd3a-14-3-3-OsFD1 complex was determined at 2.4-Å resolution (Fig. 1), using the data recorded at the BL-5A, 17A and AR-NW12A. The binding sites in GF14 for Hd3a are more than 20 Å apart from those for OsFD1, and yeast two-hybrid assays using GF14 mutants confirmed that the two partners bound independently. Therefore, GF14 forms a stable complex with Hd3a and OsFD1 simultaneously, and mediates indirect binding between Hd3a and OsFD1. This complex was named Florigen Activation Complex (FAC).

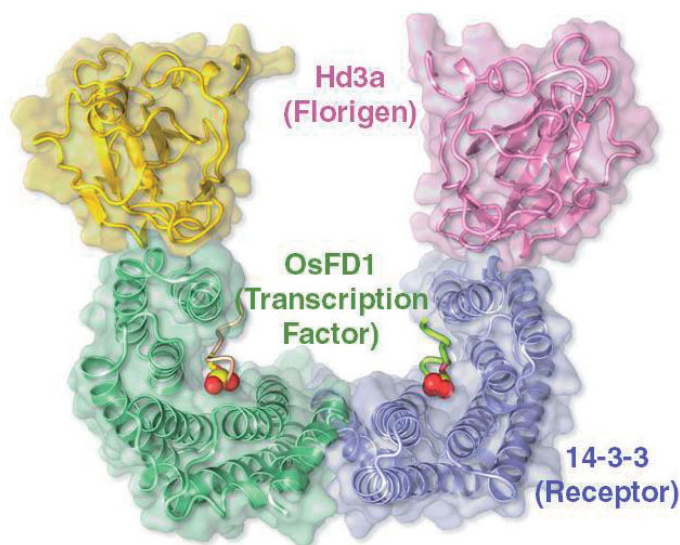


Figure 1
Structure of the Florigen Activation Complex (FAC). The FAC hetero-hexameric structure is represented as a ribbon, composed of two Hd3a molecules (florigen, gold and magenta), a 14-3-3 dimer (receptor, dark green and blue) and two OsFD1 peptides (transcription factor, khaki and light green). Oxygen atoms in the phosphate groups of phosphoserine 192 of OsFD1 are shown as red spheres.

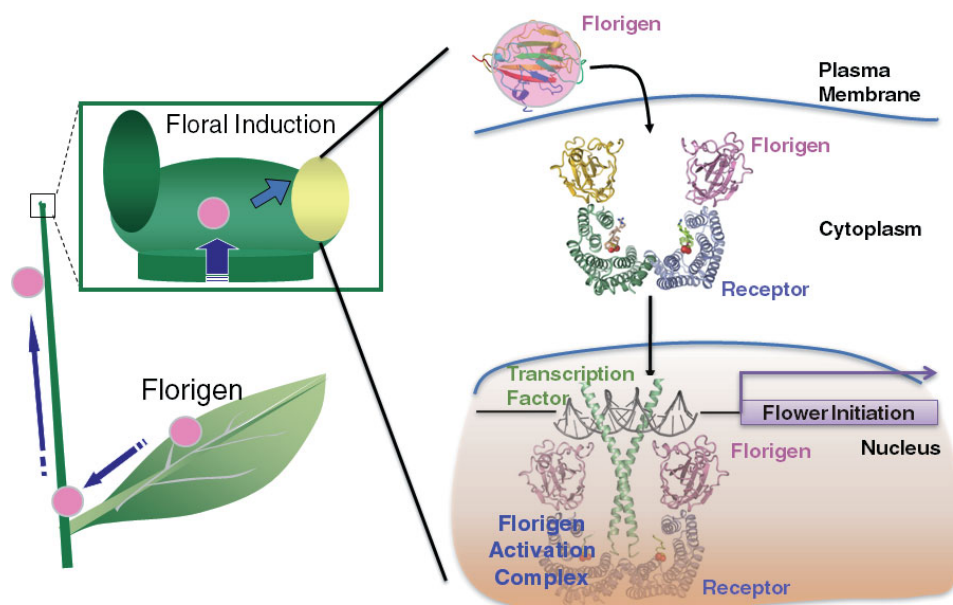


Figure 2

Model of the FAC formation. Florigen (Hd3a) is produced in leaves and is transmitted through the phloem to the shoot apex. Once florigen enters a shoot apical cell, it initially binds the florigen receptor (14-3-3 proteins) in the cytoplasm. When the florigen–receptor complex enters the nucleus, it forms a complex with the transcription factor (OsFD1), which is retained in the nucleus, and activates the flower initiation gene transcription, leading to floral induction.

Based on biochemical, biophysical, and physiological experiments using rice cultured cells and transgenic rice plants, it was shown that the florigen Hd3a forms a complex with 14-3-3 protein and OsFD1, and this complex formation is required for floral induction [1] (Fig. 2). In this model, the 14-3-3 proteins act as intracellular receptors for Hd3a (florigen), which is transported from the leaves to the shoot apex. Once Hd3a enters cells in the shoot apex, it initially binds the 14-3-3 proteins in the cytoplasm. At this stage of development, OsFD1 is being expressed in the shoot apex cells, and when the Hd3a-14-3-3 complex enters the nucleus, it forms a ternary complex with OsFD1, which will be retained in the nucleus. The formed FAC then activates the *AP1* transcription, leading to floral induction. By its nature, Hd3a-14-3-3 complex may also interact with other bZIP transcription factors containing the R-x-x-(S/T)-A-P-F motif, putative interaction that provides a mechanistic basis for the proposed participation of florigen in processes other than flowering, such as potato tuber formation [3]. Therefore, together with the discovery of the florigen

receptor and the unraveling of the FAC structure, the possibility of manipulating florigen and other interacting regulators may pave the way for improving various important traits, such as early/late flowering, increased crop and fruit yields, and biofuel crop production.

REFERENCES

- [1] K. Taoka, I. Ohki, H. Tsuji, K. Furuita, K. Hayashi, T. Yanase, M. Yamaguchi, C. Nakashima, Y.A. Purwestri, S. Tamaki, Y. Ogaki, C. Shimada, A. Nakagawa, C. Kojima and K. Shimamoto, *Nature*, **476** (2011) 332.
- [2] S. Tamaki, S. Matsuo, H.L. Wong, S. Yokoi and K. Shimamoto, *Science*, **316** (2007) 1033.
- [3] C. Navarro, J.A. Abelenda, E. Cruz-Oró, C.A. Cuéllar, S. Tamaki, J. Silva, K. Shimamoto and S. Prat, *Nature*, **478** (2011) 119.

BEAMLIN

5A

K. Taoka¹, I. Ohki¹, H. Tsuji¹, C. Kojima^{1,2} and K. Shimamoto¹ (¹NASIT, ²Osaka Univ.)

Crystal Structure of Channelrhodopsin, a Light-Gated Cation Channel: All Cations Lead through the Monomer

Channelrhodopsin (ChR) is a light-gated cation channel derived from algae that conducts cations, including sodium ions, in a light-dependent manner. Because the inward flow of sodium ions triggers the neuron firing, neurons expressing ChRs can be controlled by light even within freely moving mammals. Although ChR has been broadly applied to neuroscience research, little is known about its molecular mechanisms. We determined the crystal structure of ChR at 2.3 Å resolution and revealed its molecular architecture, especially the cation-conducting pathway. The integration of structural and electrophysiological analyses provided insight into the molecular basis for the remarkable function of ChR, and paved the way for the design of ChR variants with novel properties.

Organisms from bacteria to humans perceive light and use the information for visual and non-visual functions, including ATP synthesis and circadian rhythm. In most cases, the perception of light is mediated by rhodopsin family proteins, which consist of seven-transmembrane (7-TM) domains and covalently linked retinal chromophores. Based on their functions, rhodopsin family proteins can be divided into four distinct classes: photoisomerase, signal transducer, ion pump, and the most recently discovered class, ion channel (Fig. 1).

Channelrhodopsin (ChR) was originally isolated from tiny green algae, *Chlamydomonas Reinhardtii*, and identified as a light-gated cation channel in 2002 [1]. In early 2005, it was found that ChRs could be expressed in mammalian neurons to mediate the precise control of action potential firing in response to light pulses. ChRs have now been used to control neuronal activity in a wide range of animals, but virtually nothing is known about how a 7-TM protein can form a light-switchable

channel for cations. Although a rough helical arrangement was visible in the recently published electron microscopic (EM) structure of ChR at 6 Å resolution [2], the details of amino acid positioning and channel function remained completely lacking. A high-resolution structure would be of enormous value, not only to enhance understanding of the mechanism of this new class of rhodopsin family proteins, but also to guide the way to designing ChR variants with novel functions related to spectrum, selectivity, and kinetics.

To solve the crystal structure of ChR, we expressed a chimeric ChR between ChR1 and ChR2 in Sf9 insect cells. The crystals were obtained in a lipidic mesophase, and the structure was solved by the multiple anomalous dispersion (MAD) method, using mercury-derivatized crystals. As far as we know, this is the first example of phase determination by MAD for a crystal obtained in lipidic mesophase. We finally determined the crystal structure of ChR in the closed state at 2.3 Å resolution.

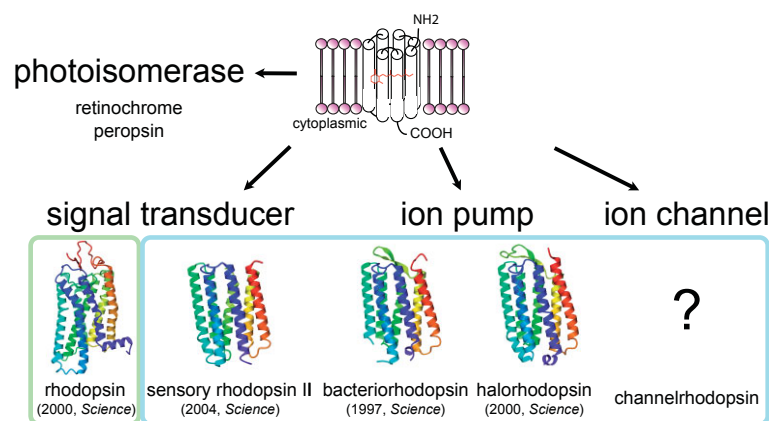


Figure 1
Classification of rhodopsin family proteins.

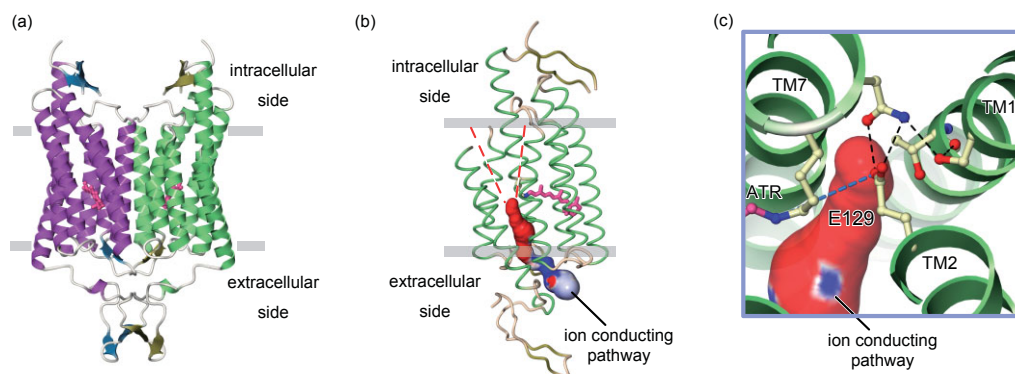


Figure 2

The structures of ChR. (a) Overall structure of ChR dimer. Each protomer is shown in a *ribbon* representation (*green* and *magenta*) and retinal chromophores are depicted by a *stick* model (*pink*). (b) The ion-conducting pathway. The putative intracellular vestibule is shown by *red dashed lines*. (c) The possible channel gate. Hydrogen bonds are shown by *black dashed lines*, and the *blue dashed line* represents a possible proton transfer pathway.

ChR is composed of an N-terminal extracellular domain, the 7-TM domains connected by three cytoplasmic and extracellular loops, and the C-terminal intracellular domain [Fig. 2(a)]. Of particular note is that, as previously predicted from EM [2], ChR is tightly associated into a dimer *via* interfacial interactions between the N-domain, ECL1, TM3 and TM4 of each molecule. This result is surprising because all other known microbial rhodopsins form trimer or tetramer. This is the first example of microbial rhodopsin to adopt a dimer conformation.

To further understand the ChR structure, we compared our ChR with the most well studied microbial rhodopsin, bacteriorhodopsin (BR). Although the primary sequence identity between ChR and BR is as low as 15%, the overall structure of ChR is well superimposed on that of BR. TM3 to TM6 are very similar, and the position of the retinal chromophore is well conserved, whereas there are two distinct features between ChR and BR. First, ChR has additional N-terminal and C-terminal domains, and more importantly, the extracellular ends of TM1 and TM2 are tilted compared to those of BR. Because of this tilt, ChR has a larger pore formed by TM1, 2, 3, and 7. The calculated electrostatic surface potential reveals that this pore is strongly electronegative, so we assumed that this pore acts as the cation-conducting pathway in ChR [Fig. 2(b)]. To verify this hypothesis, we expressed the mutants of the pore-lining residues in HEK293 cells and recorded photocurrents in response to blue light pulses. Most mutants showed altered properties, including photo-conductance, kinetics, and ion preference. Therefore, we suggest that this pore actually acts as the cation-conducting pathway.

While this cation-conducting pathway is open toward the extracellular side, the cytoplasmic side of the pathway is occluded by Glu129 [Fig. 2(c)]. Although the calculated *pKa* of Glu129 suggests that this residue is protonated in the closed state, E129Q mutant shows a

strongly decreased photocurrent. Thus, we assume that Glu129 acts as the putative channel gate-keeper, and that the gating is regulated by the protonation change of Glu129 during the photocycle. Recent FT-IR studies also support our idea [3].

In this study [4], we determined the first crystal structure of a light-gated cation channel, in the closed/dark state at 2.3 Å resolution, and provided insights into ChR dimerization, retinal binding, and cation conductance. In the field of ChR, there are two hypotheses about the cation-conducting pathway. One is that the pathway comprises helices from a single ChR molecule, and the other is that the ChR dimer assembles to form the conducting pathway using elements from each of the two ChRs. This study strongly supports the former hypothesis and will accelerate the basic mechanistic understanding of this remarkable photoreceptor protein. This high-resolution information, along with electrophysiological analyses, will also guide the way to designing ChR variants with ideal properties, such as enhanced potassium ion selectivity and red-shifted absorption spectrum.

REFERENCES

- [1] G. Nagel, D. Ollig, M. Fuhmann, S. Kateriya, A.M. Musti, E. Bamberg and P. Hegemann, *Science*, **296** (2002) 2395.
- [2] M. Müller, C. Bamann, E. Bamberg and W. Kühlbrandt, *J. Mol. Biol.*, **414** (2011) 86.
- [3] K. Eisenhauer, J. Kuhne, E. Ritter, A. Berndt, S. Wolf, F. Bartl, P. Hegemann and K. Gerwert, *J. Biol. Chem.*, **287** (2012) 6904.
- [4] H.E. Kato, F. Zhang, O. Yizhar, C. Ramakrishnan, T. Nishizawa, K. Hirata, J. Ito, Y. Aita, T. Tsukazaki, S. Hayashi, P. Hegemann, A.D. Maturana, R. Ishitani, K. Deisseroth and O. Nureki, *Nature*, **482** (2012) 369.

BEAMLINES

AR-NW12A and 1A

H.E. Kato and O. Nureki (The Univ. of Tokyo)

Structural Analysis of the Mammalian Cell Polarity Protein Complex mInsc and LGN

Interaction between the cell polarity proteins mInsc (mammalian homolog of Inscuteable) and LGN (Leu-Gly-Asn repeat-enriched protein) plays a crucial role in mitotic spindle orientation during asymmetric cell division. We determined the crystal structure of the LGN-binding domain (LBD) of mInsc in complex with the N-terminal tetratricopeptide repeat (TPR) motifs of LGN at 2.6 Å resolution. In the complex, mInsc-LBD adopts an elongated structure that runs antiparallel to LGN along the concave surface of the superhelix formed by the TPR motifs. Structural and biochemical analyses provide new insights into the control of mitotic spindle orientation by the mInsc-containing complex.

In mitotic cells, orientation of the mitotic spindle defines the direction of cell division and the position of two daughter cells. The mitotic spindle orientation is controlled by the evolutionarily conserved protein complex containing LGN (Leu-Gly-Asn repeat-enriched protein), NuMA (nuclear mitotic apparatus protein), and the $G\alpha i$ subunit of trimeric G_i proteins. In LGN, an intramolecular interaction between its N- and C-termini occurs, bringing this protein into an autoinhibitory conformation. The asymmetric division requires the establishment of apical-basal polarity in epithelial cells; the Par3-containing protein complex is specifically localized to the apical cortex for polarity establishment. The adaptor protein mInsc (mammalian homolog of Inscuteable) simultaneously binds to Par3 and LGN to provide a physical link between the two complexes; the link thereby couples cortical cell polarity and spindle orientation for asymmet-

ric cell division [1]. LGN and its paralog AGS3 consist of an N-terminal domain comprising eight tetratricopeptide repeat (TPR) motifs and a C-terminal region harboring four GPR (G-protein regulatory) motifs that bind to the $G\alpha i$ subunit of trimeric G proteins (Fig. 1). LGN interacts with multiple partners including mInsc, NuMA, and the C-terminal region of LGN via its TPR motifs. mInsc contains an N-terminal region highly homologous to the asymmetry domain of Pins, a fruit-fly homolog of LGN, which is responsible not only for apical cortical localization and mitotic spindle orientation along the apical-basal axis but also for interacting with Pins. However, the molecular basis for the mInsc-mediated regulation of the Par3-containing cell polarity complex and the mitotic spindle orientation regulating $G\alpha i$ -LGN-NuMA complex remains elusive.

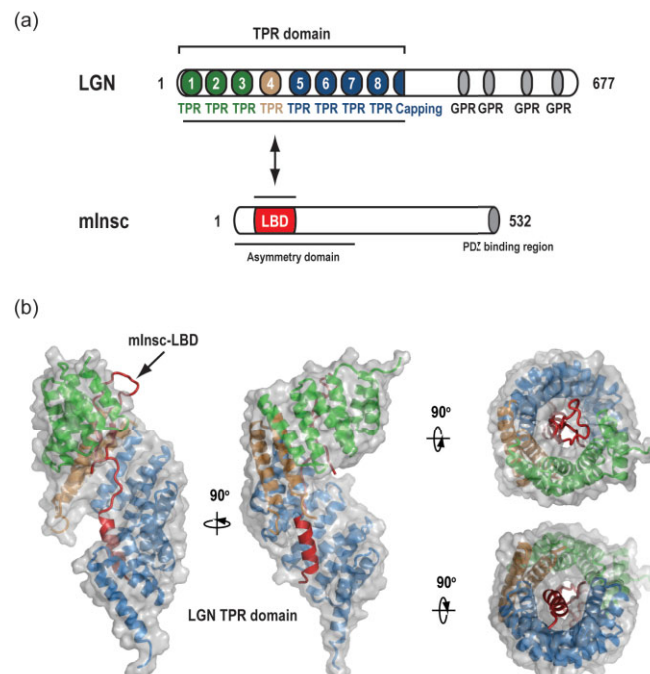


Figure 1

Structure of mInsc and LGN. (a) Domain architecture of LGN and mInsc. Human mInsc of 532 amino acids harbors an N-terminal LBD, which is located in a region corresponding to the asymmetric localization domain of *Drosophila* Insc, and a region for binding to the Par3 PDZ domains. LGN of 677 amino acids harbors an N-terminal domain composed of eight TPR motifs and a C-terminal region of four GPR motifs. (b) Orthogonal views of the overall structure of mInsc-LBD in complex with LGN TPR domain. mInsc-LBD is colored in red. The TPR domain of LGN is shown in a surface representation with the secondary structure indicated in green (TPR1-3), in orange (TPR4), and in blue (TPR5-8 and the capping helix).

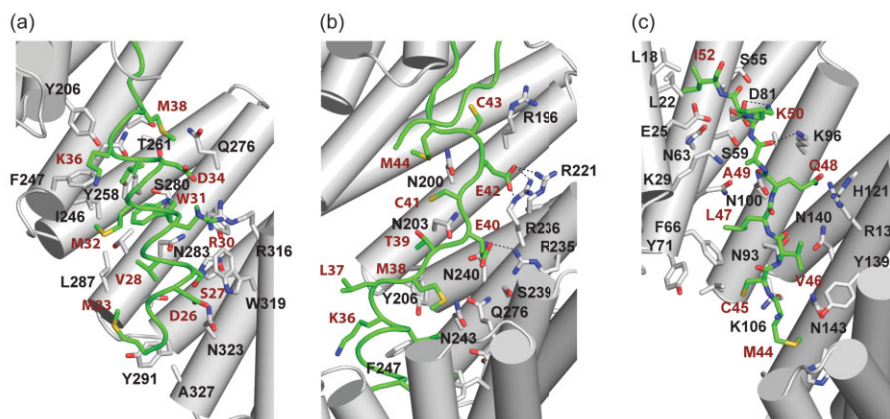


Figure 2

Interactions between mlnc-LBD and LGN-N. Recognition of the α -helix region of mlnc-LBD (a), the extended region of mlnc-LBD (b), and the β -sheet region of mlnc-LBD (c). mlnc-LBD is colored in green and LGN-N represents the cylinder model colored in gray. Residues involved in mlnc-LGN interaction are labeled.

We first mapped the regions required for the interaction between mlnc and LGN using truncated forms of mlnc and LGN. Binding experiments between mlnc and LGN revealed that the LGN-binding domain of mlnc (mlnc-LBD, residues 23-69) is sufficient for interaction with the LGN TPR motifs (LGN-N, residues 13-414). To understand the molecular mechanism underlying the interaction between mlnc-LBD and LGN TPR motifs, we determined the crystal structure of the LGN–mlnc-LBD complex at 2.6 Å resolution [2]. In the complex, mlnc-LBD forms an elongated structure containing an α -helix, and an antiparallel β -sheet linked by an extended region. LGN-N contains eight TPR motifs with a C-terminal capping helix (17 anti-parallel α -helices in total), which adopt a solenoid-like superhelix structure (Fig. 1). mlnc-LBD runs antiparallel along the concave surface of the TPR superhelix of LGN and displays an electrostatic surface complementary to the LGN groove formed by the TPR motifs. mlnc-LBD can be roughly divided into three distinct binding regions: an α -helix, an extended region, and an antiparallel β -sheet, from which strands β 1 and β 2 are connected through a 13-residues loop. All of these three regions have distinctive features in LGN binding (Fig. 2). The large interacting surface area buried at the mlnc-LGN interface is approximately 4,200 Å², suggesting a stable interaction between mlnc and LGN. Indeed, mlnc bound to LGN with an estimated K_D value of approximately 2.4 nM. Because residues critical for mlnc–LGN interaction are completely conserved, key features of the mlnc-LBD–

LGN-N complex structure appear to be maintained throughout the evolution of animals from insects to mammals.

Structural and biochemical analyses also helped to define residues that are crucial for mlnc-LGN interaction and revealed that the LGN TPR domain directly binds to the AGS3-binding protein Frmpd1 and its relative protein Frmpd4 in a manner similar to, but distinct from that of mlnc, whereas NuMA and the C-terminal region of LGN bind to the LGN TPR domain in a fashion different from that of mlnc and Frmpd proteins. To elucidate the relationship between mlnc and other LGN binding partners, we performed competition assays between mlnc and other partners. Interestingly, mlnc binds to LGN with the highest affinity among the partners investigated and efficiently replaces not only the Frmpd proteins but also NuMA and the C-terminal region of LGN, suggesting the priority of mlnc in binding to LGN. The competition between mlnc and NuMA to LGN may regulate spindle orientation during mitosis.

REFERENCES

- [1] K.H. Siller and C.Q. Du, *Nat. Cell. Biol.*, **11** (2009) 365.
- [2] S. Yuzawa, S. Kamakura, Y. Iwakiri, J. Hayase and H. Sumimoto, *Proc. Natl. Acad. Sci. USA*, **108** (2011) 19210.

BEAMLINE

17A

S. Yuzawa and H. Sumimoto (Kyushu Univ.)

Structural Basis of Measles Virus Entry and Effective Measles Vaccine

The measles virus (MV), one of the most contagious viruses, causes a common febrile disease. Although its pathological implications are well documented, the molecular mechanism of MV entry remains unclear. In this study, we determined the complex structures of MV hemagglutinin (MV-H) bound to its cellular receptor, the signaling lymphocyte activation molecule (SLAM, also called CD150). The crystal structures revealed two forms of the MV-H-SLAM tetrameric assembly, which has implications in fusion triggering for MV entry. Furthermore, the structures provided a clear explanation as to why the MV vaccine is highly effective.

Measles is a major cause of child morbidity and mortality, accounting for 4% of deaths in children under 5 years of age worldwide. The disease is characterized by fever, cough and a rash accompanied by profound immune suppression. MV, the causative agent of the disease, was first isolated in 1954, and MV vaccine was successfully developed in 1963. For nearly the past 50 years, MV vaccine has been effective against all MV strains around the world.

MV is a member of the genus *Morbillivirus* in the family *Paramyxoviridae*. MV possesses two distinct envelope glycoproteins, the attachment protein hemagglutinin (MV-H) and the fusion protein (MV-F). MV uses SLAM expressed on immune cells as a receptor. CD46, ubiquitously expressed on nucleated cells, has also been reported to be a MV receptor. However, only vaccine strains can interact with CD46, and clinically isolated (wild type) strains cannot use it as a receptor. A third epithelial cell receptor was recently identified, called Nectin 4.

To enter the target cell, MV must bind to its receptors by MV-H, then its envelope membrane must fuse with the host plasma membrane on the cell surface by MV-F. Although the mechanism by which receptor binding leads to fusion has been elusive, two models have been proposed. In the first model, upon receptor binding, MV-H undergoes a conformational change, which destabilizes the pre-fusion MV-F, leading to its refolding for membrane fusion. In the second model, MV-H serves as a clamp that stabilizes the pre-fusion MV-F. Upon receptor binding, MV-H releases the pre-fusion MV-F from the clamp to facilitate its spontaneous structural change.

To better understand the mechanism of MV entry, we determined the crystal structure of MV-H bound to its cellular receptor, SLAM (MV-H-SLAM) [1]. We had previously reported the crystal structure of MV-H alone [2]. Based on both the receptor-free and SLAM-bound forms of MV-H structures, we propose a new model for MV entry.

Initial crystals of MV-H-SLAM diffracted to 7–8 Å resolution, and then the diffraction was finally improved using protein engineering techniques [3] and collected at BL-5A to a resolution of 3.15 Å. The structural or conformational change could not be observed in either MV-H monomer or dimer with and without SLAM binding. However, two forms of the MV-H: SLAM tetrameric assembly (dimer of two dimers) were detected, termed form I (3.55 Å) and form II (3.15 Å) (Fig. 1). We propose a new model for MV entry based on these crystallographic evidences: (1) Upon binding of MV-H to the receptors, the binding mode of MV-H and SLAM allows the viral envelope and host cell membrane to come close to each other. (2) The binding to the receptors also facilitates the tetrameric assembly of MV-H, and a conformational shift from form I to form II. (3) This conformational shift serves as a trigger for the structural change of MV-F, which allows its refolding and fusion with the host cell membrane.

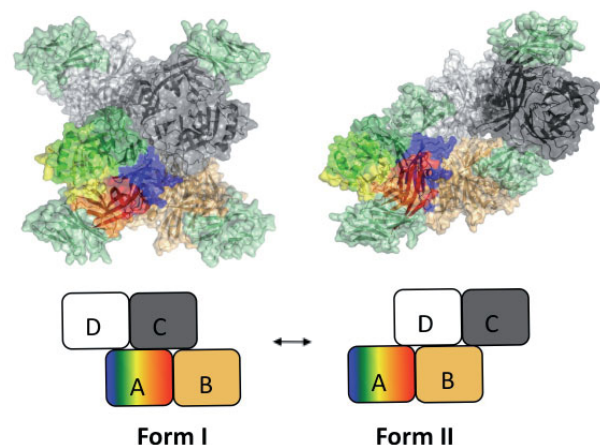


Figure 1
Two forms of MV-H: SLAM tetrameric assembly.
Top: crystal structures of MV-H: SLAM tetramers (left, form I; right, form II). Monomer A (rainbow) and B (light orange) form a dimer, while monomer C (gray) and D (white) form a second dimer. SLAM (pale green) binds to individual MV-H monomers. Bottom: schematics of two forms of MV-H tetramers.

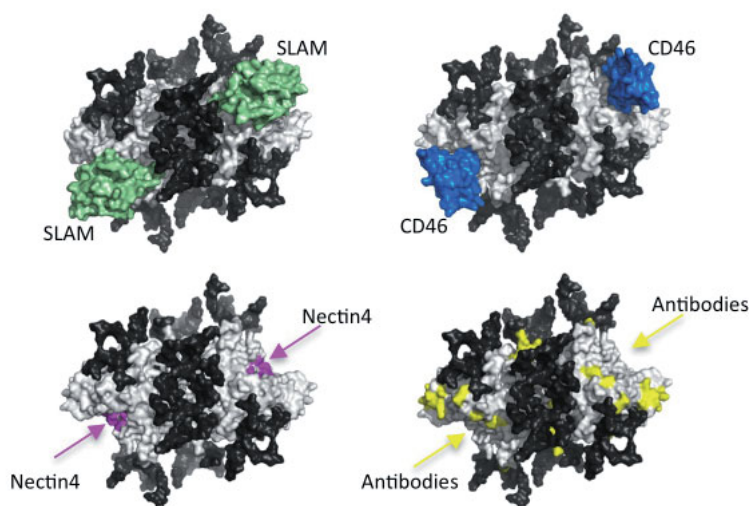


Figure 2

Structural basis for the effectiveness of the measles vaccine.

Receptor binding sites of SLAM, CD46, and Nectin 4 on MV-H overlap with a major area targeted by anti-MV-H antibodies. This region is uncovered by N-linked sugars.

MV vaccine is known as one of the most successful and effective vaccines. The structures of receptor-free and receptor-bound MV-H provide a clear explanation for its effectiveness. A large part of the MV-H surface is covered by N-linked sugars, but the receptor-binding region is exposed (Fig. 2). As a result, this area is also targeted by neutralizing antibodies. Inability to use the receptors SLAM and Nectin 4 is detrimental for MV. Therefore, MV is not allowed to have escape mutations in this receptor-binding region. In fact, this region is highly conserved in all MV strains and even in other morbilliviruses. This conservation nicely explains why MV occurs as serologically monotypic. Thus, from the structural data collected at BL-5A, we were able to not only propose a new entry model for MV, but also demonstrate why only one MV vaccine is sufficient against all strains of MV.

REFERENCES

- [1] T. Hashiguchi, T. Ose, M. Kubota, N. Maita, J. Kamishikiyo, K. Maenaka and Y. Yanagi, *Nat. Struct. Mol. Biol.*, **18** (2011) 135.
- [2] T. Hashiguchi, M. Kajikawa, N. Maita, M. Takeda, K. Kuroki, K. Sasaki, D. Kohda, Y. Yanagi and K. Maenaka, *Proc. Natl. Acad. Sci. USA.*, **104** (2007) 19535.
- [3] T. Hashiguchi, T. Ose, M. Kubota, N. Maita, J. Kamishikiyo, K. Maenaka and Y. Yanagi, *Protein Pept. Lett.*, **19** (2012) 468.

BEAMLIN

5A

T. Hashiguchi¹, T. Ose², K. Maenaka² and Y. Yanagi¹
(¹Kyushu Univ., ²Hokkaido Univ.)

Structural Basis of Arf6-MKLP1 Complex Formation on the Flemming Body Responsible for Cytokinesis

Cytokinesis is the process of cell division in which a single cell is divided into two daughter cells. Arf6 is a small GTPase involved in cytokinesis by localizing on the Flemming body (the midbody). In addition, vesicle transport from cytosol to Flemming body is also important for the completion of cytokinesis. MKLP1 (mitotic kinesin-like protein 1) is a family of kinesins involved in vesicle transport during cytokinesis, but it remains unknown how Arf6 and MKLP1 contribute to cytokinesis. Here, we show from a structural point of view how the formation of Arf6-MKLP1 complex is critical for the proper completion of cytokinesis.

Cytokinesis is the final stage of cell division. Before cytokinesis, a contractile ring constricts the plasma membrane in the equatorial region of a dividing cell to form a cleavage furrow, while an overlapping region of antiparallel microtubules from the central spindle gradually forms the Flemming body (the midbody) in the middle of the cleavage furrow. Finally, the cell undergoes abscission on either side of the Flemming body during cytokinesis. The cell shape drastically changes and membrane fission occurs during cytokinesis.

Arf (ADP-ribosylation factor) is a family of small GTPases that regulate membrane traffic by varying their GTP/GDP binding states. Arf6 can be localized to the plasma membrane and the endocytic system. It has been suggested that Arf6 is essential for the final stage of cytokinesis in mammalian cells. During cytokinesis, Arf6 transiently localizes to the Flemming body. Our previous study suggested that Arf6 is recruited to the Flemming body independently of Rab11- and FIP3-containing endosomes [1]. In this study, we determined the crystal structure of a complex between Arf6 and the C-terminal domain of MKLP1, which together with

MgcRacGAP/Cyk4 constitutes the central spindle complex at the Flemming body. Furthermore, our structure-based mutagenesis and siRNA-mediated knockdowns allowed us to critically test models of Arf6 recruitment to the Flemming body. Our findings demonstrate that the formation of Arf6-MKLP1 complex is crucial for the completion of cytokinesis [2].

The 3.0 Å crystal structure of the complex consisting of Arf6 full length (Q67L, GTP-bound form mutant) and the C-terminal domain (residues 690–807) of MKLP1 (cMKLP1) reveals a 2:2 Arf6-MKLP1 heterotetramer complex (Fig. 1). A unique extended β -sheet formed of 22 strands spans the entire Arf6-MKLP1 complex. The structure of Arf6 in the complex is similar to that of monomeric Arf6-GTP γ S (PDB: 2J5X). On the other hand, the Dali server search revealed no solved structures similar to the present cMKLP1. Monomeric cMKLP1 is composed of five strands and a long loop including the short sheet region involved in the complex formation. Additionally, we confirmed the formation of this Arf6-MKLP1 complex in solution by a combination of SAXS measurements and cross-linking experiments.

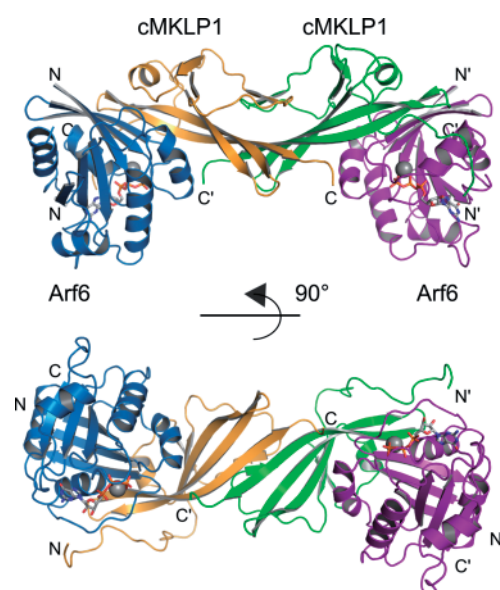


Figure 1
Overall structure of Arf6-MKLP1 complex. Cartoon representations of the Arf6-cMKLP1 complex are shown in two orthogonal views (side and bottom views, for upper and lower panels, respectively). The two Arf6 molecules are colored in skyblue and purple, and the two cMKLP1 molecules are colored in orange and green, respectively.

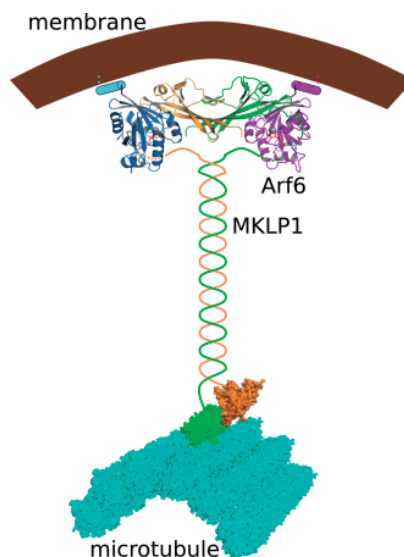


Figure 2

Model for membrane and microtubule interactions of the Arf6-MKLP1 complex. Arf6 molecules are colored in skyblue and purple with schematically represented N-terminal helices, and their myristate extensions are represented as dotted lines. MKLP1 molecules are colored in green and orange, respectively.

We have found that Arf6 is required for the binding of cMKLP1 in a GTP-dependent manner. The interface between Arf6 and cMKLP1 in the complex structure explains the GTP-dependent interaction between Arf6 and cMKLP1. Interestingly, the conformation of Arf6 changes significantly depending on its GTP/GDP-bound state. The conformational change of the switch 1 and switch 2 regions changes with a two-residue register shift in the interswitch region [3]. The $\beta 2$ strand interacts with the $\beta 5$ strand of cMKLP1 in the complex structure (GTP-bound form). In the GDP-bound form of Arf6, the switch 1 region is retracted. As a consequence, a new β -strand of Arf6, which is overlapping with the $\beta 5$ strand of cMKLP1, is formed next to the $\beta 2$ strand of Arf6 in a GDP-bound state. Taken together, these data strongly suggest that this is the reason why Arf6 can interact with MKLP1 only in its GTP-bound state.

The additional hydrogen bond formed between Tyr77^{Arf6} and Tyr754^{cMKLP1} in a hydrophobic pocket common among most small GTPases was important for the interaction between Arf6 and cMKLP1. Indeed, Arf6 (Q67L/Y77A) mutant abolished the interaction between Arf6 and cMKLP1, as shown by pull-down assay using the GST-tagged cMKLP1. Moreover, our mutant analysis confirmed that the interaction between Tyr77^{Arf6} and Tyr754^{cMKLP1} is critical for the proper completion of cyto-

kinesis. Arf6 (Q67L/Y77A)-cMKLP1 (wild type) or Arf6 (wild type)-cMKLP1 (Y754A) mutant could not be co-localized on the Flemming body. Furthermore, cMKLP1 (Y754A) mutant marginally rescued the multinucleate phenotype, different from MKLP1 (wild type), in HeLa cells with depletion of MKLP1 by siRNA treatment.

We therefore propose that two activated Arf6 molecules bind to each homodimer of MKLP1 to form the presently solved complex structure on the Flemming body for a higher fidelity of completion of cytokinesis (Fig. 2).

REFERENCES

- [1] S. Takahashi, T. Takei, H. Koga, H. Takatsu, H-W. Shin and K. Nakayama, *Genes Cells*, **16** (2011) 938.
- [2] H. Makyio, M. Ohgi, T. Takei, S. Takahashi, H. Takatsu, Y. Katoh, A. Hanai, T. Ueda, Y. Kanaho, Y. Xie, H.W. Shin, H. Kamikubo, M. Kataoka, M. Kawasaki, R. Kato, S. Wakatsuki and K. Nakayama, *EMBO J.*, **31** (2012) 2590.
- [3] S. Pasqualato, J. Ménétreay, M. Franco and J. Cherfilis, *EMBO Rep.*, **2** (2001) 234.

BEAMLINES

5A, 10C and AR-NW12A

H. Makio, M Kawasaki, R. Kato and S. Wakatsuki (KEK-PF)

Crystal Structure of the Rotor from V-ATPase Molecular Motor

Vacuolar ATPase (V-ATPase) is an ion-translocating rotary motor found in the membranes of acidic organelles and plasma membranes of eukaryotic cells. ATP hydrolysis causes the rotation of the central rotor complex, which is composed of the central stalk subunits (D-, F-, and d-subunits) and a membrane-embedded c-ring. We have determined the crystal structure of DF complex from *Enterococcus hirae* and assessed subunit-subunit interactions between V_1 -ATPase subunits. The long coiled-coil motif of the D-subunit was similar to the motifs of other known rotary complexes. The short β -hairpin region of the D-subunit seems to be preserved in V-ATPase and further involved in the regulation of V-ATPases.

The ion-translocating rotary ATPases (V-, F-, and A-ATPases) are considered to have evolved from a common ancestor. V-ATPases function as ion pumps. F-ATPases in mitochondria and A-ATPases in archaea function as ATP synthases. Nevertheless, the structure and subunit composition of A-ATPases appear closer to those of V-ATPases than F-ATPases. These ATPases share similar structures in common, which consist of a hydrophilic catalytic part (V_1 -, F_1 -, or A_1 -ATPase) and a membrane-embedded ion-transporting part (V_o -, F_o -, or A_o -ATPase) (Fig. 1). The core of the V_1 domain is composed of a hexameric arrangement of alternating A- and B-subunits (A_3B_3), responsible for the ATPase activity. The V_1 and V_o parts are connected through a central stalk, which is composed of D-, F-, and d-subunits. ATP hydrolysis induces the rotation of the central stalk and the attached membrane c-ring, which causes ion

pumping at the interface between the a-subunit and the c-ring.

V-ATPase exists in the various membrane systems of living cells from bacteria to mammals. Eukaryotic V-ATPase is located in the membranes of acidic organelles or plasma membranes, and transports H^+ to acidify organelles or intercellular matrices. These acidifications are involved in several diseases such as osteoporosis and cancer metastasis. Therefore, unraveling the molecular mechanism of V-ATPase might help to elucidate such diseases and eventually lead to drug discovery. V-ATPase from *Enterococcus hirae* acts as a primary Na^+ or Li^+ pump, instead of H^+ pump. This enzyme is composed of nine subunits (A, B, d, D, E, F, G, a, c) that are homologous to the corresponding subunits of eukaryotic V-ATPases.

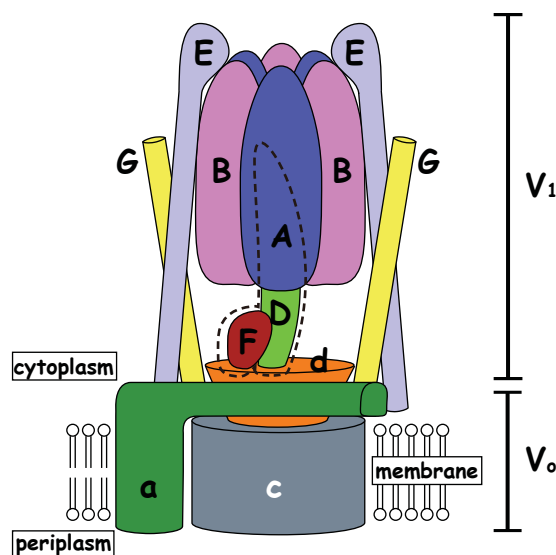


Figure 1

Schematic model of *Enterococcus hirae* V-ATPase. The DF complex is shown by the dotted line. Na^+ is transported by the pathway which consists of the a-subunit and the c-ring, from cytoplasm to periplasm.

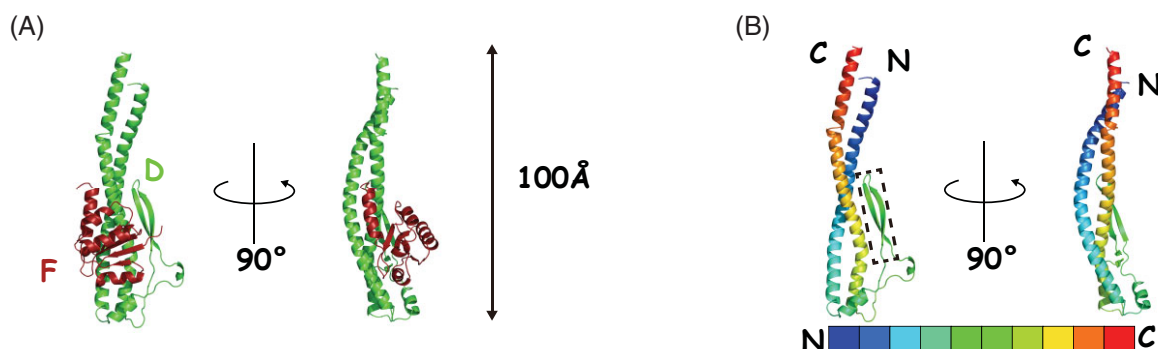


Figure 2

Crystal structure of the DF complex of *Enterococcus hirae* V₁-ATPase.

(A) Cartoon representation of the DF complex. D- and F-subunits are shown in green and dark red, respectively. (B) D-subunit is presented in blue to red from the N to C terminus. The β -hairpin region is shown by the dotted box.

We have determined the crystal structure of the DF complex from *Enterococcus hirae* at 2.0 Å resolution [1]. The structure of D comprises a long pair of N- and C-terminal helices (approximately 100 Å), which are twisted into a left-handed coiled-coil, with a short β -hairpin region (residues 89–108) [Fig. 2 (A, B)]. The coiled-coil structure seems to be conserved in A-ATPase and eukaryotic V-ATPase from sequence alignment, and is similar to both the γ -subunit of bovine F₁-ATPase and FliJ (a component of the flagellar type III protein export apparatus) with low sequence similarity. Thus, the left-handed coiled-coil structure seems to be conserved in these rotary complexes, but the short β -hairpin region of D is unique and seems to be important for specific functions of V-ATPases. To evaluate this assumption, we prepared a deletion mutant that lacked the β -hairpin region with F, and further tested the binding affinity of the mutant DF to A₃B₃, and its effect on the ATPase activity. As a result, it was found that the β -hairpin region is not essential for ATPase activity, but it stimulates the activity by approximately two-fold. Additionally, we assessed the subunit–subunit interactions between V₁-ATPase and the d-subunit by using the Biacore system (surface plasmon resonance). The binding affinity (K_d = 82 nM) of

d and DF was lower compared with other subunit–subunit interactions (A₃B₃-D, K_d = 0.8 nM; A₃B₃D-F, K_d = 3.2 nM). Previous studies on eukaryotic V-ATPases showed that the enzyme was regulated by the reversible binding of V₁-ATPase. The weak interaction between the DF complex and the d-subunit might be responsible for the regulation of V-ATPases.

In the present study, the β -hairpin region involved in the regulation of V-ATPase was identified. This region seems to be conserved also in eukaryotic V-ATPase. Therefore, our results might help to elucidate the regulation mechanism of V-ATPase.

REFERENCE

- [1] S. Saijo, S. Arai, KMM. Hossain, I. Yamato, K. Suzuki, Y. Kakinuma, Y. Ishizuka-Katsura, N. Ohsawa, T. Terada, M. Shirouzu, S. Yokoyama, S. Iwata and T. Murata, *Proc. Natl. Acad. Sci. USA*, **108** (2011) 19955.

BEAMLINE

AR-NE3A

S. Saijo^{1,2}, I. Yamato¹ and T. Murata^{2,3} (¹Tokyo Univ. of Science, ²RIKEN, ³Chiba Univ.)

Refraction-Contrast Tomosynthesis for a Breast Specimen

Refraction-contrast images based on the difference in X-ray refraction have been proved to be good at depicting objects that consist of matter with weak X-ray absorption (phase objects). However, the projection images show complicated image contrast due to overlapping of many details, which often makes image interpretation difficult. To solve this problem without greatly increasing the exposure dose for clinical use of the future prospects, we developed a novel tomographic system combining a Laue silicon crystal analyzer imaging system based on refraction-contrast and tomosynthesis utilizing reconstruction algorithms of shift-and-add and filtered back projection. This approach provided slice images of a phase object such as a breast specimen of juvenile papillomatosis, which is depicted obscurely by the difference of X-ray absorption.

Some breast cancers are missed in conventional mammography because of superimposition by normal mammary glands, often preventing the detection of tumors or minute calcifications. One possible solution might be to introduce the tomographic technique for breast imaging. With the advent of flat-panel detectors capable of high-speed data communication, conventional geometric tomography is once again attracting attention in the form of digital tomosynthesis [1]. The technique allows an arbitrary number of in-focus planes to be generated retrospectively from a set of low-dose projection radiographs that are acquired during a single scan with a limited tomographic angle. This approach solves the issue of overlapping breast tissues. However, the image contrast in this technique is still based on the difference in X-ray absorption (absorption contrast) in the same way as projection mammography, so the contrast between anatomies with similar X-ray attenuation coefficients remains obscure. In this study, aiming to acquire slice images of an object with weak X-ray absorption (phase object), we conducted a trial of refraction-contrast tomosynthesis for a breast specimen by combining the imaging system by a Laue silicon crystal analyzer (A[L]) based on refraction-contrast [2, 3] and tomosynthesis utilizing reconstruction algorithms of shift-and-add (SAA) and filtered back projection (FBP). We constructed the refraction-contrast imaging system by A[L] at BL-14B using synchrotron X-rays from the vertical wiggler of the Photon Factory. The X-ray energy was tuned to 20.0 keV. The X-ray beam was reflected and expanded horizontally by a monochromator-collimator (MC) made of a single silicon crystal. An A[L], whose role was to discriminate refracted X-rays while penetrating the object from all of the X-rays transmitting the object, was set downstream of the X-ray beam from the MC. The object (a breast specimen excised during a mastectomy from a 17-year-old female with juvenile papillomatosis) was placed between the MC and the

A[L] when the imaging was performed. An X-ray CCD camera was used as a detector. The imaging apparatus is shown in Fig. 1. Two angular positions of the A[L] (bottom of the rocking curve [B] and slope of its lower angular side [S]) were used to acquire projections for tomosynthesis. It should be noted that the rocking curve corresponds to the intensity profile for the forward diffracted X-rays without any object. The tomographic angle was $\pm 25^\circ$, and with the reconstruction algorithms of tomosynthesis, we applied SAA and FBP dedicated to a parallel X-ray beam. A *Shepp & Logan* filter was used in the FBP algorithm. In addition, absorption-contrast projection imaging of the object was also performed at the same X-ray energy for comparison.

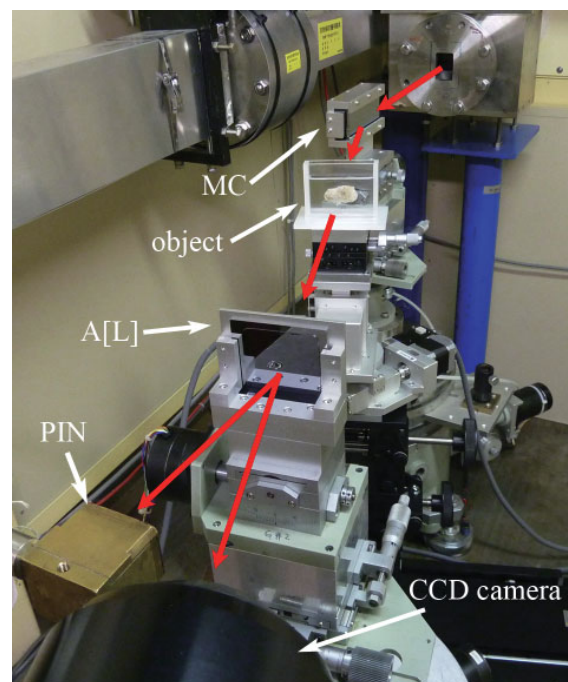


Figure 1
The apparatus for refraction-contrast tomosynthesis constructed at BL-14B. Red arrows indicate the X-ray beam path.

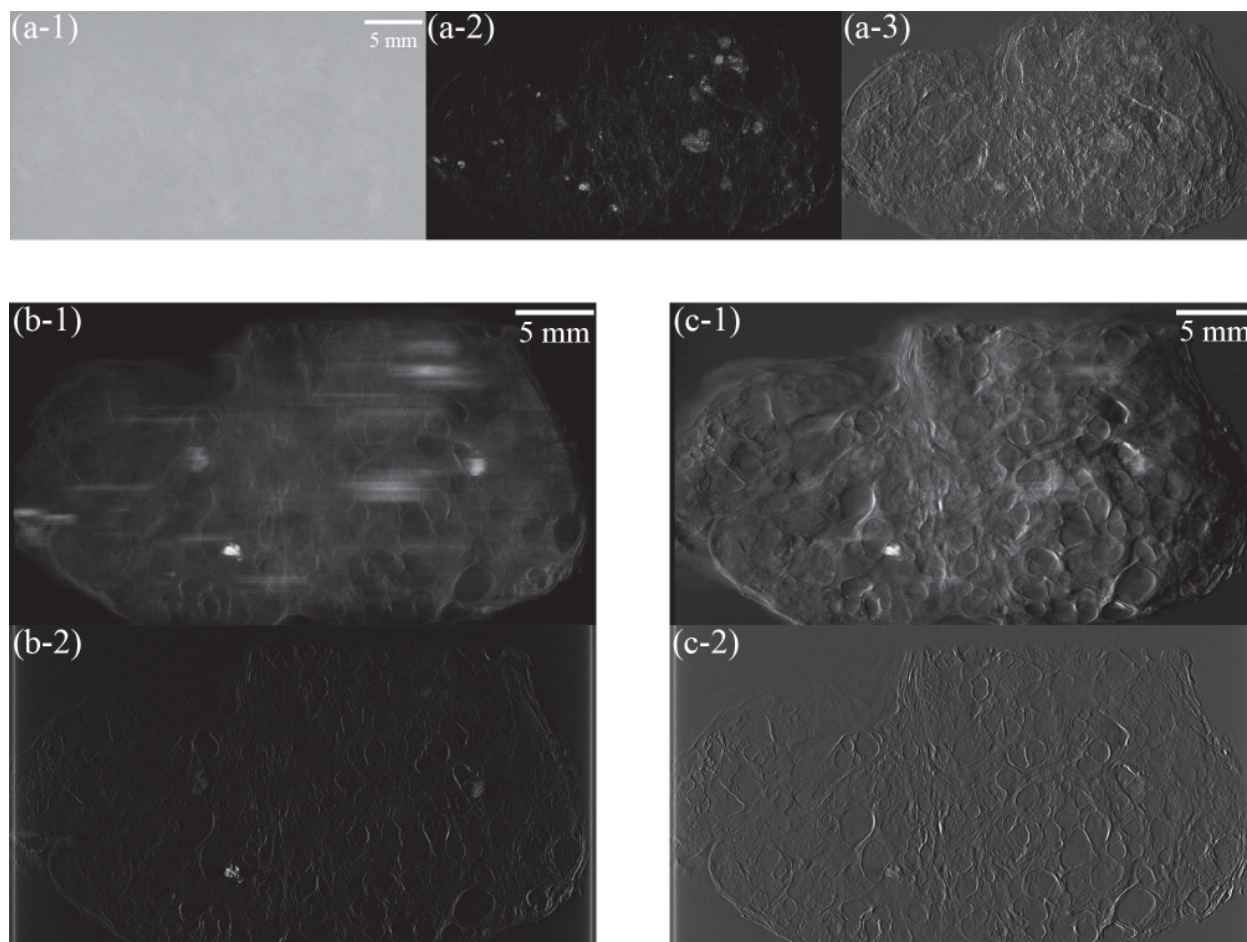


Figure 2

Projection images: absorption contrast (a-1), refraction-contrast images taken at the bottom [B] (a-2) and at the slope of the lower angular side [S] (a-3) of the rocking curve. Tomosynthesis images at the same depth: [B] by SAA (b-1), [B] by FBP (b-2), [S] by SAA (c-1), and [S] by FBP (c-2).

The results are summarized in Fig. 2. There is almost no contrast on the absorption contrast image except for the quite obscure contrast of many small cysts in (a-1), while many secretions containing calcium and cysts are depicted in (a-2) and (a-3), respectively. It is, however, difficult to distinguish individual features due to superimposition. Representative slice images by tomosynthesis using SAA and FBP algorithms for conditions [B] and [S] are shown in Fig. 2 (b-1), (b-2), (c-1), and (c-2), respectively. All the slices were reconstructed at the same slice position. It is well depicted images of secretions containing calcium existing in this plane with reduced streak-like artifacts by FBP (b-2) and cysts in the plane composed of contrast not by contours but by substances by SAA (c-1). This study confirmed that slice images of a phase object could be acquired by our proposed approach. Moreover, it was indicated that refraction-contrast images taken at [B] which contain sharp contrast should be processed by FBP, and other

refraction-contrast images with moderate contrast taken at [S] should be processed by SAA. These results suggest that refraction-contrast tomosynthesis is worthy of further investigation for improving the detection of lesions in breast specimens.

REFERENCES

- [1] J.T. Dobbins III and D.J. Godfrey, *Phys. Med. Biol.*, **48** (2003) R65.
- [2] V.N. Ingal and E.A. Beliaevskaya, *J. Phys. D*, **28** (1995) 2314.
- [3] D. Shimao, H. Sugiyama, T. Kunisada and M. Ando, *Appl. Radiat. Isot.*, **64** (2006) 868.

BEAMLINE

14B

D. Shimao¹, N. Sunaguchi², S. Ichihara³ and M. Ando⁴ (¹Ibaraki Pref. Univ. of Health Sciences, ²KEK-PF, ³Nagoya Medical Center, ⁴Tokyo Univ. of Science)

Homogeneity Characterization of Lattice Spacing of Silicon Single Crystals by a Self-Referenced Lattice Comparator at BL-3C

The lattice spacing of a perfect silicon crystal is critical when determining the Avogadro constant by the X-ray crystal density (XRCD) method [1]. In the XRCD method, the Avogadro constant, N_A , is derived from the mean molar mass, M , the density, ρ , and the lattice spacing of the (220) plane, d_{220} , of a perfect silicon crystal using the following equation:

$$N_A = \frac{M}{\rho \times \sqrt{8} \times d_{220}^3}$$

The International Avogadro Coordination (IAC) project started in 2004 has performed various measurements using a silicon crystal highly enriched with ^{28}Si isotope with the aim of achieving an uncertainty of 2×10^{-8} for N_A .

A very important precondition for achieving this goal is to have a perfect silicon crystal or at least an imper-

fect silicon crystal with a known lattice spacing distribution. This is because M , ρ , and d_{220} are measured from samples obtained from different locations in the ingot. Impurity and defect measurements of the crystal are performed for crystal characterization.

The lattice spacing of silicon is determined by combining the lattice spacing measured using a technique that involves X-ray and optical interferometry under standard conditions (i.e., 20°C and 0 Pa). The lattice spacing is required to have an expanded uncertainty of 3×10^{-9} . Impurities measured on samples throughout an ingot are used to derive the compensations at the positions of the X-ray interferometer (XINT) and spheres.

We discovered a strain pattern whose magnitude was of the order of 10^{-8} , which is too small to be observed by X-ray topography, in an ingot of a high-purity silicon crystal with natural isotopic abundances [2].

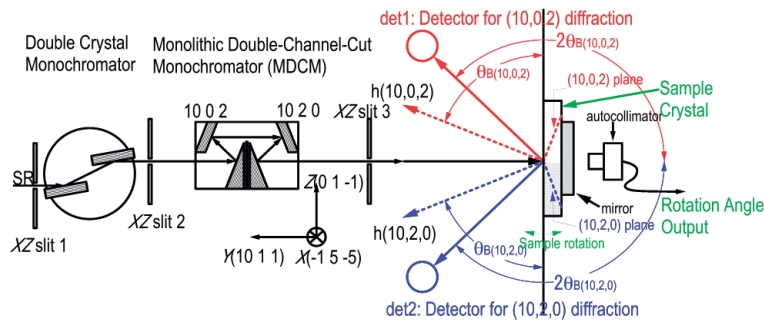


Figure 1
Schematic side view of the self-referenced lattice comparator.

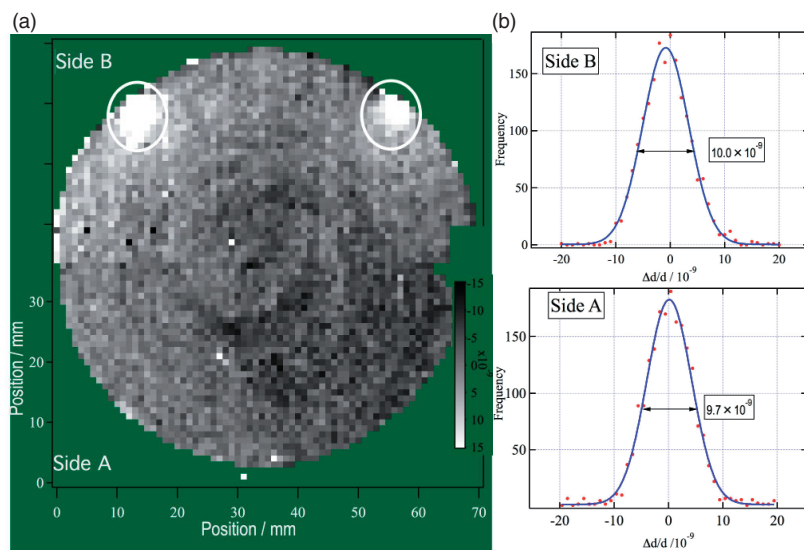


Figure 2
Lattice spacing of ^{28}Si isotopically enriched silicon on both sides of the disk. (b) Histograms of the mapping measurement results.

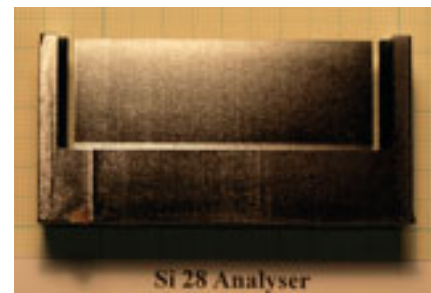


Figure 3
Photograph of the analyzer crystal of XINT (upper side is side B).

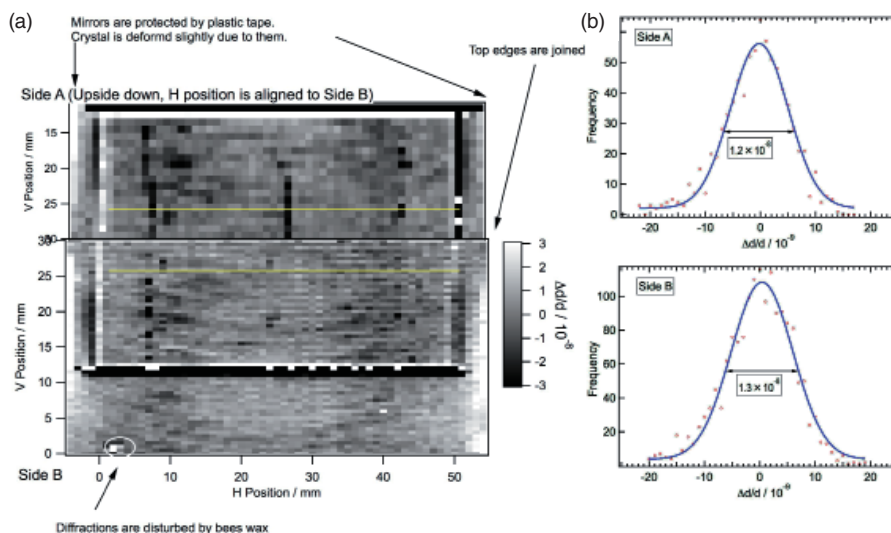


Figure 4

(a) Lattice spacing of the analyzer crystal of XINT from ^{28}Si isotopically enriched silicon. Yellow lines indicate data in Figure 5. (b) Histogram of the mapped data. Only data from the thin plate are used in calculations.

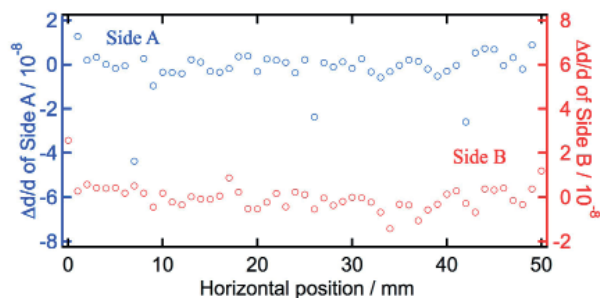


Figure 5

1D maps of the lattice spacing along the baseline. Data were obtained from the mapping data for the yellow lines in Figure 4(a). Horizontal position increases from left to right when the sample is viewed from side B.

This strain distribution has a high spatial frequency in the ingot and thus cannot be compensated by solely determining impurity concentrations at a few sampled positions. Crystals used in X-ray interferometry are also susceptible to the very small strains caused by defects introduced during crystal processing. Damage caused during fabrication and self-weight (gravity-induced) deformation of the crystal must be checked by a sensitive method. Strain measurements were performed [3] using the Self-Referenced Lattice Comparator (SRLC) installed at BL-3C, on single crystals of silicon with natural isotopic abundances, and silicon crystals highly enriched with the ^{28}Si isotope, which are all used to determine the Avogadro constant. A schematic side view of the apparatus is shown in Fig. 1.

The measurement capability, i.e. the standard deviation of repeated measurements, of the system is about 3×10^{-9} [4]. Samples from crystals with natural isotopic abundances exhibited clear pattern of striations, whereas almost no pattern was observed for crystals enriched with ^{28}Si isotope (see Figs. 2, 3, 4 and 5).

The standard deviation of the lattice spacing of the silicon single crystal highly enriched with ^{28}Si isotope was 4.7×10^{-9} , which enabled the lattice spacing to be determined with an expanded uncertainty of 3×10^{-9} .

The Avogadro constant N_A is determined from the measurements, the lattice parameter, the mass and volume of the sphere, and the molar mass to be $N_A = 6.022\,140\,78(18) \times 10^{23} \text{ mol}^{-1}$ with 3.0×10^{-8} relative uncertainty. This value differs by $16 \times 10^{-8} N_A$ from the CODATA 2006 adjusted value. This value is midway between the N_A values derived from Planck's constant obtained by NIST and NPL watt-balance using the molar Planck constant $N_A h = 3.990\,312\,682\,1(57) \times 10^{-10} \text{ J s/mol}$ [5].

REFERENCES

- [1] B. Andreas, Y. Azuma, G. Bartl, P. Becker, H. Bettin, M. Borys, I. Busch, P. Fuchs, K. Fujii, H. Fujimoto, E. Kessler, M. Krumrey, U. Kuetgens, N. Kuramoto, G. Mana, E. Massa, S. Mizushima, A. Nicolaus, A. Picard, A. Pramann, O. Rienitz, D. Schiel, S. Valkiers, A. Waseda and S. Zakel, *Metrologia*, **48** (2011) S1.
- [2] H. Fujimoto, A. Waseda, Z. Xiaowei, K. Nakayama, K. Fujii, H. Sugiyama and M. Ando, Precision Electromagnetic Measurements, 2002. Conference Digest 2002 Conference on 304 (2002); Digital Object Identifier:10.1109/CPEM.2002.1034842.
- [3] H. Fujimoto, A. Waseda and X.W. Zhang, *Metrologia*, **48** (2011) S55.
- [4] X. Zhang, H. Sugiyama, M. Ando, Y. Imai and Y. Yoda, *J. Appl. Cryst.*, **36** (2003) 188.
- [5] B. Andreas, Y. Azuma, G. Bartl, P. Becker, H. Bettin, M. Borys, I. Busch, M. Gray, P. Fuchs, K. Fujii, H. Fujimoto, E. Kessler, M. Krumrey, U. Kuetgens, N. Kuramoto, G. Mana, P. Manson, E. Massa, S. Mizushima, A. Nicolaus, A. Picard, A. Pramann, O. Rienitz, D. Schiel, S. Valkiers and A. Waseda, *Phys. Rev. Lett.*, **106** (2011) 030801.

BEAMLINER

3C

H. Fujimoto¹, A. Waseda¹ and X.W. Zhang² (¹AIST, ²KEK-PF)

Production of an Energy-Tunable Positronium Beam

An energy-tunable positronium beam has been successfully produced in the KEK Slow Positron Facility by using photodetachment of the positronium negative ion, a bound state of one positron and two electrons. The ions were generated efficiently by bombarding a Na-coated tungsten surface with a pulsed slow positron beam in the short pulse operation mode of the dedicated 55-MeV linac. The ions were then accelerated using a static electric field, and pulsed laser light with a high photon density sufficient for the photodetachment was irradiated. A positronium beam with a hitherto unrealized energy range of up to 1.9 keV was produced in an ultrahigh vacuum environment.

Positronium (Ps), a bound state of one positron and one electron, is a pure leptonic atom. Due to the neutrality and small mass of Ps, an energy-tunable beam of Ps is expected to be a powerful tool for investigations of atoms, molecules, and solid surface structures.

Ps atoms can be formed when slow positrons collide with solid surfaces or gas molecules. The maximum emission energy of Ps atoms from solid surfaces is a few eV and these neutral Ps atoms cannot be accelerated to the desired energy after formation. Thus, the only energy-tunable beam developed so far has been based on the charge exchange reaction of energetic positrons with gas molecules, where the beam energy is controlled by changing the incident positrons. The Ps energy range of such a beam is limited to below 400 eV and it is difficult to obtain ultrahigh vacuum conditions.

It has been expected that an energy-tunable Ps beam could be produced by employing the photodetachment of accelerated positronium negative ions (Ps⁻).

We reported the first successful photodetachment of Ps⁻ in FY2010 [1, 2]. In the present work, we succeeded in producing an energy-tunable Ps beam using the Ps⁻ photodetachment technique [3].

The Ps⁻ ions were generated efficiently on a Na-coated tungsten target in back-reflection geometry using a pulsed slow positron beam at the KEK-IMSS Slow Positron Facility [4]. The 55-MeV electron linac was operated in a short pulse mode. The positrons were guided by an axial magnetic field with a transport energy of 4.2 keV (Fig. 1). The beam was deflected by 45° along a curved magnetic field and was incident onto the target through an electric-field-free region between two grids, A and B, biased at 2.8 kV.

The target was a polycrystalline tungsten foil of 25 μm thickness. It was annealed in situ at 1800 K for 30 min. After cooling down to room temperature, one monolayer of Na was deposited in order to obtain high Ps⁻ emission efficiency [5].

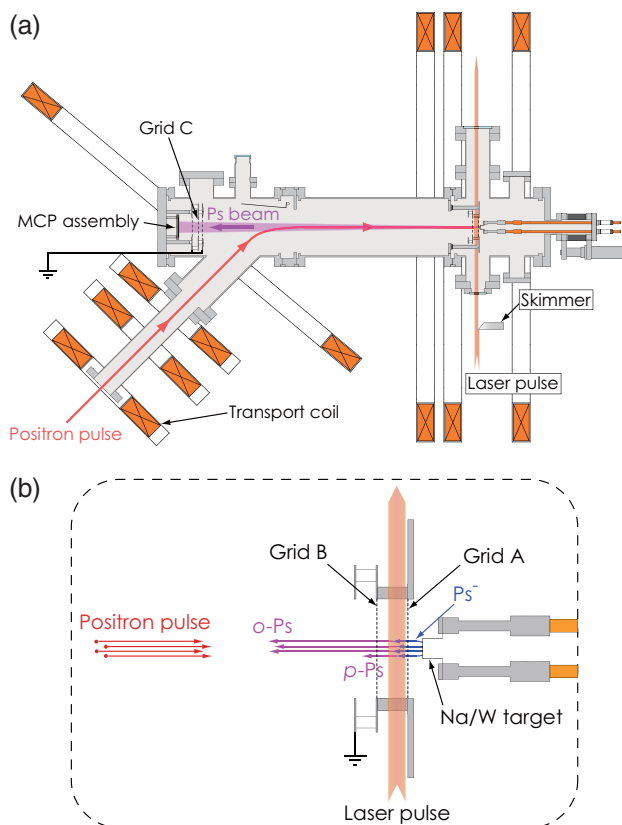


Figure 1
Schematic diagram of the Ps beam system. Reprinted with permission from *Applied Physics Letters* **100** (2012) 254102. Copyright American Institute of Physics (2012).

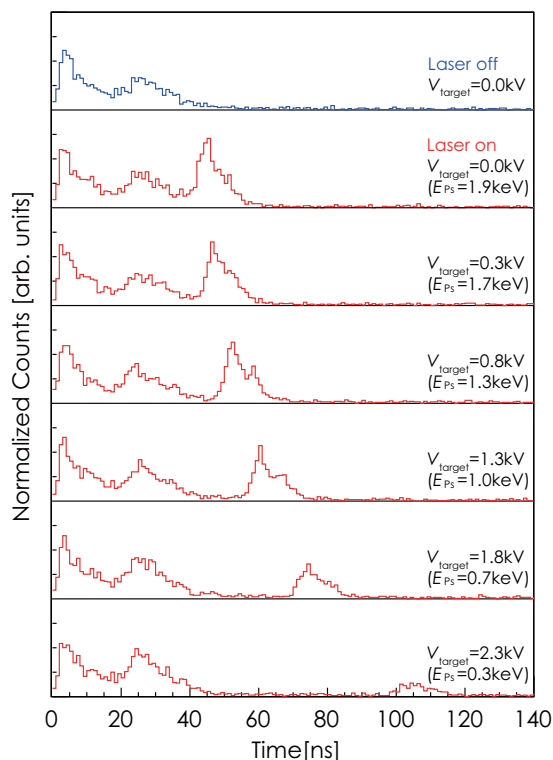


Figure 2
TOF spectra of the o-Ps atoms formed by the photodetachment of Ps⁻ ions. E_{Ps} is the Ps energy calculated from V_{target} . Reprinted with permission from *Applied Physics Letters* **100** (2012) 254102. Copyright American Institute of Physics (2012).

The target bias, V_{target} , was varied from 0 to 2.3 kV. The Ps⁻ ions emitted from the target were accelerated by the potential difference between grid A and the target. They were photodetached in the field-free region by an infrared laser light from a Q-switched Nd:YAG laser. The photon energy was 1.165 eV, which is higher than the photodetachment threshold. The orthopositronium (o-Ps) atoms formed by the photodetachment were detected using a micro-channel plate (MCP) assembly placed 80 cm downstream from the target. The time-of-flight (TOF) spectra of the o-Ps atoms were accumulated using a digital oscilloscope.

Figure 2 shows the obtained TOF spectra. Two peaks appear without laser irradiation. They do not change while the laser is on and are independent of V_{target} . While laser is on, the third peak appears; it is attributed to neutral o-Ps atoms detected by the MCP assembly. The TOF, t , of o-Ps can be expressed as

$$t = L \sqrt{\frac{3m_e}{2e(V_{grid} - V_{target})}}, \quad (1)$$

where L is the o-Ps flight distance, V_{grid} is the potential of the field-free region (2.8 kV), and m_e is the rest mass of the electron and the positron. The TOF of the third peak in Fig. 2 is consistent with Eq. (1).

The present Ps beam provides a hitherto unachieved energy range extending up to 1.9 keV. The advantages of the present method include the simultaneous attainment of high energy and ultrahigh vacuum compatibility, thus enabling the analysis of clean surfaces of solids. This successful production of an energy-tunable Ps beam paves the way to a new era of investigations of solid surfaces, such as reflection high-energy Ps diffraction and Ps scattering experiments.

REFERENCES

- [1] Y. Nagashima, *Photon Factory Activity Report 2010*, #28 (2011) A 68.
- [2] K. Michishio, T. Tachibana, H. Terabe, A. Igarashi, K. Wada, T. Kuga, A. Yagishita, T. Hyodo and Y. Nagashima, *Phys. Rev. Lett.*, **106** (2011) 153401.
- [3] K. Michishio, T. Tachibana, R.H. Suzuki, K. Wada, A. Yagishita, T. Hyodo and Y. Nagashima, *Appl. Phys. Lett.*, **100** (2012) 254102.
- [4] K. Wada, T. Hyodo, A. Yagishita, M. Ikeda, S. Ohsawa, T. Shidara, K. Michishio, T. Tachibana, Y. Nagashima, Y. Fukaya, M. Maekawa and A. Kawasuso, *Eur. Phys. J. D*, **66** (2012) 37.
- [5] H. Terabe, K. Michishio, T. Tachibana and Y. Nagashima, *New J. Phys.*, **14** (2012) 015003.

BEAMLINE

SPF

Y. Nagashima (Tokyo Univ. of Science)

Evaluation of Emittance Characteristics of Negative Electron Affinity GaAs-Based Photocathode

To produce a diffraction limited hard X-ray, an Energy Recovery Linac (ERL)-based light source is planned at the High Energy Research Organization. The parameters of the light source such as brilliance and intensity depend on the quality of the electron beam such as emittance, which is a function of the size and angular spread of the electron beam, and current. Therefore, an electron gun which produces low emittance and a high-current beam is needed. To achieve such a beam, we have developed a high-voltage DC gun with GaAs-based photocathode which has a negative electron affinity (NEA) surface condition. With this type of electron source, the emittance depends on the laser wavelength, structure of the photocathode, temperature, and other factors. Therefore, we evaluated the emittance characteristics of GaAs-based photocathodes, namely commercially available bulk GaAs, thickness controlled GaAs (about 120 nm or 1200 nm), and GaAs/GaAsP superlattice.

The electron gun is one of the most important components for an ERL. The target values of the Compact ERL are a normalized emittance of 0.1–1 mm mrad and an average current of 10–100 mA [1]. A DC gun with an NEA photocathode is one candidate for achieving the requirements of the ERL. In the ERL, it is essential to improve the quality of the electron beam generated by the photocathode gun, because the quality of synchrotron radiation strongly depends on it. The requirements for the photocathode are the generation of a low-emittance beam, high quantum efficiency (QE), and fast temporal response of the photoemission, which is important to control the time structure of the electron beam to avoid the emittance growth and a beam halo. The properties of the photocathode can be described by Mean Transverse Energy (MTE), which is related to the initial emittance, and temporal response. To measure these values, we constructed a gun test facility at the PF-AR south experimental hall (Fig. 1).

The time response depends on the thickness of the photocathode; a faster response was obtained with

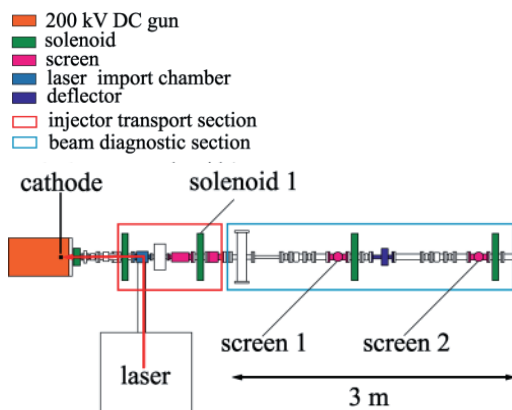


Figure 1
Outline of gun test facility at the PF-AR south experimental hall. Waist scans were executed by solenoid 1 at the positions of screen 1 and screen 2.

a thinner photocathode [2]. However, the influence of thickness on emittance was not investigated, so we evaluated the effect of cathode thickness for thickness-controlled photocathodes (Fig. 2). We also evaluated photocathodes of superlattice, which is a candidate for a high-current, low-emittance beam [3]. These photocathodes were fabricated by metal organic vapor phase epitaxy at Nagoya University.

On the surface of the photocathode, the normalized rms emittance (ϵ_{nrms}) is given by

$$\epsilon_{\text{nrms}} = \frac{1}{m_e c} \sqrt{\langle x^2 \rangle \langle p_x^2 \rangle} = \sigma_x \sqrt{\frac{2 \langle E_{kx} \rangle}{m_e c^2}},$$

where x is the transverse electron position, p_x is the momentum, m_e is the rest mass of an electron, and c is the speed of light. The brackets represent the ensemble average of all particles. σ_x is the rms size of irradiated laser, because the spatial distribution of electrons is the same as that of the laser on the surface of the photocathode. Here, $\langle E_{kx} \rangle$ represents the average of the electron transverse energy, therefore, $\langle E_{kx} \rangle$ is called Mean Transverse Energy (MTE).

Of course, the spot size of the laser beam is controllable, but the emittance degradation due to the space charge effect increases with smaller spot size of the laser for the same emission current. Therefore, a smaller value of MTE is desirable. MTE depends on the properties of the cathode material, the cathode structure, the temperature, the excited energy by photons of irradiated laser, and the surface condition. Thus, MTE is an important parameter for describing the cathode's properties.

Electron beam emittance is proportional to the spot size of irradiated laser. We measured the emittance for two laser spot diameters by the waist-scan method at a low emission current so that the space charge effect could be neglected [4]. Figure 3 shows a typical result of the measured emittance. To obtain the MTE, these results were fitted to a line intersecting the origin.

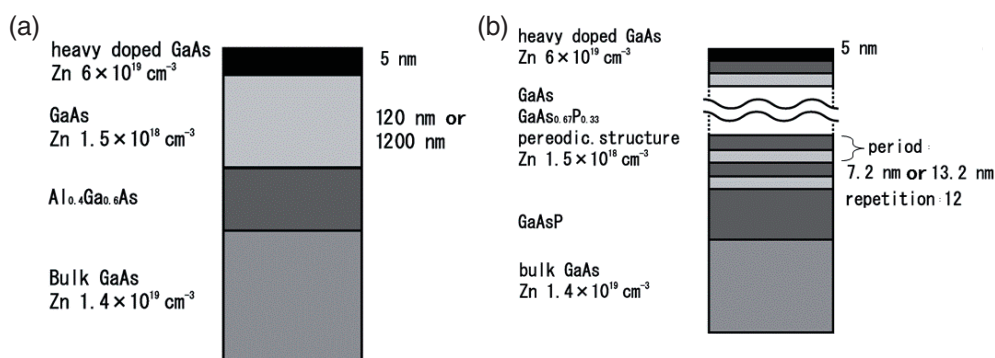


Figure 2
Crystal structure of photocathodes. (a) The samples were controlled to about the thickness of the active layer. (b) The samples have a superlattice structure. Samples SL1 and SL2 had a period of 7.2 nm and 13.2 nm.

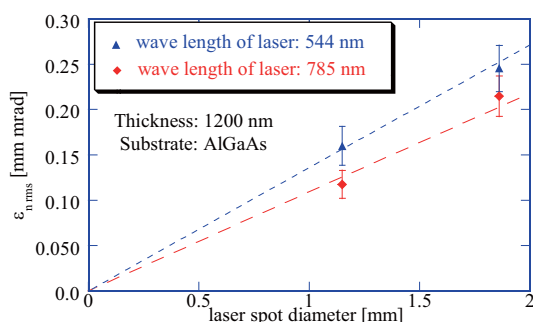


Figure 3
Typical emittance measurement result.

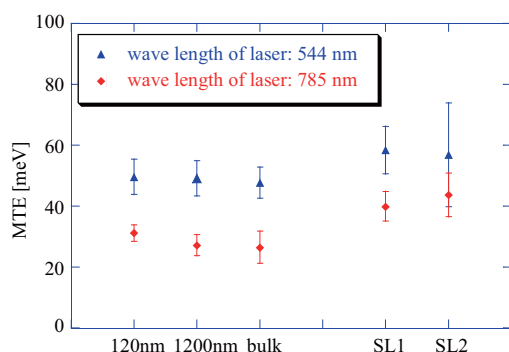


Figure 4
The MTEs of all samples.

Figure 4 shows the measured MTEs at laser wavelengths of 544 and 785 nm. No clear thickness dependence of the MTEs was observed within the error bounds. The green line shows the thermal energy at room temperature. The electrons in the photocathodes are excited, and lose kinetic energy due to some scatterings. Electrons finally reach thermal equilibrium in the photocathode, but the measured MTE does not reach the thermal energy at room temperature (about 12 meV). Furthermore, the emittance of the SL cathodes turned out to be slightly higher than that of the GaAs cathodes, as shown in Fig. 4.

Surface roughness causes changes in the initial direction of emission and distortion of electric field. The surface roughnesses of photocathodes were measured by atomic force microscopy. The roughness of thickness-controlled photocathodes and a superlattice photocathode were 7.3 nm and 33.4 nm rms. These values well explained our results.

These results suggest that the emittance is not affected by changes of thickness within a practical range. On the other hand, the temporal response is sensitive to changes of thickness. The thickness of photocathodes should be selected by considering the temporal response and quantum efficiency. A slightly higher MTE was obtained with the superlattice structure, which may have been due to its rougher surface. Therefore we are continuing to study photocathodes, such as a superlattice structure for a smooth surface, and the characteristics of temporal response of various kinds of photocathodes.

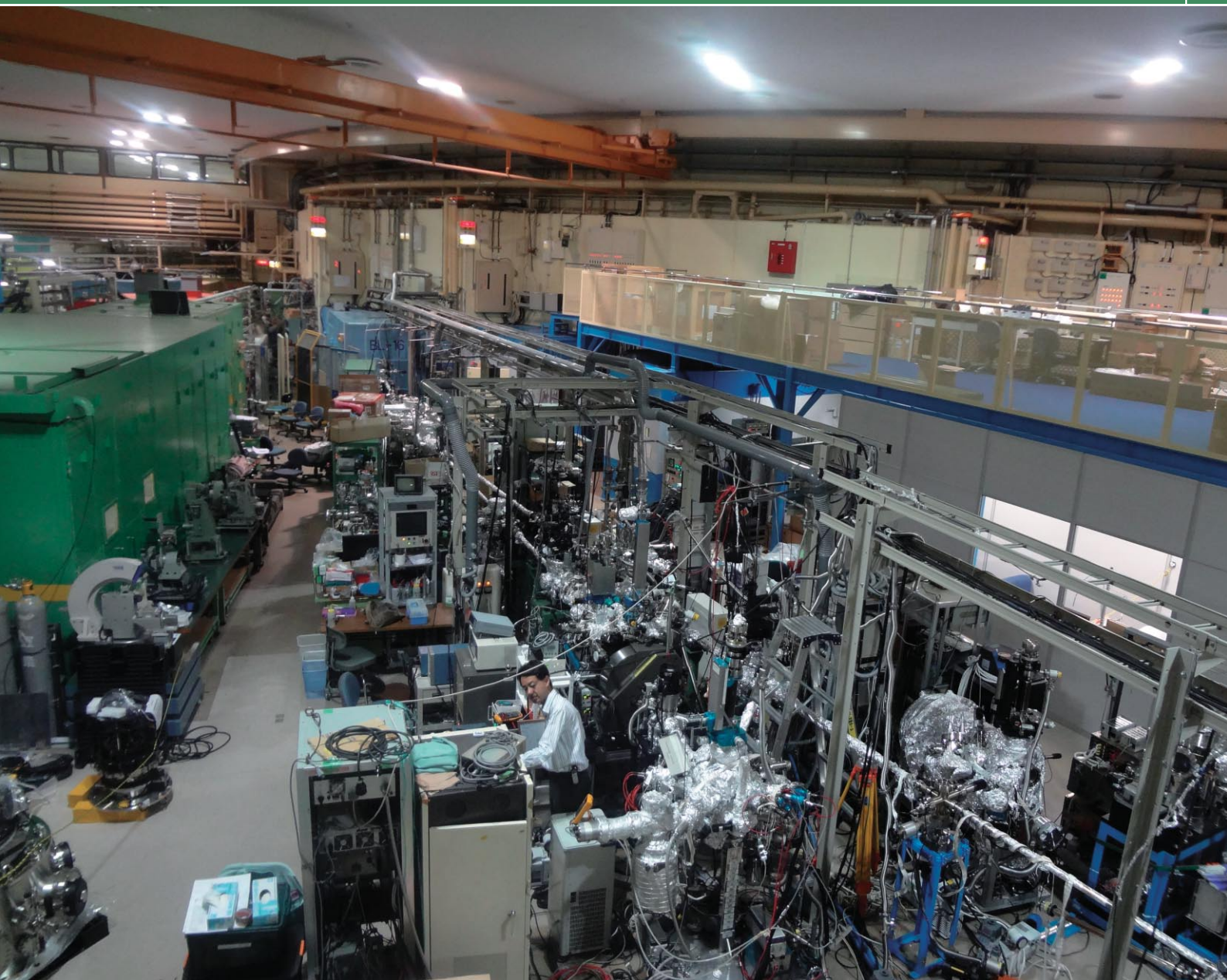
REFERENCES

*Present affiliation is JAEA.

- [1] S. Sakanaka, T. Miyajima, N. Nakamura, K. Harada, E. Kako, T. Furuya, S. Michizono, H. Nakai, K. Haga, *PF activity report 2011, #29* (2012) A 119.
- [2] K. Aulenbacher, J. Schuler, D.v. Harrach, E. Reichert, J. Röthgen, A. Subashev, V. Tioukine and Y. Yashin, *J. Appl. Phys.*, **92** (2002) 7536.
- [3] N. Yamamoto, M. Yamamoto, M. Kuwahara, R. Sakai, T. Morio, K. Tamagaki, A. Mano, A. Utsu, S. Okumi, T. Nakanishi, M. Kuriki, C. Bo, T. Ujihara and Y. Takeda, *J. Appl. Phys.*, **102** (2007) 024904.
- [4] S. Matsuba, Y. Honda, X.G. Jin, T. Miyajima, M. Yamamoto, T. Uchiyama, M. Kuwahara and Y. Takeda, *Jpn. J. Appl. Phys.*, **51** (2012) 046402.

S. Matsuba^{1,*}, Y. Honda², X.G. Jin³, T. Miyajima², M. Yamamoto², T. Uchiyama², M. Kuwahara³ and Y. Takeda³ (¹Hiroshima Univ., ²KEK-ACCL, ³Nagoya Univ.)

Experimental Facilities



EXPERIMENTAL FACILITIES

1. Newly Developed Experimental Facilities	67
1-1 Overview	
1-2 BL-6A: Small Angle X-Ray Scattering Beamline	
1-3 New Diffractometers Developed for Resonant Soft X-Ray Scattering Experiments at BL-16A and 11B	
2. Structural Biology Research Center	70
2-1 Overview	
2-2 Target Proteins Research Program (FY2007-2011)	
2-3 Highlights on In-House Structural Biology Research	
2-4 Beamlines and Technology Developments for Macromolecular Crystallography	
3. Condensed Matter Research Center	76
3-1 Overview	
3-2 Hybridized Orbital Ordering Project – Orbital Hybridization Ordering Study in Strongly Correlated Electron System and the External Field Effect	
3-3 Geometrical Correlation Project	
3-4 Molecular Crystal Project	
3-5 Surface/Interface Project – Crystalline, Magnetic and Electronic Structures at the Surface and Interface of Magnetic Thin Films and Multilayers	
3-6 Extreme Conditions Project	
3-7 Soft Matter Project	
4. The Slow Positron Facility	80
4-1 Production of Energy Tunable Positronium Beam	
4-2 RHEPD Experiments	
4-3 Positronium Time-of-Flight Experiments	
5. IMSS Instrument R&D Team	83
6. Summary of Experimental Stations	84

1

Newly Developed Experimental Facilities

1-1 Overview

Since 2005, we have carried out the beamline refurbishment program based on a well-defined beamline strategy and the areas of excellence that had been discussed with the PF users' community. The mainstay of the beamline strategy is to concentrate investment on the competent beamlines with insertion devices as light sources.

With the reinforcement of the straight sections of the 2.5-GeV PF ring, which was completed in 2005, the long and medium straight sections have been made longer so that more powerful insertion devices can be installed to cover the vacuum ultraviolet and soft X-ray region, and four new short straight sections have been produced for the installation of short period and small gap undulators (SPSGU) to supply well focused hard X-rays.

Beamlines BL-13, BL-16 and BL-28 were constructed originally for sharing the photon beam between VSX and HX users by operating the insertion device in the undulator and multipole wiggler mode. Among the three beamlines, BL-28 was renewed first as a high-performance spectroscopic beamline dedicated to photoelectron spectroscopy in the VSX region, and the second branch has been open for users' experiments since 2006. BL-16 has been completely upgraded as a fast polarization switching soft X-ray spectroscopic beamline including the beamline and the insertion device. Two tandem APPLE-II type undulators are set to different polarizations such as right- and left-hand circular polarizations, and the polarization is switched by modulating the electron orbit through the undulators, as reported in the previous activity report [1]. BL-13 was recently reconstructed as a VSX spectroscopic beamline for studying organic thin films adsorbed on well-defined surfaces using angle-resolved photoelectron spectroscopy, high-resolution X-ray photoelectron spectroscopy and X-ray absorption spectroscopy. The detailed performance was described in the last PF activity report [2].

The VSX beamline refurbishment program has required replacement of the insertion devices at BL-13 and BL-28, which were constructed in the 1980s for supplying photon beams in the VSX and HX regions. These old insertion devices do not always meet the needs of VSX users and are not adequate for utilizing the full performance of the newly constructed beamlines. Furthermore, during the test operation of the PF ring and the beamlines in June 2011, after the Great East Japan Earthquake on March 11, 2011, we found some troubles caused by earthquake damage to these old insertion devices. Therefore, these two old undulators should be replaced by new ones appropriate for the

renewed beamlines.

BL-2 was the first undulator based VSX beamline constructed in the early 1980s, and has been operated for over 25 years. The BL-2 undulator is 3.6-m long, while the length of the straight section is 9 m following the reinforcement in 2005. There are several options for making the best use of this long straight section, such as installing a long undulator or adding a long-period undulator. The beamline optics of the present BL-2 need to be renewed or improved in choosing one of these two options.

The short straight sections have been used for installing an SPSGU to supply hard X-rays. We have already constructed three HX beamlines at the short straight sections: BL-3 for materials science, and BL-1 and 17 for macromolecular crystallography. In the last straight section, we are planning to construct a complex analysis beamline using small X-ray scattering and X-ray absorption spectroscopy at BL-15.

REFERENCES

- [1] *Photon Factory Activity Report 2010*, #28 (2012) A 83.
- [2] *Photon Factory Activity Report 2010*, #28 (2012) A 82.

1-2 BL-6A: Small Angle X-ray Scattering Beamline

As reported previously, BL-6A was reconstructed for small-angle X-ray scattering (SAXS) experiments [3]. The activities that have been carried out at BL-15A were moved to the new BL-6A. The BL-15A site will be scrapped and instead a new undulator beamline for SAXS and X-ray absorption spectroscopy will be built in 2013.

The reconstruction of BL-6A began in FY2009. The old hutch and beamline components were scrapped immediately after the ring operation in March 2010. The new experimental hutch and deck with facility work were completed in FY2010 [3]. The beamline optics and diffractometer were installed in 2011. All the reconstruction work was completed during the summer shutdown of 2011. After a short commissioning and 2-day user training upon starting operation in autumn 2011, we started user operation on October 18, 2011.

The beamline layout of BL-6A is almost the same as that of BL-15A [3]. The main optics are a vertically focusing bent flat mirror and an asymmetrically cut monochromator crystal optimum for 8-keV X-rays. The surface of the mirror that had been used for a long time at the old BL-6A was cleaned by UV/ozone ashing [4], courtesy of the Light Source and Optics Division of JASRI/SPring-8. The SAXS/WAXS diffractometer used at

BL-15A [5] was installed in the experimental hutch. Two slits just after the monochromator and on the diffractometer are used for defining the beam size and preventing scattering to eliminate parasitic scattering, respectively. Two types of CCD detectors, C4880-10 and C7300 (Hamamatsu Photonics), equipped with two different sizes (6 and 9 inches) of X-ray image intensifiers (Hamamatsu Photonics) are available for SAXS experiments. A newly developed detector stage was installed to control the positions of these SAXS detectors (Fig. 1). A flat-panel sensor, C9728DK-10 (Hamamatsu Photonics), for WAXS experiments can be set on motorized stages for such experiments [5]. For the SAXS/WAXS simultaneous experiments, a digital delay pulse generator, Model 500D (Berkeley Nucleonics Corporation), is used for timing control among the detectors and apparatuses in msec order. A new BL-6A control system has been developed based on STARS, which is universally used at the Photon Factory [6]. This system can control all the motorized stages and measurement apparatuses via the network and several user-friendly GUI programs are provided.

Preliminary characterizations of the beam were carried out after tuning the optics. The FWHM beam size at the focal point was 0.498 mm (H) \times 0.245 mm (V), mea-

sured with a flat-panel sensor (C10013SK, Hamamatsu Photonics). This result is comparable to 0.443 mm (H) \times 0.188 mm (V) which is calculated by the raytracing program, SHADOW [5]. The photon flux at the sample position measured with an ionization chamber (S-1329A, Oken) was estimated to be 1.0×10^{12} phs/s and 3.6×10^{10} phs/s for the full-open and 0.6×0.6 mm² of the size-defining slit, respectively. These beam performances are promising for various SAXS activities.

REFERENCES

- [3] *Photon Factory Activity Report 2010*, #28 (2012) A 81.
- [4] T. Harada, S. Yamaguchi, M. Itou, S. Mitani, H. Maezawa, A. Mikuni, W. Okamoto, H. Yamaoka, *Applied Optics*, **30** (1991) 1165.
- [5] N. Igarashi, Y. Watanabe, Y. Shinohara, Y. Inoko, G. Matsuba, H. Okuda, T. Mori, K. Ito, *J. Phys.: Conf. Ser.*, **272** (2011) 012026.
- [6] <http://pfwww.kek.jp/stars/>
- [7] M. Sanchez del Rio, N. Canestrari, F. Jiang, F. Cerrina, *J. Synchrotron Rad.*, **18** (2011) 708.

1-3 New Diffractometers Developed for Resonant Soft X-Ray Scattering Experiments at BL-16A and 11B

Various intriguing physical properties have been discovered in strongly correlated electron systems (SCES). In such systems, the strong correlation among charge, spin, and orbital of the *3d* electrons and lattice degrees of freedom play important roles, so it is important to study these electronic states to understand the phenomena microscopically. Moreover, specific properties such as high *T_c* superconductivity and colossal magnetoresistance effects have often been reported near the metal-insulator (MI) transition, where the localized electrons, *d*-electrons in transition metals and *f*-electrons in rare earth metals, and the itinerant electrons, *O2p*, *P3p*, and so on, compete with each other. For example, superconductors generally exist in the vicinity of a quantum critical point. Hence, to elucidate the origin of these physical properties it is important to study the orbital hybridized states where itinerancy and localization of electrons compete. Recently, new types of ferroelectric (FE) compound such as multiferroics have attracted much attention. In these compounds, the hybridized orbital is also a key parameter of the polarization, so it is necessary to study the hybridized orbital state. In order to clarify these electronic states and orbital hybridized states, resonant soft X-ray scattering is an important technique, because we can utilize the *3d* transition metal *L*-edge, *4f* rare earth metal *M*-edge, *O K*-edge, and so on in the soft X-ray region, and thus can directly measure the electronic states dominating the physical properties. Moreover, the X-ray intensity of the soft X-ray region in the Photon Factory is much stronger than



Figure 1
SAXS/WAXS diffractometer in the experimental hutch of BL-6A. The new detector stage is placed at the end of the diffractometer.

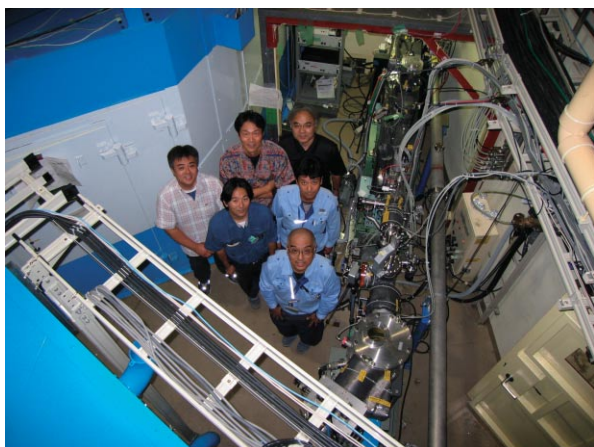


Figure 2
BL-6A construction team.

that in SPring-8. Although resonant soft X-ray scattering (RSXS) is a research subject that should be promoted in the Photon Factory, such a diffractometer has not been available so far.



Figure 3
Construction members photographed near the new diffractometer to perform RSXS measurements under magnetic field at BL-16A.

In order to elucidate the origins of physical properties in SCES, we have developed new diffractometers depending on the experimental conditions.

Figure 4(a) shows a conventional 2-circle diffractometer. To detect weak resonant signals which reflect the change of physical properties in SCES, the slits and detector must be placed in a vacuum chamber to reduce the background. Hence, the diffractometer with a large vacuum chamber was built as shown in Fig. 4(b), which can also accommodate a two-dimensional X-ray detector, a CCD camera for soft X-rays. The second diffractometer is specially designed for small angle diffraction to detect magnetic textures (skyrmions, etc.) and domain structures as shown in Fig. 4(c). We have also developed a diffractometer with a superconducting magnet (< 7.5 T) to investigate the magnetic field effect for SCES. This diffractometer has the same geometrical configuration as that at BL-3A, and we can perform studies by complementary use of hard and soft X-rays. These diffractometers are expected to lead to new discoveries in SCES.

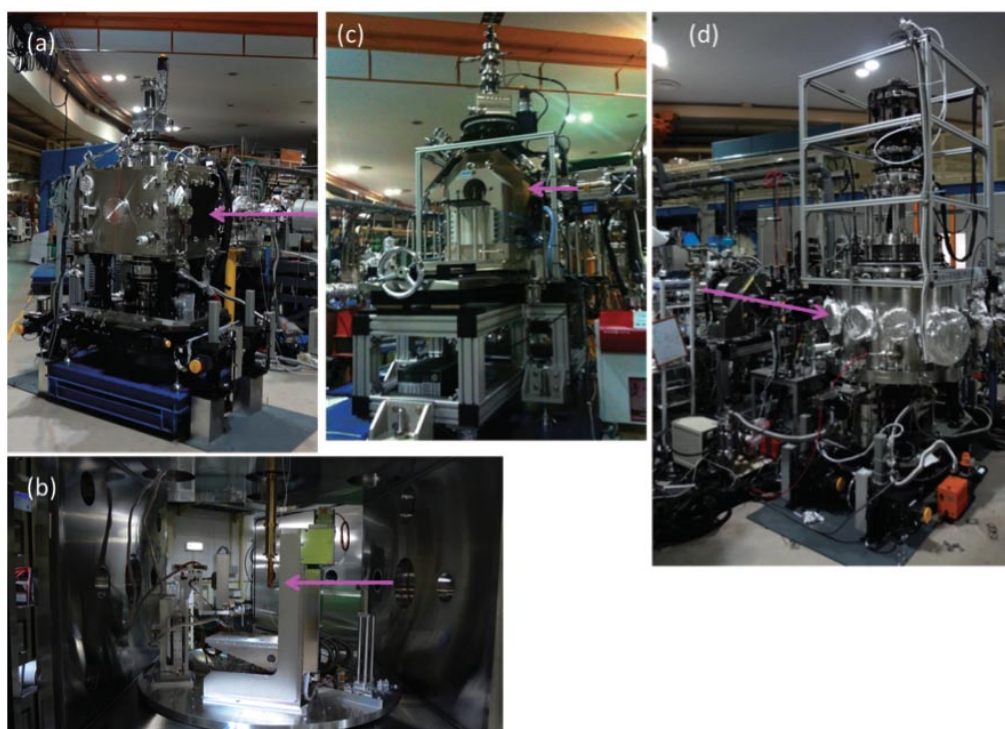


Figure 4
Conventional two-circle diffractometer: (a) outer and (b) inner side views. (c) Diffractometer for small angle resonant soft X-ray diffraction. (d) Two-circle diffractometer, which can be equipped with a superconducting magnet. Arrows indicate the direction of the incident X-ray.

2

Structural Biology Research Center

2-1 Overview

The Structural Biology Research Center (SBRC) was set up in May 2000, in the Photon Factory (PF) of the Institute of Material Structure Science (IMSS). The main tasks of the Center are to support users conducting X-ray synchrotron radiation studies of bio-macromolecules, highly advanced technical development, and in-house structural biology research. The Center now has over 30 staff, including a professor (Dr. S. Wakatsuki), four associate professors (Drs. R. Kato, N. Igarashi, M. Kawasaki and N. Shimizu), a vice associate professor (Dr. M. Hiraki) and three assistant professors (Drs. N. Matsugaki, Y. Yamada, L. Chavas) as the core members. About half of the SBRC members are engaged in beamline operation and development, and the remaining half in biological research (Fig. 1). In the beamline operation and development, Drs. Shimizu and Igarashi are responsible for small-angle X-ray scattering (SAXS), and Dr. Hiraki for robotics and automation. X-ray crystallography activities are led by Drs. Matsugaki, Yamada, Chavas, Hiraki and Igarashi, while in-house biological research is led by Drs. Kato and Kawasaki. In the structural biology building, which was built in April 2001 (430 m²) and extended twice to 765 m², all the steps necessary in structural biology research can be conducted, including protein expression, sample purification, crystallization, and biochemical and biophysical analyses of targeted proteins.

Our research activities were mainly supported by scientific funds. We built an up-to-date beamline, BL-5A, and also prepared various scientific equipment for protein expression, purification, and crystallization experiments using “Special Coordination Funds for Promoting Science and Technology” (FY2001–2003) from the Japan Science and Technology Agency (JST). Next, we participated in two large-scale projects: “Protein 3000 Project” of the Ministry of Education, Culture, Sports, Science and Technology Japan (MEXT) and



Figure 1
The members of the Structural Biology Research Center (SBRC) pictured at the meeting room of the Structural Biology Building.

JST (FY2002–2006) and “Development of System and Technology for Advanced Measurement and Analysis” of JST (FY2004–2007). In the Protein 3000 Project, the SBRC operated in one of eight consortia and conducted structural and functional analyses of post-translational modification and transport. Our consortium determined 254 protein structures and published 296 papers. To assist the Protein 3000 Project, we set aside about 30% of the bio-macromolecular crystallography beam time in the PF (a total of 327 days) for users of the eight consortia. In the “Development of System and Technology for Advanced Measurement and Analysis” project, we developed a micro-beam beamline, BL-17A, and a prototype next-generation X-ray area detector. BL-17A is the first beamline developed at the PF with a short gap undulator as a light source. The beam size can be controlled from 100 to 10 μm square, and is useful for both modest and small protein crystal experiments.

In the next five-year national project “Targeted Proteins Research Program” of MEXT and JST (FY2007–2011), the SBRC contributed via two independent programs: structural and functional research of protein transport in cells in close collaboration with the University of Tokyo and Kyoto University, and beamline development in collaboration with SPring-8, Hokkaido University, Kyoto University and Osaka University. The details of the programs are described later. The next project, Platform for Drug design, Informatics and Structural life sciences (PDIS), which provides user support and beamline development of two SR facilities, SPring-8 and PF, will start in April 2012. In addition to protein crystallography, the project includes solution scattering for macromolecules.

In addition to the above scientific research, the SBRC accepts many researchers from outside KEK who wish to collect diffraction data of their own macromolecular crystals under the Program Advisory Committee (PF PAC) system. The number of academic proposals and users has ranged from 100 to 120 in recent years as summarized in Table 1. In addition, together with advances in structure-based drug design, pharmaceutical companies require a large amount of

Table 1 Numbers PF proposals for protein crystallography beamlines in recent five years.

Type	G	P	U	S2	Total
2007	117	2	3	0	122
2008	101	0	0	1	102
2009	115	1	0	0	116
2010	103	2	1	0	106
2011	121	1	0	1	123

beam time, and thus many Japanese companies have been using beam time of the bio-macromolecular crystallography beamlines at KEK-PF. The Tsukuba Consortium (seven companies), four companies from the Pharmaceutical Consortium for Structure Analysis and three other companies are using our beamlines. Among them, Astellas Pharma Inc. financed the construction of AR-NE3A for their research.

2-2 Targeted Proteins Research Program (FY2007-2011)

Structure-Function Analysis of Protein Complexes that Regulate Vesicular Traffic

In the field of “Investigations of fundamental biological phenomena”, we have started “Structure-function analysis of protein complexes that regulate vesicular traffic”. This project is dedicated to protein targets of crucial importance but involving extreme difficulty, such as protein complexes including membrane proteins involved in membrane traffic in eukaryotic cells. Cell signaling and intracellular trafficking are the means by which eukaryotic cells deliver cargo proteins to various organelles, cell membranes, and extracellular destinations. Accurate distribution of the proteins is crucial for a range of cellular functions and activities. An increased understanding of the biological and biomedical functions of transport and modification proteins is indispensable for progress in the treatment of human diseases.

To accelerate the project, the SBRC is collaborating with Prof. Akihiko Nakano (University of Tokyo), who is working on functional researches of proteins involved in Golgi formation, post-Golgi membrane traffic and endocytosis in yeast and higher plants, Prof. Kazuhisa Nakayama (Kyoto University), who is studying proteins involved in the regulation of cell functions such as cytokinesis, cell polarity and cell mobility, and Prof. Ken Sato (University of Tokyo), who is researching transport vesicle formation from endoplasmic reticulum (ER) in yeast. Through close cooperation among these researchers, the SBRC is currently working on the expression, purification, crystallization and structure determination of target proteins that are either membrane proteins or forming macromolecular complexes. We have determined several structures of protein complexes and elucidated the molecular mechanisms of membrane traffic and cytokinesis [1-5].

Technological Development Research for Protein Structural Analysis

To determine the three-dimensional structures of bio-macromolecules by X-ray crystallography, the phase problem is one of the most important issues. Sulfur SAD (Single wavelength Anomalous Dispersion) analysis is currently one of the most attractive methods to overcome the problem, especially when heavy atom (or selenomethionine) derivative crystals of the targeted macromolecules are difficult to prepare, e.g.

integral membrane proteins and macromolecular complexes. We developed a new beamline dedicated to sulfur SAD experiments as a part of the national project “Targeted Proteins Research Program”. The beamline, BL-1A, is designed to deliver an intense lower energy beam at around 4 keV using the first harmonics of the short gap undulator as the light source, to enhance the anomalous signal from light atoms such as sulfur and phosphor. The beamline also covers the energy range of 12–13 keV with the third harmonics, allowing MAD (Multiple wavelength Anomalous Dispersion) measurements using Se, Hg, Au, or Pt atoms. The beamline was opened to the members of the program in FY2010, and some useful results have been obtained [6]. In addition to the construction of BL-1A at PF, this research project includes the development of another high-energy beamline at SPring-8 with a brilliant and small size beam, as well as the development of other environment technologies by other universities (Hokkaido, Kyoto and Osaka Universities).

2-3 Highlights on In-House Structural Biology Research

Structure and Function of ARF6-MKLP1 Complex which is Required for Cytokinesis

We have solved the structure of ARF6-MKLP1 complex which is required for cytokinesis [4]. A summary is reported in the Highlight Section of this volume (pp 52).

Crystal Structure of Linear Ubiquitin Chain

Ubiquitin regulates a wide range of biological processes such as protein degradation, DNA damage repair, and immune responses. Ubiquitin molecules polymerize into polyubiquitin chains; the C-terminal glycine of one ubiquitin can link to one of the seven lysine (Lys) residues in the second ubiquitin. Linear polyubiquitin chains are characterized by yet another type of linkage; the C-terminal glycine of one ubiquitin (distal ubiquitin) is covalently attached via a normal peptide bond to the

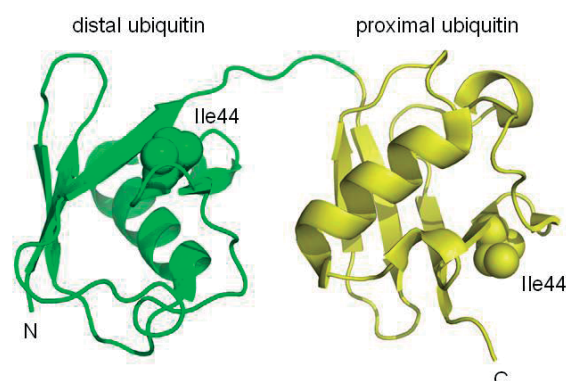


Figure 2
Crystal structure of linear diubiquitin. The C-terminus of the distal ubiquitin (green) is covalently attached to the N-terminus of the proximal ubiquitin (yellow) via a normal peptide bond. The central hydrophobic Ile44 residue of each ubiquitin is shown as a sphere model.

N-terminal methionine of the second ubiquitin (proximal ubiquitin). The specificity of polyubiquitin signaling is dictated by the linkage types of polyubiquitin chains. The linear polyubiquitin chain is involved in the activation of transcription factor NF- κ B through its specific interactions with NF- κ B essential modulator (NEMO) [7]. We also determined a crystal structure of linear diubiquitin at a resolution of 1.9 Å [8]. Although the two ubiquitin moieties do not interact with each other directly, the overall structure adopts a compact conformation (Fig. 2). This structure differs from the previously reported extended conformation, which resembles Lys63-linked diubiquitin suggesting that the linear polyubiquitin chain is intrinsically flexible and can adopt multiple conformations. Our result thus suggests the need for a wider search in conformational space in which polyubiquitin chains of different linkages might be exhibited when mediating distinct signals in various biological processes.

Structural Basis of Strict Phospholipid Binding by Human Evectin-2

Evectin-2 is a recycling endosomal protein involved in retrograde transport. One of the various kinds of phospholipids, phosphatidylserine (PS) is a relatively minor constituent of biological membranes. PS was found to be most concentrated in recycling endosomes (REs) among intracellular organelles. Evectin-2 consists of an N-terminal pleckstrin homology (PH) domain and a C-terminal hydrophobic region. The PH domain can specifically bind phosphatidylserine, which is enriched in REs, and plays an essential role in retrograde transport from REs to the trans-Golgi network [2]. We reported the structure of human Evectin-2 PH domain in complex with O-phospho-L-serine, and elucidated the molecular basis of how the head group of phosphatidylserine is recognized [2]. However, that structure could not elucidate why Evectin-2 cannot bind phosphatidic acid or phosphatidylethanolamine, which share a common moiety with phosphatidylserine. Then, we determined the crystal structure of an apo-form of human Evectin-2 PH domain whose ligand binding site is free from crystal packing [3]. Comparison between the

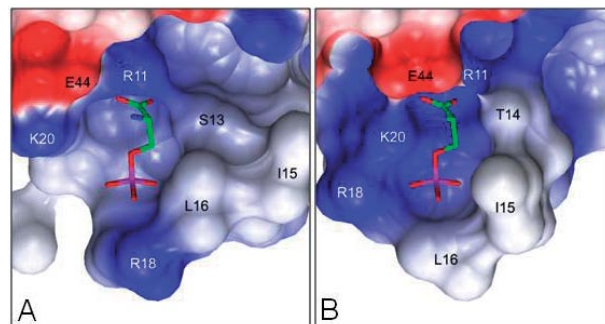


Figure 3
Ligand-binding site of Evectin-2. The apo-form (A) and the O-phospho-L-serine complex (B) structures are shown as charge distribution surface models. O-phospho-L-serine is shown as a stick model (green carbons, red oxygens and blue nitrogens). In panel A, the O-phospho-L-serine molecule from the complex structure is superimposed.

structure of the apo-form and the O-phospho-L-serine complex reveals ligand-induced conformational change evoked by the interaction between the carboxyl moiety of the head group of phosphatidylserine and the main chain N atom of Thr14 (Fig. 3). This structural change effectively explains the strict ligand specificity of PH domain of human Evectin-2.

2-4 Beamlines and Technology Developments for Macromolecular Crystallography

Beamlines

The SBRC operates five insertion device beamlines for bio-macromolecular crystallography (Table 2). More than 400 days of beam time in total were provided for user experiments in FY2011 despite the disaster (Great East Japan Earthquake of March 11). Beamlines BL-5A, AR-NW12A and AR-NE3A are mainly used for high-throughput structural biology. In particular, fully automated data collection by a pharmaceutical company has been performed routinely at the AR-NE3A. On the other hand, beamlines 1A and 17A are designed for micro-

Table 2 Summary of protein crystallography beamlines at KEK-PF.

	BL-1A	BL-5A	BL-17A	AR-NW12A	AR-NE3A
Starting year	2010	2004	2006	2003	2009
Synchrotron ring	PF (2.5 GeV, 450 mA)			PF-AR (6.5 GeV, 40-60 mA)	
Injection	continuous (top up)			twice a day (10:00, 22:00)	
X-ray source	Short Gap Undulator	Multipole Wiggler	Short Gap Undulator	Undulator	Undulator
Photon flux (photons/sec)	4.4×10^{11} (@1.1 Å)	8.6×10^{11} (@1.0 Å)	5.5×10^{10} (@0.98 Å)	3.9×10^{11} (@1.0 Å)	1.2×10^{12} (@1.0 Å)
Wavelength (Å)	0.95 ~ 1.1, 2.7	0.75 ~ 1.9	0.9 ~ 2.1	0.75 ~ 1.9	0.75 ~ 1.9
Beam size (H × V, μm)	30 × 10	270 × 150	40 × 30	200 × 170	200 × 170
Detector	ADSC Q270 Pilatus 2M-F	ADSC Q210r	ADSC Q315r	ADSC Q210r	ADSC Q270
Purpose	low energy micro beam	high throughput	low energy micro beam	high throughput	high throughput
Sample exchanger	PAM (288 samples / Dewar)				

crystal structure analysis and also for SAD phasing with light atoms using lower energy beam of around 4 keV (BL-1A), and 6–8 keV (BL-17A). As mentioned above, the lower energy SAD is currently one of the most attractive methods for solving macromolecular crystal structures. Figure 4 shows one of the successful results in which 43 kDa protein structure was solved almost completely and automatically from the data set collected at BL-1A. A pixel array X-ray detector (Pilatus 2M, Dectris) was purchased (Fig. 5), and will be installed at BL-1A in early FY2012, instead of the CCD-type detector currently in use. The replacement will improve the signal to noise ratio of a weakly diffracted beam which is critical to solve structures by the SAD method.

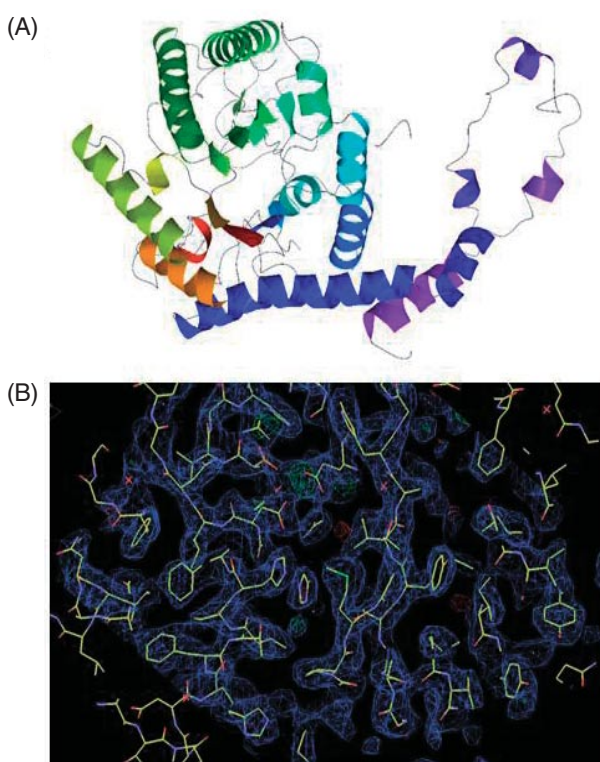


Figure 4
The protein structure solved by sulfur SAD at beamline BL-1A. The structure of glucose isomerase (MW 43 kDa) was solved by S-SAD. Ribbon diagram of the whole structure (A) and electron density map (B). Residues 4–382 out of 388 were automatically built.



Figure 5
New pixel array X-ray detector. Commissioning of the detector (Pilatus 2M, Dectris) at the PF experimental hall using a calibration X-ray source.

Technology Developments

To assist in the implementation of fully automated crystal centering at the beam position, we investigated the potential of UV LED sources in identifying macromolecular biological crystals [9]. Automation of sample centering at protein crystallography beamlines is presently achieved by focusing on sample holder recognition, while the crystalline samples are ignored completely. The capacity of soft UV to specifically highlight biological objects makes such a light source a suitable target for future development for universal centering methods with any type of sample holder (Fig. 6).

Minimization of the absorption effects of X-rays by the air and nitrogen gas surrounding a sample during data collection is important for low-energy SAD phasing, because these effects increase at lower photon energy. The absorption effects decrease the intensity of diffracted X-rays and increase the background noise in a diffraction image. We developed an He chamber and He cryo-stream system which replace the gas surrounding a sample with He, and installed them in BL-1A (Fig. 7). The He chamber is large enough to contain an X-ray area detector and is filled with helium gas. The panel face to the sample is sealed with a thin Kapton film, and when a diffraction experiment is carried out, this chamber moves close to the sample. The He cryo-stream system consists of a gas cooler made by Cryo Industries Inc. and a gas flow controller developed by

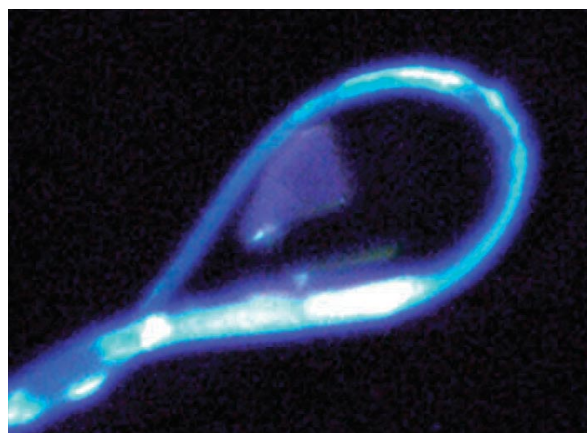


Figure 6
Protein crystals imaged by UV fluorescence. Illumination by UV LED (283 nm) of human sialidase Neu2 crystals within a nylon loop resulted in a specific fluorescence from the crystalline object.

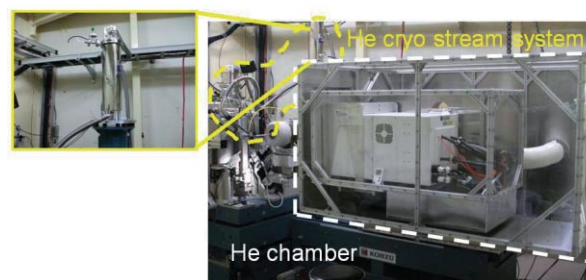


Figure 7
Helium chamber and helium cryo-stream system. He chamber and He cryo-stream system installed at BL-1A. The white and yellow broken lines indicate He chamber and He cryo-stream system, respectively.

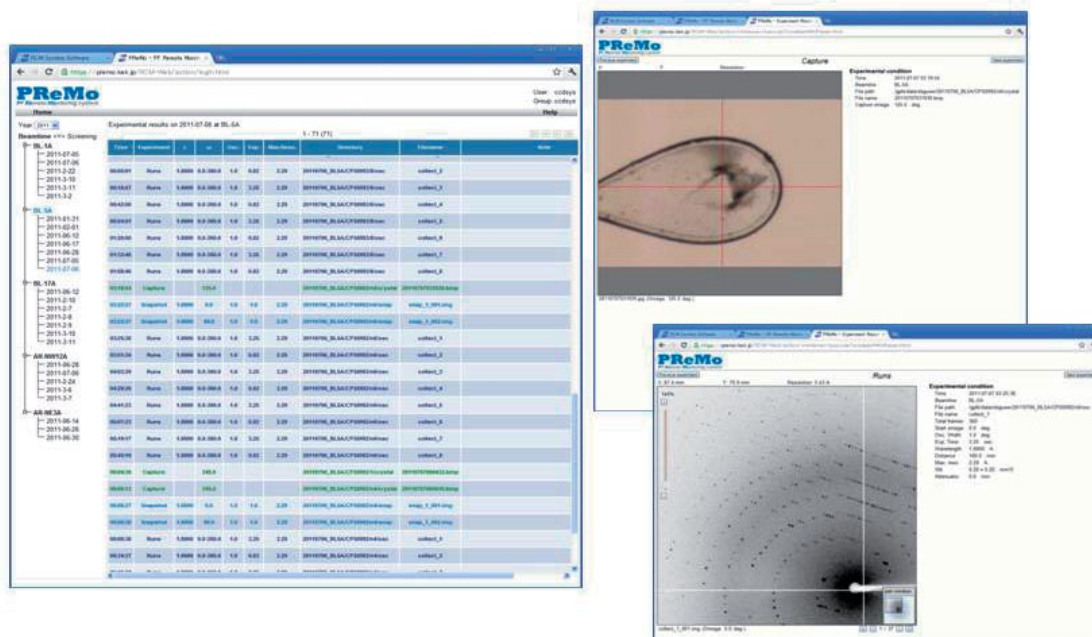


Figure 8 Upgraded web interface of PReMo. The web interface of PReMo consists of an experiment browser (left) and a results viewer (right).

us. This system can easily and quickly switch a gas flow from helium to nitrogen. This enables us to use cryo N_2 gas during sample mounting and centering, and to use cryo He gas during a diffraction experiment, thus reducing the amount of He gas consumed for the experiment.

PReMo (PF Remote Monitoring System) is a system which stores the conditions and results of diffraction experiments which are carried out at beamlines and allows users to access this information from outside of KEK via a Web browser. In FY2011, we upgraded the Web interface of PReMo to be more user-friendly (Fig. 8). A fully automated data collection system was originally developed for large-scale pharmaceutical research. In FY2011, we added a function to allow users to select a snapshot or data set collection experiment for each sample. After automated snapshot experiments of all samples stored in a sample exchange system beside the diffractometer, the user can check diffraction images via PReMo and determine data set collection conditions. Users submit information to the system through PReMo and perform automated data set collection experiments. This new automated experiment scheme was started in FY2011, and a mail-in service based on the new scheme was opened for industrial users from FY2011.

Beamlines and Technology Developments for Small-angle X-ray Scattering

There are two full-time SAXS beamlines in PF : BL-6A and BL-10C (Table 3). They have been operated by a user group because of the absence of a beamline scientist of the PF. Associate professor Dr. Shimizu arrived as a beamline scientist for SAXS in 2010, and worked with Dr. Igarashi and other support staff to refurbish BL-10C and to relocate BL-15A. Since the new BL-15A, which has a short gap undulator as the light source, is planned to be constructed for SAXS and XAFS studies, SAXS activities of BL-15A were moved to BL-6A in the summer of FY2011. Almost all the optical and experimental components were installed in the same layout as the previous BL-15A (Fig. 9A, B), but the old components and systems were replaced by new ones to improve beamline safety and user-friendliness. The PF standard control frame work (STARS) was installed to BL-6A and BL-10C and new graphical user interfaces were developed so that users can operate all the motorized stages from a remote computer.

Although there were several sets of detectors at the previous BL-15A, users had to exchange the detectors by themselves. A motorized detector stage was installed

Table 3 Summary of SAXS beamlines at KEK-PF.

	Science Target	Light Source & Optics	Detector	Beam Size (FWHM, mm) & Flux (phs/sec)	X-ray Energy (Å)
BL-6A	Hard materials Soft matters Proteins (Multi purpose, Time-resolve)	Bending magnet Flat bent mirror Asymmetric cut monochromator	2 types of XR-II CCDs PSPC (out of order) FPD for WAXS	$0.6 \times 0.6 \sim 1.0 \times 1.0$ $3.6 \sim 11 \times 10^{10}$	1.5
BL-10C	Soft matters Proteins (Solution, Static)	Bending magnet Bent cylinder mirror Double crystal monochromator	PSPC R-AXIS 7	$0.7 \times 0.7 \sim 1.0 \times 1.0$ $1.9 \sim 3.4 \times 10^{10}$	1.488

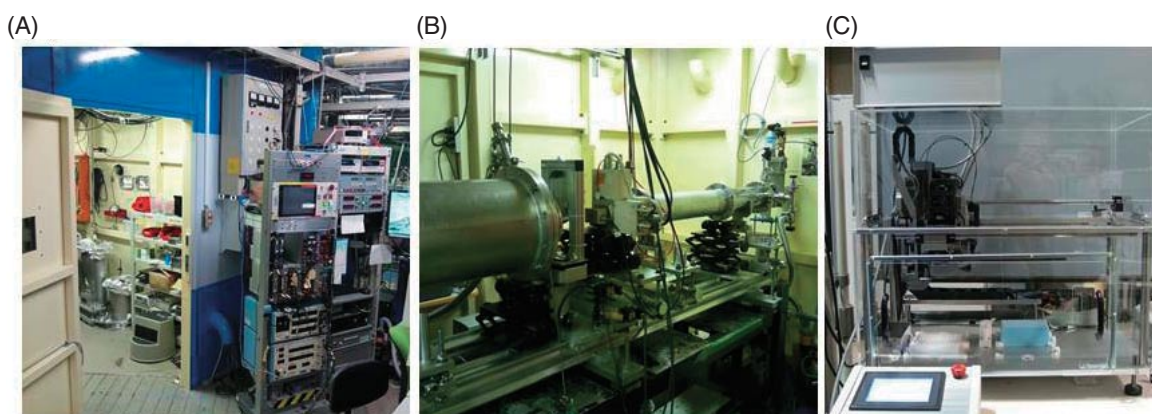


Figure 9
Refurbishment and improvement of SAXS stations. Views of BL-6A experimental hut from outside (A) and inside (B). (C) An automated sample mixing machine was developed and installed at the side of the BL-10C experimental hut.

at BL-6A, and users can easily set the detector position by presetting the position of each detector. Since simultaneous SAXS/WAXS measurements are generally conducted to evaluate the structure of a sample based on data observed in the broad angle region, we newly installed a flat panel sensor (C9728DK-10, Hamamatsu Photonics) for WAXS experiments and constructed a simultaneous measurement system which can measure at speeds of up to 3 Hz in combination with the preexisting SAXS detectors at BL-6A.

The data in the broad angle region can be measured with an imaging plate detector R-AXIS VII (Rigaku) at BL-10C. We replaced the size-definition slit from an old hand-operated one to a new motorized one to optimize the beam position and size by automatic scanning with an ammeter. We are upgrading BL-10C especially for high-throughput measurements of Bio-SAXS experiments. As part of this upgrade, we developed and installed an automated solution mixing machine (Fig. 9C), which will be extended to a solution-sample changer. Moreover, a micro-centrifuge, an ultra-micro spectrophotometer, an incubator, and so on were also installed on the BL-10C experimental hut side in order to improve the sample preparation.

REFERENCES

- [1] T. Uejima, K. Ihara, T. Goh, E. Ito, M. Sunada, T. Ueda, A. Nakano and S. Wakatsuki, *J. Biol. Chem.*, **285** (2010) 36689.
- [2] Y. Uchida, J. Hasegawa, D. Chinnapen, T. Inoue, S. Okazaki, R. Kato, S. Wakatsuki, R. Misaki, M. Koide, Y. Uchiyama, S. Iemura, T. Natsume, R. Kuwahara, T. Nakagawa, K. Mukai, E. Miyoshi, N. Taniguchi, D. Sheff, W. I. Lencer, T. Taguchi and H. Arai, *Proc. Natl. Acad. Sci. USA*, **108** (2011) 15846.
- [3] S. Okazaki, R. Kato, Y. Uchida, T. Taniguchi, H. Arai and S. Wakatsuki, *Acta Cryst. D*, **68** (2012) 117.
- [4] H. Makyio, M. Ohgi, T. Takei, S. Takahashi, H. Takatsu, Y. Katoh, A. Hanai, T. Ueda, Y. Kanaho, Y. Xie, H. W. Shin, H. Kamikubo, M. Kataoka, M. Kawasaki, R. Kato, S. Wakatsuki, and K. Nakayama, *EMBO J.*, **31** (2012) 2590.
- [5] K. Nakamura, Z. Man, Y. Xie, A. Hanai, H. Makyio, M. Kawasaki, R. Kato, H.W. Shin, K. Nakayama and S. Wakatsuki, *J. Biol. Chem.*, **287** (2012) 25478.
- [6] H. Ru, L. Zhao, W. Ding, L. Jiao, N. Shaw, W. Liang, L. Zhang, L. -W. Hung, N. Matsugaki and S. Wakatsuki, *Acta Cryst. D*, **68** (2012) 521.
- [7] S. Rahighi, F. Ikeda, M. Kawasaki, M. Akutsu, N. Suzuki, R. Kato, T. Kensche, T. Uejima, S. Bloor, D. Komander, F. Randow, S. Wakatsuki and I. Dikic, *Cell*, **136** (2009) 1098.
- [8] A. Rohaim, M. Kawasaki, R. Kato, I. Dikic and S. Wakatsuki, *Acta Cryst. D*, **68** (2012) 102.
- [9] L.M.G. Chavas, Y. Yamada, M. Hiraki, N. Igarashi, N. Matsugaki and S. Wakatsuki, *J. Synchrotron Radiat.*, **18** (2011) 11.

3

Condensed Matter Research Center

3-1 Overview

The Condensed Matter Research Center (CMRC) was established on April 1, 2009, at the Institute of Materials Structure Science (IMSS) with the aim of pursuing cutting-edge research on condensed matter science through the comprehensive use of multi-probes supplied by the IMSS, such as synchrotron radiation, neutrons, muons, and slow positrons. The CMRC has four research groups: the Correlated Electron Matter Group, the Surface/Interface Group, the Matter Under Extreme Conditions Group, and the Soft Matter Group. Through collaboration among these four groups, the CMRC has been promoting six bottom-up projects: the hybridized orbital ordering project, geometrical correlation project, molecular crystal project, surface/interface project, extreme condition project, and soft matter project (Fig. 1). In the hybridized orbital ordering project, the charge/spin/orbital orderings with hybridized orbitals have been studied under high pressure or a strong magnetic field. In the geometrical correlation project, we have determined the characteristic correlation time for fluctuation in itinerant systems with strong electron correlation under the influence of geometrical frustration using muons, neutrons, and synchrotron X-rays, which have different probing-time scales. In the molecular crystal project, electronic correlation in molecular crystal systems has been investigated to elucidate novel phenomena such as superconductivity, magnetism, ferroelectricity, and charge ordering. In the surface/interface project, crystal structures and electronic structures at the surface and interface of magnetic thin films and multilayers have been studied through depth-resolved magnetic circular dichroism (MCD)/X-ray absorption spectroscopy (XAS), resonant X-ray scattering (RXS), and neutron reflectivity. In the extreme condition project, we have studied changes in the crystal structures, electronic structures,



Figure 1
Project leaders of CMRC:
T. Otomo, H. Kumigashira, K. Amemiya, H. Nakao, R. Kumai,
T. Kondo, H. Seto, Y. Murakami (Head of CMRC), R. Kadono.

spin states, valence states, and chemical bonding of important compounds in geophysics to understand changes in their density and elastic, geological, transport, and chemical properties. In the soft matter project, we have investigated spontaneous motion under non-equilibrium conditions, the hierarchical structure of a soft matter complex resulting from self-organization, and functional soft matter interfaces for industrial applications. Some highlights of the CMRC projects are reported in the following sections.

3-2 Hybridized Orbital Ordering Project -Orbital Hybridization Ordering Study in Strongly Correlated Electron System and the External Field Effect-

The ordered states of the electronic degrees of freedom (charge, spin, and orbital) play very important roles in strongly correlated electron systems. In particular, the hybridization effect of the electronic orbitals has been a central issue in this field for a long time. In this project, both the hybridized orbital ordering between localized and itinerant electrons and the charge/spin/orbital orderings are studied under high pressure or a strong magnetic field. Resonant hard/soft X-ray scattering and inelastic neutron scattering techniques are used complementarily.

Doping Variation of Hole Orbital States in $Nd_{2-x}Sr_xNiO_4$ Studied by Polarization-Dependent Soft-X-Ray Absorption Spectroscopy [1]

X-ray absorption spectroscopy (XAS) is a strong probe for determining the local electronic structure such as the valence as well as the orbital states. In the case of superconducting layered cuprates, for example, a couple of pre-edge peaks have been clearly observed in the O *K*-edge spectra and the relationship between the orbital character and superconductivity has been intensively studied. While XAS experiments were performed also for layered nickelates for comparison with the superconducting cuprates, previous works on single crystals were limited to the low-doping region below about $x = 0.5$. We therefore investigate the orbital state variation toward the metallic region by systematically measuring the polarization-dependent O *K*-edge spectra up to $x = 1.1$.

Single-crystal samples of $Nd_{2-x}Sr_xNiO_4$ ($x = 0.3-1.1$) were grown by a high-oxygen-pressure floating-zone method. XAS experiments were carried out at undulator beamline BL-16A. The O *K*-edge data were taken in

the fluorescence-yield mode with a typical attenuation length of about 30 nm. The XAS spectra for E||a and E||c were measured using vertically and horizontally polarized X-rays in nearly-grazing incidence geometry to the *ab*-plane, respectively, for comparing and analyzing the polarized spectra more accurately. The incidence angle relative to the surface was set to 10 degrees. The measurements were performed in a high vacuum of 10^{-8} Torr, at 50 K.

Figure 2 (a) shows the polarization-dependent O *K*-edge spectra at $x = 0.5$ for E||a and E||c. Aside from the main peak at about 536 eV, a couple of pre-edge peaks are clearly observed in the lower energy region (three peaks for E||a and two peaks for E||c), labeled with letters A–D. Considering all the possible transition processes as shown in Fig. 2 (b), these pre-edge peaks at about 532 and 529 eV for $x = 0.5$ are ascribable to processes A and B, as assigned also in the previous work. This simply indicates that the holes are mainly doped into the x^2-y^2 orbital below $x = 0.5$. Figures 2 (c) and 2 (d) show the doping variation of the magnified spectra in the pre-edge region. Focusing on the variation below and above $x = 0.5$ for E||c, an additional peak assigned to process C is clearly discerned above $x = 0.6$, directly indicating the existence of Ni^{3+} sites with unoccupied $3z^2-r^2$ orbital. Above $x = 1.0$, in addition, the positions of all peaks largely shift to lower energy both for E||a and E||c. This might arise from the appearance of an additional peak assigned to process D, indicating the existence of Ni^{4+} sites as the ground state.

Eventually, doping variation of the site occupancy of the respective valence and orbital states can be roughly estimated by fitting and quantifying the pre-edge peaks B–D for E||c; the numbers of Ni^{3+} sites with occupied $3z^2-r^2$ and x^2-y^2 orbitals increase nearly linearly at about $x = 0-0.5$ and $x = 0.5-1.0$, respectively. This indicates

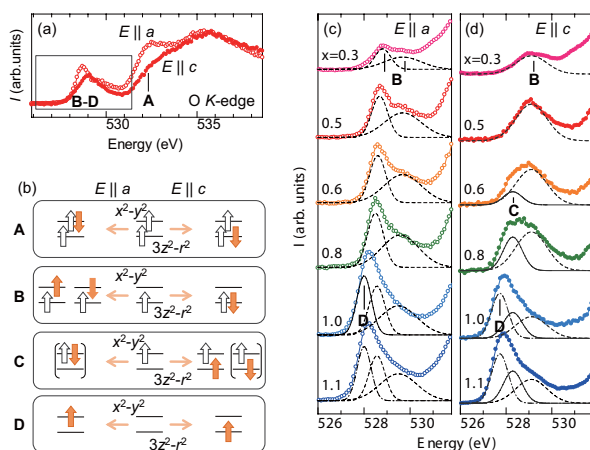


Figure 2
(a) Polarization-dependent O *K*-edge XAS spectra. (b) Schematic of the transition processes A–D corresponding to the pre-edge peaks. Filled arrows represent the transition electrons from the O 1s state to the ground Ni 3d e_g orbital state shown in the middle. Doping variation of the magnified O *K*-pre-edge spectra for (c) E||a and (d) E||c. Fittings for the peaks corresponding to the transition processes (B, C, and D) as labeled in (b) are indicated by dashed, solid, and chain curves, respectively.

that the excess holes above $x = 0.5$ are mainly doped into the $3z^2-r^2$ orbital and thus the x^2-y^2 -based checkerboard-type charge ordering or correlation can strongly persist up to the high-doping metallic region due to the multi-orbital nature.

3-3 Geometrical Correlation Project

Geometrical frustration often produces novel phenomena in strongly correlated electron systems, such as the heavy fermion state in which anomalous mass enhancement occurs. The objective of this project is to determine a characteristic correlation time for fluctuation in itinerant systems with strong electron correlation under the influence of geometrical frustration using muons, neutrons, and synchrotron X-ray, which have different probing-time scales.

Quasi-One-Dimensional Spin Dynamics in LiV_2O_4 : One-to-Three-Dimensional Crossover as a Possible Origin of Heavy Fermion State [2]

The heavy fermion behavior observed in a cubic vanadium spinel, LiV_2O_4 , has drawn much interest, since it is one of the remarkable examples in which only *d*-orbital electrons are relevant to the electronic property. We are revisiting spin fluctuation in LiV_2O_4 by examining the earlier results of muon spin rotation/relaxation measurement. Instead of the relationship for the localized electron limit, we used that between muon depolarization rate and spin fluctuation rate (ν_D) for itinerant electron systems to reanalyze the data, revealing that ν_D varies linearly with temperature (ν_D / T) over the range of $10^8-10^{12} \text{ s}^{-1}$ for $0.02 < T < 10^2 \text{ K}$. Such a linear *T* behavior as well as the magnitude of ν_D is fully consistent with the behavior of magnetic relaxation rate previously observed by inelastic neutron scattering (INS), demonstrating that μSR and INS have a common time window over a fluctuation spectrum. The linear dependence of ν_D on *T* is understood to be a specific feature predicted by a Hubbard model for intersecting one-dimensional (1D) chains. This quasi-1D character, which is coexistent with enhanced uniform susceptibility at low temperatures, supports the scenario of 1D-to-3D crossover for the microscopic origin of heavy-fermion behavior in LiV_2O_4 .

3-4 Molecular Crystal Project

In this project, electronic correlation in molecular crystal systems will be investigated to elucidate novel phenomena such as superconductivity, magnetism, ferroelectricity and charge ordering. We will analyze the crystal structure under high pressure using a pressure cell developed specifically for molecular crystals to elucidate the mechanism of superconductivity. The charge ordering state of molecular crystal systems is sometimes destroyed under an electric field. The transient

behavior from charge ordered to disordered state will be investigated using structural analysis by synchrotron X-ray.

Molecular Crystal Project: Electronic Ferroelectricity in a Molecular Crystal with Large Polarization Directing Antiparallel to Ionic Displacement [3]

The organic charge-transfer complex TTF-CA, comprising an electron donor, tetrathiafulvalene (TTF), and an acceptor, *p*-chloranil (CA) (Fig. 3 (c)), has been attracting considerable attention because of a novel ferroelectric neutral-to-ionic phase transition that occurs in it. Recently, in contrast to the conventional point-charge scenario, the first-principles calculations invoked a significantly larger spontaneous polarization (3–10 μCcm^{-2} along the *a*-direction) with two contrasting candidate electronic states. The total polarization is predicted to be directed either parallel or antiparallel to the ionic polarization, depending on the antiferromagnetic or nonmagnetic state. This prediction motivated us to experimentally determine both the magnitude and the direction of spontaneous polarization.

The TTF-CA crystal comprises *DA* alternating stacks along the *a*-axis, and the one-dimensional nature of this chain brings about the Peierls- or spin-Peierls-type structural instability, displacing pairwise the ionized *D* and *A* molecules (Fig. 3 (d)). Ferroelectricity emerges when the chain can invert its polarity, i.e., ...*DA DA*... \leftrightarrow ...*AD AD*..., where the underlines represent dimerized *DA* pairs. The crystal structure is symmetry-broken to a polar space group of *Pn* upon neutral-ionic transition (NIT) as determined by neutron and high-resolution X-ray diffraction experiments.

The symmetry-breaking of the TTF-CA crystal structure under an electric field was probed by the intensity difference between the Bijvoet pair (*hkl* versus $\bar{h}\bar{k}\bar{l}$) reflections; this difference arises from the anomalous X-

ray scattering effect. The simulation based on the crystal structures at *T* = 15 and 40 K predicts that the Bijvoet pair reflections 101 and $\bar{1}0\bar{1}$ have sufficient intensities and are the most susceptible to the anomalous X-ray scattering for the X-ray wavelength $\lambda = 1.55 \text{ \AA}$ that is used. The temperature dependence of their normalized integrated intensity $I_+ \equiv I(101)/\{I(101) + I(\bar{1}0\bar{1})\}$ and $I_- \equiv I(\bar{1}0\bar{1})/\{I(101) + I(\bar{1}0\bar{1})\}$ was observed. Immediately below *T_c*, the observed I_+ and I_- readily approach the values 0.705 or 0.295, which correspond to full polarization into either polarity according to the simulation. Therefore, the poling field of 4 kVcm^{-1} is regarded as sufficient for developing a single-domain state. By comparing the observed intensity of the Bijvoet pair (I_+ and I_-) with the simulation, we found that the positively charged TTF molecules shift toward the positive electrode and that the negatively charged CA shifts toward the negative electrode (Fig. 3 (b)). These experimental observations confirmed the recent first-principles calculations predicting an extreme contribution from electronic polarization that is directed antiparallel to the ionic displacement and governs the magnitude of polarization. The electronic ferroelectricity itself is currently one of the key issues for multiferroelectrics. The electronic response with lower energetic cost of lattice deformations promises both high-performance and high-frequency operations as well as new functionalities.

3-5 Surface/Interface Project -Crystalline, Magnetic and Electronic Structures at the Surface and Interface of Magnetic Thin Films and Multilayers-

The surface and interface of magnetic thin films play essential roles in the appearance of extraordinary magnetic properties such as perpendicular magnetic anisotropy and the giant magnetoresistance effect. We are investigating the crystalline, magnetic and electronic structures at the surface and interface of magnetic thin films and multilayers, in order to reveal the origin of the fascinating magnetic properties, which cannot be realized in bulk materials. For example, we have studied the magnetic anisotropy of Fe/Ni multilayers, magnetism at the interface between MgO and Heusler alloy, effects of ion irradiation on ultrathin films, and magnetic depth profile of Gd/Cr multilayers, mainly by means of the X-ray magnetic circular dichroism (XMCD) technique. Moreover, neutron reflectivity experiments have started at BL-17 in J-PARC. We also plan to perform muon spin rotation experiments using an ultra-slow muon source.

Origin of Ion Irradiation-Induced Perpendicular Magnetization

 [4]

We are investigating Ga⁺ irradiation-induced chang-

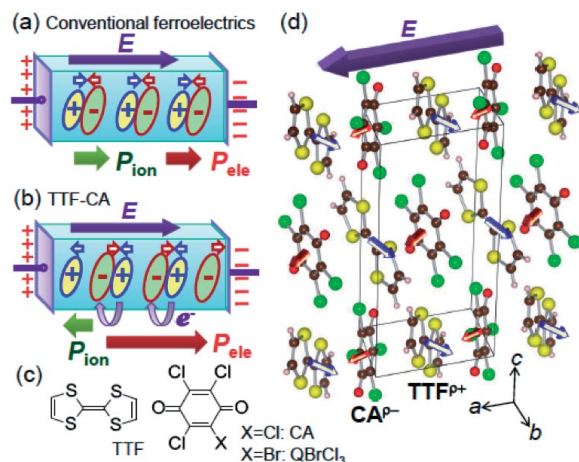


Figure 3
Schematic illustrations of the electric polarization (solid arrows) and displacement direction (small open arrows) of ions in conventional displacive-type ferroelectrics (a) and TTF-CA crystal (b). (c) Molecular structures of TTF, CA, and QBrCl₃. (d) Crystal structure of TTF-CA and molecular displacement directions under an electric field.

es in magnetic anisotropy and the crystalline structure of a Pt/Co/Pt ultrathin film by means of X-ray magnetic circular dichroism (XMCD) and extended X-ray absorption fine structure (EXAFS) techniques. XMCD analysis shows a large orbital moment difference between out-of-plane and in-plane directions, which corresponds to perpendicular magnetic anisotropy (PMA), at moderate Ga⁺ fluences, while larger fluences reduce the orbital moment difference, resulting in in-plane magnetization. From the EXAFS analysis, enhancement of PMA is directly related to an in-plane lattice expansion caused by ion irradiation and Co-Pt intermixing, which results in a large lattice distortion. Thus, the origin of the ion irradiation-induced changes in magnetic anisotropy is successfully explained.

3-6 Extreme Conditions Project

The targets of this project are compounds in the Earth's core/mantle as well as light element minerals. We are studying changes in the crystal structures, electronic structures, spin states, valence states, and chemical bonding of these compounds to understand changes in density and in elastic, geological, transport, and chemical properties. We will use diffraction and spectroscopy techniques employing synchrotron X-rays and neutrons.

3-7 Soft Matter Project

Soft matter is a subfield of condensed matter comprising a variety of physical states that are easily deformed by thermal stresses or thermal fluctuations.

They include liquids, colloids, polymers, liquid crystals, amphiphilic molecules, and a number of biological materials. These materials often self-organize into mesoscopic physical structures that are much larger than the microscopic scale (the arrangement of atoms and molecules), and yet are much smaller than the macroscopic scale of the material. The properties and interactions of these mesoscopic structures may determine the macroscopic behavior of the material. In spite of the various forms of these materials, many of their properties have common physicochemical origins, such as a large number of internal degrees of freedom, weak interactions between structural elements, and a delicate balance between entropic and enthalpic contributions to the free energy. These properties lead to large thermal fluctuations, a wide variety of forms, sensitivity of equilibrium structures to external conditions, macroscopic softness, and metastable states. Accordingly, we are investigating structural properties of soft matter such as liquids and amphiphilic molecules; structures formed under far-from-equilibrium conditions are particularly interesting. These investigations will yield basic knowledge to help solve the mystery of life.

REFERENCES

- [1] M. Uchida, Y. Yamasaki, Y. Kaneko, K. Ishizaka, J. Okamoto, H. Nakao, Y. Murakami, and Y. Tokura, *Phys. Rev. B*, **86** (2012) 165126.
- [2] R. Kadono, A. Koda, W. Higemoto, K. Ohishi, H. Ueda, C. Urano, S. Konoda, M. Nohara, and H. Takagi, *J. Phys. Soc. Jpn.*, **81** (2012) 014709.
- [3] K. Kobayashi, S. Horiuchi, R. Kumai, F. Kagawa, Y. Murakami and Y. Tokura, *Phys. Rev. Lett.*, **108** (2012) 237601.
- [4] M. Sakamaki, K. Amemiya, M.O. Liedke, J. Fassbender, P. Mazalski, I. Svekio and A. Maziewski, *Phys. Rev. B*, **86** (2012) 024418.

4

The Slow Positron Facility

The Slow Positron Facility of the Photon Factory, equipped with a dedicated 55-MeV linac, provides a high intensity, pulsed slow positron beam. The linac operates in a short-pulse mode and a long-pulse mode, at frequencies of up to 50 Hz. The intensity of the beam has been increased tenfold to 5×10^7 slow positrons/s in the long pulse mode after improving the converter/moderator assembly for producing slow positrons in 2010 [1]. The pulse width in the short-pulse mode operation became adjustable from 1 to 10 ns in 2011, while that in the long-pulse mode remains at 1 μ s. The facility is operated by a professor (Dr. T. Hyodo) and an assistant professor (Dr. K. Wada) who accommodate the research projects of users from other institutes and conduct their own research as well.

4-1 Production of Energy Tunable Positronium Beam

A method to efficiently produce the positronium negative ion (Ps^-), an exotic system composed of one positron and two electrons bound through Coulomb interaction, has been developed by Nagashima et al. [2,3]. The photodetachment of the Ps^- ions was accomplished on beamline SPF-A1 on those produced by the pulsed positron beam in this facility and a pulsed intense laser light [4,5]. Since a Ps atom is a neutral composite particle consisting of an electron and a positron, it cannot be accelerated by an electric field. However, photodetachment of the Ps^- provides a new technique for generating an energy-tunable Ps beam [6,7].

A new positron beamline branch, SPF-A3, was constructed for this purpose, where the beam is deflected by 45° along a curved magnetic field before it is incident on the target. The slow positron beam in the short pulse mode (intensity 5×10^6 slow positrons/s, width 12 ns, 50 Hz) was made incident on an annealed 25 μ m-thick W foil coated with one monolayer of Na. The Ps^- ions emitted from the target were accelerated by an electrostatic potential of 0.5–2.8 kV. Then they were photodetached by using a photon pulse (width 12 ns, 25 Hz) from a Q-switched Nd:YAG laser to form energy-tuned Ps. By synchronizing the laser pulse with every other slow positron pulse, it was possible to obtain data with the laser on and off simultaneously without concerning the fluctuation of beam intensity. The resulting *ortho*-Ps atoms traveled in the direction of acceleration of the Ps^- ions, and were detected by a pulse-counting mode MCP placed 80 cm away, squarely facing the W target. All the charged particles backscattered from the target were transported back along the curved magnetic field and were not detected by the MCP. Some of the γ -rays

from the positrons annihilating in the target were detected by the MCP and gave information on the time of the Ps formation. The time interval between detecting the γ -ray and the Ps (time of flight, TOF) clearly showed that the Ps traveled with the energy expected from the electrostatic acceleration of the Ps^- ions.

Thus the generation of an energy-tunable Ps beam was accomplished. The energy range was 300 eV to 1.9 keV. Note that this beam is ultra-high-vacuum compatible and so can be used as a probe for solid surfaces.

4-2 RHEPD Experiments

Reflection high-energy positron diffraction (RHEPD), the positron version of reflection high-energy electron diffraction (RHEED), was proposed by Ichimiya [8] and was put to practical use by Kawasuso and Okada [9]. The station for RHEPD installed on the beamline branch SPF-B1 in 2010 has yielded 14 times greater intensity than the former measurements with the ^{22}Na based beam at the Japan Atomic Energy Agency (JAEA). The station has been used for studying surface structures. This is a project of Dr. Fukaya (Kawasuso Group) of JAEA.

Compared with electron diffraction, positron diffraction is easier to interpret: (1) the exchange interaction with electrons is absent; (2) the positron is not attracted into the vicinity of the nuclei since its charge is positive; (3) the surface sensitivity is high because the inelastic scattering cross section for the positron is high and the crystal potential for the positron is positive; and (4) the scattering factor for the positron has smooth angular dependence and falls off smoothly like that of X-rays because the positron is repelled by the nuclei. Thus, positron diffraction can be used to analyze surface atomic geometry with high reliability [10].

In RHEPD, in particular, we may take advantage of the existence of total reflection under conditions such as incidence of a 10-keV positron beam with a glancing angle of less than 2° on Si surfaces. This makes the normalized RHEPD intensity nearly two orders of magnitude larger than that of RHEED. This superiority extends smoothly to the region outside the total reflection region, making RHEPD a useful tool for surface structure analysis in spite of the difficulty of obtaining an intense positron beam. Another advantage of the total reflection is the extremely high sensitivity to the topmost layer of the solid surface. In fact, the present intensity of the beam in this facility already makes RHEPD as useful as other methods for surface structure analysis.

Fukaya and co-workers conducted many studies with RHEPD even with the ^{22}Na -based slow positron

beam. However, much effort was required because the beam intensity was not strong enough and so the counts had to be accumulated repeatedly for several tens of minutes even for orienting the sample crystal. The intense slow positron beam in this facility solves this problem; the beam is intense enough to orient the crystal in real-time.

One of the first results is the determination of the atomic configuration of well-ordered and defectless Pt-induced nanowires on a Ge(001) surface at low temperatures[11]. This research was performed in conjunction with scanning tunneling microscopy (STM) and angle-resolved photoemission spectroscopy (ARPES). Although the surface periodicity is known through STM measurements as $p(4 \times 2)$ at high temperatures ($T > 110$ K) and $p(4 \times 4)$ at low temperatures ($T < 80$ K), the detailed structures were not known and four possible models had been suggested. The present work examined the models and revealed that only one of them [13] reproduced the RHEPD rocking curve at low temperatures very well. The fundamental structure determined is that Ge dimers exist on the top layer and Pt arrays are buried in the second and fourth layers. At low temperatures ($T < 80$ K), each of the topmost Ge dimers is alternately tilted in the surface normal direction, making a $p(4 \times 4)$ periodicity. At high temperatures ($T > 110$ K), each Ge dimer is flat with respect to the horizontal axis, giving rise to $p(4 \times 2)$ periodicity. This demonstrates the extremely high sensitivity of RHEPD to the position of the surface atoms in the surface normal direction.

Temperature dependence of the specular spot intensity for the one-beam condition at $\theta = 2.5^\circ$ was observed in the temperature range of 50–200 K. The intensity gradually increased between 80 K and 110 K, indicating the progress of the phase transition. This continuous change was reproduced by a power law; the order parameter is proportional to $|1 - T/T_c|^\beta$ with $\beta = 0.36 \pm 0.15$ and $T_c = 111 \pm 10$ K. The phase transition is explained as a displacive transition but the shift of the band dispersion is not directly related to a Peierls transition.

Another result of RHEPD experiments is the confirmation of the correlation of the spin splitting of the energy bands of Ag_2Pb surface alloy on an $\text{Ag}(111)$ surface

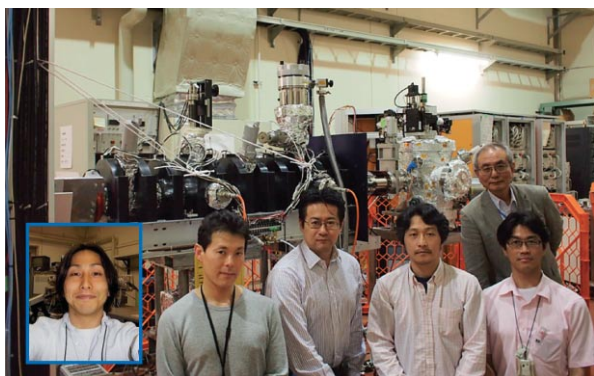


Figure 1
Construction of the RHEPD station on beamline SPF-B1.

and the outward displacement of the Pb atoms[12]. This alloy is known to show a giant Rashba effect, *i.e.*, the energy split of the surface electronic bands due to the spin-orbit interaction is much larger than that of other similar systems. It was discovered in the present research that the position of the Pb atoms shifts depending on the thickness of the $\text{Ag}(111)$ layer grown on the $\text{Si}(111)$ surface. The shift of the position of the Pb atom for each Ag thickness was determined by using RHEPD rocking curves. Then the electronic states of Ag_2Pb alloy were investigated by using ARPES, while controlling the position of the Pb atom by changing the $\text{Ag}(111)$ thickness.

Taken together, these results suggest that the magnitude of the Rashba energy depends on the outward displacement of the Pb atoms, as theoretically predicted [14]. They also suggest that the Rashba energy can be controlled by changing the Ag thickness of the substrate.

4-3 Positronium Time-of-Flight Experiments

A new Positronium time-of-flight (Ps-TOF) station as shown in Fig. 2 has been installed on beamline branch SPF-A1 by Nagashima's group. It is equipped with two scintillation counters consisting of plastic scintillators coupled with photomultiplier tubes for high magnetic field environments. They are behind lead blocks with thin slits (one 2 mm opening at 40 mm away from the sample surface and the other with 6 mm opening 120 mm away).

Using this station, the emission of Ps from an Na-coated W film was investigated. The slow positron pulse

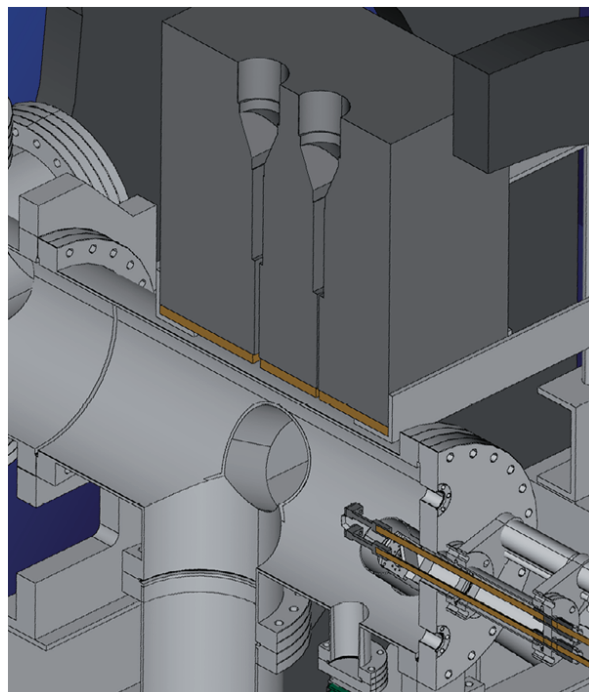


Figure 2
A cross section of the Ps TOF chamber on beamline APF-A1.

of energy of 4.2 keV was transported onto the target. The width of the positron pulse was 10 ns. A remarkable enhancement of the Ps yield was observed. The obtained TOF data provides information on the effect of the change of work function on the yield. The enhancement is tentatively attributed to the change in the electron density distribution near the surface, but the details of the TOF spectra are yet to be explained.

REFERENCES

- [1] K. Wada, T. Hyodo, A. Yagishita, M. Ikeda, S. Ohsawa, T. Shidara, K. Michishio, T. Tachibana, Y. Nagashima, Y. Fukaya, M. Maekawa and A. Kawasuso, *Eur. Phys. J. D*, **66** (2012) 37.
- [2] Y. Nagashima, T. Hakodate, A. Miyamoto and K. Michishio, *New J. Phys.*, **10** (2008) 123029.
- [3] H. Terabe, K. Michishio, T. Tachibana and Y. Nagashima, *New J. Phys.*, **14** (2012) 015003.
- [4] K. Michishio, T. Tachibana, H. Terabe, A. Igarashi, K. Wada, T. Kuga, A. Yagishita, T. Hyodo and Y. Nagashima, *Phys. Rev. Lett.*, **106** (2011) 153401.
- [5] *Photon Factory Activity Report 2010*, #28 (2012) A 68.
- [6] K. Michishio, T. Tachibana, R.H. Suzuki, K. Wada, A. Yagishita, T. Hyodo and Y. Nagashima, *Appl. Phys. Lett.* **100** (2012) 254102.
- [7] *Photon Factory Activity Report 2011*, #29 (2012) A 60.
- [8] A. Ichimiya, *Solid State Phenom.*, **28-29** (1992) 143.
- [9] A. Kawasuso and S. Okada, *Phys. Rev. Lett.*, **81** (1998) 2695.
- [10] S.Y. Tong, *Surf. Sci.*, **457** (2000) L432.
- [11] I. Mochizuki, Y. Fukaya, A. Kawasuso, K. Yaji, A. Harasawa, I. Matsuda, K. Wada and T. Hyodo, *Phys. Rev. B*, **85** (2012) 245438 .
- [12] *Photon Factory Activity Report 2011*, #29 (2012) B 73.
- [13] D. E. P. Vanpoucke and G. Brocks, *Phys. Rev. B*, **81** (2010) 085410.
- [14] G. Bihlmayer, S. Blügel, and E. V. Chulkov, *Phys. Rev. B*, **75** (2007) 195414.

5

IMSS Instrument R&D Team

The IMSS Instrument R&D team has been trying to develop a new detector system for material physics and biology since early May 2010. The detector R&D projects in the Photon Factory made steady progress in FY2011 as follows.

A. Ultra-fast signal processing system for Si-APD array X-ray detectors

The project team successfully developed a prototype detector consisting of a 64-ch Si-APD linear array and its ultra-fast ASIC circuits. The linear array had 64 pixels of $100\ \mu\text{m} \times 200\ \mu\text{m}$ with a pitch of $150\ \mu\text{m}$. The array device had a thickness of $10\ \mu\text{m}$ to guarantee a good time resolution of $100\ \text{ps}$. The front-end ASIC was newly designed to process a fast pulse of nanosecond width and a high count-rate of more than $10^8\ \text{s}^{-1}$, which were obtained from the Si-APD operating in linear mode. The spatial resolution of $100\text{-}\mu\text{m}$ order will be useful for position-selective time spectroscopy with a 100-ps time resolution. The nanosecond response of the array detector will increase the efficiency of data acquisition in time-resolved X-ray diffraction measurements by using a shorter pulse interval such as $2\ \text{ns}$ in the multi-bunch mode operation of a 500-MHz synchrotron ring. The team obtained test results with a 64-channel digital circuit using Field Programmable Gate Arrays (FPGAs) with a network processor for Ethernet, and confirmed that each channel of the prototype system had a 10-ns time resolution and a high count-rate of $> 10^7\ \text{s}^{-1}$. Figure 1 shows a time-course count distribution observed by the detector system. A mirror-focused X-ray beam of $8\ \text{keV}$ hit the linear array and the maximum count-rate was larger than $10^7\ \text{s}^{-1}$ per pixel. Four blocks of 126-ns

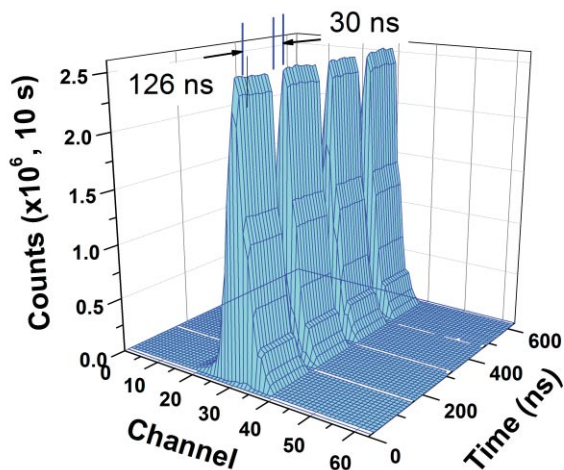


Figure 1
Time-course count distribution of 8-keV X-ray beam, measured by the 64-ch Si-APD linear array detector with a 10-ns time resolution.

X-ray pulse trains and 30-ns gaps were recorded for the multi-bunch mode operation of the PF ring by the 10-ns time resolution. A faster FPGA will be mounted in the next system and will show a 1-ns time resolution.

B. Auger-electron detector system for depth-resolved X-ray magnetic circular dichroism (XMCD)

The XMCD group working at beamline BL-16 has been preparing a multi-anode micro-channel plate (MCP) detector system, which has an angle resolution and a fast digital data read-out of 30 channels, instead of the old system consisting of a CCD and a fluorescence screen. In the new operation of the 10-Hz polarization switching at BL-16, the MCP system is expected to improve the S/N ratio and the dynamic range of output counts in XMCD measurements. Continuous 1-kHz data acquisition from each channel was already successfully achieved in test operation of the 10-Hz polarization switching with the MCP system. Data acquisition at a high count-rate of $> 10^7\ \text{s}^{-1}$ is now being prepared by developing a fast counting system using a faster ASIC amplifier.

C. Improvement of position-sensitive detector system for small-angle scattering (SAX) experiments

The SAX group tried to improve data acquisition from a position-sensitive proportional counter (PSPC) installed at BL-10C by using an FPGA and a network processor. With the help of the IMSS Neutron Science Division, they developed the TDC-NET module, which converted the time difference between two outputs from the delay-line PSPC to the position of the incident X-ray. Further improvements are under consideration such as triggering a signal for controlling the conditions around a sample, coincidentally with data acquisition.

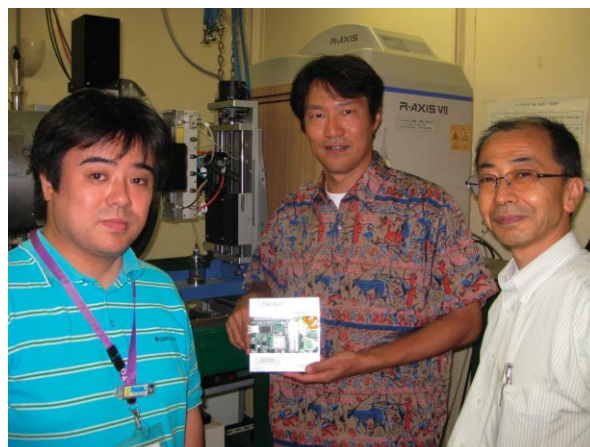


Figure 2
The SAX group with the newly developed data acquisition board.

6 Summary of Experimental Stations

About 54 experimental stations are operated at the PF Storage Ring and the PF-AR, as shown in Figs. 1 and 2. Two thirds of the stations are dedicated to research using hard X-rays, with the remaining one third used for studies in the VUV and soft X-ray energy regions. Tables 1 and 2 summarize the areas of the research carried out at experimental stations at the PF storage ring and PF-AR.

The specifications in terms of optics and performance of each experimental station differ according to experimental requirements and methodology. Tables 3 and 4 list the details of the optics of the hard X-ray stations and the soft X-ray / VUV stations. The principal performance parameters, including energy range, energy resolution, beam-spot size, and photon flux at the sample position are shown.

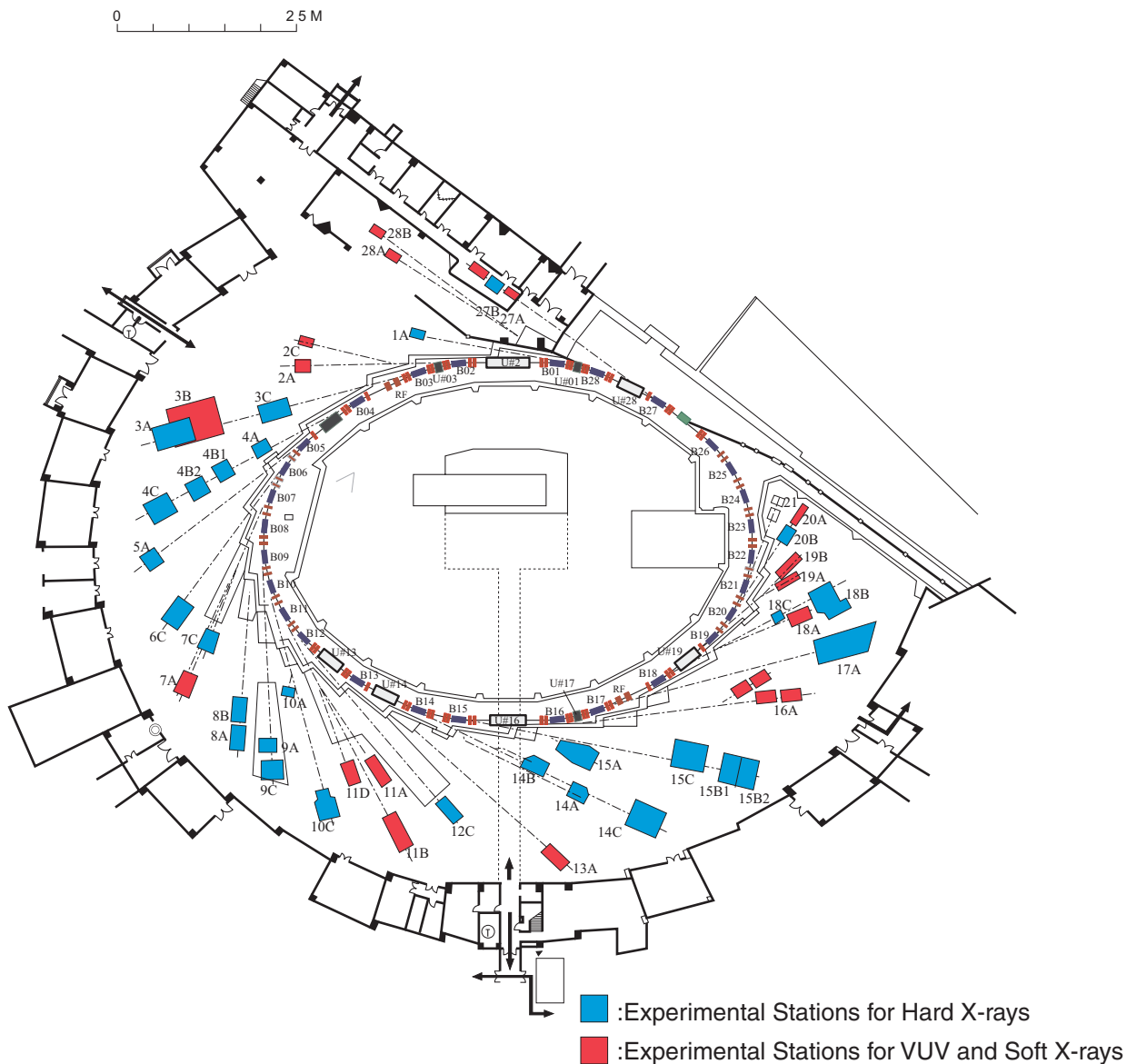


Figure 1
Plan view of the PF experimental hall, showing hard X-ray experimental stations (blue), and VUV and soft X-ray experimental stations (red).

Table 1 Complete list of experimental stations at the PF Storage Ring.

Experimental Station		Person in Charge
BL-1	(Short gap Undulator) A Macromolecular crystallography	N. Matsugaki
BL-2	(Undulator) A Soft X-ray spectroscopy C Soft X-ray spectroscopy	Y. Kitajima J. Adachi
BL-3	(A: Short Gap Undulator) A X-ray diffraction and scattering station for materials science B VUV and soft X-ray spectroscopy(◇) C Characterization of X-ray optical elements/White X-ray magnetic diffraction	H. Nakao H. Kato [Hiroasaki Univ.], A. Yagishita K. Hirano
BL-4	A Trace element analysis, X-ray microprobe B1* Micro-crystal and Micro-area structure analysis B2 High resolution Powder diffraction(♣) C X-ray diffraction and scattering	A. Iida Y. Yamasaki T. Ida[Nagoya Inst. Tech.], H. Nakao Y. Yamasaki
BL-5	(Multipole Wiggler) A Macromolecular crystallography	Y. Yamada
BL-6	A** Small-angle X-ray scattering of muscle and alloys C X-ray diffraction and scattering(♣)	N. Igarashi S. Sasaki [Tokyo Inst. Tech.] H. Kawata
BL-7	A Soft X-ray spectroscopy(♠) C X-ray spectroscopy and diffraction	J. Okabayashi [RCS], K. Amemiya H. Sugiyama
BL-8	A Weissenberg Camera for Powder/Single-crystal measurements under Extreme Conditions B Weissenberg Camera for Powder/Single-crystal measurements under Extreme Conditions	R. Kumai R. Kumai
BL-9	A XAFS C X-ray versatile station	H. Abe M. Nomura
BL-10	A X-ray diffraction and scattering C Small-angle X-ray scattering of solution sample(♣)	Y. Yamasaki S. Nojima [Tokyo Inst Tech.], N. Igarashi
BL-11	A Soft X-ray spectroscopy B Surface EXAFS, soft X-ray spectroscopy D Characterization of optical elements used in the VSX region	Y. Kitajima Y. Kitajima K. Ito
BL-12	C XAFS	H. Nitani

Experimental Station	Person in Charge
BL-13 (Undulator) A Soft X-ray photoemission spectroscopy and XAFS	K. Mase
BL-14 (Vertical Wiggler) A Crystal structure analysis and detector development B High-precision X-ray optics C Medical applications and General purpose (X-ray)	S. Kishimoto K. Hirano K. Hyodo
BL-15 A*** Small-angle X-ray scattering of muscle and alloys B1 White X-ray topography and X-ray experiments for general purpose B2 Surface and interface X-ray diffraction C High-resolution X-ray diffraction	N. Igarashi H. Sugiyama H. Sugiyama K. Hirano
BL-16 (Variable Polarization Undulator) A Soft X-ray spectroscopies with circular and linear polarization	K. Amemiya
BL-17 (Short Gap Undulator) A Macromolecular crystallography	N. Igarashi
BL-18 A Angle-resolved photoelectron spectroscopy of surfaces and interfaces(◆) B Multipurpose monochromatic hard X-ray station(◆) C High pressure X-ray powder diffraction (DAC)(♣)	K. Yaji [ISSP], A. Yagishita M. Mukhopadhyay[India, DST], N. Igarashi S. Nakano[NIMS], T. Kikegawa
BL-19 (Revolver Undulator) A Spin-resolved photoelectron spectroscopy (Mott detector)(◆) B Soft X-ray emission spectroscopy(◆)	K. Yaji [ISSP], A. Yagishita K. Yaji [ISSP], A. Yagishita
BL-20 A VUV spectroscopy(◇) B White and monochromatic beam general-purpose X-ray station(◆)	N. Kouchi [Tokyo Inst. Tech], K. Ito J. B. Aitken [ASCo.], H. Kawata
BL-21 [Accelerators Division VII] Beam position monitoring	K. Haga [Accelerators]
BL-27 (Beamline for experiments using radioisotopes) A Radiation biology, soft X-ray photoelectron spectroscopy B Radiation biology, XAFS, X-ray diffuse scattering	N. Usami N. Usami
BL-28 (Elliptical / Helical Undulator) A High-resolution VUV-SX beamline for angle-resolved photoemission B High-resolution VUV-SX spectroscopy	K. Ono K. Ono

- ♣ User group operated beamline
- ◆ External beamline
- ◇ Operated by University
- * shutdown at the end of FY2011
- ** set up at the summer of 2011
- *** shutdwon at the summer of 2011

RCS: Research Center for Spectrochemistry, the University of Tokyo
ISSP: Institute for Solid State Physics, the University of Tokyo
ASCo.: Australian Synchrotron Co-operation

Table 2 List of experimental stations at the PF-AR.

Experimental Station	Person in Charge
AR-NE1 (Multipole Wiggler) A Laser-heating high pressure X-ray diffraction and nuclear resonant scattering (DAC)	T. Kikegawa
AR-NE3 (Undulator) A Macromolecular crystallography	Y. Yamada
AR-NE5 C High pressure and high temperature X-ray diffraction (MAX-80)	T. Kikegawa
AR-NE7 A High pressure and high temperature X-ray diffraction (MAX-III), X-ray Imaging	K. Hyodo
AR-NW2 (Undulator) A XAFS/Dispersive XAFS /Time-resolved-X-ray diffraction	H. Abe
AR-NW10 A XAFS	H. Nitani
AR-NW12 (Undulator) A Macromolecular crystallography	L. Chavas
AR-NW14 (Undulator) A Time-resolved X-ray diffraction, scattering and absorption	S. Adachi

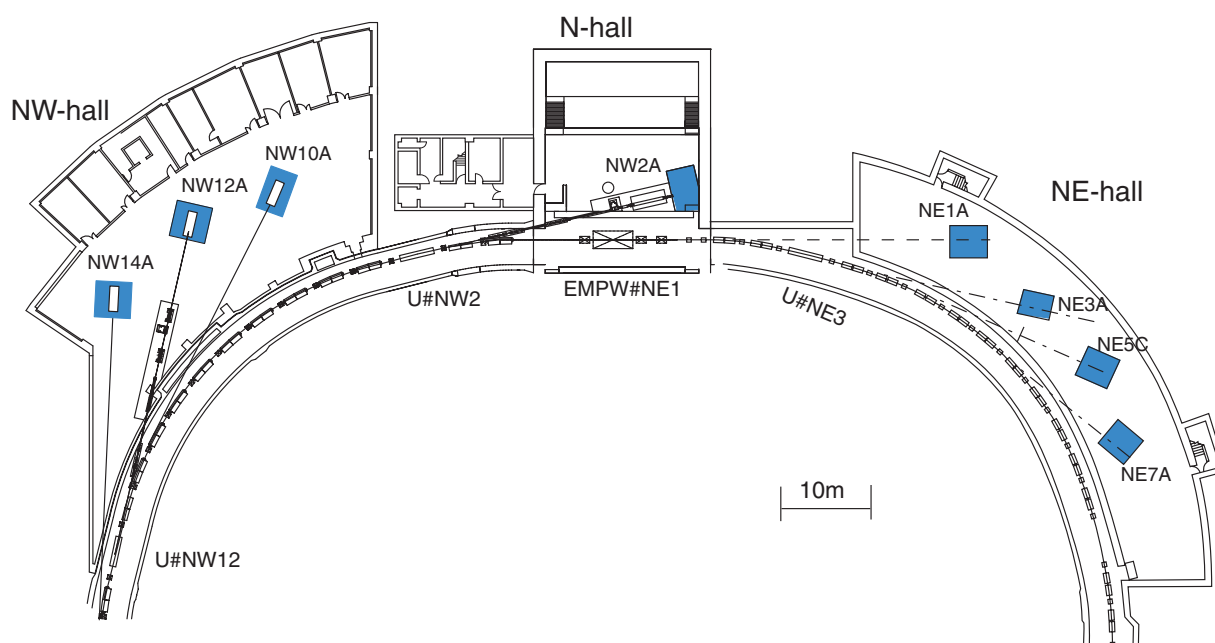


Figure 2 Plan view of beamlines in the PF-AR north-east, north, and north-west experimental halls.

Table 3 Specifications of X-ray beamline optics.

Branch Beamline	Horizontal Acceptance (mrad)	Type of Monochromator	Mirror	Photon Energy (keV)	Beam Size (H×V) (mm)	Photon Flux at Sample Position (/s)	Energy Resolution ($\Delta E/E$)×10 ⁻⁴	Reference
BL-1A	0.2	Channel-cut Si(111) Liquid N ₂ Cooling	Bimorph Si Rh-Coated Si Rh-Coated	4.5 11 ~ 13	0.03×0.01	4×10 ¹¹ @11keV	~ 2	
BL-3A	1	Flat Double Crystal Si(111)	Bent Cylinder	4 ~ 14	0.7×0.2	6×10 ¹²	~ 5	
BL-3C	1.75	Double Crystal Si(111)	None	4 ~ 20 or white	20×6(mono) 0.1×0.1(white)			
BL-4A	6	Double Crystal Sagittal Focusing	Vertical Focusing Mirror	4 ~ 20	50×4 4×1		~ 2	1
BL-4B1	4.5	Double Crystal Si(111)	None	4 ~ 35	50×5		~ 2	2
BL-4B2	4.5	Double Crystal Si(111)	Bent Cylinder	6 ~ 20	13×2		~2	3, 4
BL-4C	2	Flat Double Crystal Si(111)	Bent Cylinder	5 ~ 19	0.7×0.5		~5	5, 6
BL-5A	0.5	Micro-Channel Double Crystal Si(111)	Bent Plane Si Rh-Coated Bent Cylinder Si Rh-Coated	6.5 ~ 17	1.2×0.4	3×10 ¹¹ (0.2×0.2 mm ²)	~2	
BL-6A*	2	Bent Crystal Ge(111) ($\alpha = 8.0^\circ$)	Bent Plane ULE	8.0 (fixed)	0.5×0.2	1.0×10 ¹² /mm ² (8.0 keV, 430 mA)	~ 10	7
BL-6C	2	Flat Double Crystal Si(111)	Bent Cylinder	5 ~ 12 (~25 non-Focus)	1.2×1.2			
BL-7C	4	Double Crystal Si(111) Sagittal Focusing	Double Mirror Fused Quartz Focusing	4 ~ 20 (4 ~ 13)	5×1	1×10 ¹⁰ /6mm ² (8 keV, 300 mA) (1×10 ¹¹ when focused)	~ 2	8 - 10
BL-8A	2.22	Flat Double Crystal Si(111)	Bent Cylinder	5 ~ 19	0.82×0.52	3.2×10 ¹¹ (12.4keV, 400mA)	~ 5	11
BL-8B	2.21	Flat Double Crystal Si(111)	Bent Cylinder	5 ~ 19	0.75×0.45	2.2×10 ¹¹ (12.4keV, 400mA)	~ 5	11

Branch Beamline	Horizontal Acceptance (mrad)	Type of Monochromator	Mirror	Photon Energy (keV)	Beam Size (HxV) (mm)	Photon Flux at Sample Position (/s)	Energy Resolution ($\Delta E/E$) $\times 10^{-4}$	Reference
BL-9A	3	Double Crystal Si (111)	Collimating and Focusing Bent Conical Mirrors (Rh-Coated) Double Flat Mirror (Ni-Coated)	2.2 ~ 15	0.5x0.3	4×10^{11} (9 keV, 300 mA)	2	12, 13
BL-9C	3.5	Double Crystal Si(111)	Bent Cylinder Rh-Coated Si	4 ~ 23	1x1	5×10^{10} (9 keV, 300 mA)	~ 2	
BL-10A	1	Si(111), Si(311) Quartz(100), PG(002) Curved Si(111) ($\alpha \sim 4^\circ, 8^\circ$)	Plane Pt coated Fused Quartz	5 ~ 25	10x3		10 ~ 5	14
BL-10C	4	Double Crystal Si(111)	Bent Cylinder	4 ~ 10	1.2x0.2	$\sim 10^{11}/1.5\text{mm}^2$ (8 keV, 400 mA)	2	7
BL-12C	2	Double Crystal Si(111)	Bent Cylinder Double Flat Mirror (Ni-Coated)	4 ~ 23	0.65x0.4	$5 \times 10^{10}/1\text{mm}^2$ (8 keV, 300mA) w.Si(111)	~ 2	15
BL-14A	1.28 (Vertical)	Double Crystal Si (111) Si (311) Si (553)	Bent Cylinder Rh-coated Fused Quartz	5.1 ~ 19.1 9.9 ~ 35.6 22.7 ~ 84.5	2x1 at focus 5x38		2	16
BL-14B	2.2 (Vertical)	Double Crystal Si(111),	None	10 ~ 57	5x14		2	
BL-14C	1.96 (Vertical)	Double Crystal Si(111), Si(220)	None	5 ~ 100 or white	6x70		2	17, 18
BL-15B1 B2	2	Double Crystal Si (111)	Bent Cylinder	5 ~ 20 or white	0.6x0.4	$10^{11}/1\text{mm}^2$ (8.0keV, 350mA)	~ 2	
BL-15C	2	Double Crystal Si (111)	None	4 ~ 30	60x6			

Branch Beamline	Horizontal Acceptance (mrad)	Type of Monochromator	Mirror	Photon Energy (keV)	Beam Size (H×V) (mm)	Photon Flux at Sample Position (/s)	Energy Resolution ($\Delta E/E$)×10 ⁻⁴	Reference
BL-17A	0.1 ~ 0.2	Double Crystal Si(111) Liquid N ₂ cooling	Bent Plane Si Rh-Coated Bent Plane Si Rh-Coated	6 ~ 9 11 ~ 13	0.25×0.04	10 ¹⁰ (12.4 keV, 450mA, 0.02×0.02mm ²)	~2	19, 20
BL-18B [India, DST]	2	Double Crystal Si(111)	Plane and Bent Cylinder	6 ~ 20			~2	
BL-18C	1	Double Crystal Si(111)	Cylinder Fused Quartz, Pt-coated	6 ~ 25	0.07×0.04		~2	
BL-20B [ASCo.]	2	Channel Cut Si(111) Channel Cut Si(311) Sagittal Focusing Si(111) Double Crystal	None	4.5 ~ 21 10 ~ 36 4.5 ~ 25	25×2 25×1.5 0.6×1		~ 2 ~ 1 ~ 2	21
BL-27B	4	Double Crystal Si(111)	None	4 ~ 20	100×6		~ 2	22
AR-NE1A	0.28	Micro-Channel Double Crystal Si(111), High-resolution Channel Cut Si(4,2,2)&(12,2,2)	Bent Plane W/C Multilayer Coated Si	6 ~ 50	0.1×0.1	6×10 ¹¹ (14.4keV)	~ 2	
AR-NE3A	H:0.2 V:0.1	Double Crystal Si(111) Liquid N ₂ Cooling	Pre-Mirror Bent Flat Si Rh-Coated Post-Mirror Bent Cylinder Fused Quartz Rh-Coated	6.5 ~ 17	0.8×0.2	8×10 ¹¹ (0.2×0.2mm ²)	~ 2	23 24
AR-NE5C	3	Double Crystal Si(111)	None	30 ~ 100 or white	60×5		5	25
AR-NE7A	4	Double Crystal Si(111)	None	25 ~ 50 or white	80×3		5	
AR-NW2A	H:1.0 V:0.2	Double Crystal Si(111) Liquid N ₂ Cooling	Bent Cylinder Si Rh-Coated Bent Flat Si Rh-Coated	5 ~ 25	0.6×0.2 ~10×0.06	6×10 ¹²	~2	26-28
AR-NW10A	1.2	Si(311)	Pt-Coated Bent Cylinder Double Flat Mirror (Rh-Coated)	8 ~ 42	2.2×0.5	1×10 ¹⁰	~1	29

Branch Beamline	Horizontal Acceptance (mrad)	Type of Monochromator	Mirror	Photon Energy (keV)	Beam Size (H×V) (mm)	Photon Flux at Sample Position (/s)	Energy Resolution ($\Delta E/E$)×10 ⁻⁴	Reference
AR-NW12A	H:0.3 V:0.1	Double Crystal Si(111) Liquid N ₂ cooling	Pre-Mirror Bent Flat Si Rh-Coated Post-Mirror Bent Cylinder Si Rh-Coated	6.5 ~ 17	1.3×0.3	2×10 ¹¹ (0.2×0.2 mm ²)	~2	7
AR-NW14A	H:0.3 V:0.1	Double Crystal Si(111) Liquid N ₂ Cooling	Bent Cylinder Rh-Coated Bent Flat Rh-Coated	4.9 ~ 25	0.45×0.25	5×10 ¹²	~2	30

* set up at the summer of 2011

India DST: Department of Science & Technology
ASCo.: Australian Synchrotron Co-operation

REFERENCES

- [1] A. Iida *et al.*, *Rev. Sci. Instrum.*, **66** (1995) 1373.
[2] K. Ohsumi *et al.*, *Rev. Sci. Instrum.*, **66** (1995) 1448.
[3] Powder Diffraction User Group, *KEK Report*, **94-11** (1995).
[4] H. Toraya, H. Hibino and K. Ohsumi, *J. Synchrotron Rad.*, **3** (1996) 75.
[5] H. Iwasaki *et al.*, *Rev. Sci. Instrum.*, **60** (1989) 2406.
[6] *Photon Factory Activity Report 1995*, **#13** (1996) E-1.
[7] N. Igarashi *et al.*, *J. Phys.: Conf. Ser.*, **272** (2011) 012026
[8] M. Nomura and A. Koyama, *KEK Internal*, **93-1** (1993).
[9] M. Nomura *et al.*, *KEK Report*, **91-1** (1991).
[10] M. Nomura and A. Koyama, in "X-ray Absorption Fine Structure", ed. by S. S. Hasnain, Ellis Horwood, Chichester, (1991) 667.
[11] A. Nakao *et al.*, *AIP Conf. Proc.*, **1234** (2010) 367.
[12] M. Nomura and A. Koyama, *J. Synchrotron Rad.*, **6** (1999) 182.
[13] M. Nomura and A. Koyama, *Nucl. Instrum. Meth.*, **A467-468** (2001) 733.
[14] S. Sasaki, *Rev. Sci. Instrum.*, **60** (1989) 2417.
[15] M. Nomura and A. Koyama, *KEK Report*, **95-15** (1996).
[16] Y. Satow and Y. Iitaka, *Rev. Sci. Instrum.*, **60** (1989) 2390.
[17] *Photon Factory Activity Report 1999*, **#17** (2000) A 92.
[18] *Photon Factory Activity Report 1999*, **#17** (2000) A 103.
[19] N. Igarashi *et al.*, *AIP Conf. Proc.*, **879** (2007) 812.
[20] N. Igarashi *et al.*, *J. Synchrotron Rad.*, **15** (2008) 292.
[21] R.F. Garret *et al.*, *Rev. Sci. Instrum.*, **66** (1995) 1351.
[22] H. Konishi *et al.*, *Nucl. Instrum. Meth.*, **A372** (1996) 322.
[23] Y. Yamada *et al.*, *AIP Conf. Proc.*, **1234** (2010) 415.
[24] M. Hiraki *et al.*, *AIP Conf. Proc.*, **1234** (2010) 673.
[25] T. Kikegawa *et al.*, *Rev. Sci. Instrum.*, **66** (1995) 1335.
[26] T. Mori *et al.*, *AIP Conf. Proc.*, **705** (2004) 255.
[27] H. Kawata *et al.*, *AIP Conf. Proc.*, **705** (2004) 663.
[28] Y. Inada *et al.* *AIP Conf. Proc.*, **879** (2007) 1230.
[29] M. Nomura *et al.*, *AIP Conf. Proc.*, **882** (2007) 896.
[30] S. Nozawa *et al.*, *J. Synchrotron Rad.*, **14** (2007) 313.

Table 4 Specifications of VUV and soft X-ray beamline optics.

Beamline	Acceptance $H \times V$ (mrad) or Undulator Parameters	Type of Monochromator	Groove Density (ℓ/mm)	Energy Range (eV)	Beam Size $H \times V$ (mm)	Resolving Power ($E/\Delta E$) Photon Flux (photons/s)	Reference
BL-2A Undulator	$K = 0.5 \sim 2.2$ $\lambda_u = 6 \text{ cm}$	Double Crystal InSb (111), Si (111)	—	1740 ~ 5000	$< 1\phi$	2000, 8000 10^{11}	1 - 4
BL-2C Undulator	$K = 0.55 \sim 2.2$ $\lambda_u = 6 \text{ cm}$	Varied-Line-Space Plane Grating	1000 2200	250 ~ 1400	0.9×0.1	5000 ~ 10000 $10^{11} \sim 10^{10}$	5 - 7
BL-3B	10×2	Grazing Incidence $R = 24 \text{ m}$ $\alpha + \beta = 165^\circ$ 1800	200 600	10 ~ 280	$< 2\phi$	200 ~ 3000 $10^{12} \sim 10^9$	8, 9
BL-7A [RCS]	6×1	Varied-Line-Space Plane Grating	300 650	50 ~ 1300	2.5×0.5	1000 ~ 9000 $10^{12} \sim 10^9$	10
BL-11A	5×1	Varied-Line-Space Plane Grating	300 800 1200	70 ~ 1900	2×1	500 ~ 5000 $10^{12} \sim 10^9$	11 - 14
BL-11B	4×0.6	Double Crystal InSb (111), Si (111)	—	1724 ~ 5000	5×2	2000 10^{10}	3, 15, 16, 17
BL-11D	4×2	Grazing Incidence Varied Deviation-angle On-Blaze Mount $R_1 = 52.5 \text{ m}$ $R_3 = 22.5 \text{ m}$	2400	60 ~ 245 200 ~ 900	1×0.1	2000 10^{11}	18
BL-13A Undulator	$K_{\text{max}} = 8$ $\lambda_u = 18 \text{ cm}$	Variable-included-angle Varied-line-spacing plane grating	300 1000	30 ~ 330 100 ~ 1200	$\sim 0.2 \times 0.04$	4000 ~ 10000 $10^{12} \sim 10^9$	19 20
BL-16A Undulator	$K_{\text{max}} = 2.37$ (Circular Polarization) $K_{\text{max}} = 3.12$ (Horizontal Linear Polarization) $K_{\text{max}} = 1.98$ (Vertical Linear Polarization) $K_{\text{max}} = 1.73$ (45-deg Linear Polarization) $\lambda_u = 5.6 \text{ cm}$	Variable-included-angle varied-line-spacing plane grating	500 1000	250 ~ 1500	$\sim 0.2 \times 0.1$	4000 ~ 8000 $10^{12} \sim 10^{11}$	21
BL-18A [ISSP]	2×2	Grazing Incidence $R = 3 \text{ m}$ $\alpha + \beta = 160^\circ$ $R = 6.65 \text{ m}$ $\alpha + \beta = 167.5^\circ$	300 600 1200	15 ~ 150	$< 1\phi$	1000~2000 $10^{11} \sim 10^9$	22

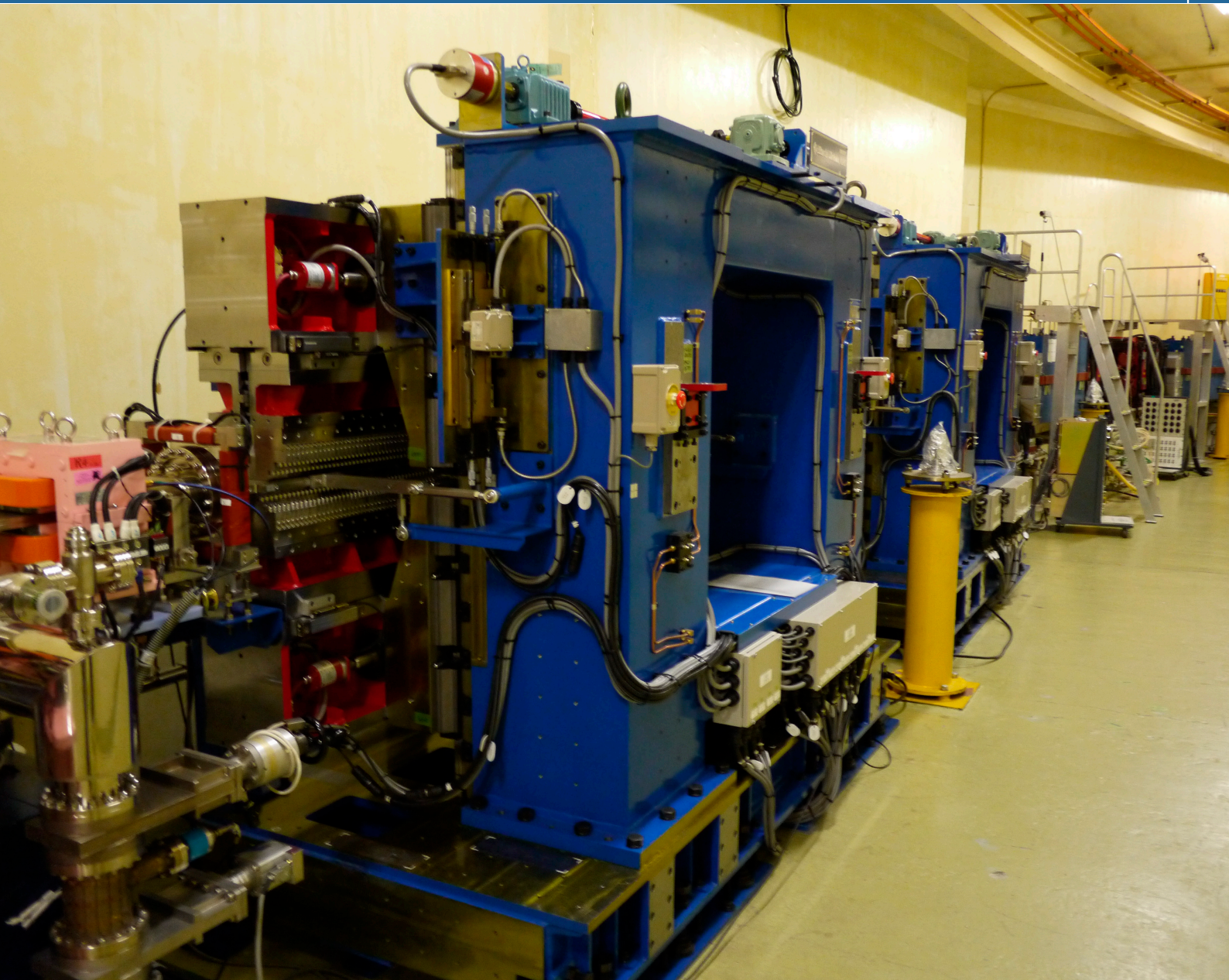
Beamline	Acceptance $H \times V$ (mrad) or Undulator Parameters	Type of Monochromator	Groove Density (ℓ/mm)	Energy Range (eV)	Beam Size $H \times V$ (mm)	Resolving Power ($E/\Delta E$) Photon Flux (photons/s)	Reference
BL-19A Revolver Undulator [ISSP]	$K = 1.0 \sim 9.0$ $\lambda_u = 16.4 \text{ cm}$ $K = 0.5 \sim 1.25$ $\lambda_u = 5 \text{ cm}$ $K = 0.5 \sim 2.5$ $\lambda_u = 7.2 \text{ cm}$	Grazing Incidence $R = 2 \text{ m}$ $\alpha + \beta = 160^\circ$ $R = 4 \text{ m}$ $\alpha + \beta = 170^\circ$	600 1200 600 1200	12 ~ 250	$< 0.7\phi$	1000 10^{12}	23, 24
BL-19B Revolver Undulator [ISSP]	$K = 1.0 \sim 5.0$ $\lambda_u = 10 \text{ cm}$	Varied-Line-Space Plane Grating	800 2400	10 ~ 1200	$< 0.5\phi$	400-4000 $10^{12} \sim 10^{11}$	24 - 26
BL-20A	28×5	3m Normal Incidence	1200 2400	5 ~ 40	2×1	300 ~ 30000 $10^{12} \sim 10^8$	27
BL-27A	5×0.5	Double Crystal InSb (111)	—	1800 ~ 4000		2000	28
BL-28A/B Helical Undulator	$K_x = 0.23 \sim 3$ $K_y = 0.23 \sim 6$ $\lambda_u = 16 \text{ cm}$	Varied-Line-Space Plane Grating	400	30 ~ 300	0.15×0.05	30000 10^{12}	29

RCS: Research Center for Spectrochemistry, the University of Tokyo
ISSP: Institute for Solid State Physics, the University of Tokyo

REFERENCES

- [1] H. Maezawa *et al.*, *Nucl. Instrum. Meth.*, **A246** (1986) 310.
[2] Y. Kitajima *et al.*, *Rev. Sci. Instrum.*, **63** (1992) 886.
[3] Y. Kitajima, *J. Elec. Spec. Relat. Phenom.*, **80** (1996) 405.
[4] Y. Kitajima, *J. Synchrotron Rad.*, **6** (1999) 167.
[5] Y. Yan and A. Yagishita, *KEK Report*, **95-9** (1995).
[6] M. Watanabe *et al.*, *Proc. SPIE*, **3150** (1997) 58.
[7] M. Watanabe *et al.*, *Nucl. Instrum. Meth.*, **A467-468** (2001) 512.
[8] A. Yagishita *et al.*, *Nucl. Instrum. Meth.*, **A306** (1991) 578.
[9] S. Masui *et al.*, *Rev. Sci. Instrum.*, **63** (1992) 1330.
[10] K. Amemiya *et al.*, *J. Elec. Spectrosc. Relat. Phenom.*, **124** (2002) 151.
[11] K. Amemiya *et al.*, *J. Synchrotron Rad.*, **3** (1996) 282.
[12] K. Amemiya *et al.*, *Proc. SPIE Proceedings*, **3150** (1997) 171.
[13] Y. Kitajima *et al.*, *J. Synchrotron Rad.*, **5** (1998) 729.
[14] Y. Kitajima *et al.*, *J. Elec. Spectrosc. Relat. Phenom.*, **101-103** (1999) 927.
[15] T. Ohta *et al.*, *Nucl. Instrum. Meth.*, **A246** (1986) 373.
[16] M. Funabashi *et al.*, *Rev. Sci. Instrum.*, **60** (1989) 1983.
[17] T. Iwazumi *et al.*, *Rev. Sci. Instrum.*, **66** (1995) 1691.
[18] *Photon Factory Activity Report 1997*, #15 (1998) A 101.
[19] K. Mase *et al.*, *AIP Conf. Proc.*, **1234** (2010) 703.
[20] A. Toyoshima *et al.*, *J. Vac. Soc. Jpn.*, **54** (2011) 580.
[21] K. Amemiya *et al.*, *AIP Conf. Proc.*, **1234** (2010) 295.
[22] S. Suzuki *et al.*, *Activity Report of SRL-ISSP*, **60** (1989).
[23] A. Kakizaki *et al.*, *Rev. Sci. Instrum.*, **60** (1989) 1893.
[24] A. Kakizaki *et al.*, *Rev. Sci. Instrum.*, **63** (1992) 367.
[25] M. Fujisawa *et al.*, *Nucl. Instrum. Meth.*, **A467-468** (2001) 309.
[26] M. Fujisawa *et al.*, *Nucl. Instrum. Meth.*, **A467-468** (2001) 313.
[27] K. Ito *et al.*, *Rev. Sci. Instrum.*, **66** (1995) 2119.
[28] H. Konishi *et al.*, *Nucl. Instrum. Meth.*, **A372** (1996) 322.
[29] K. Amemiya and T. Ohta, *J. Synchrotron Rad.*, **11** (2004) 171.

Accelerators



ACCELERATORS

1. Outline of the Accelerators	97
2. PF Ring	100
2-1 Operation Summary	
2-2 ID16 Bump	
2-3 Introduction of Hybrid Filling Mode	
2-4 Development of Optical Fiber Beam Loss Monitor for the Photon Factory	
2-5 Project to Renew the Insertion Devices at the PF Ring	
3. PF-AR	108
3-1 Operation Summary	
3-2 Update of SX Magnet Power System	

Two electron storage rings, the PF-ring and the PF-AR, as dedicated light sources were stably operated at the Photon Factory. The KEK linear accelerator with maximum electron energy of 8 GeV is used to inject electron beams into the rings. The full-energy injection of 2.5 GeV is carried out at the PF-ring, while the injection energy of 3 GeV is increased to the operation energy of 6.5 GeV at the PF-AR.

The machine parameters of the rings and the calculated spectral performances are listed in Table 1 and Table 2, respectively. The spectral distributions of synchrotron radiation (SR) from the bending magnets and the insertion devices are shown in Fig. 1.

In FY2011, the PF-ring was predominantly operated in multi-bunch mode with the energy of 2.5 GeV, while it was run in the single-bunch mode for a one-week period and the hybrid mode for a one-week period. In their modes, top-up operation was carried out with a beam current of 450.0 ± 0.1 mA, 50.0 ± 0.1 mA, and 450.0 ± 0.1 mA, respectively.

Although regular operations before the summer shutdown were stopped due to the Great East Japan Earthquake, scheduled operations have been conducted with difficulty since autumn.

Table 1 Principal beam parameters of the PF ring and PF-AR.

	PF	PF-AR
Energy	2.5 GeV	6.5 GeV
Natural emittance	34.6 nm rad	293 nm rad
Circumference	187 m	377 m
RF frequency	500.1 MHz	508.6 MHz
Bending radius	8.66 m	23.2 m
Energy loss per turn	0.4 MeV	6.66 MeV
Damping time		
Vertical	7.8 ms	2.5 ms
Longitudinal	3.9 ms	1.2 ms
Natural bunch length	10 mm	18.6 mm
Momentum compaction factor	0.00644	0.0129
Natural chromaticity		
Horizontal	-12.9	-14.3
Vertical	-17.3	-13.1
Stored current	450 mA	60 mA
Number of bunches	252	1
Beam lifetime	30-35 hr (at 450 mA)	20-25 hr (at 60 mA)

Table 2

Calculated spectral performances of the bend source and all the insertion devices at the PF ring (2.5 GeV, 450 mA) and the PF-AR (6.5 GeV, 60 mA). λ_u : period length, N : number of the periods, L : length of undulator or wiggler, $G_x(G_y)$: minimum vertical (horizontal) gap height, $B_x(B_y)$: maximum vertical (horizontal) magnetic field, Type of magnet, H: hybrid configuration, S.C.: super conducting magnet, σ_x, σ_y : horizontal or vertical beam size, σ_x, σ_y : horizontal or vertical beam divergence, $K_x(K_y)$: vertical (horizontal) deflection parameter, D : photon flux density (photons/sec/mm²/mrad²/0.1%b.w.), B : brilliance (photons/sec/mm²/mrad²/0.1%b.w.), P_T : total radiated power. Different operating modes of undulator and wiggler are denoted by -U and -W, respectively.

Name	E/I GeV/mA	λ_u cm	N	L m	$G_x(G_y)$ cm	$B_x(B_y)$ T	Type of magnet	σ_x mm	σ_y mm	σ_x mrad	σ_y mrad	$K_x(K_y)$	ϵ_1/ϵ_c keV	D	B	P_T kW
PF 2.5/450																
Bend								0.41	0.059	0.178	0.012		4	5.38E+13	3.48E+14	
SGU#01		1.2	39	0.5	0.4	0.7	P(NdFeB)	0.6	0.012	0.088	0.029	0.78		4.56E+16	9.90E+17	0.4
U#02		6	60	3.6	2.8	0.4	H(NdFeB)	0.65	0.042	0.054	0.008	2.3		2.73E+17	1.55E+18	1.07
SGU#03		1.8	26	0.5	0.4	1	P(NdFeB)	0.6	0.012	0.088	0.029	1.68		2.50E+16	5.44E+17	0.82
MPW#05-W		12	21	2.5	2.64	1.4	H(NdFeB)	0.71	0.045	0.078	0.009	16	5.9	2.22E+15	1.10E+16	8.83
MPW#13-W		18	13	2.5	2.71	1.5	H(NdFeB)	0.74	0.02	0.094	0.019	25	6.2	1.45E+15	1.47E+16	9.73
MPW#13-U												2		1.70E+16	1.57E+17	0.06
VW#14					5	5	S.C.	0.53	0.045	0.128	0.008		20.8	5.42E+13	3.59E+14	
U#16-1 & 16-2		5.6	44	2.5	2.1	0.6(0.38)	P(NdFeB)	0.654	0.042	0.055	0.008	3(2)		1.03E+18	1.82E+17	0.88
SGU#17		1.6	29	0.5	0.4	0.92	P(NdFeB)	0.6	0.012	0.088	0.029	1.37		7.88E+15	1.71E+17	0.69
Revolver#19		5	46	3.6	2.8	0.28	H(NdFeB)	0.7	0.045	0.078	0.009	1.3		1.31E+17	6.48E+17	0.31
		7.2	32			0.4	H(NdFeB)					2.7		7.17E+16	3.52E+17	0.63
		10	23			0.54	H(NdFeB)					5		4.53E+16	2.22E+17	1.15
		16.4	14			0.62	P(NdFeB)					9.5		2.02E+16	9.81E+16	1.52
EMPW#28-U		16	12	1.92	3(11)		P(NdFeB)	0.53	0.045	0.127	0.008	3(3)		1.55E+16	1.00E+16	0.26
PF-AR 6.5/60																
Bend								1	0.2	0.593	0.036		26	3.25E+13	2.59E+13	
EMPW#NE1W		16	21	3.36	3(11)	1(0.2)	P(NdFeB)	1.07	1.07	0.268	0.032	15(3)	28(90%)	1.53E+15	2.12E+15	5.52
EMPW#NE1U												3(3)		3.41E+15	4.70E+15	0.42
U#NE3		4	90	3.6	1	0.8	P(NdFeB)	1.57	0.17	0.312	0.029	3		1.08E+16	6.39E+15	3.708
U#NW2		4	90	3.6	1	0.8	P(NdFeB)	1.57	0.17	0.312	0.029	3		1.08E+16	6.39E+15	3.708
U#NW12		4	95	3.8	1	0.8	P(NdFeB)	1.57	0.17	0.312	0.029	3		1.08E+16	6.39E+15	3.912
U#NW14-36		3.6	79	2.8	1	0.8	P(NdFeB)	1.35	0.14	0.338	0.036	2.8		6.41E+15	5.41E+15	3.12
U#NW14-20		2	75	1.5	0.8	0.63	P(NdFeB)	0.75	0.07	0.383	0.038	1.17		6.41E+15	5.41E+15	0.936

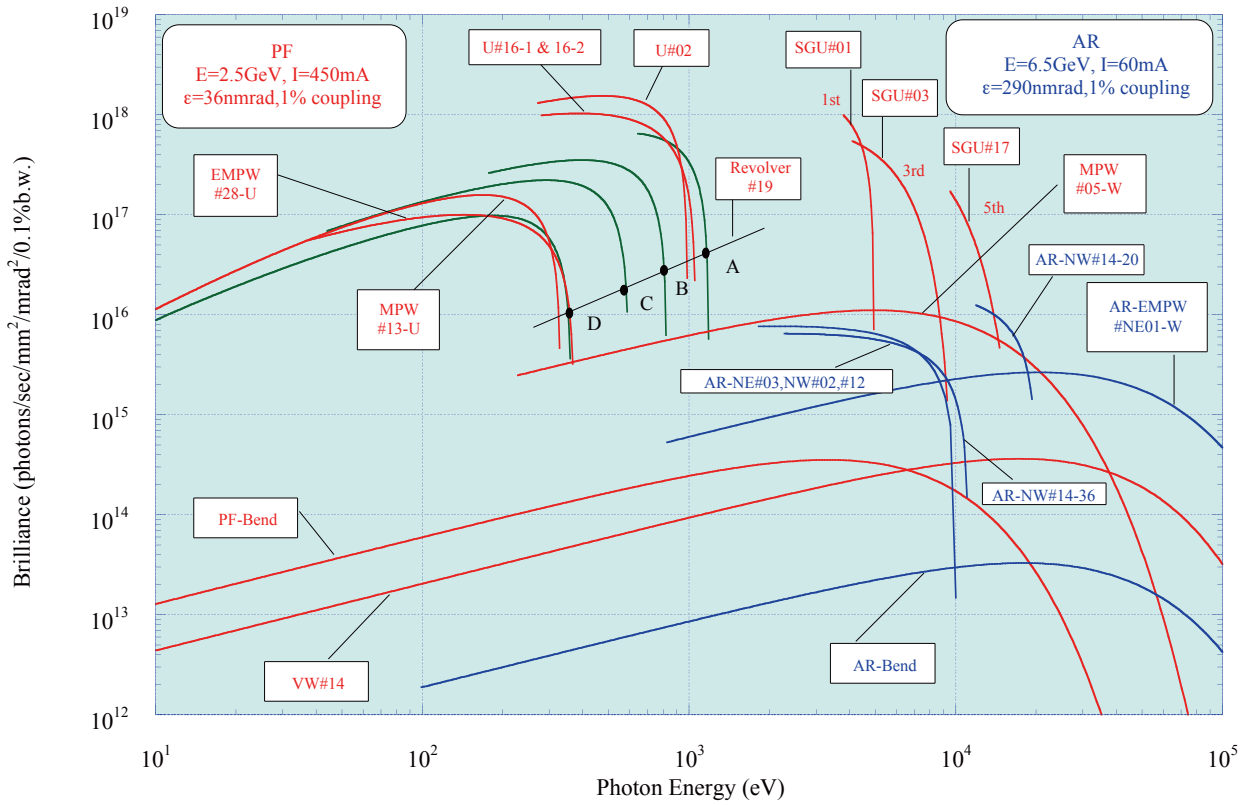


Figure 1
 Synchrotron radiation spectra available at the PF Storage Ring (2.5 GeV) and the AF-AR (6.5 GeV). Brilliance of the radiation vs. photon energy are denoted by red curves for the insertion devices, SGU#01, U#02, SGU#03, MPW#05, MPW#13, VW#14, U#16-1 & 16-2, SGU#17, Revolver#19 and EMPW#28, and bending magnets (PF-Bend) at the PF Storage Ring. Blue curves denote those for the insertion devices, EMPW#NE01, U#NE03, U#NW02, U#NW12, U#NW14-36 and U#NW14-20, and the bending magnets (AR-Bend) at the PF-AR. The name of each source is assigned in Table 2. Several insertion devices have both undulator and wiggler modes, which are denoted by u and w, respectively (the undulator mode of MPW#05 and AR-EMPW#NE01 is not shown). The spectral curve of each undulator (or undulator mode of multipole wiggler) is a locus of the peak of the first harmonic within the allowance range of K parameter. For SGU#01, SGU#03 and SGU#17, spectra are shown for the first, third and fifth harmonic regions. Spectra of Revolver#19 are shown for four kinds of period.

2-1 Operation Summary

When the Tohoku earthquake struck on March 11, 2011, the PF-ring had already been shut down as scheduled in the morning. Fortunately, no personnel were injured, and no fires were reported in the PF facilities in the immediate aftermath of the first series of strong earthquakes. The most serious damage to the accelerators was the collapse of quadrupole magnets in the Linac. Consequently, some beam ducts were fractured, and most of the 600-m Linac was exposed to the air. At the PF-ring, one of the vacuum bellows broke and half of the ring was exposed to the air. Details of the earthquake damage and the results of the magnet level survey were reported in Ref. [1]. Temporary recovery of the beam duct was accomplished quickly, and trial operation started in mid-May. The user time scheduled from May to July was cancelled, and was resumed in October 2011.

The timetable of the PF ring and PF-AR operations in FY2011 is shown in Fig. 1. The operation statistics of the PF ring are summarized in Table 1. The statistics for each fiscal year since the commencement of accelerator operation are shown in Fig. 2. The total operation time and actual user time were 4696.0 h and 2809.2 h, respectively. Before the summer shutdown, machine and beamline studies had to be carried out for recalibration, which was necessary after the earthquake; the operation time necessary for these studies was calculated to be 805.2 h. The failure time for this year was 11.7 h, and the failure percentage is shown in Fig. 3. Even in the latter half of FY2011, from October 2011 to March 2012, frequent aftershocks continued in east Japan. Sometimes the beam was dumped by the quake, and sometimes we stopped the beam operation and made a patrol of the ring tunnel according to KEK's safety rules. The number of failures caused by the earthquakes amounted to four or five in FY2011.

In the trial beam operation from May to July, an abnormal rise in vacuum pressure occurred when the single-bunch high-current beam was stored. The elastomer O-ring and the valve disc changed color due to heating as shown in Fig. 4. The RF shield mechanism became incomplete due to the earthquake and an abnormal higher order mode loss occurred in the gate valve. We removed all gate valves of the same type from the storage ring during the maintenance period in 2011. After removal of these gate valves, the quadrupole-mode longitudinal instability disappeared at a regular stored current of 450 mA; the insufficient RF shield presumably made them high impedance sources. Since we have been able to suppress the longitudinal instability without RF phase modulation, the effective brightness of SR beams has been stably improved, especially from the undulators located at the section that has a finite dispersion function [2].

In the PF-ring, the top-up operation mode was fixed as the normal operation mode. The beam current was usually maintained at 450.0 ± 0.1 mA, which corresponded to a current accuracy of $\pm 1 \times 10^{-4}$ at an injection repetition frequency of 2.0 Hz using a pulsed sextupole magnet. User operation of the hybrid mode was conducted for the first time, with a single-bunch current of 50 mA and a multi-bunch current of 400 mA. In addition, the variably polarized undulator was operated at a switching frequency of 10 Hz. Orbit correction using the feed-forward method allowed us to reduce the orbit fluctuation during the switching process to less than a few micrometers.

REFERENCES

- [1] T. Honda, et al., *Proc. IPAC'11* (2011) 2984.
- [2] *PF Activity Report 2008*, **26** (2010) 124.

Table 1 Operation statistics for PF ring in FY2011.

	Total
Ring operation time (h)	4696.0
Actual user time (h)	2809.2
Machine & BL study	805.2
Machine adjustment time (h)	1069.9
Failure time (h)	11.7

	SUN	MON	TUE	WED	THU	FRI	SAT	SUN	MON	TUE	WED	THU	FRI	SAT	SUN	MON	TUE	WED	THU	FRI	SAT
	9 17	9 17	9 17	9 17	9 17	9 17	9 17	9 17	9 17	9 17	9 17	9 17	9 17	9 17	9 17	9 17	9 17	9 17	9 17	9 17	9 17
Date	5.1	2	3	4	5	6	7	8	9	10	11	12	13	14	15	16	17	18	19	20	21
PF																					
AR																					
Date	22	23	24	25	26	27	28	29	30	31	6/1	2	3	4	5	6	7	8	9	10	11
PF																					
AR																					
Date	12	13	14	15	16	17	18	19	20	21	22	23	24	25	26	27	28	29	30	7/1	2
PF																					
AR																					
Date	3	4	5	6	7	8	9	10													
PF																					
AR																					
Date	9.18	19	20	21	22	23	24	25	26	27	28	29	30	10/1	2	3	4	5	6	7	8
PF																					
AR																					
Date	9	10	11	12	13	14	15	16	17	18	19	20	21	22	23	24	25	26	27	28	29
PF																					
AR																					
Date	30	31	11/1	2	3	4	5	6	7	8	9	10	11	12	13	14	15	16	17	18	19
PF																					
AR																					
Date	20	21	22	23	24	25	26	27	28	29	30	12/1	2	3	4	5	6	7	8	9	10
PF																					
AR																					
Date	11	12	13	14	15	16	17	18	19	20	21	22									
PF																					
AR																					
Date	1.15	16	17	18	19	20	21	22	23	24	25	26	27	28	29	30	31	2/1	2	3	4
PF																					
AR																					
Date	5	6	7	8	9	10	11	12	13	14	15	16	17	18	19	20	21	22	23	24	25
PF																					
AR																					
Date	26	27	28	29	3/1	2	3	4	5	6	7	8	9	10	11	12	13	14	15	16	17
PF																					
AR																					

PF: PF ring

AR: PF-AR

- Tuning and ring machine study
- Ring machine study
- Machine & BL study
- Short maintenance and /or machine study
- Experiment using SR
- Single bunch operation at 2.5 GeV
- Hybrid operation

Figure 1
Timetable of PF ring and PF-AR operation in FY2011.

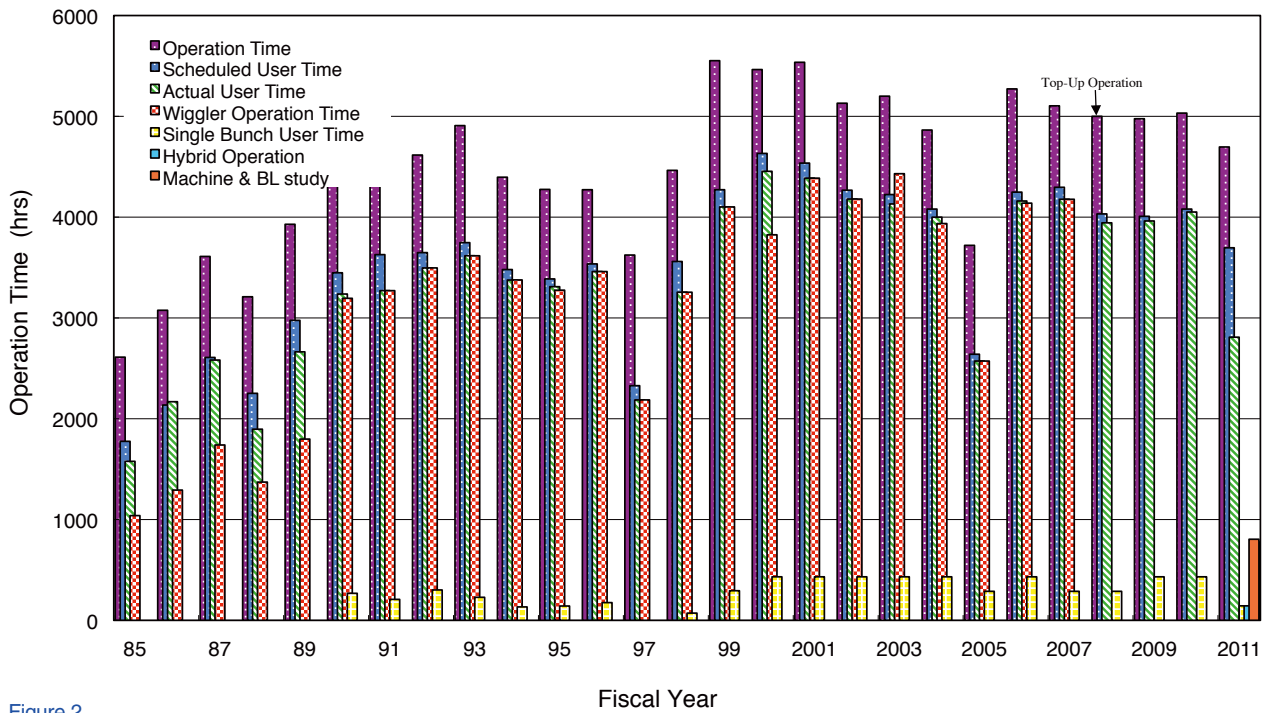


Figure 2 Total operation time, scheduled user time, actual user time, user times of various operation modes, and operation time of the machine and beamline study for PF ring in each fiscal year since commencement of accelerator operation.

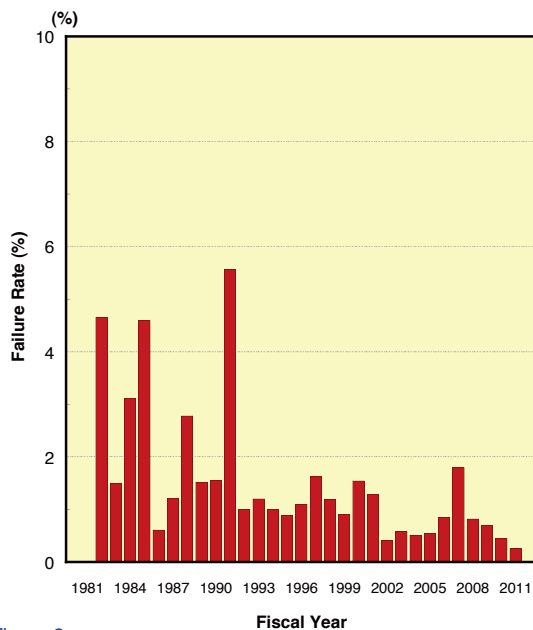


Figure 3 Failure rate for PF ring (percentage of failure time with respect to total operation time).

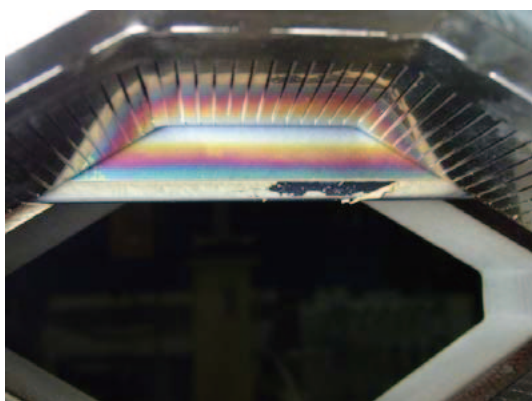


Figure 4 Gate valve damaged by trouble of the RF-shield mechanism.

2-2 ID16 Bump

At the long straight section of 8.9-m length between B15 and B16 at the PF ring, two APPLE-II type undulators were installed with five identical fast bump magnets. The fast local bump achieves fast helicity switching, and is a good method for measuring the photon helicity-dependence of materials like circular and linear dichroism using a lock-in technique. The designed bump frequency is 10 Hz and the required bump angle is 0.3 mrad to separate photons from the two undulators.

In order to achieve user runs with fast local bump, the unwanted beam oscillation around the ring should be suppressed to smaller than 1/10 of the beam size, which is about 30 μm for the horizontal direction and 3 μm for the vertical direction. After system adjustment with feed-forward correction, the 10-Hz beam disturbance was kept small around the ring as shown in Fig. 5. During the test operation on December 8, 2011, all users were asked to measure the effect of the beam disturbance by the 10-Hz fast local bump. The magnitudes of the measured disturbances were most similar to those of the top-up injection for some beamlines, and so permission was given to make the 10-Hz fast local bump during normal user runs. User runs with the 10-Hz bump were conducted during the following periods in FY2011:

- 09:00, Jan. 19 to 09:00, Jan. 23 (for long-term test)
- 21:00, Feb. 22 to 09:00, Feb. 23
- 09:00, Mar. 9 to 08:30, Mar. 12

Operation of the 10-Hz bump was usually started at 08:30 and stopped at 20:30, which are the times of

PF-AR injection and mode change of other insertion devices when small orbit distortions are permitted. The DC orbit distortions shown in Fig. 6 are unavoidable when starting and stopping operation, and future machine studies will examine ways of suppressing these distortions.

During the 10-Hz operation, the users of BL-16 can freely change the parameters ρ and ϕ of ID16-1 and

ID16-2, and can freely decide to start and stop operation at two fixed times of the day during fast bump user time. The parameters of the bump kickers and feed-forward system are fixed at the beginning of the run and no adjustments are required for several months.

User runs of the 10-Hz fast bump and machine studies for improvements will continue in 2012.

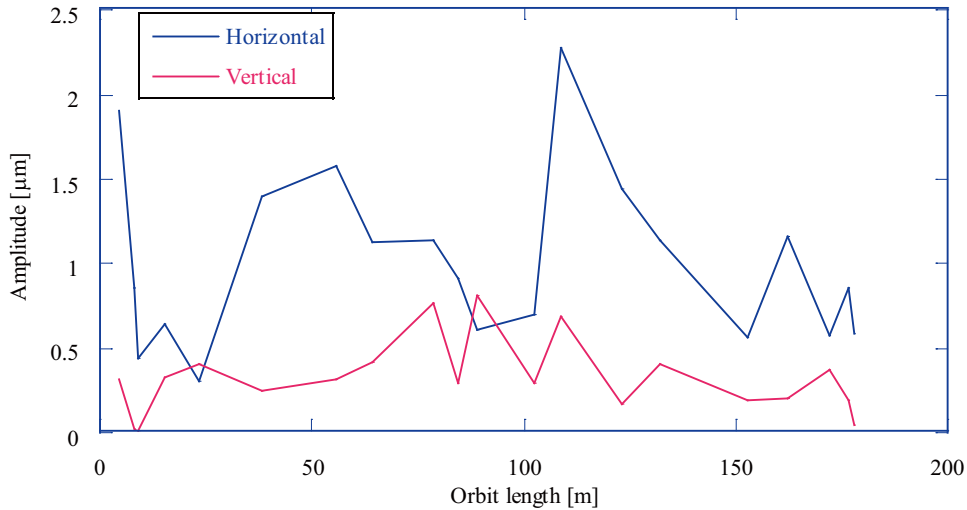


Figure 5 Amplitude of the unwanted 10-Hz beam oscillation around the ring during the 10-Hz fast bump operation.

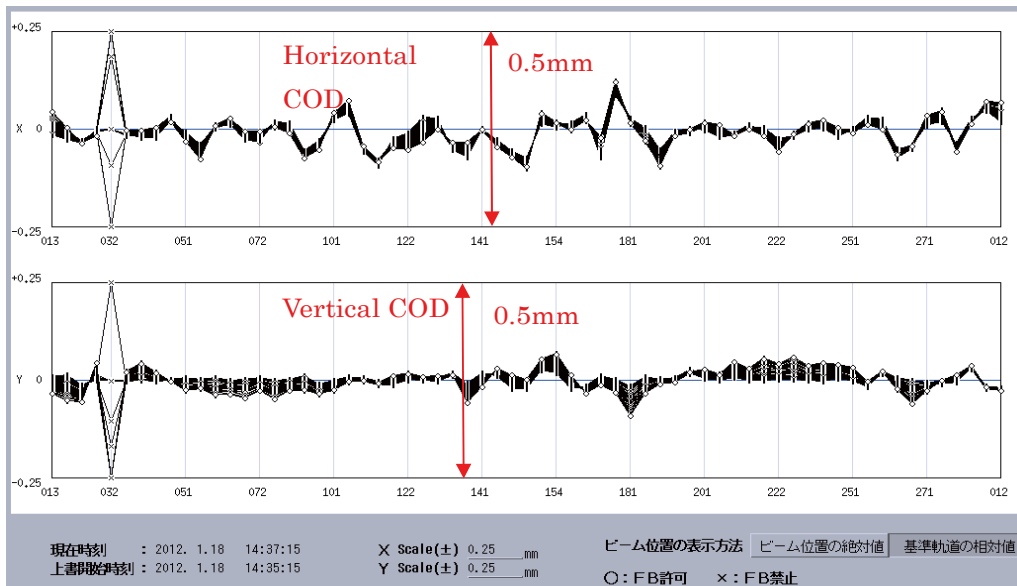


Figure 6 Test measurements of the temporal DC COD change upon starting or stopping the 10-Hz fast bump without vertical fast orbit feedback. For user runs, the vertical changes are much smaller due to the vertical fast orbit feedback correction.

2-3 Introduction of Hybrid Filling Mode

The hybrid filling pattern, which consists of short bunch trains and high-current single bunches, enables us to share the use of limited machine time between multi-bunch and single-bunch users. At the PF-ring, the feasibility of this attractive operation mode has been studied since October 2008 with the development of a free-rotation mechanical light chopper [3, 4]. As the result of resolving technical problems [5] and two joint studies with SR users, user operation with the hybrid filling pattern was achieved in February 2012. This is the first time hybrid operation has been introduced in the PF-ring.

Figure 7 shows the filling pattern in the hybrid mode measured with a beam position monitor. The pattern is composed of 130 low-current bunches ($3.1 \text{ mA/bunch} \times 130 = 400 \text{ mA}$) and a high-current single bunch (50 mA/bunch) located on the opposite side of the ring from the bunch train. A total stored current of 450 mA is achieved, the same as usual multi-bunch operation. We succeeded in maintaining the hybrid filling pattern for six days by the flexible top-up injection [6] without any trouble. The coupled-bunch instabilities in the multi-bunch component were completely suppressed by using a bunch-by-bunch feedback system [7]. The single-bunch impurity was kept below 10^{-6} by a gated RF-knockout. Figure 8 compares temperature distributions along the ring between the hybrid and usual single-bunch operations. These distributions are similar to each other with the exception of temperatures around the ceramic duct for the RF-Q magnet and the bellows duct downstream of VW#14. The RF-Q ceramic duct where a relatively large amount of heat generation was observed is scheduled to be removed during the summer maintenance of 2012. A streak image of the hybrid filling pattern is shown in Fig. 9. The RMS bunch lengths of the multi-bunch and single-bunch components were measured to be 37 ps and 56 ps, respectively. The lifetimes of each component were also measured to be around 9 hours and 2 hours, respectively: the lifetime of the single-bunch component is much shorter than that of the multi-bunch component due to the Touschek effect. We will modify the contents of the hybrid operation based on evaluations and requests of users.

REFERENCES

- [3] K. Ito, F. Penent, Y. Hikosaka, E. Shigemasa, I. Suzuki, J. Eland and P. Lablanquie, *Rev. Sci. Instrum.*, **80** (2009) 123101.
- [4] *Photon Factory Activity Report 2008*, #26 (2010) A125.
- [5] R. Takai, T. Obina, Y. Tanimoto, T. Honda, M. Shimada, Y. Kobayashi and T. Mitsuhashi, *Proc. IPAC'10* (2010) 2564.
- [6] *Photon Factory Activity Report 2009*, #27 (2011) A114.
- [7] *Photon Factory Activity Report 2009*, #27 (2011) A113.

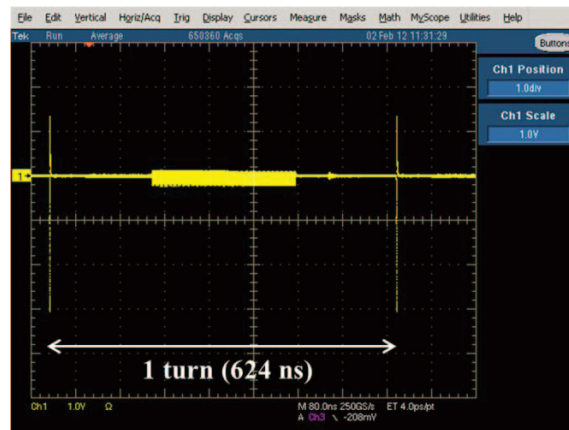


Figure 7 Hybrid filling pattern consisting of 130 low-current bunches ($3.1 \text{ mA/bunch} \times 130 = 400 \text{ mA}$) and a high-current single bunch (50 mA/bunch) located on the opposite side of the ring from the bunch train.

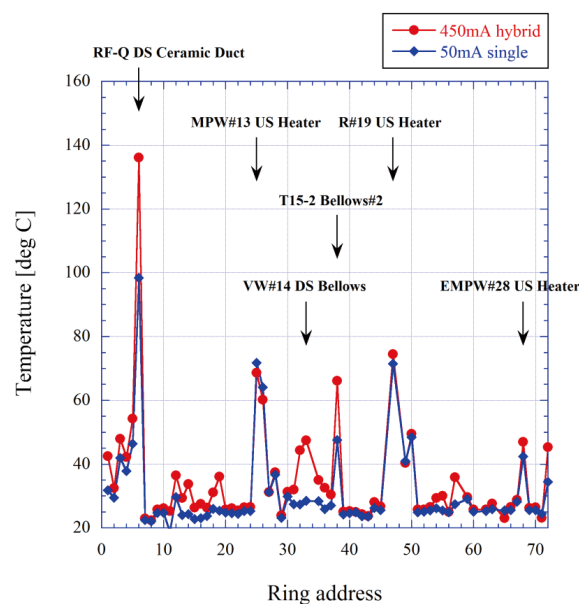


Figure 8 Comparison of temperature distributions along the ring between the hybrid and usual single-bunch operations.

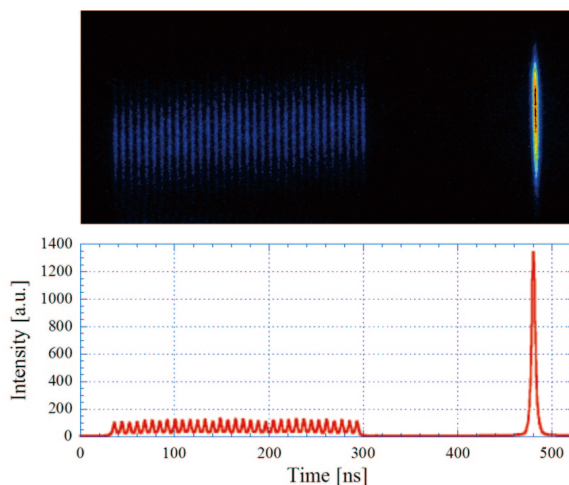


Figure 9 Hybrid filling pattern observed with a streak camera. The upper part shows the two-dimensional streak image, and the lower part shows the relative bunch intensity plotted against time.

2-4 Development of Optical Fiber Beam Loss Monitor for the Photon Factory

A beam loss monitor using optical fibers has been developed to determine the loss point of the injected beam at the Photon Factory 2.5-GeV electron storage ring. Large-core optical fiber was installed along the vacuum chamber of the storage ring in order to cover the whole storage ring continuously. In total, 10 optical fibers with the length of 30 m are used. Both ends of the fiber are fed out of the radiation shield of the ring, and a photomultiplier tube (PMT) is attached on the upstream side of the fiber. If the electrons are not captured in the storage ring, they will hit the vacuum chamber and produce secondary electrons. Then the electrons that pass through the glass core of the optical fiber produce Cherenkov light. The sensitivity of the PMT (Hamamatsu H10721-110) is sufficiently high to detect the loss at the PF ring, and its short rise-time of about 0.6 ns is fast enough to determine the location of the beam loss point.

Figure 10 shows an example beam loss during injection measured from B12 to the vertical wiggler,

VW14. The blue line (CH1) and the red line (CH2) show the beam loss detected at the outer-side and inner-side of the storage ring, respectively. The peak is clearly located at the vacuum chamber with bellows. The distance between components and the corresponding time-difference between pulses does not match in some locations because the optical fiber cannot be laid straight and deviates outside the components. For example, the vertical superconducting wiggler (VW14) has a large body, and so the length of the optical fiber is much longer than the electron orbit length.

In the KEK-PF, two kinds of injection system have been used for routine operation: kicker magnets and a pulsed sextupole magnet (PSM). The fiber loss monitor is useful for analyzing the turn-by-turn difference of the beam loss pattern. Figure 11 shows an example of PMT voltage with the two injection methods. The kicker injection indicates a large loss at the first turn and fourth turn, whereas the PSM injection shows no loss of beam at the first turn, but a large loss at the second turn. Detailed analysis is under way, and the monitor will be used for injection tuning.

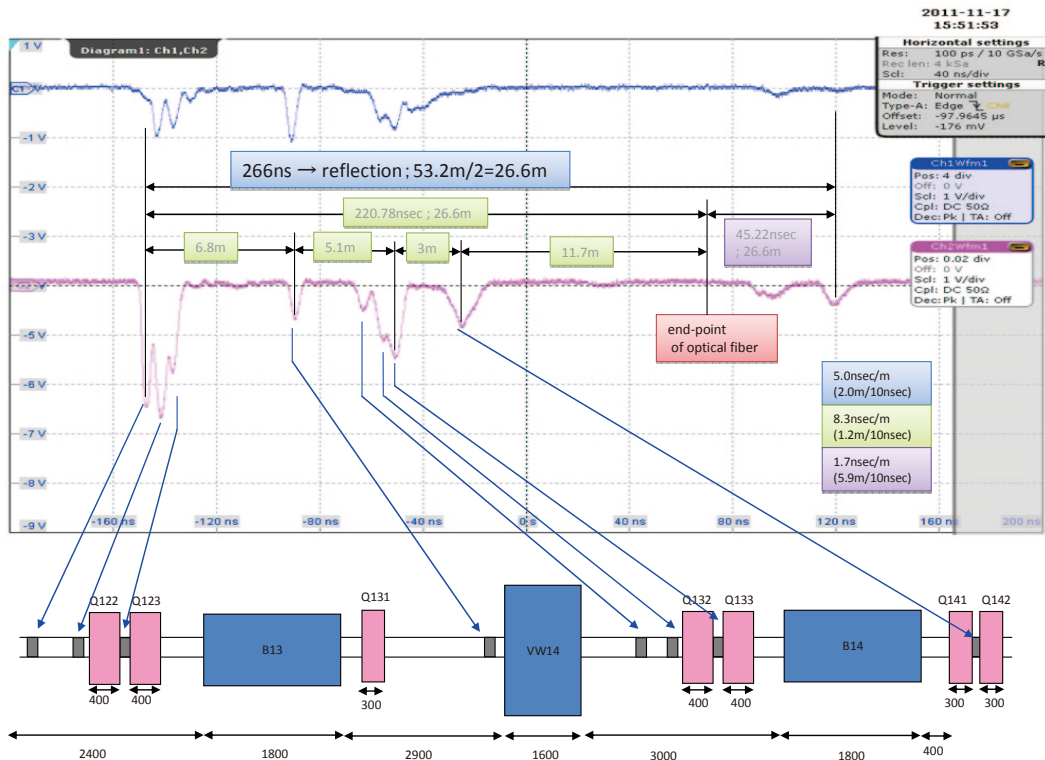


Figure 10
Example of beam loss signal and layout of storage ring components.

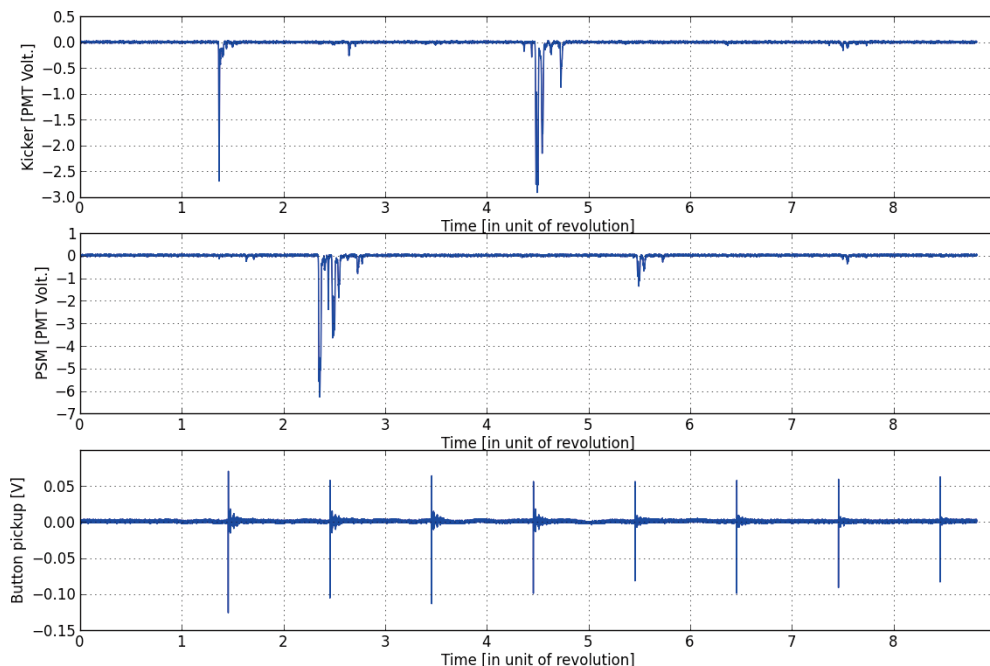


Figure 11
 Beam loss signal with two injection methods. Upper and middle figures show the PMT output voltage for kicker injection and PSM injection, respectively. The bottom figure shows the results for a button-type pickup electrode near the loss monitor.

2-5 Project to Renew the Insertion Devices at the PF Ring

2-5-1 A New Short Gap Undulator (SGU#15)

At the PF ring, we constructed three short gap undulators (SGU) at the four short straight sections of 1.4-m length. For the remaining straight section, B14-15, we are planning to construct a new SGU#15 as a light source for both small-angle X-ray scattering experiments and XAFS experiments. SGU#15 will be the fourth SGU, with a period length of 17.6 mm, number of periods of 27 and maximum deflection parameter of 1.61. The photon energy region of SGU#15 is wide,

from 2 keV to 15 keV. To cover this entire energy region, the higher harmonics of undulator radiation will be used up to the 9th higher harmonics. Figure 12 shows a calculated spectrum of SGU#15. Construction of SGU#15 will be finished by the end of 2012 and we will install it in the PF ring in the summer of 2013.

2-5-2 Design of the Undulators for the VUV-SX Light Source Renewal Project

As part of the VUV-SX beamline renewal project, we are investigating the design of the new undulators for BL-02, BL-13 and BL-28, which will be called U#02-2, U#13 and U#28, respectively. All these undulators are designed as elliptically polarizing undulators (EPUs) to

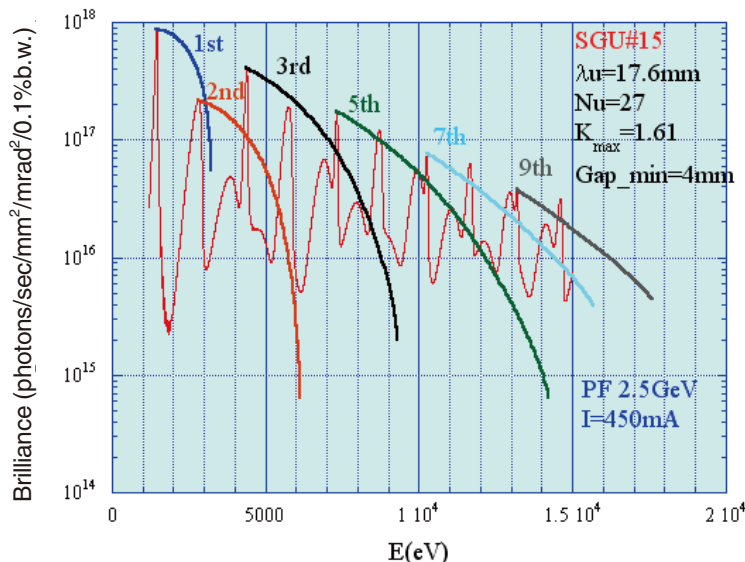


Figure 12
 Calculated spectrum of SGU#15.

obtain various polarization states, not only circular (left-handed and right-handed) polarization but also linear (horizontal and vertical) polarization. We renewed the present undulators for BL-13 and BL-28 to utilize the extended straight section effectively. For BL-02, we plan to move the existing undulator (U#02) to the downstream of the B01-B02 straight section, and install a new undulator (U#02-2) tandem at the upstream of U#02. We will use U#02 and U#02-2 exclusively to obtain photons over a wide energy region at the single beamline. The photon energy region of U#02 is from 400 eV to 2 keV

and the target energy region of U#02-2 is from 15 eV to 300 eV with the first harmonic radiation of EPU.

Table 2 shows the designed parameters of the new undulators. The period length of both U#02-2 and U#28 is 160 mm, while that of U#13 is under investigation and is around 80 mm. Figure 13 shows typical calculated spectra of U#13 and U#28. Figure 14 compares the spectral properties of U#02 and U#02-2.

We will construct these three undulators by fiscal 2013 and install them in the PF ring step by step during 2014.

Table 2 Basic parameters of the new undulators in the PF ring.

Name	Period length (mm)	Number of periods	Length (m)	Maximum Bx, By (T)	Target photon energy region (eV)	Type of undulator
U#02-2	160	17	2.72	0.33, 0.33	30-300	EPU
U#13	76	47	3.57	0.68, 0.34	50-1500	EPU
U#28	160	22	3.52	0.33, 0.33	30-300	EPU

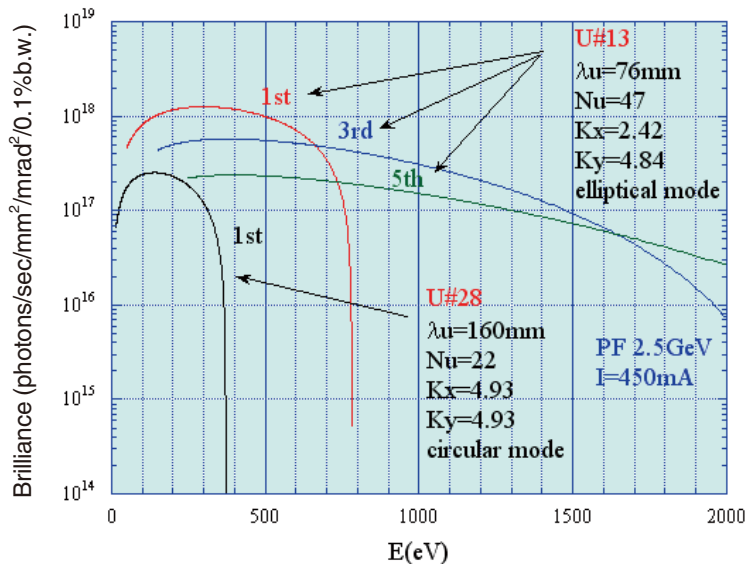


Figure 13 Typical calculated spectra of U#13 and U#28.

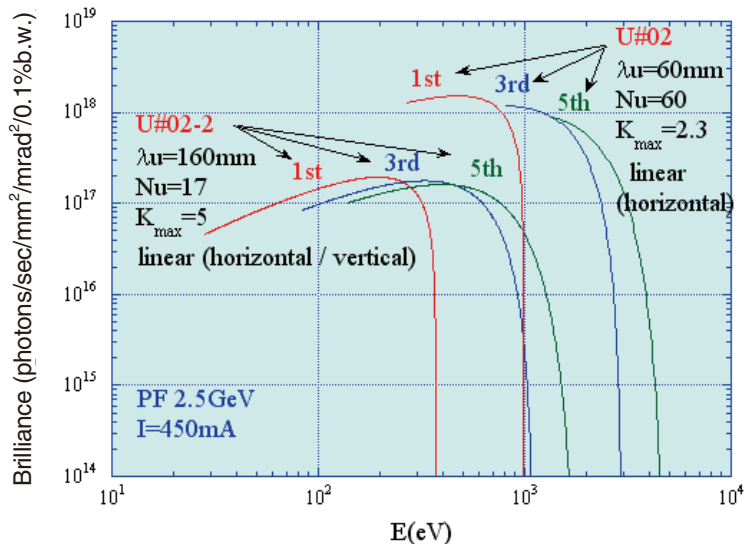


Figure 14 Comparison of photon energy region of U#02 and U#02-2.

3-1 Operation Summary

The user operation scheduled in May, June and July was canceled for the restoration work after the Great East Japan Earthquake. Operation of the trial beam started on June 1 and continued to July 7, and regular user operation was resumed in October. As a result of this schedule change, the total operation time in FY2011 fell to about 4000 h as shown in Fig.1, and the scheduled user time decreased to some 30 % lower than the previous year as shown in Table 1.

At the storage ring of the PF-AR, fortunately the beam ducts kept the vacuum during the two-week blackout after the earthquake, but in the summer maintenance of 2011, a vacuum break occurred at an all-metal gate valve. This was probably caused by accumulated damage from the frequent large aftershocks.

Figure 2 shows the results of the magnet level survey in April and July after the earthquake. The displacements from the survey data of 2009 are plotted and the displacement in one year from 2008 to 2009 is also shown for reference. The April survey shows multiple peaks of over 0.5 mm, most of which appeared near the expansion joints of the ring tunnel indicated by the red lines in Fig. 2, and yet these peaks had almost disappeared by the July survey. Many cracks were found at the expansion joints in the ring tunnel; inflow of ground-

water from some of these cracks increased temporarily just after the earthquake, then gradually decreased to a normal level in a few months.

The operation statistics for the PF-AR during the last seven years are summarized in Table 1. The mean time between failures (MTBF) was estimated for the regular user time, and the sources of failures are classified in Table 2. The MTBF of FY2011 was similar to that of the previous year. As usual, the most frequent failure was a sudden drop of beam lifetime attributed to trapped dust. In addition, the tendency of frequent troubles with the magnet power supply continued. Beam dumps or interruptions of user operation caused by large aftershocks were recorded five times.

The obsolete magnet power supplies are being updated step by step. The power supplies for the sextupole magnets were manufactured in FY2011 and will be installed during the summer maintenance of 2012.

A new plan to build a direct beam transport (BT) tunnel from the injector linac to the PF-AR has been approved. Two new injection plans are being considered: (1) to inject 4-GeV positron beams provided for the Super KEKB LER, and (2) to inject full-energy 6.5-GeV electron beams using the new direct BT lines. It is essential to achieve simultaneous injection of the PF-AR with the other three storage rings no later than the start of the physics run of the Super KEKB in 2015.

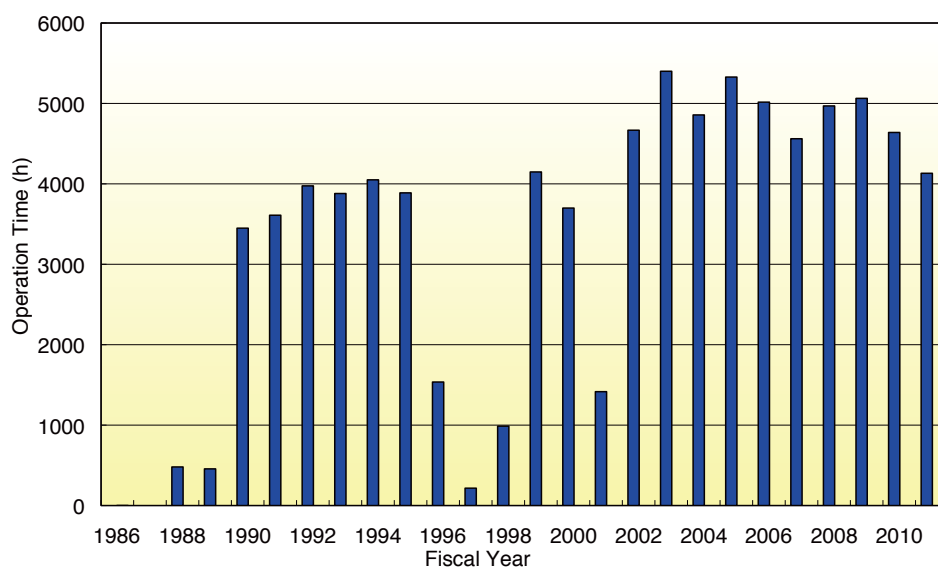


Figure 1
Operation time as a function of fiscal year.

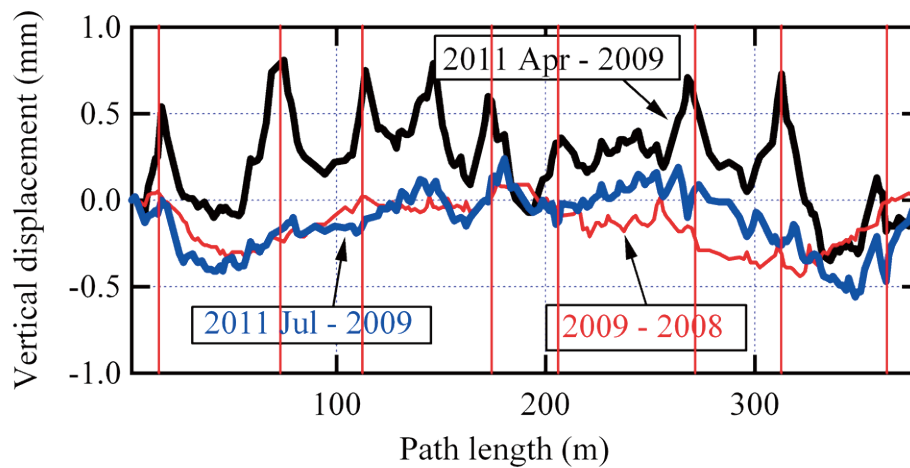


Figure 2
Vertical displacement of PF-AR magnet just after the earthquake.

Table 1
Mean time between failures (MTBF) of PF-AR from FY2005 to FY2011.

Fiscal year	2005	2006	2007	2008	2009	2010	2011
Total operation time (h)	5313	5016	4561	4969	5063	4608	4080
Scheduled user time (h)	4456	4032	3624	4344	4392	4032	2904
No. of failures	79	51	60	40	41	74	49
Total down time (h)	69.3	55.1	45.2	41.7	91.0	73.7	38.7
MTBF (h)	56.4	79.1	60.4	108.6	107.1	54.5	59.3
Mean down time (h)	0.9	1.1	0.8	1.0	2.2	1.0	0.8

Table 2
Classification of failures based on the source of trouble.

Fiscal year	2005	2006	2007	2008	2009	2010	2011
RF	12	10	1	4	8	10	5
Magnet	4	1	1	2	2	10	8
Injection	4	3	8	9	1	6	4
Vacuum	2	6	2	0	2	1	0
Dust trap	37	24	39	15	16	24	20
Insertion devices	0	1	0	0	0	0	0
Control / Monitor	4	0	1	1	1	2	1
Cooling water	5	1	0	3	4	4	1
Safety / Beamline	9	4	5	5	7	17	3
Earthquake	2	0	1	0	0	0	5
Electricity	0	1	2	1	0	0	2
Total	79	51	60	40	41	74	49

3-2 Update of SX Magnet Power System

About 30 years ago, the AR was constructed as an MR injector in the TRISTAN project. The AR had 40 sextupole magnets, which were divided into 4 families, namely SXF1, SXF2, SXD1 and SXD2. The magnet strings were powered by 4 magnet power supplies. The current in the cable flowed clockwise in the tunnel and returned to the source. This arrangement of the cabling naturally formed a one-turn coil loop.

After the TRISTAN project, the AR was converted to a dedicated light source which was named PF-AR. The lattice has 38 sextupole magnets.

In February 2011, a surprising trouble occurred: the current of each power supply jumped simultaneously. For a while, the situation continued and then returned to the normal current. This abnormal situation sometimes occurred. An investigation revealed that the output current was affected by an external noise of 7 MHz. The noise was due to self-oscillation in a high-frequency power amplifier in the beam feedback system. The noise was transmitted through the one-turn loop of SX cabling.

We decided to update the SX power system. Since the dedicated light source operation, the beam optics have been fixed. The currents of SXF1 and that of SXF2 are the same. Also, the currents of SXD1 and SXD2 are the same. Therefore, the SXF1 (SXD1) loop and SXF2

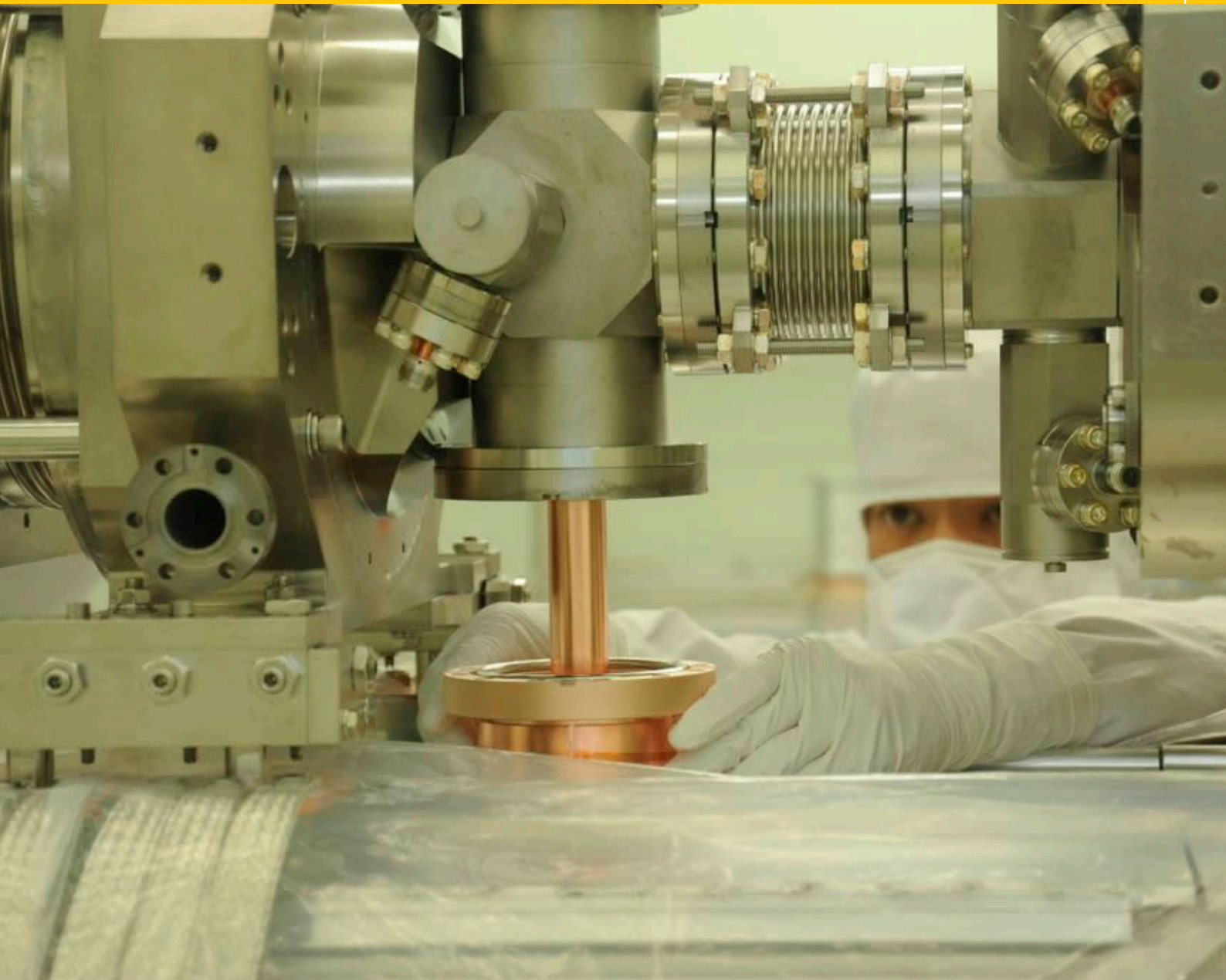
(SXD2) loop can be combined and fed from one power supply. The current circulates in two opposite loops in order to minimize the external field disturbance.

Two power supplies were fabricated in FY2011, and the current stability and the robustness against noise are improved. The new 2 power supplies and the old 4 power supplies are scheduled to be exchanged during the shutdown in the summer of 2012 (Fig. 3).



Figure 3
SXF and SXD power supplies in the factory.

Future Light Source



Future Light Source

1. ERL Project Overview	113
2. 3-GeV ERL Design	116
3. cERL	119
3-1 cERL Overview	
3-2 cERL Gun and Injector Beamline	
3-3 cERL Lattice and Optics	
3-4 cERL Magnets	
3-5 Superconducting Cavities	
3-6 RF Power Supply	
3-7 Cryogenic System	
3-8 Status of Construction	

1

ERL Project Overview

The ERL is a future X-ray light source designed based on state-of-the-art superconducting linear accelerator technology, which will offer far higher performance than the existing storage ring. The high repetition rate, short pulse, high spatial coherence and high brightness of the ERL will enable the filming of ultrafast atomic-scale movies and determination of the structure of heterogeneous systems on the nano-scale. These unique capabilities of the ERL will drive forward a distinct paradigm shift in X-ray science from “static and homogeneous” systems to “dynamic and heterogeneous” systems, in other words, from “time- and space-averaged” analysis to “time- and space-resolved” analysis.

This paradigm shift will make it possible to directly witness how heterogeneous functional materials work in real time and space, and will enable predictions to be made in order to design and innovate better functional materials which will eventually solve the grand challenges of society and support life in future. Such functional materials will continue to be used in indispensable technologies such as catalysts, batteries, superconductors, biofuels, random access memories, spintronics devices and photoswitches. On the other hand, life itself is an intrinsically heterogeneous and dynamic system. Structural biology based on the existing storage ring technology has greatly contributed to determining the static atomic coordinates of proteins which are useful information for rational drug design. The ERL will contribute to biological science and biotechnology by shedding light on the heterogeneity and complexity of cellular functions. In short, the ERL will be an unprecedented tool that will bridge the critical gaps in our understanding of material science and technology.

In addition, continuous improvement of linear accelerator technology will result in further quantum leaps in X-ray science in the future. One possibility is the realization of a fully coherent X-ray free-electron laser. Although self-amplified spontaneous emission X-ray free-electron lasers (SASE-XFELs) have been constructed around the world, the X-ray beam from SASE-XFEL is essentially not fully coherent in the temporal domain. By configuring a Bragg diamond cavity for lasing in the X-ray region, it is proposed that an X-ray free-electron laser oscillator (XFEL-O) will be feasible by taking full advantage of the unprecedented electron beam quality of the ERL. The XFEL-O is planned to be constructed in the second phase of the ERL project.

As a future project of the KEK Photon Factory, we propose to construct a 3-GeV ERL that can be upgraded to become the X-FELO. The conceptual layout of the 3-GeV ERL is shown in Fig. 1. In the first stage of the project, we construct a 3-GeV ERL which comprises an injector linac, a superconducting main linac, and a return loop. In the return loop, we will install 20 to 30 insertion devices which are used to emit synchrotron radiation. Using state-of-the-art undulator technology, we cover a broad spectrum range of synchrotron radiation from vacuum ultra-violet (VUV) to hard X-rays. In the second stage of the project, we will build an X-FELO system which comprises a long undulator and an X-ray resonator. To deliver high-energy beams for the X-FELO system, we change the path length in the return loop by a half RF wavelength of 115.3 mm. The beams are then accelerated again (without energy recovery) through the main linac up to 6 GeV. Then, the beams are used to drive the X-FELO. The details of the 3GeV-

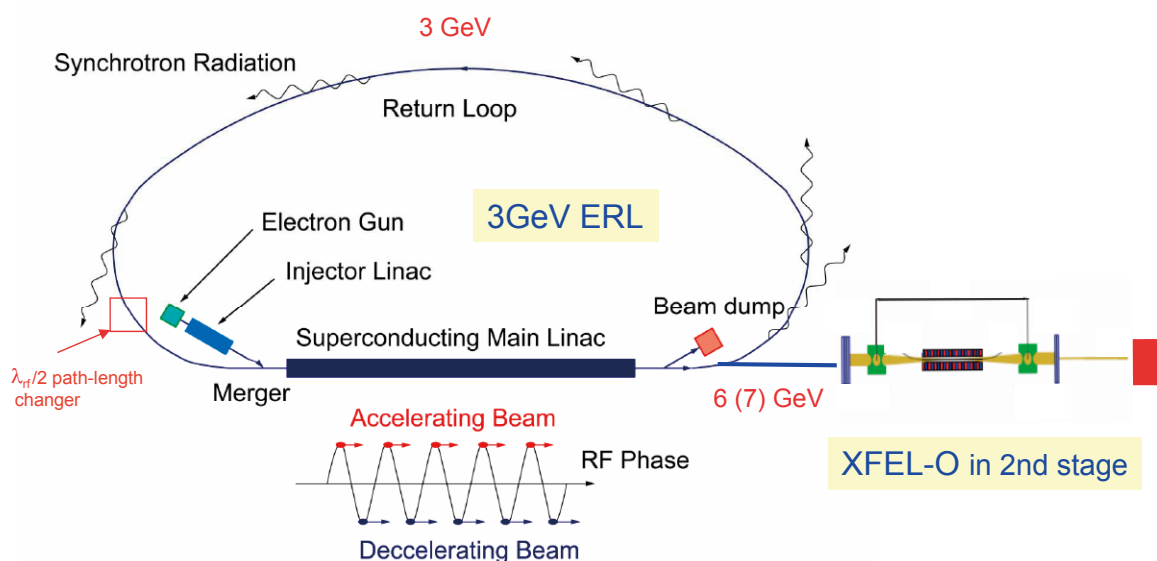


Figure 1
Conceptual layout of 3-GeV ERL plan integrated with an X-ray free electron-laser oscillator (XFEL-O).

ERL design are described in the following section.

KEK established the ERL Project Office in April 2006. Because a GeV-class ERL machine has not been constructed anywhere in the world, it is necessary to first construct a compact ERL (cERL) with an energy of 35 MeV that can be used for developing several critical accelerator components such as a high-brilliance DC photocathode electron gun and superconducting cavities for the injector and main accelerator. In fiscal 2011, such main accelerator components were successfully developed and operation of the beam will start at the end of fiscal 2012.

KEK and JAEA organized the ERL2011 from October 16 to 21, which was the 50th ICFA Advanced Beam Dynamics Workshop on Energy Recovery Linacs to discuss accelerator technologies and applications based on the ERL (Fig. 2). The workshop was a success with 140 participants from 9 countries worldwide. The number of overseas participants was 61, including 26 from the USA, 13 from Germany, 11 from China, 4 from the

UK, 3 from Russia, 2 from Switzerland, 1 from Korea, and 1 from Slovenia. All of the presentation files were posted on the ERL2011 Indico-page of the Scientific program at the ERL 2011 site [1]. The next ERL workshop is to be held in BINP, Novosibirsk in 2013.

Science case which is opened by the ERL project was also discussed by the ERL Science Workshop II (April 2011), first ERL symposium (July 2011), IMSS symposium 2011 (December 2011), and second ERL symposium (March 2012). The sub-title of both ERL symposiums was "Synchrotron radiation to realize the sustainable society", and Dr. Hiroshi Komiyama, former president of the University of Tokyo, and Prof. Ei-ichi Negishi of Purdue University, who won the Nobel Prize for Chemistry in 2010, gave special plenary talks at each symposium. In addition to the plenary talk by Prof. Negishi, addresses (video letters) from Prof. Keith Hodgson of SSRL, Dr. Helmut Dosch of DESY and Prof. Maury Tigner of Cornell University gave presentations at the second ERL symposium (Fig. 3).



Figure 2
Group photo of the ERL2011 (October 16-21), which was the 50th ICFA Advanced Beam Dynamics Workshop on Energy Recovery Linacs.

(a)



(b)



Figure 3
(a) Prof. Ei-ichi Negishi of Purdue University, Winner of the Nobel Prize for Chemistry in 2010 and (b) Prof. Keith Hodgson of SSRL, at the occasion of the second ERL symposium (March 2012).

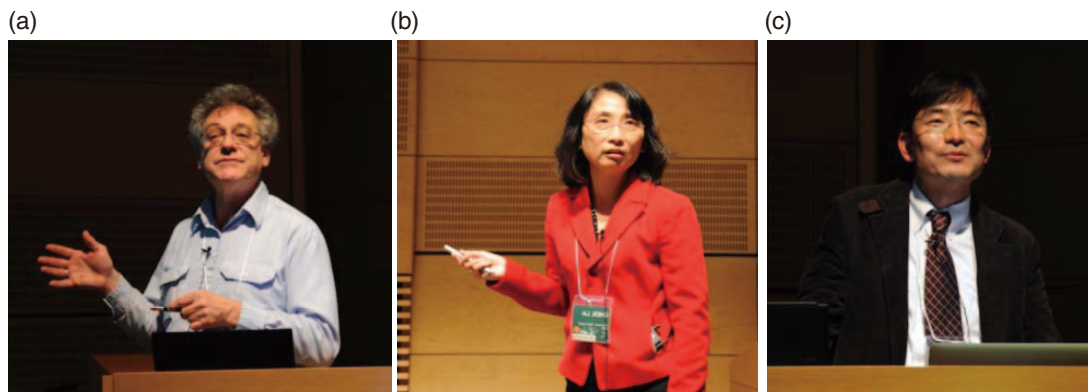


Figure 4
Photographs of Dr. Sol Gruner (Cornell University) (a), Dr. Lin X. Chen (ANL) (b) and Dr. Ryu Abe (Hokkaido University) (c) at the IMSS symposium.

We invited Dr. Sol Gruner (Cornell University), Dr. Lin X. Chen (ANL) and Dr. Ryu Abe (Hokkaido University) to the IMSS symposium in December 2010 to provide scientific updates (Fig. 4). Dr. Gruner presented the summary talk of the XDL2011 workshop, which was a series of workshops devoted to the science of diffraction-limited high repetition rate, hard X-ray sources, and was held at Cornell University during the month of June 2011. The Photon Factory was one of the co-organizers of the workshop [2]. Dr. Lin X. Chen presented her work on time-resolved X-ray absorption spectroscopy on photo-excited transient states by using APS with time resolution of several pico seconds. Then she emphasized the importance of femto-second time resolution in order to clarify the dynamics of materials. Dr. Ryu Abe presented the chemistry of visible-light-responsive photo-catalysts

for the production of hydrogen from solar power. He also summarized the future challenges for development, such as direct observation of the photo-catalyst reaction itself and the carrier recombination process.

We published the Preliminary Conceptual Design Report for the 3GeV-ERL upon the occasion of the second ERL symposium [3]. According to the CDR, we will organize the International Advisory Committee to evaluate our 3GeV-ERL project and also to obtain critical comments for the project next fiscal year.

REFERENCES

- [1] http://erl2011.kek.jp/scientific_program/index.html
- [2] http://erl.chess.cornell.edu/gatherings/2011_Workshops/index.htm
- [3] http://pfwww.kek.jp/ERLoffice/detabase/ERL_Preliminary_Design_Report_web.pdf

2

3-GeV ERL Design

The ERL-based light source consists of a 3-GeV ERL and a 6-7 GeV XFEL-O. The 3-GeV ERL provides super-bright and/or ultra-short synchrotron radiation (SR) in the vacuum ultra-violet (VUV) to hard X-ray range, and the 6-7 GeV XFEL-O provides fully coherent radiation. In the XFEL-O operation, an electron beam is accelerated twice by the superconducting main linac of the ERL without energy recovery and fed to the XFEL-O after acceleration up to 6 GeV (or 7 GeV with an upgrade in the main linac). Typical operational modes and their parameters of the ERL-based light source are given in Table 1.

The lattice and optics design of the 3-GeV ERL was started [1, 2]. In the design, the injection energy is assumed to be 10 MeV. The main linac consists of more than 200 superconducting (SC) 9-cell cavities to accelerate the electron beam up to 3 GeV with a moderate accelerating gradient of 15 MV/m or less, which can suppress harmful field emission from the cavities. Quadrupole triplets are placed at every eight SC cavities for focusing. The optics of the main linac is mirror-symmetric for acceleration and deceleration and designed so that the betatron function is well suppressed for achieving a high BBU threshold current. The return loop of the 3-GeV ERL has 28 TBA (Triple Bend Achromat) cells with 22×6 -m and 6×30 -m long straight sections for insertion devices. The lattice and optics of these TBA cells are shown in Figs. 1 and 2. The bending radius of the bending magnet is sufficiently long to suppress the incoherent SR effects. Figure 3 shows the preliminary result of the optical functions for the main linac and the return loop of the 3-GeV ERL. In this op-

tics, the emittance growth and energy spread increase due to incoherent and coherent SR are negligibly small for both Ultimate and XFEL-O modes. Figure 4 shows the tentative layout of the ERL light source in the KEK Tsukuba campus.

Figure 5 shows examples of the calculated spectral brightness for VUV-SX (soft X-ray) and X-ray undulators [3]. As shown in this figure, the 3-GeV ERL can provide undulator radiation with the maximum spectral brightness of $10^{22} - 10^{23}$ phs/s/mm²/mrad²/0.1%b.w. The 6-7 GeV XFEL-O generates spatially and temporally coherent X-rays with the brightness of about 10^{26} phs/s/mm²/mrad²/0.1%b.w. [4]. For future development, a 300-m long straight section is reserved in the middle of the return loop. This section has major potential for (1) EEHG (Echo-Enabled Harmonic Generation) including attosecond pulse generation [5, 6], (2) 3-GeV XFEL-O using the higher harmonics [7], (3) a very long undulator with spectral brightness of up to $10^{23} - 10^{24}$ phs/s/mm²/mrad²/0.1%b.w. and so on.

REFERENCES

- [1] N. Nakamura, *Proc. of IPAC12* (2012) 1040.
- [2] M. Shimada et al., FLS2012, Newport News.
- [3] K. Tsuchiya, private communication.
- [4] K. J. Kim, Y. Shvyd'ko and S. Reiche, *Phys. Rev. Lett.*, **100** (2008) 244802.
- [5] G. Stupakov, *Phys. Rev. Lett.*, **102** (2009) 074801.
- [6] D. Xiang, E. Colby, M. Dunning, S. Gilevich, C. Hast, K. Jobe, D. McCormick, J. Nelson, T. Raubenheimer, K. Soong, G. Stupakov, Z. Szalata, D. Walz, S. Weathersby and M. Woodley, *Phys. Rev. ST Accel. Beams*, **12** (2009) 060701.
- [7] J. Dai, H. Deng and Z. Dai, *Phys. Rev. Lett.*, **108** (2012) 034802.

Table 1 Typical operational modes and their parameters for the ERL-based light source.

	HC ^{†1}	HF ^{†2}	UL ^{†3}	US ^{†4}	XFEL-O
Beam energy	3 GeV				6-7 GeV
Beam current	10 mA	100 mA	100 mA	77 μ A	20 μ A
Bunch charge	7.7 pC	77 pC	77 pC	77 pC	20 pC
Repetition rate	1.3 GHz	1.3 GHz	1.3 GHz	1 MHz	1 MHz
Norm. emittance	0.1 mm \cdot mrad	1.0 mm \cdot mrad	0.1 mm \cdot mrad	-	0.2 mm \cdot mrad
Emittance	17 pm \cdot rad	170 pm \cdot rad	17 pm \cdot rad	-	15 pm \cdot rad
Energy spread	2×10^{-4}	2×10^{-4}	2×10^{-4}	-	5×10^{-5}
Bunch length	2 ps	2 ps	2 ps	< 100 fs	1 ps

^{†1} HC: High Coherence mode, ^{†2} HF: High Flux mode, ^{†3} UL: Ultimate mode, ^{†4} US: Ultra-Short Pulse mode

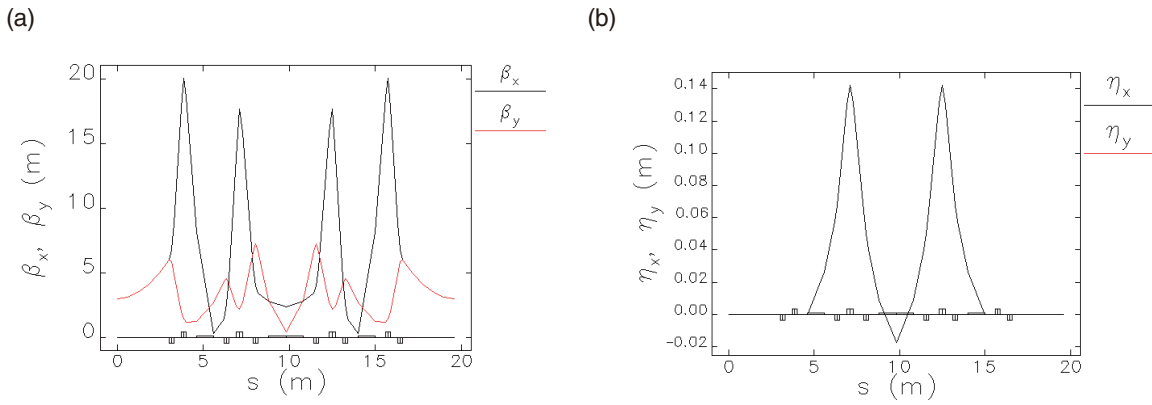


Figure 1
Betatron (a) and dispersion (b) functions of the TBA cell with a 6-m straight section in the return loop for the 3-GeV ERL.

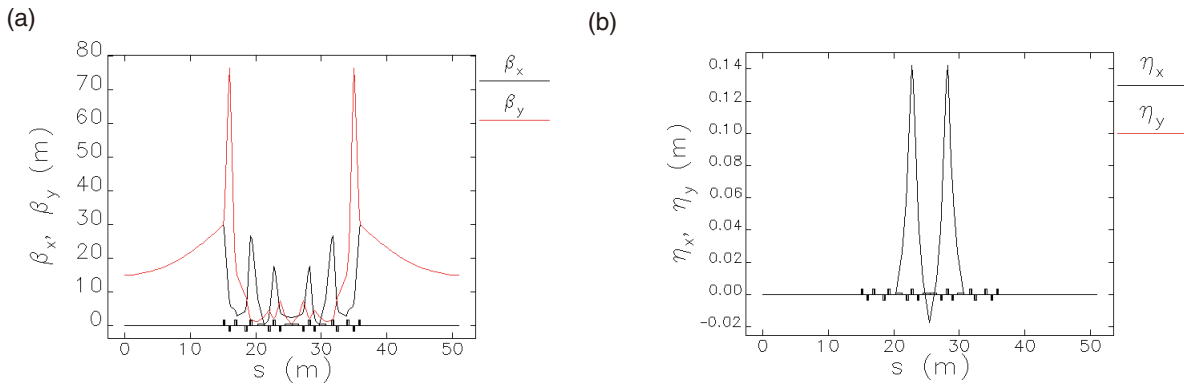


Figure 2
Betatron (a) and dispersion (b) functions of the TBA cell with a 30-m straight section in the return loop for the 3-GeV ERL.

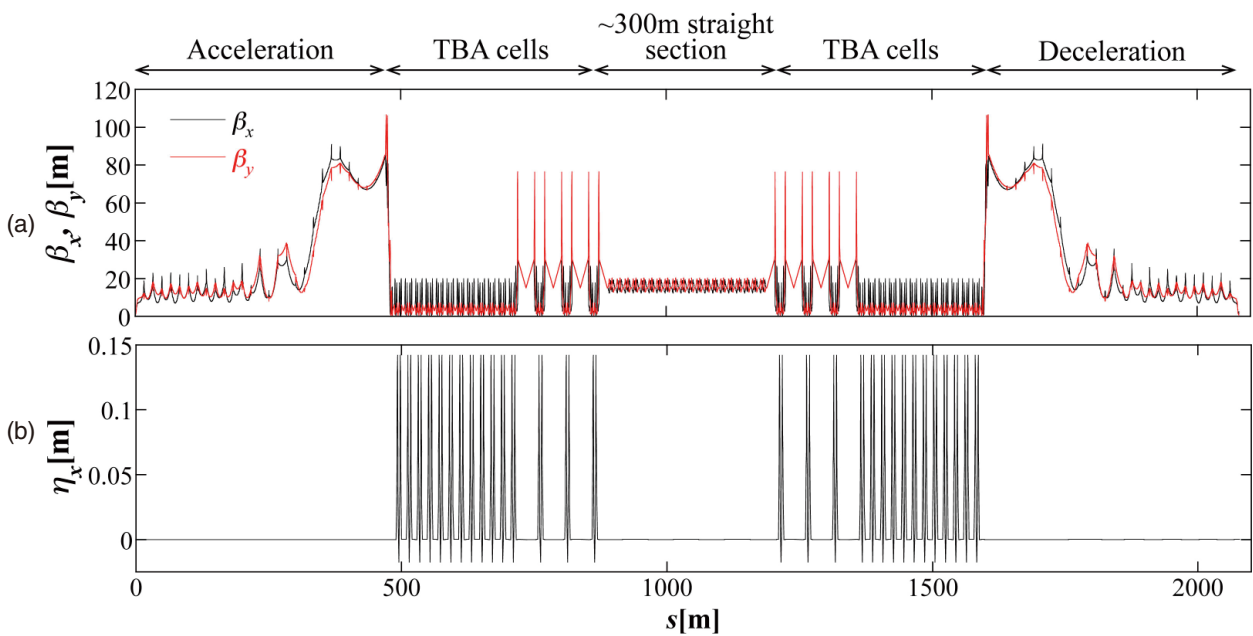


Figure 3
Betatron (a) and dispersion (b) functions of the main linac and the return loop for the 3-GeV ERL.

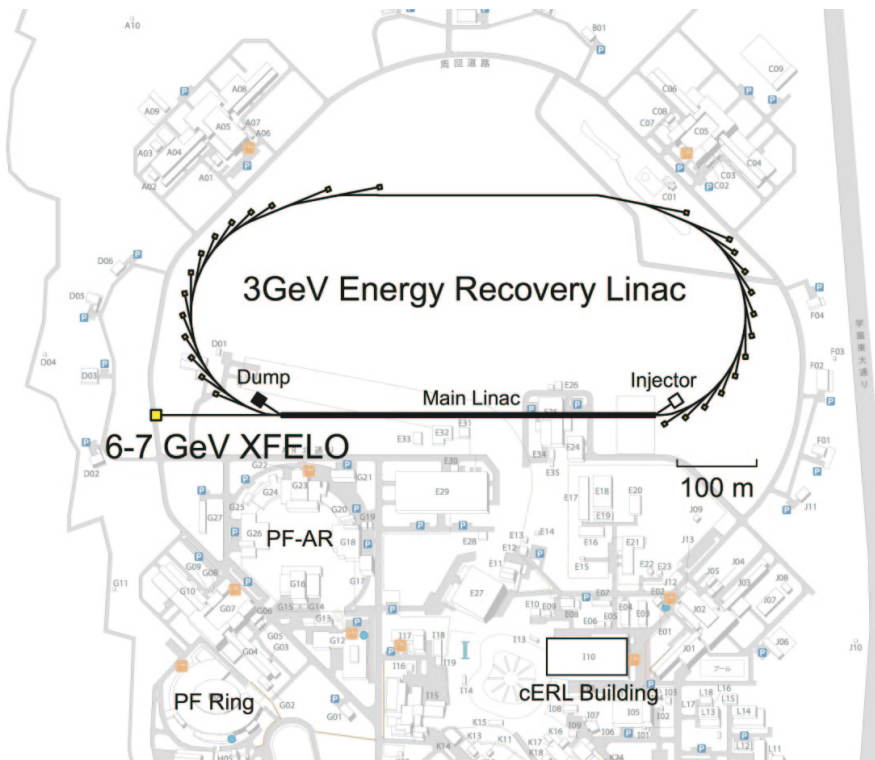


Figure 4
Tentative layout of the ERL-based light source at KEK Tsukuba campus

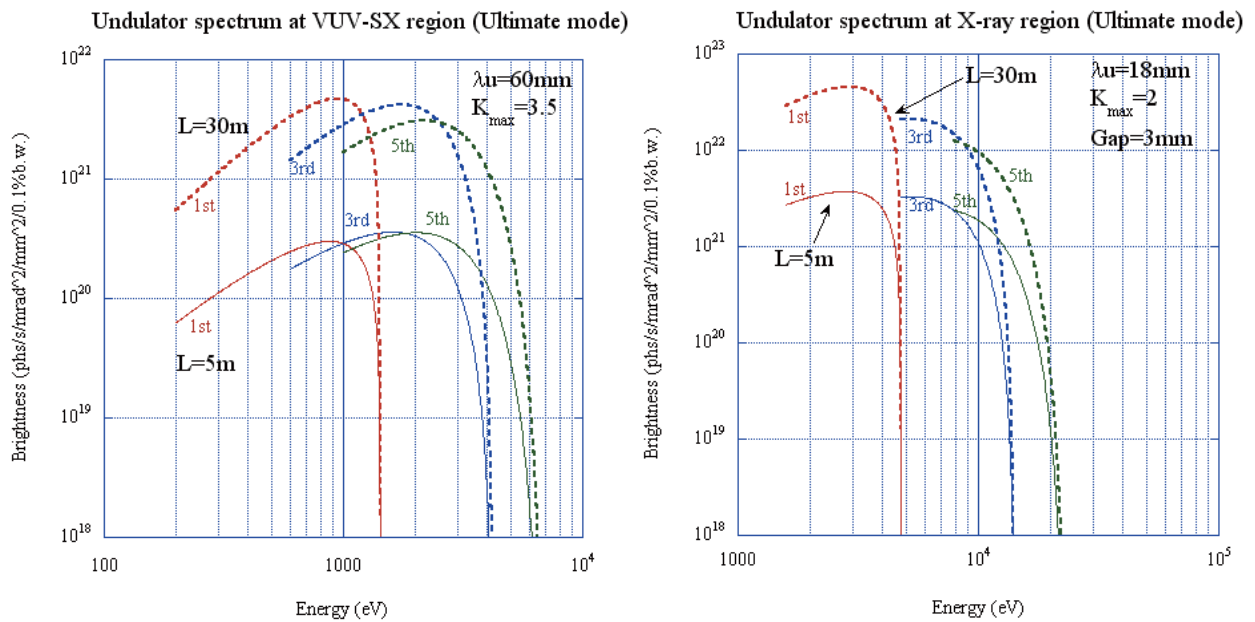


Figure 5
Examples of calculated spectral brightness for VUV-SX and X-ray undulators.

3

cERL

3-1 cERL Overview

The 3-GeV Energy Recovery Linac (ERL) has been proposed [1, 2] for a future project of the Photon Factory at KEK. To develop key technologies for our ERL project, we have been actively researching such components as the high-brightness electron guns and superconducting (SC) cavities since 2006. To demonstrate the production and recirculation of ultra-low emittance beams, we are constructing the Compact ERL (cERL) [3, 4] at KEK. The cERL will comprise a 5-MeV injector, a main linac, and a return loop, as well as RF sources, power supplies, and a cryogenic system, as shown in Fig. 1. The principal parameters of the cERL are given in Table 1. We plan to commission the cERL-injector in the spring of 2013, and the recirculating loop in the autumn of 2013.

In the following sections, we report the status of development and construction of each subsystem: the de-

velopment of high-brightness electron guns and a drive-laser system are reported in Section 3-2, the design and optimization of the cERL lattice and beam optics in Section 3-3, and the production and measurement of magnets in Section 3-4. A superconducting cryomodule for the injector, containing three 2-cell cavities, has been assembled and installed in the cERL beamline, as described in Section 3-5-1. The other superconducting cryomodule for the main linac, containing two 9-cell cavities, is ready for assembly, as described in Section 3-5-2. Four of the five RF sources for the cERL have been installed, as also reported in Section 3-6. A cryogenic system for the cERL was installed and performance tests are under way step by step, as described in Section 3-7. Construction of radiation shielding for the cERL started in February 2012, and will be finished at the end of September 2012, as described in Section 3-8.

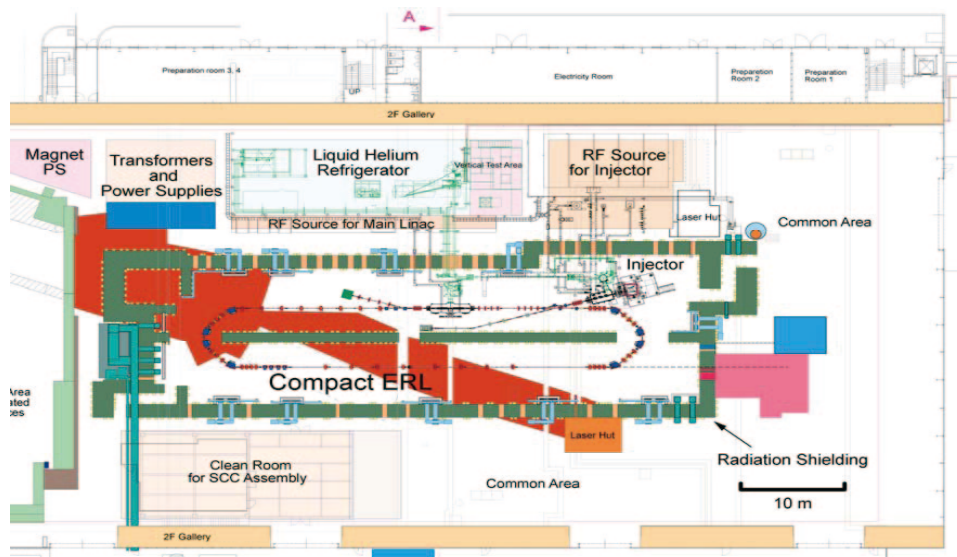


Figure 1
Planned layout of the Compact ERL (35 MeV version).

Table 1 Principal parameters of the Compact ERL.

Parameter	Value
Kinetic energy of electron beams (initial)	35 MeV
(maximum)	245 MeV
Kinetic energy of electrons from the injector (initial)	5 MeV
Beam current (initial)	10 mA (7.7 pC/bunch)
(future goal)	100 mA (77 pC/bunch)
Normalized emittance (at 7.7 pC/bunch)	0.3 - 1 mm·mrad
(at 77 pC/bunch)	1 mm·mrad
RF frequency	1.3 GHz
Bunch length in rms (usual operation)	1–3 ps
(under bunch compression)	< 100 fs

REFERENCES

- [1] "Energy Recovery Linac Preliminary Design Report", Institute of Materials Structure Science, High Energy Accelerator Research Organization (KEK).
- [2] N. Nakamura, "Review of ERL Projects at KEK and Around the World", *Proc. IPAC12* (2012) 1040.
- [3] R. Hajima, N. Nakamura, Y. Kobayashi and S. Sakanaka (ed.), *KEK Report 2007-7/JAEA-Research 2008-032*, Feb. 2008.
- [4] S. Sakanaka, H. Kawata, Y. Kobayashi, N. Nakamura, R. Hajima, "Construction Status of the Compact ERL", *Proc. IPAC12* (2012) 607.

3-2 cERL Gun and Injector Beamline

Aiming for initial beam operation of the cERL in March 2013, two high-brightness photocathode DC electron-gun systems, a drive laser system, and an injector beamline are being developed to achieve normalized emittance of less than 1 mm-mrad, beam current of 10 mA, and a sufficiently long cathode lifetime.

For the first gun system, which is being developed at JAEA, high-voltage processing up to 526 kV with a cathode electrode and NEG pumps in place, and extraction of an electron beam of 5.7 μA with bias voltage of 300 kV have been achieved. A test for extracting a high beam current of 10 mA is scheduled for the summer of 2012. Thanks to the remarkable progress of the first gun system, we have selected it as the electron gun for the initial beam operation of the cERL, and it is due to be installed in the ERL development building in the autumn of 2012. Figure 2 shows the first gun system developed by JAEA.

For the second gun system, which is being developed by KEK, work is continuing on developing the vacuum system to achieve the extreme-high vacuum of 1×10^{-10} Pa and the high-voltage power supply system of up to 600 kV. To achieve the extreme-high vacuum, the outgassing rate and pumping speed of the system are critical aspects. The total outgassing rate of the second gun vacuum system, which consists of a titanium chamber, ceramic insulators and guard ring electrodes, was

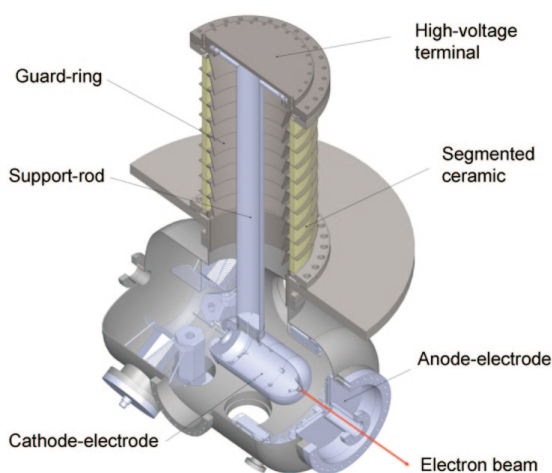


Figure 2
The first DC electron gun system developed at JAEA.

precisely measured to be 1.0×10^{-10} Pa m^3/s by the rate-of-rise (RoR) method, which is two orders of magnitude lower than that of the conventional SUS chamber. The pumping speed of a 4 K bakeable cryopump was measured using a standard conductance element developed by AIST, and the preliminary results are shown in Fig. 3. The measured pumping speed was about 1000 L/s for CH_4 , N_2 , CO and CO_2 at vacuum pressure of 1×10^{-9} Pa. Since the conductance of the pumping port was limited in the measurements, the pumping speed of the gun system, which has larger conductance, is estimated to be three times larger than the measured value. The high-voltage power supply system has been improved to fix the discharge in the circuit, and high-voltage processing is scheduled to start in the summer of 2012.

As the drive laser of the photocathode gun, a high-average-power laser amplifier based on a Yb-doped photonic-crystal fiber has been developed [5], and 70 W output power with a 1.3 GHz repetition rate at 1064 nm wavelength has been demonstrated. This will be converted to the second harmonic of 532 nm, and then will be delivered to the cathode. The achieved laser power is sufficient to generate an electron beam of 10 mA.

Tests of the injector beamline, which connects with the photocathode gun, are continuing in the PF-AR south experimental hall. The laser chamber and screen chambers have been modified to reduce outgassing and to increase the pumping speed. After the beamline has been tested in the PF-AR south experimental hall, it is scheduled to be transferred to and constructed in the ERL development building in the winter of 2012. In the initial beam operation, the injector diagnostic beamline, which connects with the injector in a straight line, will be used to measure the quality of the injector beam. It is also scheduled to be constructed in the winter of 2012.

Development of the photocathode is a key part of developing the gun system. In the ultimate mode of the ERL light source, the cathode requires low emittance, a fast time response, and robustness. The initial emittance and the time response were measured using the gun test beamline for thickness-controlled GaAs sam-

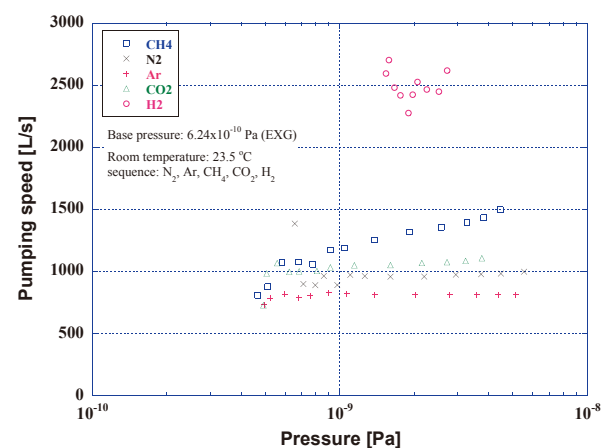


Figure 3
Preliminary results of pumping speed measurement for 4 K bakeable cryopump.

ples and GaAs/GaAsP superlattice [6, 7]. No clear dependence on cathode thickness was seen for cathodes with thicknesses of 100 and 1000 nm, indicating that conduction electrons are mostly relaxed within a range of 100 nm in the crystal.

REFERENCES

- [5] Y. Honda, *Proc. IPAC12* (2012) 1530.
 [6] S. Matsuba, Y. Honda, X. Jin, T. Miyajima, M. Yamamoto, T. Uchiyama, M. Kuwahara and Y. Takeda, *Jpn. J. Appl. Phys.*, **51** (2012) 046402.
 [7] S. Matsuba, *Photon Factory Activity Report 2011*, #29 (2012) 62.

3-3 cERL Lattice and Optics

The cERL initially comprises a 5-MeV injector, a superconducting main linac with two 9-cell cavities in a cryomodule and a single return loop. The first target of the cERL is the normalized emittance of 1 mm-mrad for the beam current of 10 mA at the beam energy of 35 MeV. The beam energy can be increased up to 125 MeV by increasing the number of cavities and can be doubled to 245 MeV by installing a second return loop [8].

Figure 4 shows the latest design of the 35-MeV single-loop configuration [9]. The lattice and optics from the injector to the main linac have been designed by simulation including space charge effects for the first cERL commissioning [10]. By modifying the arrangement of eight quadrupole magnets between the merger and the main linac, the horizontal and vertical normalized emittances just after the main linac were improved to less than 0.3 mm-mrad for the bunch charge of 7.7 pC (beam current of 10 mA), as shown in Fig. 5. Figure 6 shows the betatron and dispersion functions from after the main linac to the beam dump in the normal operation mode. The two arc sections with non-zero dispersion have the same isochronous optics in the normal operation mode and are designed so that the normalized emittance is well preserved against the CSR effects.

In the bunch compression mode, the first arc section has non-isochronous optics with a positive momentum compaction factor and the second arc section with a negative one. The bunch is accelerated off-crest by the main linac, compressed after the first arc and decompressed after the second arc. Four sextupole magnets

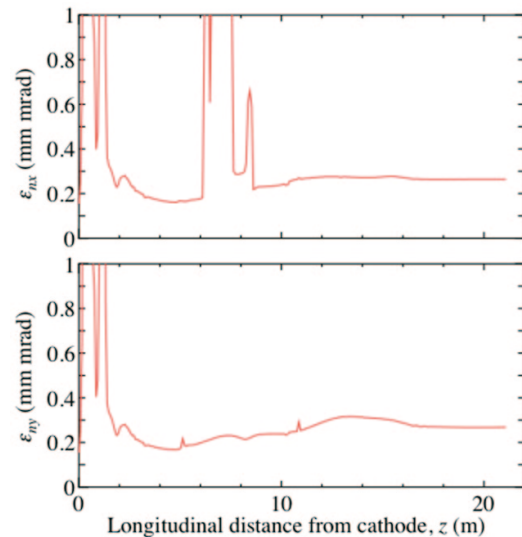


Figure 5
Simulation results for horizontal (upper) and vertical (bottom) normalized emittances from the DC photocathode gun to the main linac.

for each arc section are used to compensate second-order momentum compaction. The simulation result shows that the bunch can be compressed to about 150 fs for the bunch charge of 77 pC and the injection bunch length of 1–2 ps, as shown in Fig. 7. In order to guarantee the momentum acceptance for the bunch compression mode, the physical aperture of the beam pipe has an octagon-like shape with the horizontal and vertical half widths of 35 mm (H) and 20 mm (V) in the two arc sections, while it basically has a round shape with radius of 25 mm in the straight sections.

Beam loss due to residual-gas scattering was calculated and as a result the beam pipe radius at the beam dump line was increased to about 50 mm from 25 mm because the beam loss can be significant after the deceleration by the main linac. The space charge effects after the main linac to the beam dump are being studied and the lattice and optics for a laser-Compton scattering X-ray experiment in the straight section opposite to the main linac are being designed.

REFERENCES

- [8] M. Shimada, K. Harada, Y. Kobayashi, T. Miyajima, N. Nakamura and S. Sakanaka, *Proc. IPAC11* (2011)1909
 [9] N. Nakamura, *Proc. IPAC12* (2012)1040.
 [10] T. Miyajima *et al.*, ERL2011, Tsukuba.

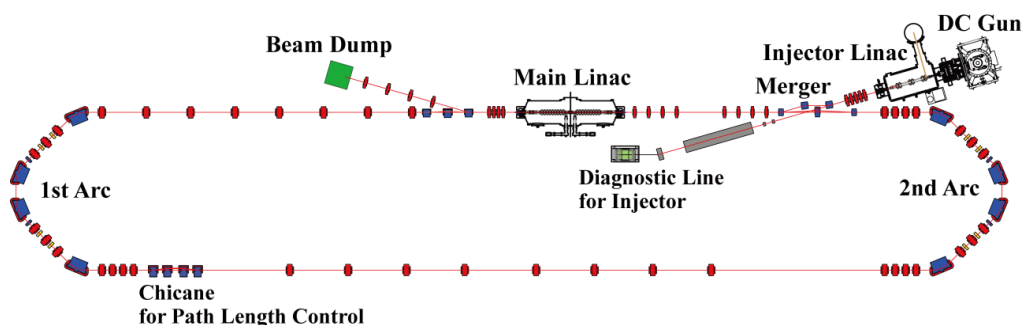


Figure 4
Latest design of the 35-MeV single-loop configuration.

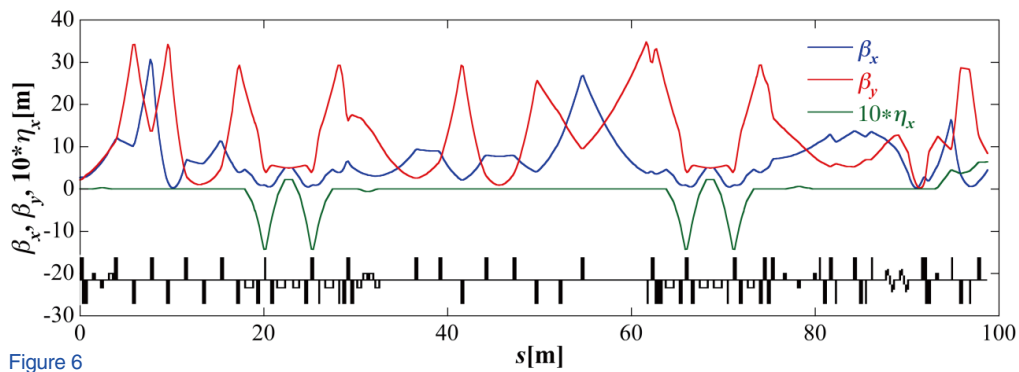


Figure 6
Betatron and dispersion functions of the cERL from after the main linac to the beam dump.

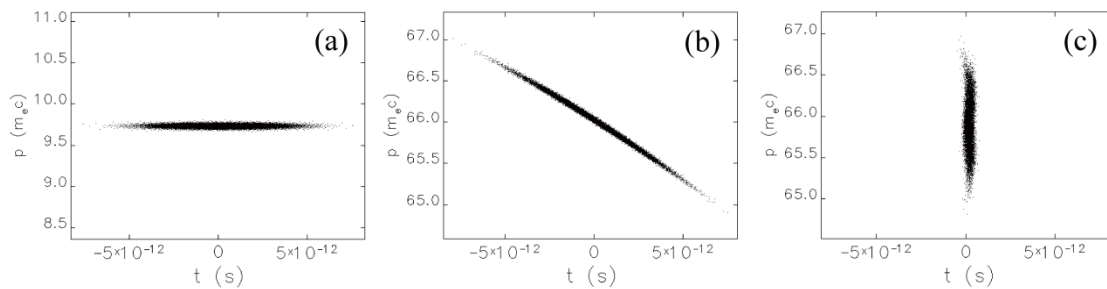


Figure 7
Simulated temporal and momentum distributions of an electron bunch (a) before and (b) after the main linac and (c) after the first arc section in the bunch compression mode.

3-4 cERL Magnets

A prototype of the main sector bending magnet was designed and manufactured in 2010. The remaining seven magnets were manufactured in 2011, as shown in Fig. 8. The magnetic measurements are conducted for the prototype, as shown in Fig. 9.

Fifty-six quadrupole magnets were manufactured (Fig. 10). Twelve of them having a core length of 10 cm are used for the low energy (5 MeV) part while the other 44 magnets having a core length of 20 cm are used for the high energy part (≥ 35 MeV). For the 35-MeV operation, 280-turn coils of electric wire are used.

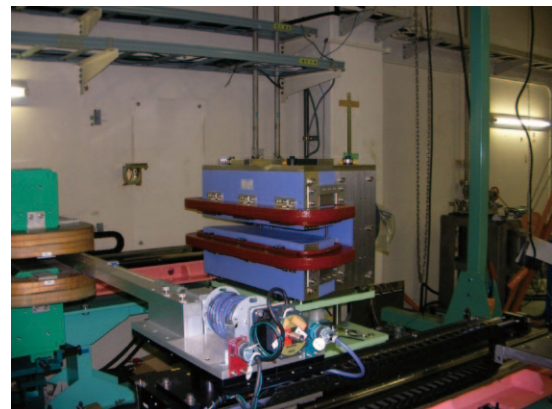


Figure 9
Magnetic measurement of the bending magnet.



Figure 8
Sector-type bending magnets.



Figure 10
Quadrupole magnets.

3-5 Superconducting Cavities

3-5-1 Two-cell Cavities for the Injector

In the injector cryomodule for the cERL, electron beams of 10 mA are accelerated from the beam energy of 500 keV to 5 MeV. The injector cryomodule containing three 2-cell cavities was designed, as shown in Fig. 11 [11]. Each cavity is driven by two input couplers to reduce the required RF power handling capacity and also to compensate for coupler kick. The 2-cell cavities are dressed with a helium (He) jacket made of titanium, and magnetic shields are put inside the two-Kelvin (2K) He jacket. A higher-order-mode (HOM) coupler scheme was chosen for HOM damping, and five loop-type HOM couplers are attached on both beam pipes of each cavity. Efficient cooling of RF feedthroughs for HOM pick-up antennas is an important issue. A slide-jack tuner with a pair of piezo elements is attached at the thick titanium base-plates for the frequency tuning system. RF input couplers are a critical component in a high-power application of superconducting cavities. A coaxial coupler with a single disk-type ceramic window is used for the continuous-wave (CW) input couplers.

The limitation on cavity performance in the 2-cell cavities was not only thermal quenching at defects on the RF surface in the cells, but also the drop in Q_0 values due to heating-up at the niobium (Nb) antenna tip of the HOM pick-up probe. New RF feedthroughs with more efficient cooling performance were developed, as shown in Fig. 12 [12]. An Nb antenna was joined with a center conductor made of Kovar by a screw in the original RF feedthrough (Type-0). In Type-I feedthroughs, the Nb antenna was joined by brazing, and the material of the center conductor was changed to molybdenum (Mo) to increase the thermal conduction. Furthermore, the material of the outer conductor was changed from

Kovar to copper to improve the cooling efficiency by liquid-He (Type-II). Finally, a male pin for connecting the center conductor was applied in the Type-II feedthroughs. These new RF feedthroughs were tested in the vertical tests of the 2-cell cavities. The final vertical test results in each cavity are shown in Fig. 13. In the No. 4 cavity test with five Type-I feedthroughs, the obtained maximum accelerating gradient (E_{acc}) was limited by the drop of Q_0 values due to heating-up of the Nb antenna tip. On the other hand, the limitation in cavities No. 3 and No. 5 with Type-II feedthroughs was thermal quenching at the cell without heating at the Nb antenna. All cavities achieved an accelerating gradient (E_{acc}) of higher than 20 MV/m, which exceeds the operating gradient in the cERL injector.

Conditioning of six input couplers for the injector cryomodule was carried out by using a newly developed 300 kW CW klystron. The high-power RF test stand used for conditioning a pair of input couplers is shown in Fig. 14. A water cooling channel was inserted inside the inner conductor of the input couplers. The coaxial line between an RF window and a doorknob-type transition was cooled by nitrogen gas flow. The outer surface of the test stand was cooled by air blown from two electric fans. Conditioning of these input couplers was carefully carried out up to 200 kW in a short pulsed operation with a duty of less than 1%, and 30–40 kW in CW operation [13].

Assembly of the injector cryomodule was started in April 2012 [14]. All components such as input couplers, beam tubes, RF feedthroughs and vacuum parts were carefully rinsed, and were dried in a class-10 clean room. All of the RF feedthroughs for HOM couplers were replaced with new Type-II feedthroughs, as shown in Fig. 12. Six input couplers were mounted in the upper and lower ports of three 2-cell cavities. Three cavities

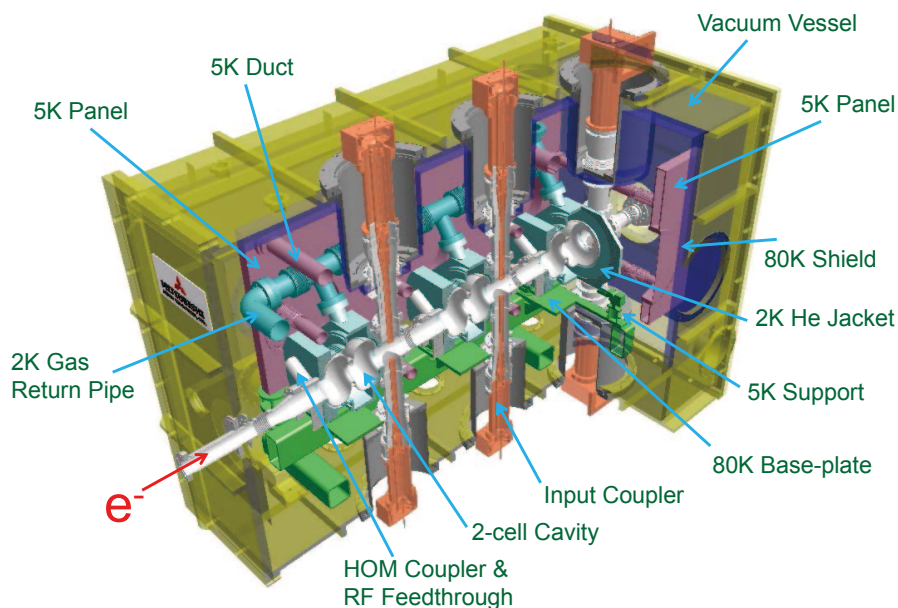


Figure 11
Injector cryomodule for cERL.

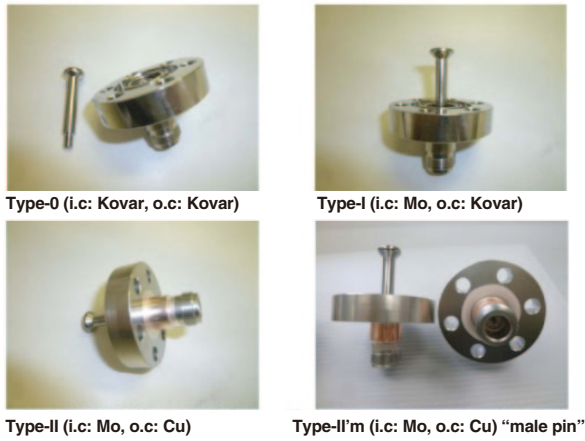


Figure 12

Four types of RF feedthrough with HOM pick-up antenna made of niobium; material of inner conductor (i.c) and outer conductor (o.c).

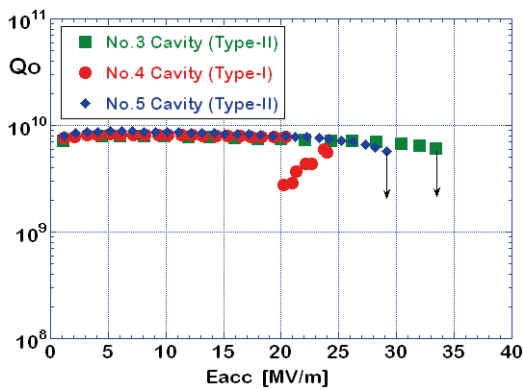


Figure 13

Final vertical test results of three 2-cell cavities attached with five RF feedthroughs at the five HOM couplers.

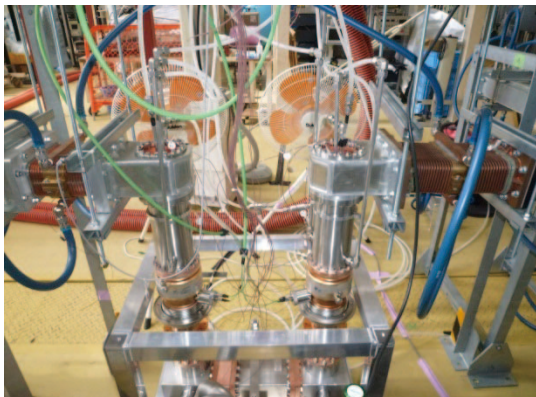


Figure 14

High power RF test stand for conditioning a pair of input couplers.



Figure 15

String assembly of three 2-cell cavities with six input couplers in a class-10 clean room.

were strung with two interconnected bellows, and two beam tubes were attached to both ends. The completed cavity string assembly is shown in Fig. 15. Attachment of the frequency tuner system and alignment of three cavities were carried out. After cold mass assembly such as the cooling pipeline of 2K-He, two reservoir panels of 5K-He and thermal shields of 80K-N₂, the string cavities were inserted into the vacuum vessel. The whole assembly of the injector cryomodule was completed by the end of June 2012, and the cryomodule was installed in the beam line. The first cool-down test of the cryomodule is scheduled for September 2012.

REFERENCES

- [11] S. Noguchi, E. Kako, M. Satoh, T. Shishido, K. Watanabe and Y. Yamamoto, *Proc. IPAC'10* (2010) 2944.
- [12] K. Watanabe, E. Kako, S. Noguchi and T. Shishido, *Proc. HOMSC'12* (2012) WG-A.
- [13] E. Kako, S. Noguchi, T. Shishido, K. Watanabe and Y. Yamamoto, *Proc. IPAC'12* (2012) 2230.
- [14] E. Kako, Y. Kondo, S. Noguchi, T. Shishido, K. Watanabe, Y. Yamamoto, H. Hitomi and K. Sennyu, *Proc. IPAC'12* (2012) 2239.

3-5-2 Nine-cell Cavities for the Main Linac

Development of the basic technologies of the main components has finished and the components for the prototype module of the cERL main linac are now being manufactured. Cold tests of the two 9-cell cavities were carried in a vertical cryostat, and a maximum accelerating gradient of 25 MV/m was achieved (Fig. 16). Field emission at 15 MV/m was sufficiently low and Q value of $>1 \times 10^{10}$ was obtained. After the performance test, each cavity was filled with Ar gas and was welded in the titanium He vessel.

Among the main components, a pair of input couplers was completed, and mounted in a cleanroom onto the power test assembly as shown in Fig. 17. Power conditioning up to 20 kW will be performed before fitting the couplers to the cavity.

Fabrication of the two types of HOM dampers is under way, that is, the small beam pipe (SBP) and the large beam pipe (LBP). A ferrite cylinder of IB004 is bonded to the copper pipe by the hot-isostatic-pressing (HIP) method. Figure 18 shows a completed one which is connected to the LBP of the cavity. Movement of a frequency tuner was tested on the prototype tuner, which is based on the slide-jack structure developed for the ILC cavities. A few micro-meters of movement is smoothly obtained by a piezo tuner to compensate the cavity frequency with a response of 300 Hz/ μ m.

The main linac module (Fig. 19) is scheduled to be assembled in the summer of 2012, which will be followed by a cold test in the autumn. The clean environment and tools for the final assembling are now being prepared.

(a)



(b)

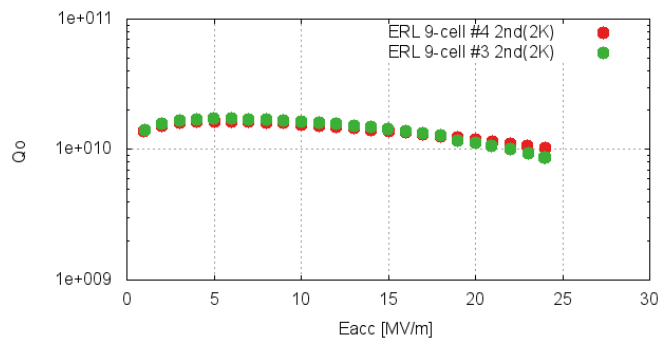


Figure 16

(a) A pair of 9-cell Nb cavities for the cERL main linac. The cavities were annealed, frequency-tuned and electro-polished before the cold performance test in a vertical cryostat. After warming, the test cavities were filled with pure Ar gas and welded to a titanium helium vessel.
 (b) The Q-E plot of the 9-cell cavities for the cERL main linac module.

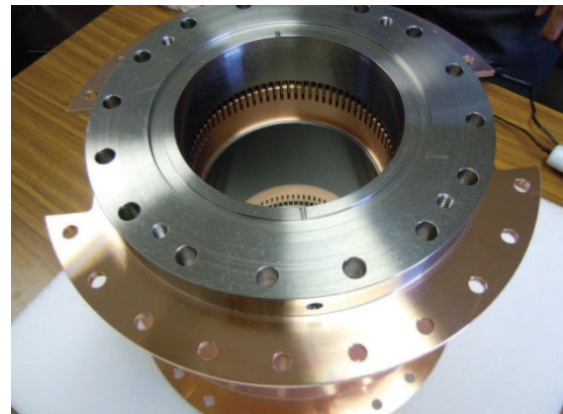


Figure 17

A pair of input couplers was completed, and mounted onto a power test assembly in a clean room. Each coupler has double ceramic windows, cold and warm, to allow the couplers to be assembled in a cryostat without opening the cavity. The ceramics are protected by the interlocks of both the arc detector and vacuum pressure. Thermal anchors of the outer conductor and a nitrogen gas flow in the inner conductor make it possible to feed CW-RF power of 20 kW in full reflection mode. These couplers are to be processed up to 20 kW soon.

Figure 18

A HOM damper with a ferrite absorber. The cERL module contains two LHOM dampers and one SHOM damper. A cylinder of IB004 ferrite is bonded to the inner surface of a copper beam pipe by the HIP method and absorbs HOM power. A short bunched beam of 77 pC induces a wide-range HOM of 150 W in a 9-cell cavity, which is cooled by LN2. A pair of vacuum bellows with a comb-type RF shield is used to isolate the damper thermally from the 2K cavity.

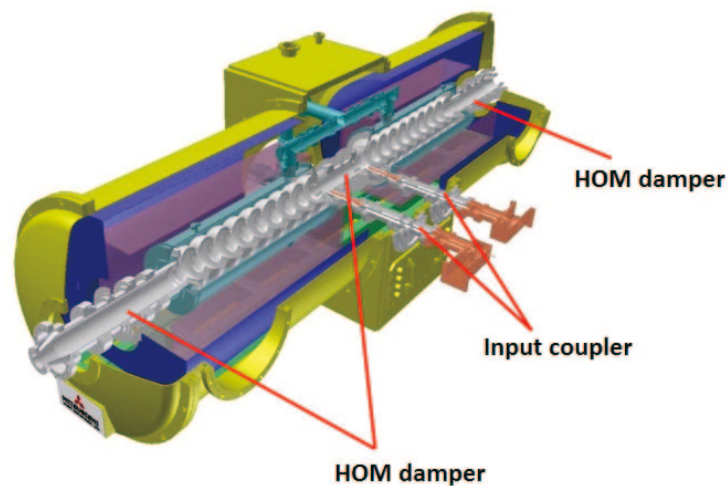


Figure 19

A sketch of the prototype module of the cERL main linac. A pair of 9-cell cavities is connected with HOM dampers which are cooled by LN2.

3-6 RF Power Supply

A total of five RF sources such as klystrons and inductive-output-tubes (IOTs) will be used at the cERL. The RF configuration is summarized in Table 2. Four RF sources have been installed in the ERL development building. After the Great East Japan Earthquake, the minimum recovery work was carried out at a 300 kW klystron and the klystron was used for the coupler conditioning as shown in Fig. 20. A 30 kW IOT and a 30 kW klystron have also been tested. Figure 21 shows the test assembly of a 30 kW klystron.

RF stability of 0.1% in amplitude and 0.1 deg. in phase is required for the low-level RF system (LLRF) of the cERL. In order to satisfy these requirements, it is

especially important to minimize the drift of the amplitude and the phase. Since the experimental hall (outside the radiation shield) has no air-conditioner, a diurnal temperature range of more than 10°C is expected. According to the phase measurements of RF cable at various temperatures, phase drift of 0.5 deg./°C/100m is obtained, which means that the cable temperature should be regulated to within 0.5°C for 40 m (to regulate 0.1 degree in phase). Temperature regulation inside the cable ducts is planned to suppress changes in atmospheric temperature. Figure 22 shows a cable duct with water cooling channel. Two channels will be combined and heat insulation will cover the duct. It has been confirmed that this configuration will suppress temperature drift within 0.1°C.

Table 2 RF configuration at cERL.

Item	Unit	Buncher	Inj-1	Inj-2	Inj-3	ML-1	ML-2
Power required	kW	4.5	10	37	37	11	11
Power output	kW	6.2	17	122		11	11
RF source		IOT	Klystron	Klystron		IOT	IOT
Power available	kW	20	30	300		>15	>15



Figure 20
Coupler test stand with 300 kW klystron.



Figure 21
Evaluation of the 30 kW klystron.



Figure 22
Cable shield for temperature regulation. It consists of an aluminum shield with water cooling channel and plastic thermal insulator.

3-7 Cryogenic System

Operation of the cryogenic system for the compact ERL was officially approved by Ibaraki prefecture under the High Pressure Gas Safety Act in the summer of 2010. Before the cryomodules of the superconducting RF cavities for the injector and the main linacs are connected to the two-Kelvin (2K) helium-refrigerator cold boxes of the cryogenic system, the performance of the cryogenic system on its own should be measured at the temperature of liquid helium and also at the operating temperature of the superconducting cavities, i.e. at 2K. Figure 23 shows the two 2K helium refrigerator cold boxes under cold tests in the ERL development building. A helium liquefier/refrigerator, a 3000L liquid helium storage vessel and a helium gas pumping system are located behind radiation shield walls. The cold box on the right, shown in Fig. 24, is for the cryomodule of the injector linac superconducting RF cavities, and the one on the left, shown in Fig. 25, is for the main linac. Both of the boxes are connected with a high-performance transfer line to reduce the heat load on the cryogenics system.

The cold test for the cryogenic system was carried out step by step. The static heat load to each 2K refrigerator cold box, which means no heat load from the superconducting RF cavities to the cold box, was found to be about 1 W for each, as expected from our experience. The cooling power of the cryogenic system is mainly dependent on the pumping capacity of the helium gas pumping system of the cryogenic system. One pair of rotary oil pump and mechanical booster pump employed in the helium gas pumping system can evacuate helium gas at the flow rate of about 10 m³/h at room temperature, which corresponds to a cooling power of about 10 W at 2K. We have installed four units of the combined vacuum pumps, and so the cooling power is expected to be about 40 W at 2K. An electric heater in the 2K refrigerator cold box was used to simulate the dynamic heat load from the superconducting RF cavities. The results of the cryogenic test of the two cold boxes under operation among the four pump units showed that one cold box had cooling power of about 20 W at 2K, while the other cold box was kept at 2K without any dynamic heat load. It is concluded that each cold box has cooling power of about 20 W, and thus with four vacuum pumps, the cryogenic system can absorb heat load of about 40 W at 2K in total.

In fiscal 2012, it is planned that both of the cryomodules of superconducting RF cavities for the injector and main linacs will be connected to the cryogenic system with high-performance connection lines under the High Pressure Gas Safety Act. Though we will increase the number of units to eight next fiscal year and then the cooling power will be enhanced up to about 80 W at 2K, it is still necessary to estimate precisely the total heat load to the cryogenic system from the two cryomodules for the injector and main linacs.



Figure 23
2K helium refrigerator cold boxes which will be connected with cryomodules of superconducting RF cavities for injector and main linacs.



Figure 24
2K helium refrigerator cold box for injector linac under cold test.



Figure 25
2K helium refrigerator cold box for the main linac under cold test.

3-8 Status of Construction

In the ERL Test Facility (renamed from the East Counter Hall), construction of the radiation shield for the cERL started in February 2012. The radiation shield consists of about 300 concrete blocks, amounting to 4,800 tons. Before these blocks were installed, the hall was surveyed in order to prepare a flat base for setting the blocks. After installing the wall part blocks, ceiling blocks were mounted in order. The radiation shield will be completed in September 2012, and the cERL components will be installed by the end of March 2013 (Fig. 26).



Figure 26
Construction of the cERL radiation shield.

Users Program & Outreach Activities



Users Program and Outreach Activities

1. Experimental Proposals	131
1-1 Scientific Proposals	
1-2 Industrial Proposals	
1-3 Statistics of the Proposals	
2. Workshops and Seminars	134
2-1 PF Symposium	
2-2 PF Workshops	
2-3 IMSS Seminars	
3. Graduate School Education	135
4. International Collaboration	136
4-1 Overview	
4-2 Australian Beamline	
4-3 Indian Beamline	
4-4 Support for Korean Synchrotron Users during the Shutdown of PLS	
4-5 Cooperation to SESAME Project	
4-6 XDL2011 Workshops	
5. Photon Factory Science Advisory Committee (PF-SAC)	138

1 Experimental Proposals

1-1 Scientific Proposals

The Photon Factory accepts experimental proposals submitted by researchers mainly at universities and research institutes inside and outside Japan. The proposals are reviewed by the PF Program Advisory

Committee (PF-PAC), and those that are favorably recommended are accepted and formally approved by the Advisory Committee for the Institute of Materials Structure Science. The number of accepted proposals over the period 2000-2011 is shown in Table 1, where S1/S2, U, G, and P denote Special, Urgent, General and

Table 1 Number of proposals accepted for the period 1999-2011.

FY	2000	2001	2002	2003	2004	2005	2006	2007	2008	2009	2010	2011
S1	0	0	0	1	1	0	1	0	0	0	0	0
S2	2	2	3	2	0	3	6	1	4	6	3	2
U	0	5	3	2	4	0	1	7	3	2	2	0
G	308	339	321	318	382	310	388	403	402	397	407	415
P	17	18	16	9	13	10	22	14	14	14	16	11

Table 2 List of S-type proposals effective in FY2011.

Proposal No.	Spokesperson	Title
2008S2-002	M. Ando Tokyo Univ. of Sci.	Basic study of high performance refraction-based X-ray imaging toward clinical and pathological application
2008S2-003	M. Oshima Univ. of Tokyo	Electronic structure analysis of new functional materials by high-resolution nano-spectroscopy
2008S2-004	Y. Wakabayashi KEK-PF	Structural materials science under magnetic fields — mainly on magnetic field induced phase transition —
2009S2-001	S. Adachi KEK-PF	Real-time structural dynamics studies for materials and biological sciences
2009S2-003	R. Kumai AIST	Structural study for the origin of phase transition in correlated electron system
2009S2-005	A. Fujimori Univ. of Tokyo	High-resolution ARPES of novel superconductors and related material
2009S2-006	T. Takeda Univ. of Tsukuba	Biomedical and material imaging using X-ray interferometer
2009S2-007	J. Yoshinobu Univ. of Tokyo	Electronic states and charge transfer dynamics of organic molecules on surfaces
2009S2-008	H. Nakao KEK-PF	Condensed matter studied by resonant soft/hard X-ray scattering
2010S2-001	K. Amemiya KEK-PF	Exploration of spintronics materials by soft X-ray polarization switching
2010S2-003	Y. Nagashima Tokyo Univ. of Sci.	Laser spectroscopy of positronium negative ions and its applications
2010S2-004	A. Nakao KEK-PF	Structural studies of molecular crystals under extreme conditions
2011S2-003	M. Oshima Univ. of Tokyo	Operando analysis of green nano-device structures by high-resolution electron spectroscopy
2011S2-005	T. Tsukihara Univ. of Hyogo	Target protein research program

Preliminary proposals, respectively. The number of current G-type proposals each year has been around 800 for the past few years. A full list of the proposals effective in FY2011 and their scientific output can be found in Part B of this volume.

S-type proposals are divided into two categories, S1 and S2. S1 proposals are self-contained projects of excellent scientific quality, and include projects such as the construction and improvement of beamlines and experimental stations which will be available for general users after the completion of the project. S2 proposals are superior-grade projects that require the full use of synchrotron radiation or a large amount of beam time. Table 2 lists the S-type projects effective in FY2011. The current status and results to date of S1 and S2 proposals must be reported at the PF Symposium held at the end of every Japanese fiscal year. The scientific output of S1 and S2 proposals is presented in the Highlights of Part A and in the Users' Reports of Part B of this volume.

Proposals are categorized into five scientific disciplines, and reviewed by the five subcommittees of PF-PAC: 1) electronic structure, 2) structural science, 3) chemistry and new materials, 4) life science I (protein crystallography), and 5) life science II. Figure 1 shows the distribution by research field of the proposals accepted by the subcommittees in FY2011.

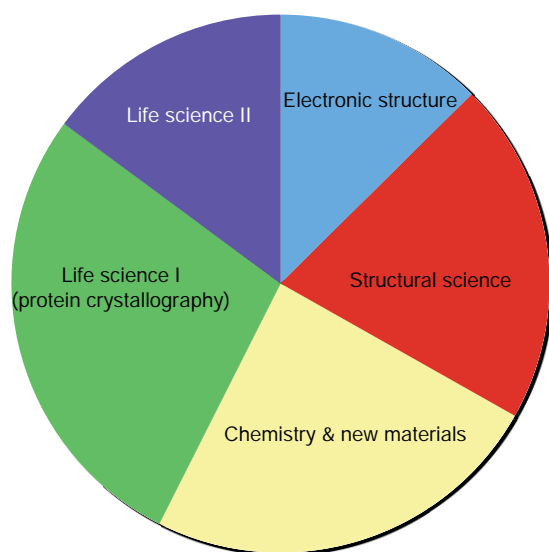


Figure 1
Distribution by scientific field of experimental proposals accepted in FY2011.

1-2 Industrial Proposals

The S, U, G, and P-type proposals are opened for nonproprietary industrial research by limited companies that can apply for the Grant-in-Aid for Scientific Research. Besides these, 29 proprietary industrial projects (Y-type) and 12 nonproprietary collaborative studies with private companies (C-type) were conducted.

Fourteen trial-use programs for industrial applica-

tions are carried out with the financial support of a MEXT project, the Open Advanced Research Facilities Initiative. Among these, 8 are newly approved, 5 are continued from FY2010 and one is an XAFS training course. About half of the companies are continuing Y or C-type projects after the end of the trial-use program.

1-3 Statistics of the Proposals

The number of users, for all types of proposals, has reached 3,266. Although the number of experimental stations has decreased, the approved academic proposals and number of users have increased annually, as shown in Fig. 2. This indicates a high and increasing demand for synchrotron radiation and can be attributed to continuous improvements in the storage rings, beamlines, and end stations. The synchrotron has become one of the most important research tools to carry out advanced science experiments and developments. About 19% of the proposals are conducted by new spokespersons, which indicates that the Photon Factory is open to public academic scientists. Figure 3 shows the demographics and distribution of users by institution and position. Around three-fourths of the users belong to universities, with approximately 60% of the users associated with national universities. Sixty percent of the university users are graduate and undergraduate students; this indicates that the Photon Factory plays an important role in both research and education in universities. The geographical distribution of the Photon Factory users is shown in Fig. 4 and Fig. 5. Approximately 60% of the users come from the eastern part of Japan. Nevertheless, there are users from all over Japan, which also indicates the immense contribution of the Photon Factory to research and education in Japan. The registered number of papers published in 2011 based on experiments at the PF was 599 at the time of this writing and is expected to exceed 650. In addition, 36 doctoral and 99 master theses have been presented thus far, which indicates the significant role of the Photon Factory in graduate-level university education.

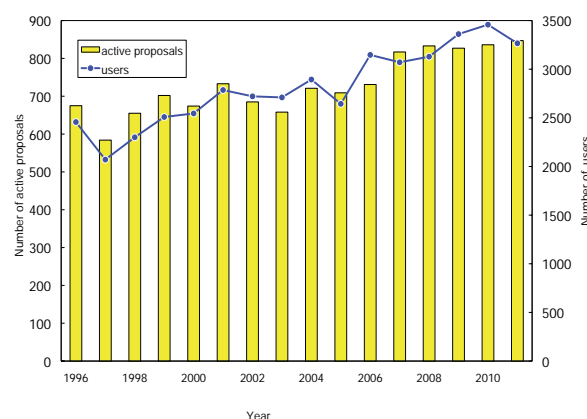


Figure 2
Number of registered PF users and scientific proposals over the period 1996-2011.

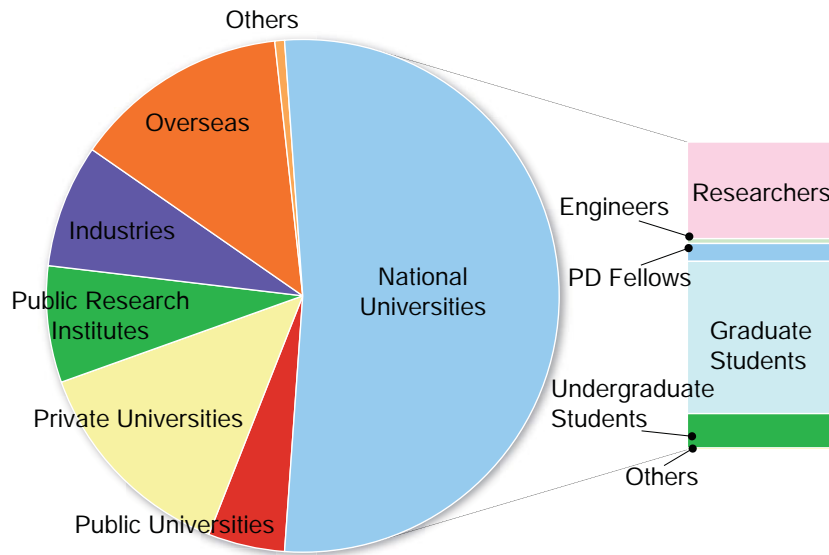


Figure 3
Distribution of users in terms of institution and position.

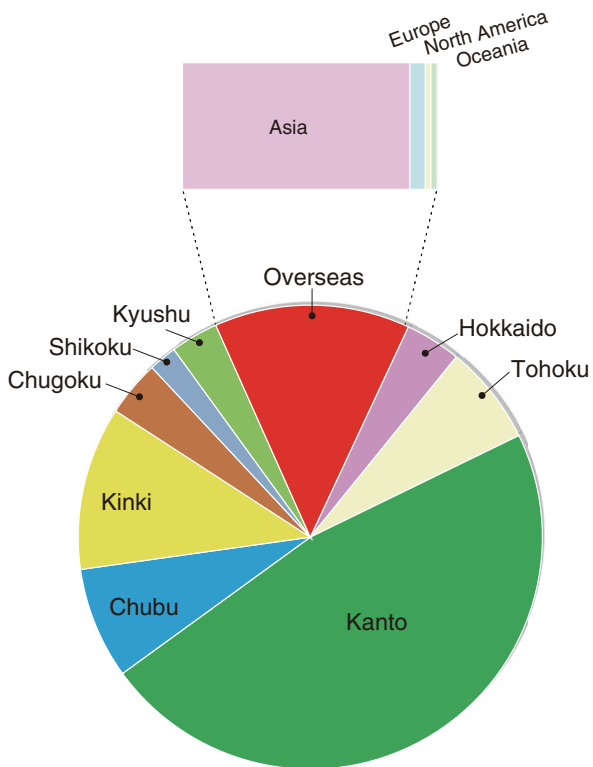


Figure 4
Regional distribution of the spokespersons of proposals accepted in FY2011.

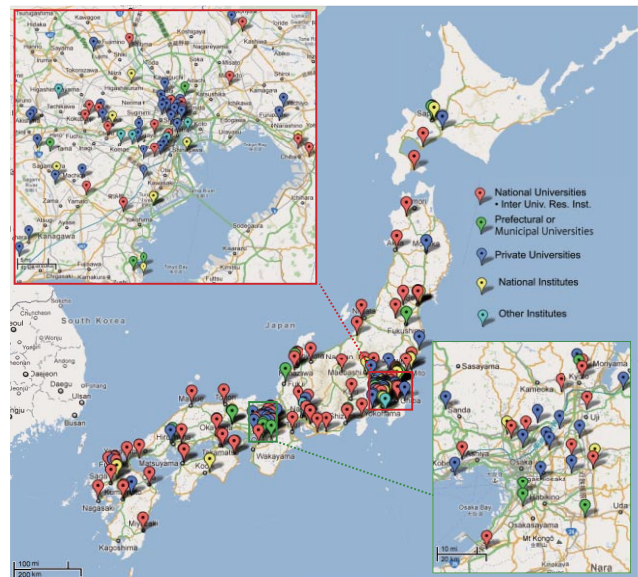


Figure 5
Affiliation of Photon Factory users in FY 2011 (domestic users only).

2 Workshops and Seminars

2-1 PF Symposium

The 28th PF Symposium, the annual users' meeting, was held on July 12-13, 2011 at the EPOCHAL Tsukuba under the support of the PF user's community and KEK. This meeting was originally scheduled to hold on March 14-15, however because of the big earthquake on March 11 in Japan, it was postponed. This symposium has been already reported in ACR2010.

The 29th PF Symposium, the annual users' meeting, was held on March 12-13, 2012 at the EPOCHAL Tsukuba under the support of the PF user's community and KEK. More than 377 users and PF staff participated in the symposium. The main purpose of the PF Symposium is to discuss the present status and future projects of the PF, and is that users and the PF staff promote mutual friendship through scientific presentations and discussion. In addition, this year is a memorial one, because we mark the 30th anniversary of PF counting from the year of 1982, when the first light beam was delivered. We hence had special lectures from three professors who have greatly contributed to PF: Prof. K. Kohra, the first director of PF, Prof. T. Sasaki, the first head of the former Detector Division, and Prof. K. Hodgson from SSRL, who have worked for a long time as the chair of the PF Science Advisory Committee. Their talks particularly about efforts at the early days were not only very interesting but also urged us to create a new fruitful future for the next decades.



2-2 PF Workshops

Seven PF workshops were held in FY2011. Anyone can propose such a workshop. Free discussion is made upon a specific scientific topic in synchrotron-radiation research and its related application fields. The proceedings of the workshops are found in the KEK proceedings, which are available at the KEK Library.

- (1) "ERL Science Workshop II" held on April 27-28, 2011. KEK Proceedings 2011-1 (in Japanese).
- (2) "Prospect on Synchrotron Radiobiology Focusing on Inhomogeneous Energy Deposition" held on July 14-15, 2011.
- (3) "Recent Development of the Experimental Techniques in High-Pressure Research on Synchrotron Radiation Sources II: Multi-anvil-type High-pressure Apparatus" held on August 2-3, 2011. KEK Proceedings 2011-10 (in Japanese).
- (4) "Recent Development of GI-SAS and their Application" held on September 5-6, 2011. KEK Proceedings 2011-11 (in Japanese).
- (5) "Micro beam utilized XAFS, XRF and SAXS Experiments at PF" held on September 7-8, 2011. KEK Proceedings 2011-12 (in Japanese).
- (6) "Current Status and Progress of Condensed Matter Research by Soft X-ray Spectroscopic and Scattering Measurements" held on September 13-14, 2011. KEK Proceedings 2011-13 (in Japanese).
- (7) "Exploring Magnetic Thin Films and Multilayers: from the Characterization to the Development of Novel Materials" held on October 14-15, 2011. KEK Proceedings 2012-1 (in Japanese).

2-3 Seminars

The seminars hosted by each scientific project in the Institute of Materials Structure Science (IMSS) were arranged as the seminars hosted by IMSS; those are called "IMSS Seminar" and "IMSS Danwakai". This seminar will provide an opportunity to exchange the knowledge among a wide range of sciences, such as synchrotron, neutron and muon. The seminars were held in FY2011 (<http://imss.kek.jp/seminar/imss-danwakai/2011/index.html>).

3 Graduate School Education

KEK is one of the core organizations of the Graduate University for Advanced Studies (SOKENDAI) with the Departments of Materials Structure Science, Accelerator Science, and Particle and Nuclear Physics. Some of the PF staff members are in charge of giving lectures and supervising graduate students. There is also a system of Joint PhD (JPHD) students, who are accepted by the PF to pursue advanced studies under the supervision of PF staff members towards their PhD degrees in collaboration with their home universities. The number of graduate students who entered SOKENDAI during the past fifteen years is shown in Table 1.

SOKENDAI has been offering a flexible five-year PhD course: the five-year PhD course for undergraduate students and a three-year course for master's degree holders.

SOKENDAI-KEK held its "open campus day" for young researchers and college students at the Tsukuba campus on July 7, 2011 and half-day guidance meetings for potential young candidates in early summer 2011 in Osaka, Tokyo and Kyushu.

In addition to the SOKENDAI and JPHD graduate students, a number of doctoral theses have been written based on research carried out at the PF. Figure 1 shows the number of graduate students who obtained a PhD degree related to scientific activities at the PF.

Table 1 Number of SOKENDAI and JPHD students at the PF over the period 1997-2011.

FY	SOKENDAI	JPHD
1997	10	5
1998	9	14
1999	6	11
2000	8	12
2001	10	8
2002	12	13
2003	12	7
2004	14	5
2005	14	6
2006	9	10
2007	6	13
2008	6	10
2009	6	9
2010	5	10
2011	4	5

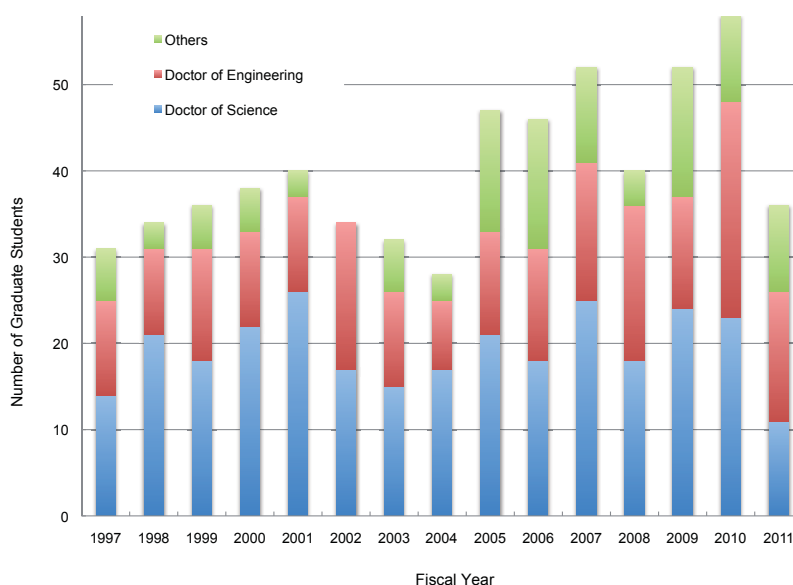


Figure 1
Number of students who obtained doctoral degrees based on scientific activities at the PF.

4 International Collaboration

4-1 Overview

The Photon Factory is collaborating internationally in various ways. Two stations, BL-20B and BL-18B, are operated by Australian and Indian organizations, respectively. The Australian National beamline BL-20B was constructed by the Australian Nuclear Science and Technology Organization (ANSTO) and has been operated since 1992. The Indian beamline BL-18B was leased to the Department of Science and Technology (DST) of the Government of India, and started operation in 2009. The Photon Factory is also collaborating with international synchrotron radiation communities through meetings, workshops, and schools.

4-2 Australian Beamline

The Australian beamline BL-20B was originally constructed by ANSTO in 1992, and Australian Synchrotron (AS) took over operation of the beamline at the PF from 2008. In FY2011, 22 experiments were carried out at BL-20B. Most of them used the XAFS technique, especially fluorescent XAFS experiments on environmental and biological systems. Twenty-eight papers based on BL-20B experiments were published in 2011.

4-3 Indian Beamline

The DST, Government of India and KEK agreed to set up an Indian beamline at the Photon Factory in 2008 with the Saha Institute of Nuclear Physics (SINP) as a key institute of India. Beamline 18B is leased to DST, and SINP set up two diffractometers and related detection systems. Although the opening of the beamline to public Indian users was delayed owing to the earthquake, 13 experiments were carried out at BL-18B, and 3 papers on the results were published in 2011.



Figure 1
Dr. Srikumar Banerjee, Chairman of the Atomic Energy Commission, visited the Indian Beamline on January 23, 2012.

4-4 Support for Korean Synchrotron Users during the Shutdown of PLS

Pohang Light Source (PLS) users utilized the Photon Factory during the construction and commissioning phase of Pohang Light Source II (PLS II) (December 2010 – July 2012). Based on the MOU, the Photon Factory provided beam time to PLS users and Pohang Accelerator Laboratory (PAL) sent beamline scientists to support the experiments of PLS users at the Photon Factory. About 32 proposals were approved by PF-PAC in FY2011. Despite the shutdown owing to the earthquake, the beamline was used for 125.3 hours in FY2011.

4-5 Cooperation to SESAME Project

Synchrotron-light for Experimental Science and Applications in the Middle East (SESAME) is a synchrotron radiation facility under construction in Amman, Jordan as a collaborative project among countries in the Middle East under the auspices of UNESCO. SESAME is expected to be operational in 2015, and KEK is continuously supporting the construction and potential user community at SESAME in various ways. As one of the activities, the SESAME-JSPS School of Synchrotron Radiation Science was held, which is intended to serve as a platform for transferring knowledge to young scientists, engineers and students in SESAME countries. The school was originally planned to be held from March 17 to 21, 2011, in Amman, Jordan. However, due to the earthquake on March 11 in Japan, the school was postponed until November 2011. The workshop consisted of lectures and practice sessions in materials science, structural biology, electronic structure, XAFS and X-ray fluorescence analysis, in line with the needs of the SESAME Phase-I beamlines.



Figure 2
Participants of the SESAME-JSPS School.

4-6. XDL2011 Workshops

Workshops on science at the hard X-ray diffraction limit (XDL2011) were held at Cornell University in June 2011. A series of six workshops was co-sponsored by the Photon Factory, CHESS, DESY, and SSRL, and devoted to science with diffraction-limited, high repetition rate, hard X-ray sources, e.g., Energy Recovery Linac and Ultimate Storage Ring sources. In total, 488 participants gathered with high expectations and interest. The titles of the six workshops were as follows.

- WS1: Diffraction Microscopy, Holography and Ptychography using Coherent Beams
- WS2: Biomolecular Structure from Nanocrystals and Diffuse Scattering
- WS3: Ultra-fast Science with "Tickle and Probe"
- WS4: High-pressure Science at the Edge of Feasibility
- WS5: Materials Science with Coherent Nanobeams at the Edge of Feasibility
- WS6: Frontier Science with X-ray Correlation Spectroscopies using Continuous Sources

5

Photon Factory Science Advisory Committee (PF-SAC)

Meetings of the Photon Factory Science Advisory Committee (PF-SAC) have been held every nine months since the first PF-SAC in April 2007, providing ongoing advice on the operation and strategic planning for the Photon Factory. The sixth PF-SAC meeting was held on October 6 and 7, 2011. It had originally been scheduled for mid-March 2011, but was postponed by almost a half year due to the Great East Japan Earthquake on March 11.

Table 1 shows a list of members for the sixth PF-SAC. The Photon Factory distributed in advance presentation files and a list of discussion points (Table 2) on which the Photon Factory wished to receive advice from the PF-SAC. On the first day of the meeting, the Photon Factory staff and users presented the present situation and strategy relevant to the discussion points and several recent scientific topics. Following Q&A and discussion for each presentation, PF-SAC met in closed sessions in the evening of the first day and the morning of the second day, and formulated the observations,

conclusions and recommendations.

Regarding the sixth discussion point in Table 2, the PF-SAC notes that the 3 GeV ERL will provide the Japanese VUV-SX community with extremely high-brilliance soft X-ray beams. The source characteristics are superior to existing Japanese soft X-ray SR sources and will provide Japan with a world-class facility. Other itemized questions and the answers from the PF-SAC can be found at:

http://pfwww.kek.jp/SAC11Oct/PFSAC2011_executivesummary.pdf

To assess specific areas of PF scientific activities, subcommittee meetings of the PF-SAC have been held since 2008. The time-resolved science subcommittee (chaired by Dr. Robert Schönlein) met on February 15 and 16, 2011 to review the activities of the “Development in Future SRR Group” of the Photon Factory. The close-out report of the subcommittee can be found at:

http://pfwww.kek.jp/SAC11Feb_TRsub/index.html

Table 1 PF-SAC members of 2011.

FONTES Ernest	Cornell High Energy Synchrotron Source
GLUSKIN Efim	Advanced Photon Source
HODGSON Keith	Stanford University, Chairperson of Committee
IWASAWA Yasuhiro	University of Electro-Communications Tokyo
IYE Yasuhiro	Institute for Solid State Physics, The University of Tokyo
LINDAU Ingolf	Stanford University
MIKI Kunio	Kyoto University
MIZUKI Junichiro	Japan Atomic Energy Agency
PARMIGIANI Fulvio	University of Trieste
REE Moonhor	Pohang Accelerator Laboratory/PSTEC
ZHAO Zhentang	Shanghai Synchrotron Radiation Facility
SAILE Volker	University of Karlsruhe

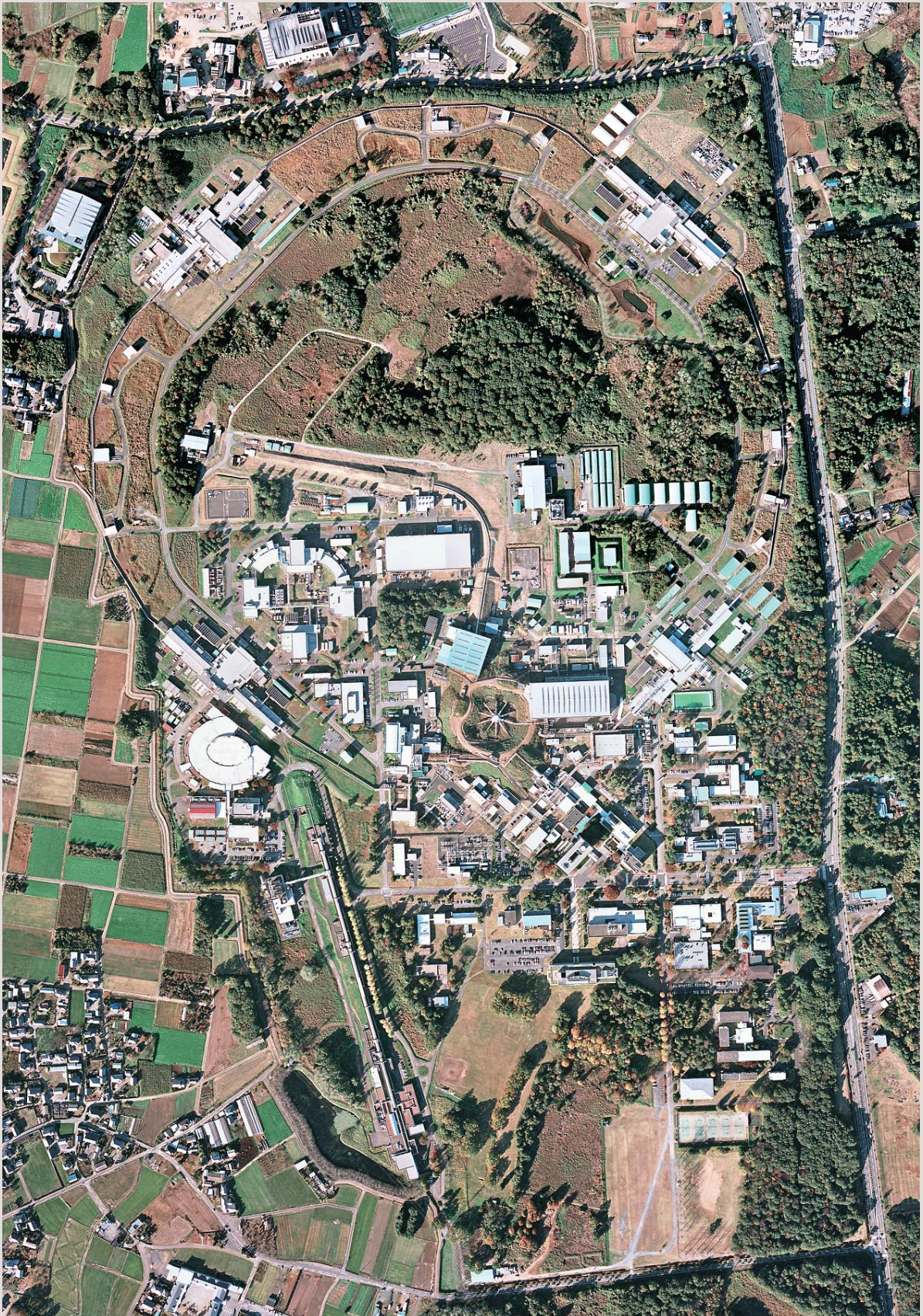
Table 2 List of discussion points.

1	How effective were the earthquake recovery and refurbishment processes, and the coordination with other SR facilities for experiments during recovery?
2	Relation between PF operation and KEKB upgrade
3	Is the second phase of the refurbishment plan aggressive enough?
4	How does PF-SAC evaluate the results and suggestions of the two subcommittees: condensed matter and materials & chemistry?
5	Is the plan for the transition from PF-Kondankai to a more independent and full-membership PF User Association sound and timely?
6	Are we moving in the right direction and fast enough towards the realization of ERL? Is the change of energy from 5 GeV to 3 GeV reasonable?
7	Are we focused enough in the recruitment campaign?
8	Comments on science topics and discussions with group leaders and scientists

Appendices



1. Site and Organization





KEK consists of four research institutions, i.e., the Institute of Materials Structure Science (IMSS), the Institute of Particle and Nuclear Studies (IPNS), the Accelerator Laboratory (AL), and the Applied Research Laboratory. As shown in Fig. 1, the IMSS constitutes the Synchrotron Radiation Divisions I and II, the Neutron Science Division, the Muon Science Division, the Structural Biology Research Center, and the Condensed Matter Research Center. Table I shows a list of the members of the Advisory Committee of the IMSS.

Photon Factory (PF) consists of two divisions of the IMSS (the Synchrotron Radiation Divisions I and II) and the Accelerator Division VII of the AL as shown in the organization chart of Fig. 2. The staff members

of the PF list in Table 2. Synchrotron Radiation Science Divisions I and II consist of seven groups such as “Electronic Structure”, “Structural Material Science”, “Materials Chemistry”, “Life Sciences”, “Beamline Engineering, Technical Services & Safety”, “User Support and Dissemination”. The Accelerator Division VII has six groups, which are named Light Source Group I to VI. The missions of each group are as follows: Group I is in charge of orbits, magnets, and insertion devices, Group II of RF, SC cavities and so on, Group III mainly of vacuum, Group IV mainly of beam diagnostics and accelerator control, Group V of front-end, safety and so on, and Group VI mainly of electron guns.

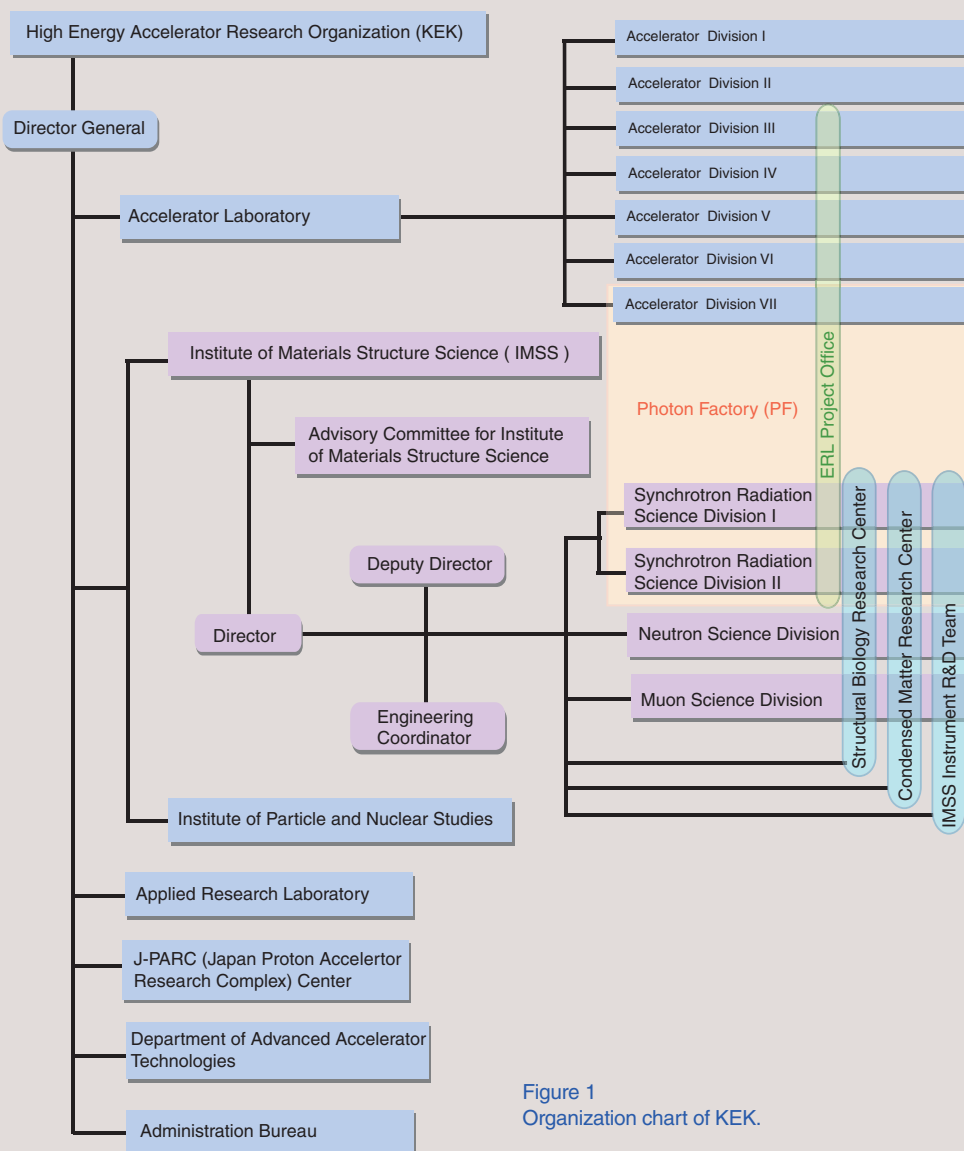


Figure 1 Organization chart of KEK.

Table 1 The members of the Advisory Committee for Institute of Materials Structure Science.

AKIMITSU, Jun	Aoyama Gakuin University
ASAKURA, Kiyotaka	Hokkaido University, CRC
BAN, Shuichi	Applied Research Laboratory, KEK
ENOMOTO, Atsushi	Accelerator Laboratory, KEK
FUJII, Yasuhiko	Comprehensive Research Organization for Science and Society
IKEDA, Susumu*	Neutron Science Division, IMSS, KEK
ITO, Kenji	Photon Factory, IMSS, KEK
KADONO, Ryosuke	Muon Science Division, IMSS, KEK
KAWATA, Hiroshi	Photon Factory, IMSS, KEK
KISHIMOTO, Shunji	Photon Factory, IMSS, KEK
KOBAYASHI, Yukinori	Photon Factory, Accelerator Laboratory, KEK
MIKI, Kunio	Kyoto University
MIYAKE, Yasuhiro	Muon Science Division, IMSS, KEK
MURAKAMI, Youichi	Photon Factory, IMSS, KEK
NOMURA, Masaharu	Photon Factory, IMSS, KEK
OSHIMA, Masaharu	The University of Tokyo
SAITO, Naohito	Institute of Particle and Nuclear Studies, KEK
SAKATA, Makoto**	Nagoya University
SETO, Hideki	Neutron Science Division, IMSS, KEK
SHIBAYAMA, Mitsuhiro	ISSP, The University of Tokyo
TAKATA, Masaki	RIKEN/SPring-8
TORIKAI, Eiko	University of Yamanashi
WAKATSUKI, Soichi	Photon Factory, IMSS, KEK
YAMADA, Kazuyoshi	Tohoku University, WPI-AIMR

* Chairperson ** Vice-Chairperson

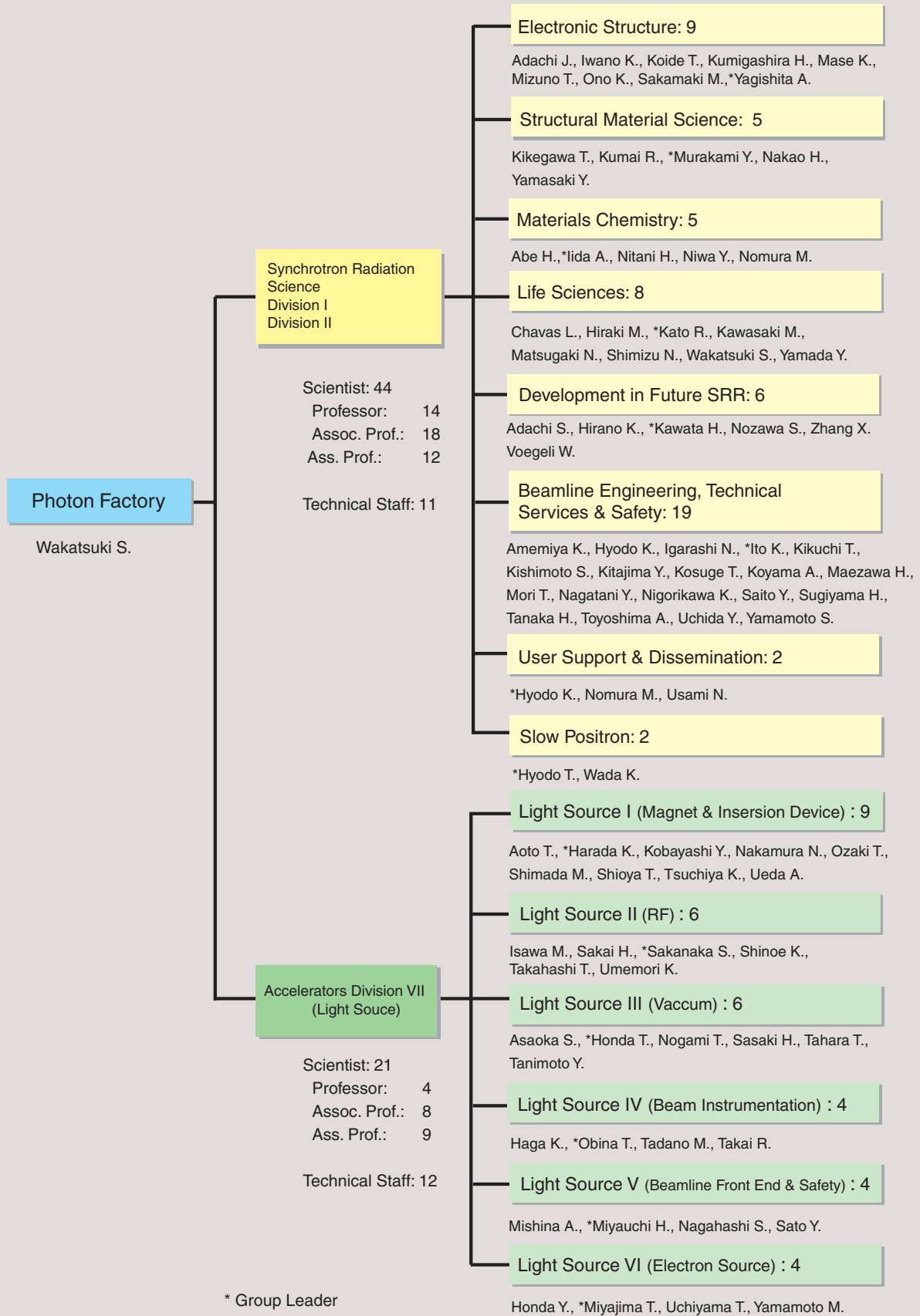


Figure 2
Organization chart of PF (as of March 31, 2012) .

Table 2 Staff members of the Photon Factory.

Name	Group [§]	e-mail address
Research Staff		
Director		
WAKATSUKI, Soichi	LS	soichi.wakatsuki*kek.jp
Synchrotron Radiation Science Division I & II		
ABE, Hitoshi	MC	hitoshi.abe*kek.jp
ADACHI, Jun-ichi	ES	jun-ichi.adachi*kek.jp
ADACHI, Shinichi	DF (SMS)	shinichi.adachi*kek.jp
AMEMIYA, Kenta	BETSS (ES)	kenta.amemiya*kek.jp
CHAVAS, Leonard	LS	leonard.chavas*kek.jp
HIRAKI, Masahiko	LS	masahiko.hiraki*kek.jp
HIRANO, Keiichi	DF	keiichi.hirano*kek.jp
HYODO, Kazuyuki	BETSS (USD)	kazuyuki.hyodo*kek.jp
HYODO, Toshio	SPF	toshio.hyodo*kek.jp
IGARASHI, Noriyuki	BETSS (LS)	noriyuki.igarashi*kek.jp
IIDA, Atsuo	MC	atsuo.iida*kek.jp
ITO, Kenji	BETSS (ES)	kenji.ito*kek.jp
IWANO, Kaoru	ES (DF)	kaoru.iwano*kek.jp
KATO, Ryuichi	LS	ryuichi.kato*kek.jp
KAWASAKI, Masato	LS	kawasaki*pfweis.kek.jp
KAWATA, Hiroshi	DF	hiroshi.kawata*kek.jp
KIKEGAWA, Takumi	SMS	takumi.kikegawa*kek.jp
KIKUCHI, Takashi	BETSS	takashi.kikuchi*kek.jp
KISHIMOTO, Shunji	BETSS (DF)	syunji.kishimoto*kek.jp
KITAJIMA, Yoshinori	BETSS (ES)	yoshinori.kitajima*kek.jp
KOIDE, Tsuneharu	ES	tsuneharu.koide*kek.jp
KOSUGE, Takashi	BETSS	takashi.kosuge*kek.jp
KOYAMA, Atsushi	BETSS	atsushi.koyama*kek.jp
KUMAI, Reiji	SMS	reiji.kumai*kek.jp
KUMIGASHIRA, Hiroshi	ES	hiroshi.kumigashira*kek.jp
MAEZAWA, Hideki	BETSS	hideki.maezawa*kek.jp
MASE, Kazuhiko	ES	kazuhiko.mase*kek.jp
MATSUGAKI, Naohiro	LS	naohiro.matsugaki*kek.jp
MIZUNO, Tomoya	ES	tmizuno*post.kek.jp
MORI, Takeharu	BETSS	takeharu.mori*kek.jp
MURAKAMI, Youichi	SMS	youichi.murakami*kek.jp
NAGATANI, Yasuko	BETSS	yasukon*post.kek.jp
NAKAO, Hironori	SMS	hironori.nakao*kek.jp
NIGORIKAWA, Kazuyuki	BETSS	kazuyuki.nigorikawa*kek.jp
NITANI, Hiroaki	MC	hiroaki.nitani*kek.jp
NIWA, Yasuhiro	MC (BETSS)	yasuhiro.niwa*kek.jp
NOMURA, Masaharu	MC	masaharu.nomura*kek.jp
NOZAWA, Shunsuke	DF	noz*post.kek.jp
ONO, Kanta	ES	kanta.ono*kek.jp
SAITO, Yuuki	BETSS	yuuki.saito*kek.jp
SAKAMAKI, Masako	ES	masakos*post.kek.jp
SHIMIZU, Nobutaka	LS	nobutaka.shimizu*kek.jp
SUGIYAMA, Hiroshi	BETSS (DF)	hiroshi.sugiyama*kek.jp

Name	Group ^s	e-mail address
TANAKA, Hirokazu	BETSS	hirokazu.tanaka*kek.jp
TOYOSHIMA, Akio	BETSS	akio.toyoshima*kek.jp
UCHIDA, Yoshinori	BETSS	yoshinori.uchida*kek.jp
USAMI, Noriko	USD (LS)	noriko.usami*kek.jp
VOEGELI, Wolfgang	DF	wolfgang.voegeli*kek.jp
WADA, Ken	SPF	ken.wada*kek.jp
YAGISHITA, Akira	ES	akira.yagishita*kek.jp
YAMADA, Yusuke	LS	yama*post.kek.jp
YAMAMOTO, Shigeru	BETSS	shigeru.yamamoto*kek.jp
YAMASAKI, Yuichi	SMS	yuichi.yamasaki*kek.jp
ZHANG, Xiaowei	DF	zhang.xiaowei*kek.jp
Accelerator Division VII		
AOTO, Tomohiro	Light Source I	tomohiro.aoto*kek.jp
ASAOKA, Seiji	Light Source III	seiji.asaoka*kek.jp
HAGA, Kaiichi	Light Source IV	kaiichi.haga*kek.jp
HARADA, Kentaro	Light Source I	kentaro.harada*kek.jp
HONDA, Tohru	Light Source III	tohru.honda*kek.jp
HONDA, Yosuke	Light Source VI	yosuke*post.kek.jp
ISAWA, Masaaki	Light Source II	isawa*post.kek.jp
KOBAYASHI, Yukinori	Light Source I	yukinori.kobayashi*kek.jp
MISHINA, Atsushi	Light Source V	
MIYAJIMA, Tsukasa	Light Source VI	tsukasa.miyajima*kek.jp
MIYAUCHI, Hiroshi	Light Source V	hiroshi.miyauchi*kek.jp
NAGAHASHI, Shinya	Light Source V	shinya.nagahashi*kek.jp
NAKAMURA, Norio	Light Source I	norio.nakamura*kek.jp
NOGAMI, Takashi	Light Source III	takashi.nogami*kek.jp
OBINA, Takashi	Light Source IV	takashi.obina*kek.jp
OZAKI, Toshiyuki	Light Source I	ozaki*post.kek.jp
SAKAI, Hiroshi	Light Source III	sakai.hiroshi*kek.jp
SAKANAKA, Shogo	Light Source II	shogo.sakanaka*kek.jp
SASAKI, Hiroyuki	Light Source III	hiroyuki.sasaki*kek.jp
SATO, Yoshihiro	Light Source V	yoshihiro.sato*kek.jp
SHIMADA, Miho	Light Source I	miho.shimada*kek.jp
SHINOE, Kenji	Light Source II	kenji.shinoe*kek.jp
SHIOYA, Tatsuro	Light Source I	tatsuro.shioya*kek.jp
TADANO, Mikito	Light Source IV	mikito.tadano*kek.jp
TAHARA, Toshihiro	Light Source III	ttahara*post.kek.jp
TAKAHASHI, Takeshi	Light Source II	takeshi.takahashi*kek.jp
TAKAI, Ryota	Light Source IV	ryota.takai*kek.jp
TANIMOTO, Yasunori	Light Source III	yasunori.tanimoto*kek.jp
TSUCHIYA, Kimichika	Light Source I	kimichika.tsuchiya*kek.jp
UCHIYAMA, Takashi	Light Source VI	takashi.uchiyama*kek.jp
UEDA, Akira	Light Source I	akira.ueda*kek.jp
UMEMORI, Kensei	Light Source II	kensei.umemori*kek.jp
YAMAMOTO, Masahiro	Light Source VI	masahiro*post.kek.jp

Name	Group [§]	e-mail address
Guest Professor		
ASAKURA, Kiyotaka	(Hokkaido Univ.)	
HAJIMA, Ryoichi	(JAEA)	
ISHIHARA, Sumio	(Tohoku Univ.)	
KATO, Masahiro	(IMS)	
KONDO, Tadashi	(Osaka Univ.)	
KOSHIHARA, Shinya	(Tokyo Inst. Tech.)	
MORITOMO, Yutaka	(Tsukuba Univ.)	
NAKAGAWA, Atsushi	(Osaka Univ.)	
NAMIKAWA, Kazumichi	(Tokyo Univ. of Sci.)	
NODA, Yukio	(Tohoku Univ.)	
OHKUMA, Haruo	(JASRI/SPring-8)	

Postdoctoral Fellow

OKAZAKI, Seiji	okazakis*post.kek.jp
SATO, Tokushi	tosato*post.kek.jp
SUDAYAMA, Takaaki	takaaki.sudayama*kek.jp
YONEMURA, Hiroki	Hiroki.yonemura*kek.jp

The Graduate University for Advanced Studies

MATSUI, Takuto
 NAKAMURA, Kensuke
 OHKUBO, Ken
 WU, Yanlin
 MABIED, Ahmed

[§] Synchrotron Radiation Science Division

ES	Electronic Structure
SMS	Structural Material Science
MC	Materials Chemistry
LS	Life Sciences
DF	Development in Future SRR
BETSS	Beamline Engineering, Technical Services and Safety
USD	User Support and Dissemination
SP	Slow Positron

Italic: the additional post

2. Awards

The Commendation for Science and Technology by the Minister of Education, Culture, Sports, Science and Technology, Prizes for Science and Technology

WAKATSUKI Soichi (KEK-PF)

“Advancements of Synchrotron X-Ray Crystallography and Structural Studies on Protein Transport and Modifications”

The Commendation for Science and Technology by the Minister of Education, Culture, Sports, Science and Technology, Prizes for Science and Technology

KAKIMOTO Kenichi (Nagoya Inst. of Tech.)

“Study on Lead-Free Niobate Piezoelectric Ceramics”

The Commendation for Science and Technology by the Minister of Education, Culture, Sports, Science and Technology, The Young Scientists' Prize

FUKAI Shuya (The Univ. of Tokyo)

“Research on Cell Signaling Complexes by X-Ray Crystallography” (12C and NW10A)

5th International Conference on New Diamond and Nano Carbons (NDNC2011)

Young Scientist Award (Best Poster Award)

KATO Yukako (AIST)

“Structure and Electric Property Analysis of Dislocations in Single Crystal Diamond (001)” (15C)

The Society of Rheology, Award for Young Scientists

FUJII Shuji (Nagaoka Univ. of Tech.)

“Shear-Induced Onion Formation of Polymer-Grafted Lamellar Phase” [1] (10C)

The Protein Science Young Investigator Travel Grants/The Protein Society Finn Wold Travel Awards (IX European Symposium of The Protein Society)

ARAI Ryoichi (Shinshu Univ.)

“Crystal Structure of a Dimeric *De Novo* Four-Helix Bundle Protein WA20” [2] (5A, 6A and NW12A)

The 7th PASJ Award for Young Scientists

SHIMADA Miho (KEK-ACC)

“Studies on the Beam Dynamics by using Coherent Synchrotron Radiation”

Japan Society for Simulation Technology, Award for Young Scientists

SUNAGUCHI Naoki (KEK-PF)

“Simulation Study on Refraction Contrast X-Ray Computed Tomography using Dark-Field Imaging Laue Case Analyzer Crystal” (14C)

Young Scientist Award of the Society for Atomic Collision Research

YAMASAKI Masakazu (Tohoku Univ.)

“Photoelectron Dynamics Studied by Means of Molecular-Frame Photoelectron Angular Distributions” [3,4] (12C)

Best Poster Awards at the Annual Symposium of the Japan Society for Molecular Science

KAWASAKI Naoya¹, WANG Heng¹, HAMANAKA Shun¹, YOKOYAMA Toshihiko², YOSHIKAWA Hirofumi¹

AWAGA Kunio¹ (¹Nagoya Univ., ²IMS)

“Studies on Solid-State Electrochemistry of Rechargeable Batteries using Nanohybrid Materials between Polyoxometalates and SWNT” [5] (12C and NW10A)

1st International Meeting of Medical Olympicus Association (MOA) 1st High Prize for the Paper

SHIMAO Daisuke (Ibaraki Pref. Univ. of Health Sci.)

“A Trial on Refraction-Contrast Tomosynthesis for a Breast Specimen” (14B)

PDB40 Travel Award (Protein Data Bank 40th Anniversary Symposium)

ARAI Ryoichi (Shinshu Univ.)

“Domain-Swapped Dimeric Structure of a *De Novo* Four-Helix Bundle Protein WA20” [2] (5A, 6A and NW12A)

The Prize of The Japan Radiation Research Society

KOBAYASHI Katsumi (KEK-PF)

“Research on the Initial Processes in Radiobiological Effects using Synchrotron Radiation” (27A and 27B)

The Surface Science Society of Japan, Award for Young Scientists

ABE Hitoshi (KEK-PF)

“Magnetic and Film Structures of NO, CO Adsorbed Fe/Cu (001)”

Annual Meeting of The Biophysical Society of Japan Kyushu Branch, Good Presentation Award

KOGA Yukari (Kumamoto Univ.)

“pH Dependence of Substrate Recognition in Human MTH1” (NW12A)

The Japan Society of High Pressure Science and Technology, Prize

TAKEMURA Kenichi (NIMS)

“Development of Basic Technologies for the DAC, Study of Structural Phase Transitions of the Elements, and Determination of Equation of States ”

CERI, Best Paper Award

OZAWA Kenichi¹, KAKUBO Takashi², AMINO Naoya² (¹Tokyo Inst. of Tech. ²Yokohama Rubber Co., Ltd.)

“Angle-Resolved Photoemission Spectroscopy (ARPES) Analysis of Brass Surface after Rubber Vulcanization Treatment and After Aging”

The 16th JSSR Scientific Award, Award for Young Scientists

TOYODA Satoshi (The Univ. of Tokyo)

“Electronic Structure Analysis of MOSFET Gate Stack Structure Studied by Synchrotron-Radiation Photoemission Spectroscopy”

Wakashachi Award for Young Scientists

YOSHIKAWA Hirofumi (Nagoya Univ.)

“Development of Functional Porous Carbon Materials and their Applications to Energy Materials” [5-9] (12C and NW10A)

The Chemical Society of Japan Award

NISHIKAWA Keiko (Chiba Univ.)

“Pioneering and Developing Studies on Structural Chemistry Based on Fluctuations ”

Akasaki Prize

YOSHIKAWA Hirofumi (Nagoya Univ.)

“Development of Novel Rechargeable Batteries using Molecular Clusters as Cathode Active Materials”[5-9] (12C and NW10A)

Award of the Flux Growth Society of Japan, Research Award, 2011

ISHIZAWA Nobuo (Nagoya Inst. of Tech.)

“Precise Structure Analysis of Flux-Grown Single Crystals by Synchrotron X-Rays” (14A)

REFERENCES

[1] *Soft Matter*, **8** (2012) 5381.

[2] *J. Phys. Chem. B*, **12** (2012) 6789.

[3] *Phys. Rev. Lett.*, **101** (2008) 043004.

[4] *J. Phys. B*, **42** (2009) 051001.

[5] *Angew. Chem. Int. Ed.*, **50** (2011) 3471.

[6] *J. Am. Chem. Soc.*, **134** (2012) 4918.

[7] *Chem. Asin J.*, **6** (2011) 1074.

[8] *Inorg. Chem.*, **48** (2009) 9057.

[9] *Chem. Commun.*, **30** (2007) 3169.

3. Theses

Lists of doctoral theses, which were written based on the PF experiments.

Doctor of Science

PORCEL, Erika (Universite Paris Sud 11)

“Use of Nanoparticles for Improvement of Hadron Therapy” (27A and 27B)

Doctor of Engineering

SUN, Qing-Fu (The Univ. of Tokyo)

“Virus Inspired Multi-Component Self-Assembly of Molecular Spheres” (17A, NW2A, NE3A and NW12A)

Doctor of Philosophy in Science

SINGH, Vijay Raj (The Univ. of Tokyo)

“X-Ray Magnetic Circular Dichroism Study of Oxide-Based Magnetic Materials and Half-Metallic Alloys” (16A)

Doctor of Science

WANG, Heng (Nagoya Univ.)

“Investigation into the Reaction Mechanism of Molecular Cluster Batteries by XAFS, NMR, and Magnetic Analysis” (12C and NW10A)

Doctor of Biomedical Sciences

KAWAKUBO, Atsushi (Nagasaki Univ.)

“Zinc as an Essential Trace Element in the Acceleration of Matrix Vesicles-Mediated Mineral Deposition” (4A)

Doctor of Science

NAKATO, Aiko (Tohoku Univ.)

“Thermal Evolution of Primitive Hydrous Asteroids Inferred from Mineralogy, Isotope and Chemical Compositions of Dehydrated Carbonaceous Chondrites ” (3A and 9C)

Doctor of Engineering

NII, Yoichi (Tohoku Univ.)

“Spin-Orbital-Lattice Coupling in Spinel-Type Oxide Compounds” (3A)

Doctor of Engineering

YOSHIMATSU, Kohei (The Univ. of Tokyo)

“Metallic Quantum Well States in Oxide Artificial Structure Studied by Photoemission Spectroscopy ” (28A)

Doctor of Science

NISHIDA, Keisukei (Tohoku Univ.)

“Density and Sound Velocity Measurements of Liquid Fe-S at High Pressure: Implications for the Earth’s and the Lunar Core” (14C2 and NE7A)

Doctor of Science

CHEN, Zhiwen (Osaka Univ.)

“Precursor-Dependent Local Structure of Rh/Al₂O₃ Catalysts Analyzed by Scanning Tunneling Microscopy and X-ray Absorption Fine Structure ” (NW10A)

Doctor of Science

KOJIMA, Tatsuhiko (Tokyo Inst. of Tech.)

“Effects of the Solvents on Hydrogen-Bond-Assisted Molecular Aggregations of Protonated Decavanadate Anions in Solution and Crystalline States” (NW2A)

Doctor of Engineering

OTANI, Junji (Kyoto Univ.)

“Structural Analysis of Epigenetic Mark Readers” (5A, 17A, NE3A and NW12A)

Doctor of Science
 NAKANO, Shogo (Hiroshima Univ.)
 “Structural and Functional Analysis of Assimilatory Nitrite Reductase ” (17A and NW12A)

Doctor of Engineering
 KASAI, Hidetaka (The Univ. of Tokyo)
 “Study of Self-Diffusion in Fe under High Hydrogen Pressure by Nuclear Resonant X-Ray Forward Scattering” (NE1A)

Doctor of Science
 OHTOMI, Eisuke (Kyushu Univ.)
 “Studies on Freezing Transitions of Wetting Films and Its Effect on Foam Film Stability” (7C)

Doctor of Science
 KAVEENGA, Rasika Koswattage (Kobe Univ.)
 “Selective Adsorption of Atomic Hydrogen on a h-BN Thin Film” (11A and 13C)

Doctor of Science
 TAKEICHI, Yasuo (The Univ. of Tokyo)
 “Structure, Electronic Properties and Magnetism of Ultrathin Fe Films on Pd(001)” (18A and 19A)

Doctor of Science
 SHINOZAKI, Ayako (Ehime Univ.)
 “Reaction of Forsterite and Hydrogen Molecules under High Pressure and Temperature.” (18C)

Doctor of Science
 NARITA, Ayumi (Ibaraki Univ.)
 “Study for Chemical-State of Interface between Organic Molecule and Oxide Surface using Core-Level Spectroscopy ” (27A)

Doctor of Engineering
 WADA, Takahiro (Hokkaido Univ.)
 “Reaction Mechanism Analysis of Ni Phosphide Hydrodesulfurization Catalyst by Operando Quick XAFS” (9A, 9C and NW10A)

Doctor of Engineering
 NAGAE, Takayuki (Nagoya Univ.)
 “Structural Study of Proteins using High-Pressure Protein Crystallography: Pressure Effects and Pressure Adaptation of Proteins from Deep-Sea Bacteria” (5A, NE3A and NW12A)

Doctor of Engineering
 FUJITA, Daishi (The Univ. of Tokyo)
 “Protein Encapsulation within Synthetic Molecular Hosts” (1A, 17A and NE3A)

Doctor of Engineering
 IWASA, Junji (The Univ. of Tokyo)
 “Synthesis and Functionalization of M24L48 Spherical Complexes” (1A, 17A and NE3A)

Doctor of Engineering
 UCHIDA, Masaki (Nagoya Inst. of Tech.)
 “Spectroscopic Study on Charge-Spin-Orbital Coupled Phenomena in Mott-Transition Oxides” (16A)

Doctor of Science
 KAWABE, Yoshiteru (Tokyo Univ. of Science)
 “Study on Na₂MnxFe_{1-x}PO₄F Cathode Materials for Rechargeable Na-ion Batteries” (12C)

4. Publication List

1A

L. M. G. Chavas, Y. Yamada, M. Hiraki, N. Igarashi, N. Matsugaki and S. Wakatsuki
UV LED lighting for Automated Crystal Centring
J. Synchron Rad., **18** (2011) 11.

T. Osawa, S. Kimura, N. Terasaka, H. Inanaga, T. Suzuki and T. Numata
Structural Basis of tRNA Agmatinylation Essential for AUA Codon Decoding
Nature Structural Molecular Biology, **18** (2011) 1275.

T. Osawa, H. Inanaga, S. Kimura, N. Terasaka, T. Suzuki and T. Numata
Crystallization and Preliminary X-Ray Diffraction Analysis of an Archaeal tRNA-Modification Enzyme, TiaS, Complexed with tRNA^{Ile2} and ATP
Acta Cryst. F, **67** (2011) 1414.

J. Y. Yoon, J. Kim, S. J. Lee, H. S. Kim, H. N. Im, H.-J. Yoon, K. H. Kim, S.-J. Kim, B. W. Han and S. W. Suh
Structural and Functional Characterization of *Helicobacter pylori* DsbG
FEBS Lett., **585** (2011) 3862.

Former 1B

H. Ikemoto, A. Goyo and T. Miyanaga
Size Dependence of the Local Structure and Atomic Correlations in Tellurium Nanoparticles
J. Phys. Chem. C, **115** (2011) 2931.

Y. Yamanari, Y. Suzuki, K. Imai, E. Shikoh, A. Fujiwara, N. Kawasaki, N. Ikeda, Y. Kubozono and T. Kambe
Electronic Phase Transition of the Valence-Fluctuating Fulleride Eu_{2.75}C₆₀
Phys. Rev. B, **83** (2011) 245103.

H. Yamaoka, T. Kambe, T. Sato, Y. Ishida, M. Matsunami, R. Eguchi, Y. Senba and H. Ohashi
Electronic State of an Organic Molecular Magnet: Soft X-Ray Spectroscopy Study of α -TDAE-C₆₀ Single Crystal
Phys. Rev. B, **84** (2011) 161404(R).

Former 1C

T. Yamazaki, S. Hashimoto, T. Kakiuchi, K. Mase and M. Tanaka
Auger Electron Spectra of Hydrogenated Si(111)-1x1 Surface Obtained from Si-L₂₃VV Auger Electron Si-2p Photoelectron Coincidence Measurements
J. Phys.: Conf. Ser., **288** (2011) 012016.

T. Kakiuchi, M. Tahara, S. Hashimoto, N. Fujita, M. Tanaka, K. Mase and S. Nagaoka
Surface-Site-Selective Study of Valence Electronic States of a Clean Si(111)-7x7 Surface using Si-L₂₃VV Auger Electron and Si-2p Photoelectron Coincidence Measurements
Phys. Rev. B, **83** (2011) 035320.

2C

K. Iwaya, R. Shimizu, H. Aida, T. Hashizume and T. Hitosugi
Atomically Resolved Silicon Donor States of β -Ga₂O₃
Appl. Phys. Lett., **98** (2011) 142116.

Y. Komuro and Y. Matsumoto
Electron Beam Irradiation-Induced Reduction of SnO₂ Deposited on TiO₂(110) Surfaces
J. Phys. Chem. C, **115** (2011) 6618.

J. W. Liu, A. Kobayashi, S. Toyoda, H. Kamada, A. Kikuchi, J. Ohta, H. Fujioka, H. Kumigashira and M. Oshima
Band Offsets of Polar and Nonpolar GaN/ZnO Heterointerfaces Determined by Synchrotron Radiation Photoemission Spectroscopy
Phys. Status Solidi, **248** (2011) 956.

Y. Tezuka, N. Nakajima and O. Morimoto
Detailed Measurement of Ti 2p Resonant X-Ray Raman Scattering of TiO₂ and its Polarization Dependence Measurements
J. Elec. Spec. Relat. Phenom., **184** (2011) 216.

H. Nogawa, A. Chikamatsu, Y. Hirose, S. Nakao, H. Kumigashira, M. Oshima and T. Hasegawa
Carrier Compensation Mechanism in Heavily Nb-Doped Anatase Ti_{1-x}Nb_xO_{2+ δ} Epitaxial Thin Films
J. Phys. D: Appl. Phys., **44** (2011) 365404.

T. Ohsawa, J. Okubo, T. Suzuki, H. Kumigashira, M. Oshima and T. Hitosugi
An *n*-Type Transparent Conducting Oxide: Nb₁₂O₂₉
J. Phys. Chem. C, **115** (2011) 16625.

K. Yoshimatsu, K. Horiba, H. Kumigashira, T. Yoshida, A. Fujimori and M. Oshima
Metallic Quantum Well States in Artificial Structures of Strongly Correlated Oxide
Science, **333** (2011) 319.

T. Yamamoto, R. Yasuhara, I. Ohkubo, H. Kumigashira and M. Oshima
Formation of Transition Layers at Metal/Perovskite Oxide Interfaces Showing Resistive Switching Behaviors
J. Appl. Phys., **110** (2011) 053707.

S. Chakraverty, K. Yoshimatsu, Y. Kozuka, H. Kumigashira, M. Oshima, T. Makino, A. Ohtomo and M. Kawasaki
Magnetic and Electronic Properties of La₂VMnO₆ Ordered Double Perovskite Thin Films
Phys. Rev. B, **84** (2011) 132411.

S. Toyoda, H. Kamada, H. Kumigashira and M. Oshima
Chemical-State Resolved Depth Profile and Band Discontinuity in TiN/HfSiON Gate Stack Structure with AlO_x Cap Layer
J. Appl. Phys., **110** (2011) 104107.

E. Sakai, K. Yoshimatsu, K. Shibuya, H. Kumigashira, E. Ikenaga, M. Kawasaki, Y. Tokura and M. Oshima
Competition between Instabilities of Peierls Transition and Mott Transition in W-Doped VO₂ Thin Films
Phys. Rev. B, **84** (2011) 195132.

M. Oshima, S. Toyoda, K. Horiba, R. Yasuhara and H. Kumigashira
Synchrotron Radiation Nano-Spectroscopy of Dielectrics for LSI and ReRAM
ECS Transactions, **41(3)** (2011) 453.

S. Kurosumi, N. Nagamura, S. Toyoda, K. Horiba, H. Kumigashira, M. Oshima, S. Furutsuki, S. Nishimura, A. Yamada and N. Mizuno
Resonant Photoemission Spectroscopy of the Cathode Material Li_xFePO₄ for Lithium Ion Battery
J. Phys. Chem. C, **115** (2011) 25519.

3A

H. Nakao, T. Murata, D. Bizen, Y. Murakami, K. Ohoyama, K. Yamada, S. Ishiwata, W. Kobayashi and I. Terasaki
Orbital Ordering of Intermediate-Spin State of Co³⁺ in Sr₃YCo₄O_{10.5}
J. Phys. Soc. Jpn., **80** (2011) 023711.

N. Abe, K. Taniguchi, H. Sagayama, H. Umetsu and T. Arima
Correlation between the Mobility of Domain Wall and Polarization Flop Direction in a Slanted Magnetic Field in the Helimagnetic Ferroelectrics Tb_{1-x}Dy_xMnO₃
Phys. Rev. B, **83** (2011) 060403.

T. Shirasawa, K. Sakamoto, T. Takahashi and H. Tochiara
Atomic and Valence-Band Electronic Structures of the Epitaxial SiON Layer on the SiC(0001): X-Ray Diffraction and Angle-Resolved Photoemission Spectroscopy Investigations
Surf. Sci., **605** (2011) 328.

T. Arima
Spin-Driven Ferroelectricity and Magneto-Electric Effects in Frustrated Magnetic Systems
J. Phys. Soc. Jpn., **80** (2011) 052001.

Y. Krockenberger, J. S. Lee, D. Okuyama, H. Nakao, Y. Murakami, M. Kawasaki and Y. Tokura
Garnet Superlattice as a Transparent Above-Room-Temperature Polar Magnet
Phys. Rev. B, **83** (2011) 214414.

R. Yamamoto, C. Bell, Y. Hikita, H. Y. Hwang, H. Nakamura, T. Kimura and Y. Wakabayashi
Structural Comparison of *n*-Type and *p*-Type LaAlO₃/SrTiO₃ Interfaces
Phys. Rev. Lett., **107** (2011) 036104.

Y. Tokunaga, D. Okuyama, T. Kurumaji, T. Arima, H. Nakao, Y. Murakami, Y. Taguchi and Y. Tokura
Multiferroicity in NiBr₂ with Long-Wavelength Cycloidal Spin Structure on a Triangular Lattice
Phys. Rev. B, **84** (2011) 060406.

S. Chakraverty, A. Ohtomo, D. Okuyama, M. Saito, M. Okude, R. Kumai, T. Arima, Y. Tokura, S. Tsukimoto, Y. Ikuhara and M. Kawasaki
Ferrimagnetism and Spontaneous Ordering of Transition Metals in Double Perovskite La₂CrFeO₆ Films
Phys. Rev. B, **84** (2011) 064436.

H. Sagayama, S. Ohtani, M. Saito, N. Abe, K. Taniguchi and T. Arima
Magnetic-Field Effects on Jahn-Teller Distortion in Ferroelastic Magnetic Insulator Fe_{1-x}Mn_xCr₂O₄
Appl. Phys. Lett., **99** (2011) 082506.

K. Shibuya, D. Okuyama, R. Kumai, Y. Yamasaki, H. Nakao, Y. Murakami, Y. Taguchi, T. Arima, M. Kawasaki and Y. Tokura
X-Ray Induced Insulator-Metal Transition in a Thin Film of Electron-Doped VO₂
Phys. Rev. B, **84** (2011) 165108.

T. Matsumura, D. Okuyama, T. Mouri and Y. Murakami
Successive Magnetic Phase Transitions of Component Orderings in DyB₄
J. Phys. Soc. Jpn., **80** (2011) 074701.

T. Matsumura, T. Yonemura, K. Kunimori, M. Sera and F. Iga
Behavior of the Antiferroquadrupolar Moments in the Antiferromagnetic Ordered Phase of CeB₆
J. Phys. Soc. Jpn., **80** (2011) SA054.

K. Ikeuchi, H. Nakao, Y. Murakami, S. Miyasaka and Y. Tokura
Er L₃-Edge Resonant Elastic X-Ray Scattering Study of Orbital Ordering in ErVO₃
Diamond Light Source Proc., **1** (2011) e123.

N. Ikeda, M. Kubota, H. Hayakawa, H. Akahama, D. Ohishi, A. Nakanishi, T. Funabiki, Y. Matsuo, N. Kimizuka, T. Kambe, S. Mori and J. Kano
Electric Field Response of Stoichiometric LuFe₂O₄ Ferroelectrics, **414** (2011) 41.

T. Noguchi, T. Nakamura, T. Ushikubo, N. T. Kita, J. W. Valley, R. Yamanaka, Y. Kimoto and Y. Kitazawa
A Chondrule-Like Object Captured by Space-Exposed Aerogel on the International Space Station
Earth and Planetary Sci. Lett., **309** (2011) 198.

T. Nakamura, T. Noguchi, M. Tanaka, M. E. Zolensky, M. Kimura, A. Tsuchiyama, A. Nakato, T. Ogami, H. Ishida, M. Uesugi, T. Yada, K. Shirai, A. Fujimura, R. Okazaki, S. A. Sandford, Y. Ishibashi, M. Abe, T. Okada, M. Ueno, T. Mukai, M. Yoshikawa and J. Kawaguchi

Itokawa Dust Particles: A Direct Link between S-Type Asteroids and Ordinary Chondrites
Science, **333** (2011) 1113.

T. Noguchi, T. Nakamura, M. Kimura, M. E. Zolensky, M. Tanaka, T. Hashimoto, M. Konno, A. Nakato, T. Ogami, A. Fujimura, M. Abe, T. Yada, T. Mukai, M. Ueno, T. Okada, K. Shirai, Y. Ishibashi and R. Okazaki

Incipient Space Weathering Observed on the Surface of Itokawa Dust Particles
Science, **333** (2011) 1121.

K. Bajo, T. Akaida, N. Ohashi, T. Noguchi, T. Nakamura, Y. Nakamura, H. Sumino and K. Nagao
Single Grain Noble Gas Analysis of Antarctic Micrometeorites by Stepwise Heating Method with a Newly Constructed Miniature Furnace
Earth Planet and Space, **63** (2011) 1097.

T. Onoue, T. Nakamura, T. Haranosono and C. Yasuda
Composition and Accretion Rate of Fossil Micrometeorites Recovered in Middle Triassic Deep-Sea Deposits
Geology, **39** (2011) 567.

3B

S. Obara, R. Kobayashi, S. Yagi, Y. Tohyama, G. Kutluk, T. Osawa, K. Ogura, T. Shibata, Y. Azuma and T. Nagata

A Crossed Photon-Atom Beam Method for Absolute Measurement of Total Photoionization Cross Sections on Isolated Metal Atoms: Measurements on Ba and Eu Atoms
Nucl. Instrum. Meth. Phys. Res. B, **269** (2011) 263.

M. Koide, E. Kayama, T. Osawa, S. Tsuge, Y. Tohyama, S. Obara, S. Hasegawa, Y. Azuma, F. Koike and T. Nagata

Photoabsorption Spectra of Double- and Triple-Excitations above the Calcium $3p$ Threshold
J. Phys. Soc. Jpn., **80** (2011) 034301.

3C

H. Fujimoto, A. Waseda and X. Zhang
Profile Measurement of Polished Surface with Respect to a Lattice Plane of a Silicon Crystal using a Self-Referenced Lattice Comparator
Int. J. of Automation Technology, **5** (2011) 179.

H. Fujimoto, A. Waseda and X. W. Zhang
Homogeneity Characterization of Lattice Spacing of Silicon Single Crystals by a Self-Referenced Lattice Comparator
Metrologia, **48** (2011) S55.

K. Kobayashi, T. Nagao and M. Ito
Radial Integrals for the Magnetic Form Factor of 5d Transition Elements
Acta Cryst. A, **67** (2011) 473.

M. Ito, A. Sato, R. Yamaki, M. Naito, K. Kobayashi, T. Nagao, K. Suzuki, H. Sakurai, H. Maruyama, M. Itou and Y. Sakurai
X-Ray Magnetic Diffraction and Magnetic Compton Scattering of Pd-Co and Pt-Fe
Acta Cryst. A, **67** (2011) C530.

K. Suzuki, M. Ito, N. Tsuji, T. Tadenuma, Y. Oba, A. Sato, R. Nagayasu, H. Adachi, H. Nakao, Y. Murakami, Y. Taguchi, Y. Tokura, Y. Sakurai and Y. Onuki
Application of Upgraded X-Ray Magnetic Diffraction Experimental System to $3d$ - and $4f$ -Electron Ferromagnets
e-J. Surf. Sci. Nanotech., **9** (2011) 134.

N. Watanabe, T. Sasaya, Y. Imai, S. Iwata, K. Zama and S. Aoki
Observation of Phase Objects by using an X-Ray Microscope with a Foucault Knife-Edge
AIP Conf. Proc., **1365** (2011) 313.

B. Andreas, Y. Azuma, G. Bartl, P. Becker, H. Bettin, M. Borys, I. Busch, M. Gray, P. Fuchs, K. Fujii, H. Fujimoto, E. Kessler, M. Krumrey, U. Kuetgens, N. Kuramoto, G. Mana, P. Manson, E. Massa, S. Mizushima, A. Nicolaus, A. Picard, A. Pramann, O. Rienitz, D. Schiel, S. Valkiers and A. Waseda
Determination of the Avogadro Constant by Counting the Atoms in a ^{28}Si Crystal
Phys. Rev. Lett., **106** (2011) 030801.

B. Andreas, Y. Azuma, G. Bartl, P. Becker, H. Bettin, M. Borys, I. Busch, P. Fuchs, K. Fujii, H. Fujimoto, E. Kessler, M. Krumrey, U. Kuetgens, N. Kuramoto, G. Mana, E. Massa, S. Mizushima, A. Nicolaus, A. Picard, A. Pramann, O. Rienitz, D. Schiel, S. Valkiers, A. Waseda and S. Zakel
Counting the Atoms in a ^{28}Si Crystal for a New Kilogram Definition
Metrologia, **48** (2011) S1.

E. Massa and A. Nicolaus
International Determination of the Avogadro Constant
Metrologia, **48** (2011) E01.

Former 3C2

N. Watanabe, M. Hoshino and S. Aoki
Elemental Mapping Using Full-Field Fluorescence Imaging Microscope
Oyo Butsuri, **80** (2011) 983, (*in Japanese*).

4A

T. Mukaide, M. Watanabe, K. Takada, A. Iida, K. Fukuda and T. Noma

Quantitative Effective Atomic Number Imaging using Simultaneous X-Ray Absorption and Phase Shift Measurement

Appl. Phys. Lett., **98** (2011) 111902.

Y. Takanishi, I. Nishiyama, J. Yamamoto, Y. Ohtsuka and A. Iida

Remarkable Effect of Lateral Substituent on the Molecular Ordering of Chiral Liquid Crystal Phases: A Novel Bromo-Containing Dichiral Compound Showing SmC* Variants

J. Mater. Chem., **21** (2011) 4465.

B. Mongkhonsin, W. Nakbanpote, I. Nakai, A. Hokura and N. Jearanaikoon

Distribution and Speciation of Chromium Accumulated in *Gynura pseudochina* (L.) DC

Environmental and Experimental Botany, **74** (2011) 56.

K. Naemura, D. Ikuta, H. Kagi, S. Odake, S. Ohi, T. Uyeda, T. Kobayashi, M. Svojtka and T. Hirajima

Diamond and Other Possible Ultra-Deep Evidence Discovered in the Orgenic Pinel-Garnet Peridotite from the Moldanubian Zone of the Bohemian Massif, Czech Republic

Ultrahigh-Pressure Metamorphism: 25 Years After the Discovery of Coesite and Diamond, (2011) 77.

L. Bayes-Garcia, T. Calvet, M. A. Cuevas-Diarte, S. Ueno and K. Sato

Heterogeneous Microstructures of Spherulites of Lipid Mixtures Characterized with Synchrotron Radiation Microbeam X-Ray Diffraction

Cryst. Eng. Comm., **13** (2011) 6694.

S. Mitsunobu, Y. Takahashi, S. Utsunomiya, A. M. Matthew, Y. Terada, T. Iwamura and M. Sakata

Identification and Characterization of Nanosized Tripuhyite in Soil Near Sb Mine Tailing

Am. Mineral., **96** (2011) 1171.

A. Iida

Elemental Depth Profiling with a Wire in Microbeam X-Ray Fluorescence Analysis

X-Ray Spectrom., **40** (2011) 376.

W. Satake, T. Mikouchi and M. Miyamoto

Redox States of Geochemically-Enriched Shergottites as Inferred from Fe Micro-XANES Analysis of Maskelynite and Plagioclase

Antarctic Meteorites, **XXXIV** (2011) 76.

T. Noguchi, T. Itai, M. Kawaguchi, S. Takahashi and S. Tanabe

Applicability of Human Hair as a Bioindicator for Trace Elements Exposure

Interdisciplinary Studies on Environ. Chem., **6** (2011) 73.

4B1

D. Frank, M. Zolensky, J. Martinez, T. Mikouchi, K. Ohsumi, K. Hagiya, W. Satake, L. Le, D. Ross and A. Peslier

A CAI in the Ivuna CI1 Chondrite

42nd Lunar and Planetary Science Conf., **XLII** (2011) 2785.

4B2

K. Fujii, H. Uekusa, M. Fukano and H. Koshima

Metastable Polymorphic Form of Isopropylbenzophenone Derivative Directly Obtained by the Solid-State Photoreaction Investigated by *ab initio* Powder X-Ray Diffraction Analysis

CrystEngComm, **13** (2011) 3197.

M. Yashima, S. Matsuyama, R. Sano, M. Itoh, K. Tsuda and D. Fu

Structure of Ferroelectric Silver Niobate AgNbO₃

Chem. Mater., **23** (2011) 1643.

M. Yashima

Ion Diffusion Mechanism in Ion-Conducting Materials through Neutron Diffractometry

HAMON, **21** (2011) 96, (*in Japanese*).

M. Yashima

Crystal Structure and Electron-Density Distribution of Visible-Light Responsive Photocatalysts for Water Decomposition

J. Fuel Cell Tech., **10** (2011) 111, (*in Japanese*).

S. Ishihara, K. Kakimoto and I. Kagomiya

Densification of (Na,K)NbO₃ Piezoelectric Ceramics by Two-Step Mixing Process

J. Mater. Sci., **46** (2011) 3822.

M. Suzuki, K. Imai, H. Wakabayashi, A. Arita, K. Johmoto, H. Uekusa and K. Kobayashi

Photorearrangements in Spiro-Conjoined Cyclohexa-2,5-dien-1-one

Tetrahedron, **67** (2011) 5500.

K. Omoto, T. Hashimoto, K. Sasaki, T. Terai, T. Hoshino and M. Yashima

Structural Analysis of Li₂TiO₃ by Synchrotron X-Ray Diffraction at High Temperature

J. Nucl. Mater., **417** (2011) 692.

K. Kasugai, S. Hashimoto, K. Imai, A. Sakon, K. Fujii, H. Uekusa, N. Hayashi and K. Kobayashi

Supramolecular Networks in Crystalline Inclusion Complexes Formed from a New Family of Hosts, 2, 2-Bis(4-hydroxy-3-phenylphenyl)-1H-indene-1,3(2H)-dione

Cryst. Growth Design, **11** (2011) 4044.

M. Yashima, Y. Yonehara and H. Fujimori

Experimental Visualization of Chemical Bonding and Structural Disorder in Hydroxyapatite through Charge and Nuclear-Density Analysis

J. Phys. Chem. C, **115** (2011) 25077.

T. Ida
Particle Statistics of Capillary Specimen in Synchrotron Powder Diffractometry
J. Appl. Cryst., **44** (2011) 911.

T. Ida, T. Goto and H. Hibino
Evaluation of Crystallite Size Distribution by a Capillary Spinner-Scan Method in Synchrotron Powder Diffractometry
IOP Conf. Ser.: Mater. Sci. Eng., **18** (2011) 022002.

H. Nakano, T. Ida, M. Takemoto and H. Ikawa
Crystal Structures of Solid Solution $(\text{Ba}_{1-x}\text{Ca}_x)(\text{Sc}_{1/2}\text{Nb}_{1/2})\text{O}_3$ System
IOP Conf. Ser.: Mater. Sci. Eng., **18** (2011) 082023.

T. Ida, T. Goto and H. Hibino
Particle Statistics in Synchrotron Powder Diffractometry
Z. Kristallogr. Proc., **1** (2011) 69.

4C

S. Ishiwata, T. Nakano, I. Terasaki, H. Nakao, Y. Murakami, Y. Uwatoko and M. Takano
Uniaxial Colossal Magnetoresistance in the Ising Magnet $\text{SrCo}_{12}\text{O}_{19}$
Phys. Rev. B, **83** (2011) 020401.

H. Nakao, T. Murata, D. Bizen, Y. Murakami, K. Ohoyama, K. Yamada, S. Ishiwata, W. Kobayashi and I. Terasaki
Orbital Ordering of Intermediate-Spin State of Co^{3+} in $\text{Sr}_3\text{YCo}_4\text{O}_{10.5}$
J. Phys. Soc. Jpn., **80** (2011) 023711.

K. Otsubo, Y. Wakabayashi, J. Ohara, S. Yamamoto, H. Matsuzaki, H. Okamoto, K. Nitta, T. Uruga and H. Kitagawa
Bottom-Up Realization of a Porous Metal-Organic Nanotubular Assembly
Nature Materials, **10** (2011) 291.

T. Arima
Spin-Driven Ferroelectricity and Magneto-Electric Effects in Frustrated Magnetic Systems
J. Phys. Soc. Jpn., **80** (2011) 052001.

H. Abe, H. Saitoh, H. Nakao and K. Yamamoto
Anisotropic Local Structure of Decagonal Quasicrystals by DAFS
Philosophical Magazine, **91** (2011) 2491.

Y. Yamasaki, D. Okuyama, M. Nakamura, T. Arima, M. Kawasaki, Y. Tokura, T. Kimura and Y. Wakabayashi
Interfacial Structure of Manganite Superlattice
J. Phys. Soc. Jpn., **80** (2011) 07360.

T. Takeuchi, K. Tatsumura, I. Ohdomari, T. Shimura and M. Nagase
X-Ray Diffraction Profiles of Si Nanowires with Trapezoidal Cross-Sections
Physica B, **406** (2011) 2559.

T. Sakurai, T. Ohashi, H. Kitazume, M. Kubota, T. Suemasu and K. Akimoto
Structural Control of Organic Solar Cells Based on Nonplanar Metallophthalocyanine/ C_{60} Heterojunctions using Organic Buffer Layers
Organic Electronics, **12** (2011) 966.

K. Uosaki, J. Morita, T. Katsuzaki, S. Takakusagi, K. Tamura, M. Takahashi, J. Mizuki and T. Kondo
In Situ Electrochemical, Electrochemical Quartz Crystal Microbalance, Scanning Tunneling Microscopy, and Surface X-Ray Scattering Studies on Ag/AgCl Reaction at the Underpotentially Deposited Ag Bilayer on the Au(111) Electrode Surface
J. Phys. Chem. C, **115** (2011) 12471.

H. Sakuma, T. Kondo, H. Nakao, K. Shiraki and K. Kawamura
Structure of Hydrated Sodium Ions and Water Molecules Adsorbed on the Mica/Water Interface
J. Phys. Chem. C, **115** (2011) 15959.

T. Matsumura, D. Okuyama, T. Mouri and Y. Murakami
Successive Magnetic Phase Transitions of Component Orderings in DyB_4
J. Phys. Soc. Jpn., **80** (2011) 074701.

R. Fukuta, S. Miyasaka, K. Hemmi, S. Tajima, D. Kawana, K. Ikeuchi, Y. Yamasaki, A. Nakao, H. Nakao, Y. Murakami and K. Iwasa
Effects of Cation-Size Variance on Spin and Orbital Orders in $\text{Eu}_{1-x}(\text{La}_{0.254}\text{Y}_{0.746})_x\text{VO}_3$
Phys. Rev. B, **84** (2011) 140409(R).

K. Ishii, S. Ishihara, Y. Murakami, K. Ikeuchi, K. Kuzushita, T. Inami, K. Ohwada, M. Yoshida, I. Jarrige, N. Tatami, S. Niioka, D. Bizen, Y. Ando, J. Mizuki, S. Maekawa and Y. Endoh
Polarization-Analyzed Resonant Inelastic X-Ray Scattering of the Orbital Excitations in KCuF_3
Phys. Rev. B, **83** (2011) 241101.

Y. Wakabayashi, J. Takeya and T. Kimura
Interface Structure of the Rubrene Crystal Field Effect Transistor
J. Appl. Phys., **110** (2011) 102206.

K. Ikeuchi, H. Nakao, Y. Murakami, S. Miyasaka and Y. Tokura
Er L_{3-Edge} Resonant Elastic X-Ray Scattering Study of Orbital Ordering in ErVO_3
Diamond Light Source Proc., **1** (2011) e123.

N. Ikeda, M. Kubota, H. Hayakawa, H. Akahama, D. Ohishi, A. Nakanishi, T. Funabiki, Y. Matsuo, N. Kimizuka, T. Kambe, S. Mori and J. Kano
Electric Field Response of Stoichiometric LuFe_2O_4
Ferroelectrics, **414** (2011) 41.

M. M. Islam, A. Yamada, T. Sakurai, M. Kubota, S. Ishizuka, K. Matsubara, S. Niki and K. Akimoto
Cu-Dependent Phase Transition in Polycrystalline CuGaSe₂ Thin Films Grown by Three-Stage Process
J. Appl. Phys., **110** (2011) 014903.

5A

M. Kanagawa, T. Satoh, A. Ikeda, Y. Nakano, H. Yagi, K. Kato, K. Kojima-Aikawa and Y. Yamaguchi
Crystal Structures of Human Secretory Proteins ZG16p and ZG16b Reveal a Jacalin-Related β -Prism Fold
Biochem. Biophys. Res. Commun., **404** (2011) 201.

T. Hashiguchi, T. Ose, M. Kubota, N. Maita, J. Kamishikiryo, K. Maenaka and Y. Yanagi
Structure of the Measles Virus Hemagglutinin Bound to its Cellular Receptor SLAM
Nature Structural Molecular Biology, **18** (2011) 135.

L. M. G. Chavas, Y. Yamada, M. Hiraki, N. Igarashi, N. Matsugaki and S. Wakatsuki
UV LED lighting for Automated Crystal Centring
J. Synchron Rad., **18** (2011) 11.

J. Igarashi, K. Kobayashi and A. Matsuoka
A Hydrogen-Bonding Network Formed by the B10-E7-E11 Residues of a Truncated Hemoglobin from *Tetrahymena pyriformis* is Critical for Stability of Bound Oxygen and Nitric Oxide Detoxification
J. Biol. Inorg. Chem., **16** (2011) 599.

D. Sasaki, M. Fujihashi, N. Okuyama, Y. Kobayashi, M. Noike, T. Koyama and K. Miki
Crystal Structure of Heterodimeric Hexaprenyl Diphosphate Synthase from *Micrococcus luteus* B-P 26 Reveals that the Small Subunit is Directly Involved in the Product Chain Length Regulation
J. Biol. Chem., **286** (2011) 3729.

N. Okazaki, T. Arimori, M. Nakazawa, K. Miyatake, M. Ueda and T. Tamada
Crystallization and Preliminary X-Ray Diffraction Studies of the Catalytic Domain of a Novel Chitinase, a Member of GH Family 23, from the Moderately Thermophilic Bacterium *Ralstonia* sp. A-471
Acta Cryst. F, **67** (2011) 494.

X. Pan, M. Li, T. Wan, L. Wang, C. Jia, Z. Hou, X. Zhao, J. Zhang and W. Chang
Structural Insights into Energy Regulation of Light-Harvesting Complex CP29 from Spinach
Nature Structural Molecular Biology, **18** (2011) 309.

K. Nishi, T. Ono, T. Nakamura, N. Fukunaga, M. Izumi, H. Watanabe, A. Suenaga, T. Maruyama, Y. Yamagata, S. Curry and M. Otagiri
Structural Insights into Differences in Drug-Binding Selectivity between Two Forms of Human α_1 -Acid Glycoprotein Genetic Variants, the A and F1*S Forms
J. Biol. Chem., **286** (2011) 14427.

T. Yoshizawa, H. Hashimoto, T. Shimizu, M. Yamabe, N. Shichijo, K. Hanada, H. Hirano and M. Sato
Purification, Crystallization and X-Ray Diffraction Study of Basic 7S Globulin from Soybean
Acta Cryst. F, **67** (2011) 87.

Y. Tanaka, N. Hirano, J. Kaneko, Y. Kamio, M. Yao and I. Tanaka
2-Methyl-2,4-pentanediol Induces Spontaneous Assembly of Staphylococcal α -Hemolysin into Heptameric Pore Structure
Protein Science, **20** (2011) 448.

M. Hagiwara, K. Maegawa, M. Suzuki, R. Ushioda, K. Araki, Y. Matsumoto, J. Hoseki, K. Nagata and K. Inaba
Structural Basis of an ERAD Pathway Mediated by the ER-Resident Disulfide Reductase ERdj5
Molecular Cell, **41** (2011) 432.

Y. Sato, R. Natsume, Z. Prokop, J. Brezovsky, R. Chaloupkova, J. Damborsky, Y. Nagata and T. Senda
Molecular Bases of Enantioselectivity of Haloalkane Dehalogenase DbjA
Kessyogakkaishi, **53** (2011) 124, (*in Japanese*).

M. Senda, H. Tanaka, T. Ishida, K. Horiike and T. Senda
Crystallization and Preliminary Crystallographic Analysis of D-Serine Dehydratase from Chicken Kidney
Acta Cryst. F, **67** (2011) 147.

S. J. Lee, H. S. Kim, D. J. Kim, H. J. Yoon, K. H. Kim, J. Y. Yoon and S. W. Suh
Crystal Structures of LacD from *Staphylococcus aureus* and LacD.1 from *Streptococcus pyogenes*: Insights into Substrate Specificity and Virulence Gene Regulation
FEBS Lett., **585** (2011) 307.

W.-Y. Jeng, N.-C. Wang, M.-H. Lin, C.-T. Lin, Y.-C. Liaw, W.-J. Chang, C.-I. Liu, P.-H. Liang and A. H.-J. Wang
Structural and Functional Analysis of Three β -Glucosidases from Bacterium *Clostridium cellulovorans*, Fungus *Trichoderma reesei* and Termite *Neotermes koshunensis*
J. Struct. Biol., **173** (2011) 46.

T. Ohnuma, T. Numata, T. Osawa, M. Mizuhara, K. M. Varum and T. Fukamizo
Crystal Structure and Mode of Action of a Class V Chitinase from *Nicotiana tabacum*
Plant Mol. Biol., **75** (2011) 291.

M. Unno, M. Shinohara, K. Takayama, H. Tanaka, K. Teruya, K. Doh-ura, R. Sakai, M. Sasaki and M. Ikeda-Saito
Binding and Selectivity of the Marine Toxin Neodysiherbaine A and its Synthetic Analogues to GluK1 and GluK2 Kainate Receptors
J. Mol. Biol., **413** (2011) 667.

- T. Saitoh, M. Igura, Y. Miyazaki, T. Ose, N. Maita and D. Kohda
Crystallographic Snapshots of Tom20-Mitochondrial Presequence Interactions with Disulfide-Stabilized Peptides
Biochemistry, **50** (2011) 5487.
- H.-J. Kang, K. Kubota, K. Miyazono and M. Tanokura
Expression, Purification, Crystallization and Preliminary X-Ray Analysis of the KaiC-Like Protein PH0187 from the Hyperthermophilic Archaeon *Pyrococcus horikoshii* OT3
Acta Cryst. F, **67** (2011) 144.
- T. Mase, K. Kubota, K. Miyazono, Y. Kawarabayasi and M. Tanokura
Crystal Structure of Flap Endonuclease 1 from Hyperthermophilic Archaeon *Desulfurococcus amylolyticus*
Acta Cryst. F, **67** (2011) 209.
- K. Kubota, K. Nagata, M. Okai, K. Miyazono, W. Soemphol, J. Ohtsuka, A. Yamamura, H. Toyama, K. Matsushita and M. Tanokura
The Crystal Structure of L-Sorbose Reductase from *Gluconobacter frateurii* Complexed with NADPH and L-Sorbose
J. Mol. Biol., **407** (2011) 543.
- D. Sasaki, M. Fujihashi, Y. Iwata, M. Murakami, T. Yoshimura, H. Hemmi and K. Miki
Structure and Mutation Analysis of Archaeal Geranylgeranyl Reductase
J. Mol. Biol., **409** (2011) 543.
- H. Sakuraba, K. Koga, K. Yoneda, Y. Kashima and T. Ohshima
Structure of a Multicopper Oxidase from the Hyperthermophilic Archaeon *Pyrobaculum Aerophilum*
Acta Cryst. F, **67** (2011) 753.
- H. Sakuraba, T. Kawai, K. Yoneda and T. Ohshima
Crystal Structure of UDP-Galactose 4-Epimerase from the Hyperthermophilic Archaeon *Pyrobaculum calidifontis*
Arch. Biochem. Biophys., **512** (2011) 126.
- T. Tonozuka, T. Miyazaki and A. Nishikawa
Structural Similarity between a Starch-Hydrolyzing Enzyme and an N-Glycan-Hydrolyzing Enzyme: Exohydrolases Cleaving α -1,X-Glucosidic Linkages to Produce β -Glucose
Trends in Glycoscience and Glycotechnology, **23** (2011) 93.
- T. Nakamura, T. Tonozuka, S. Ito, Y. Takeda, R. Sato, I. Matsuo, Y. Ito, K. Oguma and A. Nishikawa
Molecular Diversity of the Two Sugar-Binding Sites of the β -Trefoil Lectin HA33/C (HA1) from *Clostridium botulinum* Type C Neurotoxin
Arch. Biochem. Biophys., **512** (2011) 69.
- K. Taoka, I. Ohki, H. Tsuji, K. Furuuta, K. Hayashi, T. Yanase, M. Yamaguchi, C. Nakashima, Y. A. Purwestri, S. Tamaki, Y. Ogaki, C. Shimada, A. Nakagawa, C. Kojima and K. Shimamoto
14-3-3 Proteins Act as Intracellular Receptors for Rice Hd3a Florigen
Nature, **476** (2011) 332.
- S. Fushinobu, M. Hidaka, A. M. Hayashi, T. Wakagi, H. Shoun and M. Kitaoka
Interactions between Glycoside Hydrolase Family 94 Cellobiose Phosphorylase and Glucosidase Inhibitors
J. Appl. Glycosci., **58** (2011) 91.
- S. Fushinobu, T. Uno, M. Kitaoka, K. Hayashi, H. Matsuzawa and T. Wakagi
Mutational Analysis of Fungal Family 11 Xylanases on pH Optimum Determination
J. Appl. Glycosci., **58** (2011) 107.
- M. Okuda, T. Shiba, D-K. Inaoka, K. Kita, G. Kurisu, S. Mineki, S. Harada, Y. Watanabe and S. Yoshinari
A Conserved Lysine Residue in the Crenarchaea-Specific Loop is Important for the Crenarchaeal Splicing Endonuclease Activity
J. Mol. Biol., **405** (2011) 92.
- Y. Uchida, J. Hasegawa, D. Chinnapen, T. Inoue, S. Okazaki, R. Kato, S. Wakatsuki, R. Misaki, M. Koike, Y. Uchiyama, S. Iemura, T. Natsume, R. Kuwahara, T. Nakagawa, K. Nishikawa, K. Mukai, E. Miyoshi, N. Taniguchi, D. Sheff, W. I. Lencer, T. Taguchi and H. Arai
Intracellular Phosphatidylserine is Essential for Retrograde Membrane Traffic through Endosomes
Proc. Natl. Acad. Sci. USA, **108** (2011) 15846.
- M. Kanagawa, T. Satoh, A. Ikeda, Y. Adachi, N. Ohno and Y. Yamaguchi
Structural Insights into Recognition of Triple-Helical β -Glucans by an Insect Fungal Receptor
J. Biol. Chem., **286** (2011) 29158.
- D.-F. Li, N. Zhang, Y.-J. Hou, Y. Huang, Y. Hu, Y. Zhang, S.-J. Liu and D.-C. Wang
Crystal Structures of the Transcriptional Repressor RolR Reveals a Novel Recognition Mechanism between Inducer and Regulator
PLoS ONE, **6** (2011) e19529.
- H. S. Kim, S. J. Lee, H. J. Yoon, D. R. An, D. J. Kim, S.-J. Kim and S. W. Suh
Crystal Structures of YwqE from *Bacillus subtilis* and CpsB from *Streptococcus pneumoniae*, Unique Metal-Dependent Tyrosine Phosphatases
J. Struct. Biol., **175** (2011) 442.
- Z. Fujimoto, H. Ichinose, P. Biely and S. Kaneko
Crystallization and Preliminary Crystallographic Analysis of the Glycoside Hydrolase Family 115 α -Glucuronidase from *Streptomyces pristinaespiralis*
Acta Cryst. F, **67** (2011) 68.

- A. Zheng, R. Yamamoto, M. Sokabe, I. Tanaka and M. Yao
Crystallization and Preliminary X-Ray Crystallographic Analysis of eIF5B Δ N and the eIF5B Δ N-eIF1A Δ N Complex
Acta Cryst. F, **67** (2011) 730.
- H. Hirano and Y. Matsuura
Sensing Actin Dynamics: Structural Basis for G-actin-Sensitive Nuclear Import of MAL
Biochem. Biophys. Res. Commun., **414** (2011) 373.
- Y. Yasutake, H. Ota, E. Hino, S. Sakasegawa and T. Tamura
Structures of Burkholderia Thailandensis Nucleoside Kinase: Implications for the Catalytic Mechanism and Nucleoside Selectivity
Acta Cryst. D, **67** (2011) 945.
- S. Isogai, D. Morimoto, K. Arita, S. Unzai, T. Tenno, J. Hasegawa, Y.-S. Sou, M. Komatsu, K. Tanaka, M. Shirakawa and H. Tochio
Crystal Structure of the Ubiquitin-Associated (UBA) Domain of p62 and its Interaction with Ubiquitin
J. Biol. Chem., **286** (2011) 31864.
- H. Narita, A. Nakagawa, Y. Yamamoto, T. Sakisaka, Y. Takai and M. Suzuki
Refolding, Crystallization and Preliminary X-Ray Crystallographic Study of the Whole Extracellular Regions of Nectins
Acta Cryst. F, **67** (2011) 344.
- H. Tanaka, M. Senda, N. Venugopalan, A. Yamamoto, T. Senda, T. Ishida and K. Horiike
Crystal Structure of a Zinc-Dependent D-Serine Dehydratase from Chicken Kidney
J. Biol. Chem., **286** (2011) 27548.
- A. Kitamura, T. Sengoku, M. Nishimoto, S. Yokoyama and Y. Bessho
Crystal Structure of the Bifunctional tRNA Modification Enzyme MnmC from *Escherichia coli*
Protein Sci., **20** (2011) 1105.
- T. Shibahara, T. Satomura, R. Kawakami, T. Ohshima and H. Sakuraba
Crystallization and Preliminary X-Ray Analysis of a Dye-Linked D-Lactate Dehydrogenase from the Aerobic Hyperthermophilic Archaeon *Aeropyrum pernix*
Acta Cryst. F, **67** (2011) 1425.
- R. Suzuki, Z. Fujimoto, T. Shiotsuki, M. Momma, A. Tase, M. Miyazawa and T. Yamazaki
Structural Mechanism of JH Delivery in Hemolymph by JHBP of silkworm, *Bombyx mori*
Sci. Rep., **1** (2011) 133.
- S. Horita, Y. Yamanaka, A. Yamamura, A. Okada, J. Nakayama, K. Nagata and M. Tanokura
Crystallization and Preliminary X-Ray Analysis of a Putative Sensor Histidine Kinase Domain, the C-Terminal Domain of HksP4 from *Aquifex aeolicus* VF5
Acta Cryst. F, **67** (2011) 803.
- T. Arimori, H. Tamaoki, T. Nakamura, H. Kamiya, S. Ikemizu, Y. Takagi, T. Ishibashi, H. Harashima, M. Sekiguchi and Y. Yamagata
Diverse Substrate Recognition and Hydrolysis Mechanisms of Human NUDT5
Nucleic Acids Res., **39** (2011) 8972.
- T. Osawa, S. Kimura, N. Terasaka, H. Inanaga, T. Suzuki and T. Numata
Structural Basis of tRNA Agmatinylation Essential for AUA Codon Decoding
Nature Structural Molecular Biology, **18** (2011) 1275.
- N. N. Noda, K. Satoo, Y. Fujioka, H. Kumeta, K. Ogura, H. Nakatogawa, Y. Ohsumi and F. Inagaki
Structural Basis of Atg8 Activation by a Homodimeric E1, Atg7
Molecular Cell, **44** (2011) 462.
- T. Osawa, H. Inanaga, S. Kimura, N. Terasaka, T. Suzuki and T. Numata
Crystallization and Preliminary X-Ray Diffraction Analysis of an Archaeal tRNA-Modification Enzyme, TiaS, Complexed with tRNA^{Tle2} and ATP
Acta Cryst. F, **67** (2011) 1414.
- M. Maki, H. Suzuki and H. Shibata
Structure and Function of ALG-2, a Penta-EF-Hand Calcium-Dependent Adaptor Protein
Sci. China Life Sci., **54** (2011) 770.
- N. Nuemket, Y. Tanaka, K. Tsukamoto, T. Tsuji, K. Nakamura, S. Kozaki, M. Yao and I. Tanaka
Structural and Mutational Analyses of the Receptor Binding Domain of Botulinum D/C Mosaic Neurotoxin: Insight into the Ganglioside Binding Mechanism
Biochem. Biophys. Res. Commun., **411** (2011) 433.
- K. Yamashita, Y. Kawai, Y. Tanaka, N. Hirano, J. Kaneko, N. Tomita, M. Ohta, Y. Kamio, M. Yao and I. Tanaka
Crystal Structure of the Octameric Pore of Staphylococcal γ -Hemolysin Reveals the β -Barrel Pore Formation Mechanism by Two Components
Proc. Natl. Acad. Sci. USA, **108** (2011) 17314.
- N. Suzuki, Y.-M. Kim, Z. Fujimoto, M. Momma, H.-K. Kang, K. Funane, M. Okuyama, H. Mori and A. Kimura
Crystallization and Preliminary Crystallographic Analysis of Dextranase from *Streptococcus mutans*
Acta Cryst. F, **67** (2011) 1542.

S. Saijo, S. Arai, K. M. M. Hossain, I. Yamato, K. Suzuki, Y. Kakinuma, Y. Ishizuka-Katsura, N. Ohsawa, T. Terada, M. Shirouzu, S. Yokoyama, S. Iwata and T. Murata.

Crystal Structure of the Central Axis DF Complex of the Prokaryotic V-ATPase
Proc. Natl. Acad. Sci. USA, **108** (2011) 19955.

B. Zheng, W. Yang, X. Zhao, Y. Wang, Z. Lou, Z. Rao and Y. Feng

Crystal Structure of Hyperthermophilic Endo- β -1,4-glucanase: Implications for Catalytic Mechanism and Thermostability
J. Biol. Chem., **287** (2011) 8336.

H. Tanaka, T. Nogi, N. Yasui, K. Iwasaki and J. Takagi
Structural Basis for Variant-Specific Neuroigin-Binding by α -Neurexin

PLoS One, **6** (2011) e19411.

S. Fujita-Sato, S. Ito, T. Isobe, T. Ohya, K. Wakabayashi, K. Morishita, O. Ando and F. Isono
Structural Basis of Digoxin That Antagonizes ROR γ t Receptor Activity and Suppresses Th17 Cell Differentiation and Interleukin (IL)-17 Production
J. Biol. Chem., **286** (2011) 31409.

K. Akaji, H. Konno, H. Mitsui, K. Teruya, Y. Shimamoto, Y. Hattori, T. Ozaki, M. Kusunoki and A. Sanjoh

Structure-Based Design, Synthesis, and Evaluation of Peptide-Mimetic SARS 3CL Protease Inhibitors
J. Med. Chem., **54** (2011) 7962.

T. Nagai, H. Unno, M. W. Janczak, T. Yoshimura, CD. Poulter and H. Hemmi

Covalent Modification of Reduced Flavin Mononucleotide in Type-2 Isopenentenyl Diphosphate Isomerase by Active-Site-Directed Inhibitors
Proc. Natl. Acad. Sci. USA, **108** (2011) 20461.

Z. Fujimoto and K. Kimura

Crystal Structure of Bacteriophage Φ NIT1 Zinc Peptidase PghP that Hydrolyzes γ -Glutamyl Linkage of Bacterial Poly- γ -Glutamate
Proteins, **80** (2011) 722.

X. Liu, H. Zhang, X.-J. Wang, L.-F. Li and X.-D. Su
Get Phases from Arsenic Anomalous Scattering: *De Novo* SAD Phasing of Two Protein Structures Crystallized in Cacodylate Buffer
PLoS One, **6** (2011) e24227.

T. Imagawa, T. Tsurumura, Y. Sugimoto, K. Aki, K. Ishidoh, S. Kuramitsu and H. Tsuge

Structural Basis of Free Reduced Flavin Generation by Flavin Reductase from *Thermus Thermophilus* HB8
J. Biol. Chem., **286** (2011) 44078.

T. Tomita, T. Kuzuyama and M. Nishiyama
Structural Basis for Leucine-Induced Allosteric Activation of Glutamate Dehydrogenase
J. Biol. Chem., **286** (2011) 37406.

H. Xiang, M. Niyama, S. Sugiyama, H. Adachi, K. Takano, S. Murakami, T. Inoue, Y. Mori, M. Ishikawa, H. Matsumura and E. Katoh

Crystallization and Preliminary X-Ray Crystallographic Analysis of a Helicase-Like Domain from a Tomato Mosaic Virus Replication Protein
Acta Cryst. F, **67** (2011) 1649.

E. Matsuoka, Y. Tanaka, M. Kuroda, Y. Shouji, T. Ohta, I. Tanaka and M. Yao

Crystal Structure of the Functional Region of Uro-Adherence Factor A from *Staphylococcus saprophyticus* Reveals Participation of the B Domain in Ligand Binding
Protein Science, **20** (2011) 406.

F. Yu, Y. Tanaka, K. Yamashita, T. Suzuki, A. Nakamura, N. Hirano, T. Suzuki, M. Yao and I. Tanaka

Molecular Basis of Dihydrouridine Formation on tRNA
Proc. Natl. Acad. Sci. USA, **108** (2011) 19593.

F. Yu, Y. Tanaka, S. Yamamoto, A. Nakamura, S. Kita, N. Hirano, I. Tanaka and M. Yao

Crystallization and Preliminary X-Ray Crystallographic Analysis of Dihydrouridine Synthase from *Thermus thermophilus* and its Complex with tRNA
Acta Cryst. F, **67** (2011) 685.

Y. Yasutake and T. Tamura

Efficient Production of Active Form of Vitamin D₃ by Microbial Conversion: Comprehensive Approach from the Molecular to the Cellular Level
Synthesiology, **4** (2011) 222, (*in Japanese*).

G. Ju, K. Ninou, H. Kamiya, S. Fuchi, M. Tabuchi and Y. Takeda

X-Ray Characterization at Growth Temperatures of In_xGa_{1-x}N Growth by MOVPE
Journal of Crystal Growth, **318** (2011) 1143.

K. Ninou, G. Ju, H. Kamiya, S. Fuchi, M. Tabuchi and Y. Takeda

Novel System for X-Ray CTR Scattering Measurement on in-situ Observation of OMVPE Growth of Nitride Semiconductor Heterostructures
J. Cryst. Growth, **318** (2011) 1139.

H. Tameoka, T. Kawase, M. Tabuchi and Y. Takeda
Development of X-Ray Diffractometer for in-situ Observation of Thin-Film Crystal Growth Equipped with Focusing Monochromator
Phys. Status Solidi C, **8** (2011) 294.

Y. Moriwaki, J. M. M. Caaveiro, Y. Tanaka, H. Tsutsumi, I. Hamachi and K. Tsumoto

Molecular Basis of Recognition of Antibacterial Porphyrins by Heme-Transporter IsdH-NEAT3 of *Staphylococcus aureus*
Biochemistry, **50** (2011) 7311.

Former 6A

M. Suea, C. Nakamura, T. Miyamoto and S. Yajima
Active-Site Architecture of Benzoxazinone-Glucoside β -D-Glucosidases in Triticeae
Plant Science, **180** (2011) 268.

J. Igarashi, K. Kobayashi and A. Matsuoka
A Hydrogen-Bonding Network Formed by the B10-E7-E11 Residues of a Truncated Hemoglobin from *Tetrahymena pyriformis* is Critical for Stability of Bound Oxygen and Nitric Oxide Detoxification
J. Biol. Inorg. Chem., **16** (2011) 599.

T. Hatakeyama, T. Kamiya, M. Kusunoki, S. Nakamura-Tsuruta, J. Hirabayashi, S. Goda and H. Unno
Galactose Recognition by A Tetrameric C-Type Lectin, CEL-IV, Containing the EPN Carbohydrate-Recognition Motif
J. Biol. Chem., **286** (2011) 10305.

T. Tonozuka, T. Miyazaki and A. Nishikawa
Structural Similarity between a Starch-Hydrolyzing Enzyme and an N-Glycan-Hydrolyzing Enzyme: Exohydrolases Cleaving α -1,X-Glucosidic Linkages to Produce β -Glucose
Trends in Glycoscience and Glycotechnology, **23** (2011) 93.

S. Fushinobu, M. Hidaka, A. M. Hayashi, T. Wakagi, H. Shoun and M. Kitaoka
Interactions between Glycoside Hydrolase Family 94 Cellobiose Phosphorylase and Glucosidase Inhibitors
J. Appl. Glycosci., **58** (2011) 91.

S. Fushinobu, T. Uno, M. Kitaoka, K. Hayashi, H. Matsuzawa and T. Wakagi
Mutational Analysis of Fungal Family 11 Xylanases on pH Optimum Determination
J. Appl. Glycosci., **58** (2011) 107.

T. Kinoshita, Y. Sekiguchi, H. Fukada, T. Nakaniwa, T. Tada, S. Nakamura, K. Kitaoura, H. Ohno, Y. Suzuki, A. Hirasawa, I. Nakanishi and G. Tsujimoto
A Detailed Thermodynamic Profile of Cyclopentyl and Isopropyl Derivatives Binding to CK2 Kinase
Mol. Cell. Biochem., **356** (2011) 97.

N. Igarashi, Y. Watanabe, Y. Shinohara, Y. Inoko, G. Matsuba, H. Okuda, T. Mori and K. Ito
Upgrade of the Small Angle X-Ray Scattering Beamlines at the Photon Factory
J. Phys.: Conf. Ser., **272** (2011) 012026.

M. Maki, H. Suzuki and H. Shibata
Structure and Function of ALG-2, a Penta-EF-Hand Calcium-Dependent Adaptor Protein
Sci. China Life Sci., **54** (2011) 770.

K. Kawamura, T. Yamada, K. Kurihara, T. Tamada, R. Kuroki, I. Tanaka, H. Takahashi and N. Niimura
X-Ray and Neutron Protein Crystallographic Analysis of the Trypsin-BPTI Complex
Acta Cryst. D, **67** (2011) 140.

G. Ju, K. Ninoi, H. Kamiya, S. Fuchi, M. Tabuchi and Y. Takeda
X-Ray Characterization at Growth Temperatures of $\text{In}_x\text{Ga}_{1-x}\text{N}$ Growth by MOVPE
Journal of Crystal Growth, **318** (2011) 1143.

K. Ninoi, G. Ju, H. Kamiya, S. Fuchi, M. Tabuchi and Y. Takeda
Novel System for X-Ray CTR Scattering Measurement on in-situ Observation of OMVPE Growth of Nitride Semiconductor Heterostructures
J. Cryst. Growth, **318** (2011) 1139.

H. Tameoka, T. Kawase, M. Tabuchi and Y. Takeda
Development of X-Ray Diffractometer for in-situ Observation of Thin-Film Crystal Growth Equipped with Focusing Monochromator
Phys. Status Solidi C, **8** (2011) 294.

6C

S. Hosokawa, N. Happo, K. Hayashi, K. Mimura, K. Wakita, W. Hu, H. Ishii, M. Yoshimura, J. Jeyakanthan and N. Mamedov
Three-Dimensional Atomic Images of TlInSe_2 Thermoelectric Material Obtained by X-Ray Fluorescence Holography
Jpn. J. Appl. Phys., **50** (2011) 05FC06.

N. Happo, Y. Takehara, M. Fujiwara, K. Tanaka, S. Senba, S. Hosokawa, K. Hayashi, W. Hu, M. Suzuki and H. Asada
Local Structure around Ge Atoms in IV-VI Ferromagnetic Semiconductor $\text{Ge}_{0.6}\text{Mn}_{0.4}\text{Te}$ by X-Ray Fluorescence Holography
e-J. Surf. Sci. Nanotech., **9** (2011) 247.

S. Hosokawa, T. Ozaki, N. Happo and K. Hayashi
Applications of X-Ray Fluorescence Holography to Materials Sciences
e-J. Surf. Sci. Nanotech., **9** (2011) 265.

K. Hayashi
Recent Advances in X-Ray Fluorescence Holography
e-J. Surf. Sci. Nanotech., **9** (2011) 363.

D. S. Kim, T. C. Ozawa, K. Fukuda, S. Ohshima, I. Nakai and T. Sasaki
Soft-Chemical Exfoliation of $\text{Na}_{0.9}\text{Mo}_2\text{O}_4$: Preparation and Electrical Conductivity Characterization of a Molybdenum Oxide Nanosheet
Chemistry of Materials, **23** (2011) 2700.

T. C. Ozawa, K. Fukuda, Y. Ebina, K. Kosuda, A. Sato, Y. Michiue, K. Kurashima and T. Sasaki
A Bona Fide Two-Dimensional Percolation Model: An Insight into the Optimum Photoactivator Concentration in $\text{La}_{2/3-x}\text{Eu}_x\text{Ta}_2\text{O}_7$ Nanosheets
Sci. Technol. Adv. Mater., **11** (2011) 044601.

T. Shibata, G. Takanashi, T. Nakamura, K. Fukuda, Y. Ebina and T. Sasaki
Titanoniobate and Niobate Nanosheet Photocatalysts: Superior Photoinduced Hydrophilicity and Enhanced Thermal Stability of Unilamellar Nb_3O_8 Nanosheet
Energy Environ. Sci., **4** (2011) 535.

7A

K. Amemiya and M. Sakamaki
NiO-Like Single Layer Formed on a Ni/Cu(001) Thin Film Revealed by the Depth-Resolved X-Ray Absorption Spectroscopy
Appl. Phys. Lett., **98** (2011) 012501.

K. Amemiya and M. Sakamaki
Sub-nm Resolution Depth Profiling of the Magnetic Structure of Thin Films by the Depth-Resolved X-Ray Magnetic Circular Dichroism Technique
J. Phys. D, **44** (2011) 064018.

O. Endo, T. Horikoshi, N. Katsumata, K. Otani, T. Fujishima, H. Goto, K. Minami, K. Akaike, H. Ozaki, R. Sumii, K. Amemiya, M. Nakamura and N. Kosugi
Incommensurate Crystalline Phase of *n*-Alkane Monolayers on Graphite (0001)
J. Phys. Chem. C, **115** (2011) 5720.

O. Endo, H. Ozaki, R. Sumii, K. Amemiya, M. Nakamura, and N. Kosugi
Orientation of *n*-Alkane in Thin Films on Graphite (0001) Studied using C K-NEXAFS
J. Elec. Spec. Relat. Phenom., **184** (2011) 257.

M. Kiguchi, K. Takai, V. L. J. Joly, T. Enoki, R. Sumii and K. Amemiya
Magnetic Edge State and Dangling Bond State of Nanographene in Activated Carbon Fibers
Phys. Rev. B, **84** (2011) 045421.

D. Asakura, M. Okubo, Y. Mizuno, T. Kudo, H. Zhou, K. Amemiya, F. M. F. de Groot, J.-L. Chen, W.-C. Wang, P.-A. Glans, C. L. Chang, J.-H. Guo and I. Honma
Electron Delocalization in Cyanide-Bridged Coordination Polymer Electrodes for Li-Ion Batteries Studied by Soft X-Ray Absorption Spectroscopy
Phys. Rev. B, **84** (2011) 045117.

M. Sakamaki and K. Amemiya
Element Specific Magnetic Anisotropy Energy of Alternately Layered FeNi Thin Films
Appl. Phys. Express, **4** (2011) 073002.

T. Maruyama, S. Sakakibara, S. Naritsuka and K. Amemiya
Initial Stage of Carbon Nanotube Formation Process by Surface Decomposition of SiC: STM and NEXAFS Study
Diamond and Related Materials, **20** (2011) 1325.

J. Okabayashi, S. Kono, Y. Yamada and K. Nomura
Fabrication and Magnetic Properties of Fe and Co Co-Doped ZrO_2
AIP Advances, **1** (2011) 042138.

7C

N. Ahmed, Y. Shibata, T. Taniguchi and Y. Izumi
Photocatalytic Conversion of Carbon Dioxide into Methanol using Zinc-Copper-M(III) (M = Aluminum, Gallium) Layered Double Hydroxides
J. Catal., **279** (2011) 123.

K. Mori and H. Yamashita
Design of Colloidal and Supported Metal Nanoparticles: Their Synthesis, Characterization, and Catalytic Application
J. Jpn. Petrol. Inst., **54** (2011) 1.

Y. Horiuchi, Y. Shimizu, T. Kamegawa, K. Mori and H. Yamashita
Design of Superhydrophobic Surfaces by Synthesis of Carbon Nanotubes over Co-Mo Nanocatalysts Deposited under Microwave Irradiation on Ti-Containing Mesoporous Silica Thin Films
Phys. Chem. Chem. Phys., **13** (2011) 6309.

K. Mori, K. Watanabe, M. Kawashima, M. Che and H. Yamashita
Anchoring of Pt(II) Pyridyl Complex to Mesoporous Silica Materials: Enhanced Photoluminescence Emission at Room Temperature and Photooxidation Activity using Molecular Oxygen
J. Phys. Chem. C, **115** (2011) 1044.

T. Wada, K. K. Bando, K. Kawai and K. Asakura
In-situ XAFS for Monitoring the Structure of Catalysts under More Realistic Reaction Conditions
Shokubai, **53** (2011) 150, (*in Japanese*).

T. Kamegawa, N. Suzuki, M. Che and H. Yamashita
Synthesis and Catalytic Performance of Single-Site Ti-Containing Hierarchical Macroporous Silica with Mesoporous Frameworks
Langmuir, **27** (2011) 2873.

T. Kamegawa, N. Suzuki and H. Yamashita
Design of Macroporous TiO_2 Thin Film Photocatalysts with Enhanced Photofunctional Properties
Energy Environ. Sci., **4** (2011) 1411.

K. R. Priolkar, D. N. Lobo, P. A. Bhobe, S. Emura and A. K. Nigam
Role of Ni-Mn Hybridization in the Magnetism of the Martensitic State of Ni-Mn-In Shape Memory Alloys
EPL, **94** (2011) 38006.

- F. Liu, K. Asakura, H. He, Y. Liu, W. Shan, X. Shi and C. Zhang
Influence of Calcination Temperature on Iron Titanate Catalyst for the Selective Catalytic Reduction of NO_x with NH₃
Catal. Today, **164** (2011) 520.
- F. Liu, K. Asakura, H. He, W. Shan, X. Shi and C. Zhang
Influence of Sulfation on Iron Titanate Catalyst for the Selective Catalytic Reduction of NO_x with NH₃
Appl. Catal. B, **103** (2011) 369.
- H. Sato, H. Maso, Y. Utsumi, H. Kurihara, Y. Mukaegawa, Y. Tezuka, T. Iwazumi, F. Iga, M. Tsubota, H. Namatame and M. Taniguchi
Polarization-Dependent Ti K X-Ray Absorption and Emission Studies of Ti₂O₃ Single Crystal
J. Elec. Spec. Relat. Phenom., **184** (2011) 184.
- J. Ding, T. Fan, D. Zhang, K. Saito and Q. Guo
Structural and Optical Properties of Porous Iron Oxide
Solid State Communications, **151** (2011) 802.
- Y. Horiuchi, H. Ura, T. Kamegawa, K. Mori and H. Yamashita
Low-Temperature Synthesis of Highly Hydrophilic Ti-Containing Mesoporous Silica Thin Films on Polymer Substrates by Photocatalytic Removal of Structure-Directing Agents
J. Mater. Chem., **21** (2011) 236.
- Y. Horiuchi and H. Yamashita
Design of Mesoporous Silica Thin Films Containing Single-Site Photocatalysts and their Applications to Superhydrophilic Materials
Appl. Catal. A, **400** (2011) 1.
- S. Ishihara, K. Kakimoto and I. Kagomiya
Densification of (Na,K)NbO₃ Piezoelectric Ceramics by Two-Step Mixing Process
J. Mater. Sci., **46** (2011) 3822.
- J. Ohyama, A. Yamamoto, K. Teramura, T. Shishido and T. Tanaka
Modification of Metal Nanoparticles with TiO₂ and Metal-Support Interaction in Photodeposition
ACS Catal., **1** (2011) 187.
- Y. Cheng, H. Kajiro, H. Noguchi, A. Kondo, T. Ohba, Y. Hattori, K. Kaneko and H. Kanoh
Tuning of Gate Opening of an Elastic Layered Structure MOF in CO₂ Sorption with a Trace of Alcohol Molecules
Langmuir, **27** (2011) 6905.
- N. Kitamura, K. Uchino and Y. Idemoto
Crystal and Electronic Structures of CePO₄-Based Proton-Electron Mixed Conductors by using Synchrotron X-Rays
ECS Transactions, **33** (2011) 59.
- F. Liu, W. Shan, X. Shi, C. Zhang and H. He
Research Progress in Vanadium-Free Catalysts for the Selective Catalytic Reduction of NO with NH₃
Chin. J. Catal., **32** (2011) 1113. (*in Chinese*).
- T. Ohkubo, M. Nishi and Y. Kuroda
Actual Structure of Dissolved Zinc Ion Restricted in Less than 1 Nanometer Micropores of Carbon
J. Phys. Chem. C, **115** (2011) 14954.
- T. T. John, K. R. Priolkar, A. Bessiere, P. R. Sarode and B. Viana
Effect of [OH⁻] Linkages on Luminescent Properties of ZnO Nanoparticles
J. Phys. Chem. C, **115** (2011) 18070.
- S. Kageyama, S. Seino, T. Nakagawa, H. Nitani, K. Ueno, H. Daimon and T. A. Yamamoto
Formation of PtRu Alloy Nanoparticle Catalyst by Radiolytic Process Assisted by Addition of DL-Tartaric Acid and its Enhanced Methanol Oxidation Activity
J. Nanoparticle. Res., **13** (2011) 5275.
- J. Kugai, R. Kitagawa, S. Seino, T. Nakagawa, Y. Ohkubo, H. Nitani, H. Daimon and T. A. Yamamoto
γ-Fe₂O₃-Supported Pt-Cu Nanoparticles Synthesized by Radiolytic Process for Catalytic CO Preferential Oxidation
Appl. Catal. A, **406** (2011) 43.
- Y. Ohkubo, M. Shibata, S. Kageyama, S. Seino, T. Nakagawa, J. Kugai and T. A. Yamamoto
Radiation Induced Synthesis of Au-Pd Nanoparticles of Random Alloy Structure Supported on Carbon Particles using the High Energy Electron Beam
Mater. Lett., **65** (2011) 2165.
- T. A. Yamamoto, S. Kageyama, S. Seino, H. Nitani, T. Nakagawa, R. Horioka, Y. Honda, K. Ueno and H. Daimon
Methanol Oxidation Catalysis and Substructure of PtRu/C Bimetallic Nanoparticles Synthesized by a Radiolytic Process
Appl. Catal. A, **396** (2011) 68.
- M. Tada, N. Ishiguro, T. Uruga, H. Tanida, Y. Terada, S. Nagamatsu, Y. Iwasawae and S. Ohkoshi
μ-XAFS of Single Particle of a Practical NiO_x/Ce₂Zr₂O_y Catalyst
Phys. Chem. Chem. Phys., **13** (2011) 14910.
- H. Einaga, Y. Teraoka and A. Ogata
Benzene Oxidation with Ozone over Manganese Oxide Supported on Zeolite Catalysts
Catal. Today, **164** (2011) 571.
- S. Furukawa, Y. Hitomi, T. Shishido, K. Teramura and T. Tanaka
π Back-Bonding of Iron(II) Complexes Supported by Tris(pyrid-2-ylmethyl)amine and its Nitro-Substituted Derivatives
J. Phys. Chem. A, **115** (2011) 13589.

A. Yamada, N. Iwane, S. Nishimura, Y. Koyama and I. Tanaka
 Synthesis and Electrochemistry of Monoclinic $\text{Li}(\text{Mn}_x\text{Fe}_{1-x})\text{BO}_3$: A Combined Experimental and Computational Study
J. Mater. Chem., **21** (2011) 10690.

A. Yamada, S. Matsumoto and Y. Nakamura
 Direct Solid-State Synthesis and Large-Capacity Anode Operation of $\text{Li}_{3-x}\text{Fe}_x\text{N}$
J. Mater. Chem., **21** (2011) 10021.

Former 8A

T. Kakiuchi, N. Fujita, K. Mase, M. Tanaka and S. Nagaoka
 Local Valence Electronic States of SiO_2 Ultrathin Films Grown on $\text{Si}(100)$ Studied Using Auger Photoelectron Coincidence Spectroscopy: Observation of Upward Shift of Valence-Band Maximum as a Function of SiO_2 Thickness
J. Phys. Soc. Jpn., **80** (2011) 084703.

8A

K. Saito, Y. Yamamura, N. Kikuchi, A. Nakao, S. Yasuzuka, Y. Akishige and Y. Murakami
 Polarization Reversal by Intramolecular Disorder in Organic Ferroelectrics: Trichloroacetamide
Cryst. Eng. Comm., **13** (2011) 2693.

M. Nihei, Y. Sekine, H. Suganami, K. Nakazawa, A. Nakao, H. Nakao, Y. Murakami and H. Oshio
 Controlled Intramolecular Electron Transfers in Cyanide-Bridged Molecular Squares by Chemical Modifications and External Stimuli
J. Am. Chem. Soc., **133** (2011) 3592.

H. Sakai, J. Fujioka, T. Fukuda, D. Okuyama, D. Hashizume, F. Kagawa, H. Nakao, Y. Murakami, T. Arima, A. Q. R. Baron, Y. Taguchi and Y. Tokura
 Displacement-Type Ferroelectricity with Off-Center Magnetic Ions in Perovskite $\text{Sr}_{1-x}\text{Ba}_x\text{MnO}_3$
Phys. Rev. Lett., **107** (2011) 137601.

S. Horiuchi, R. Kumai and Y. Tokura
 Hydrogen-Bonding Molecular Chains for High-Temperature Ferroelectricity
Adv. Mater., **23** (2011) 2098.

K. Ishizaka, M. S. Bahrany, H. Murakawa, M. Sakano, T. Shimojima, T. Sonobe, K. Koizumi, S. Shin, H. Miyahara, A. Kimura, K. Miyamoto, T. Okuda, H. Namatame, M. Taniguchi, R. Arita, N. Nagaosa, K. Kobayashi, Y. Murakami, R. Kumai, Y. Kaneko, Y. Onose and Y. Tokura
 Giant Rashba-Type Spin Splitting in Bulk BiTeI
Nature Materials, **10** (2011) 521.

R. Fukuta, S. Miyasaka, K. Hemmi, S. Tajima, D. Kawana, K. Ikeuchi, Y. Yamasaki, A. Nakao, H. Nakao, Y. Murakami and K. Iwasa
 Effects of Cation-Size Variance on Spin and Orbital Orders in $\text{Eu}_{1-x}(\text{La}_{0.254}\text{Y}_{0.746})_x\text{VO}_3$
Phys. Rev. B, **84** (2011) 140409(R).

H. Minemawari, T. Yamada, H. Matsui, J. Tsutsumi, S. Haas, R. Chiba, R. Kumai and T. Hasegawa
 Inkjet Printing of Single-Crystal Films
Nature, **475** (2011) 364.

W. Kobayashi, Y. Hayashi, M. Matsushita, Y. Yamamoto, I. Terasaki, A. Nakao, H. Nakao, Y. Murakami, Y. Moritomo, H. Yamauchi and M. Karppinen
 Anisotropic Thermoelectric Properties Associated with Dimensional Crossover in Quasi-One-Dimensional $\text{SrNbO}_{3.4+d}$ ($d \sim 0.03$)
Phys. Rev. B, **84** (2011) 085118.

8B

H. Ikemoto, A. Goyo and T. Miyanaga
 Size Dependence of the Local Structure and Atomic Correlations in Tellurium Nanoparticles
J. Phys. Chem. C, **115** (2011) 2931.

A. Kobayashi, Y. Suzuki, T. Ohba, S. Noro, H.-C. Chang and M. Kato
 Ln-Co-Based Rock-Salt-Type Porous Coordination Polymers: Vapor Response Controlled by Changing the Lanthanide Ion
Inorg. Chem., **50** (2011) 2061.

A. Kobayashi, K. Ohbayashi, R. Aoki, H.-C. Chang and M. Kato
 Synthesis, Structure and Photophysical Properties of a Flavin-Based Platinum(II) Complex
Dalton Trans., **40** (2011) 3484.

K. Saito, Y. Yamamura, N. Kikuchi, A. Nakao, S. Yasuzuka, Y. Akishige and Y. Murakami
 Polarization Reversal by Intramolecular Disorder in Organic Ferroelectrics: Trichloroacetamide
Cryst. Eng. Comm., **13** (2011) 2693.

H. Miyasaka, N. Motokawa, T. Chiyo, M. Takemura, M. Yamashita, H. Sagayama and T. Arima
 Stepwise Neutral-Ionic Phase Transitions in a Covalently Bonded Donor/Acceptor Chain Compound
J. Am. Chem. Soc., **133** (2011) 5338.

T. Akitsu, Y. Endo, M. Okawara, Y. Kimoto and M. Ohwa
 Influence of Water Molecules on Properties of Binuclear or Bridged Structures for Chiral $\text{Cu}^{\text{II}}\text{-Ni}^{\text{II}}$, $\text{Cu}^{\text{II}}\text{-Pd}^{\text{II}}$, and $\text{Cu}^{\text{II}}\text{-Pt}^{\text{II}}$ Tetracyano-Bimetallic Assemblies
The Open Crystallogr. J., **4** (2011) 2.

- T. Akitsu and S. Sonoki
Isotope Effects for Lattice Strain and Pseudo Jahn-Teller Distortion of Chiral Cyanide-Bridged Cu(II)-Co(III), Cr(III), and Fe(III) Bimetallic Assemblies
The Open Crystallogr. J., **4** (2011) 8.
- T. Akitsu, M. Ohwa, Y. Endo, S. Sonoki, Y. Aritake and Y. Kimoto
Some Factors and Effects on Thermally Structural Changes of Lattice for Cyanide-Bridged Bimetallic Assemblies of Cu(II)
The Open Crystallogr. J., **4** (2011) 25.
- T. Akitsu, Y. Endo, Y. Kimoto and M. Ohwa
Novel Thermally-Accessible Structural Distortion and Lattice Strain of a Chiral Cyanide-Bridged Cu (II)-Ni (II) Complex
The Open Crystallogr. J., **4** (2011) 21.
- K. Marumoto, N. Arai, H. Goto, M. Kijima, K. Murakami, Y. Tominari, J. Takeya, Y. Shimoi, H. Tanaka, S. Kuroda, T. Kaji, T. Nishikawa, T. Takenobu and Y. Iwasa
Microscopic Mechanisms behind the High Mobility in Rubrene Single-Crystal Transistors as Revealed by Field-Induced Electron Spin Resonance
Phys. Rev. B, **83** (2011) 075302.
- K. Nakayama, Y. Hirose, J. Soeda, M. Yoshizumi, T. Uemura, M. Uno, W. Li, M. J. Kang, M. Yamagishi, Y. Okada, E. Miyazaki, Y. Nakazawa, A. Nakao, K. Takimiya and J. Takeya
Patternable Solution-Crystallized Organic Transistors with High Charge Carrier Mobility
Adv. Mater., **23** (2011) 1626.
- S. Tao, H. Matsuzaki, H. Uemura, H. Yada, T. Uemura, J. Takeya, T. Hasegawa and H. Okamoto
Optical Pump-Probe Spectroscopy of Photocarriers in Rubrene Single Crystals
Phys. Rev. B, **83** (2011) 075204.
- S. Shinamura, I. Osaka, E. Miyazaki, A. Nakao, M. Yamagishi, J. Takeya and K. Takimiya
Linear- and Angular-Shaped Naphthodithiophenes: Selective Synthesis, Properties, and Application to Organic Field-Effect Transistors
J. Am. Chem. Soc., **133** (2011) 5024.
- Y. Okada, M. Uno, Y. Nakazawa, K. Sasai, K. Matsukawa, M. Yoshimura, Y. Kitaoka, Y. Mori and J. Takeya
Low-Temperature Thermal Conductivity of Bulk and Film-Like Rubrene Single Crystals
Phys. Rev. B, **83** (2011) 113305.
- M. Sadakiyo, T. Yamada and H. Kitagawa
Hydroxyl Group Recognition by Hydrogen-Bonding Donor and Acceptor Sites Embedded in a Layered Metal-Organic Framework
J. Am. Chem. Soc., **133** (2011) 11050.
- T. Tajiri, S. Saisho, Y. Komorida, M. Mito, H. Deguchi and A. Kohno
Effects of Anisotropic Strain on Perovskite $\text{LaMnO}_{3+\delta}$ Nanoparticles Embedded in Mesoporous Silica
J. Appl. Phys., **110** (2011) 044307.
- J. Soeda, Y. Hirose, M. Yamagishi, A. Nakao, T. Uemura, K. Nakayama, M. Uno, Y. Nakazawa, K. Takimiya and J. Takeya
Solution-Crystallized Organic Field-Effect Transistors with Charge-Acceptor Layers: High-Mobility and Low-Threshold-Voltage Operation in Air
Adv. Mater., **23** (2011) 3309.
- M. Uno, K. Nakayama, J. Soeda, Y. Hirose, K. Miwa, T. Uemura, A. Nakao, K. Takimiya and S. Takeya
High-Speed Flexible Organic Field-Effect Transistors with a Three-Dimensional Structure
Adv. Mater., **23** (2011) 3047.
- T. Ito, T. Ushiyama, Y. Yanagisawa, R. Kumai and Y. Tomioka
Growth of Highly Insulating Bulk Single Crystals of Multiferroic BiFeO_3 and their Inherent Internal Strains in the Domain-Switching Process
Cryst. Growth Design, **11** (2011) 5139.
- W. Kobayashi, Y. Hayashi, M. Matsushita, Y. Yamamoto, I. Terasaki, A. Nakao, H. Nakao, Y. Murakami, Y. Moritomo, H. Yamauchi and M. Karppinen
Anisotropic Thermoelectric Properties Associated with Dimensional Crossover in Quasi-One-Dimensional $\text{SrNbO}_{3.4+d}$ ($d \sim 0.03$)
Phys. Rev. B, **84** (2011) 085118.
- H. Kyakuno, K. Matsuda, H. Yahiro, Y. Inami, T. Fukuoka, Y. Miyata, K. Yanagi, Y. Maniwa, H. Kataura, T. Saito, M. Yumura and S. Iijima
Confined Water Inside Single-Walled Carbon Nanotubes: Global Phase Diagram and Effect of Finite Length
J. Chem. Phys., **134** (2011) 244501.

9A

N. Ahmed, Y. Shibata, T. Taniguchi and Y. Izumi
Photocatalytic Conversion of Carbon Dioxide into Methanol using Zinc-Copper-M(III) (M = Aluminum, Gallium) Layered Double Hydroxides
J. Catal., **279** (2011) 123.

T. Wada, K. K. Bando, K. Kawai and K. Asakura
In-situ XAFS for Monitoring the Structure of Catalysts under More Realistic Reaction Conditions
Shokubai, **53** (2011) 150, (*in Japanese*).

Y. Idemoto, T. Hasegawa, N. Kitamura and Y. Uchimoto
Dependence of Thermodynamic Stability, Crystal and Electronic Structures and Battery Characteristic on Synthetic Condition and Li Content for $\text{Li}_x\text{Mn}_{0.5}\text{Ni}_{0.5}\text{O}_2$ as a Cathode Active Material of Li-Ion Battery
Electrochemistry, **79** (2011) 15, (*in Japanese*).

- C. Tokoro, H. Koga, Y. Oda, S. Owada and Y. Takahashi
XAFS Investigation for As(V) Co-Precipitation Mechanism with Ferrihydrite
J. Mining and Materials Processing Institute of Jpn., **127** (2011) 213, (*in Japanese*).
- M. Hatakeyama, H. Kishi, Y. Kita, K. Imai, K. Nishio, S. Karasawa, Y. Masaike, S. Sakamoto, A. Sandhu, A. Tanimoto, T. Gomi, E. Kohda, M. Abe and H. Handa
A Two-Step Ligand Exchange Reaction Generates Highly Water-Dispersed Magnetic Nanoparticles for Biomedical Applications
J. Mater. Chem., **21** (2011) 5959.
- F. Liu, K. Asakura, H. He, W. Shan, X. Shi and C. Zhang
Influence of Sulfation on Iron Titanate Catalyst for the Selective Catalytic Reduction of NO_x with NH₃
Appl. Catal. B, **103** (2011) 369.
- M. Hori, K. Shozugawa and M. Matsuo
Improvement of Speciation Analysis for Chromium by X-Ray Absorption Fine Structure and Estimation of the Reduction of Hexavalent Chromium in Soil
Bunseki Kagaku, **60** (2011) 379, (*in Japanese*).
- Y. Horiuchi, K. Fujiwara, T. Kamegawa, K. Mori and H. Yamashita
An Efficient Method for the Creation of a Superhydrophobic Surface: Ethylene Polymerization over Self-Assembled Colloidal Silica Nanoparticles Incorporating Single-Site Cr-Oxide Catalysts
J. Mater. Chem., **21** (2011) 8543.
- H. Yamaguchi, H. Shibata, K. Maejima, H. Tampo, K. Matsubara, A. Yamada and S. Niki
Local Structure around Dopant Site in Ga-Doped ZnO from Extended X-Ray Absorption Fine Structure Measurements
J. Phys. Soc. Jpn., **80** (2011) 074602.
- Y. Suzuki, M. Yamamoto, T. Saito, T. Miyanaga, S. Ohwada, A. Iwakoshi, T. Nanke and T. Kobayashi
Anomalous Infrared and Visible Light Absorption and Local Structure of Ag-Au Core/Shell Nanoparticles
Appl. Phys. A, **103** (2011) 81.
- Y. Cheng, H. Kajiro, H. Noguchi, A. Kondo, T. Ohba, Y. Hattori, K. Kaneko and H. Kanoh
Tuning of Gate Opening of an Elastic Layered Structure MOF in CO₂ Sorption with a Trace of Alcohol Molecules
Langmuir, **27** (2011) 6905.
- F. Liu, W. Shan, X. Shi, C. Zhang and H. He
Research Progress in Vanadium-Free Catalysts for the Selective Catalytic Reduction of NO with NH₃
Chin. J. Catal., **32** (2011) 1113, (*in Chinese*).
- T. Kashiwabara, Y. Takahashi, M. Tanimizu and A. Usui
Molecular-Scale Mechanisms of Distribution and Isotopic Fractionation of Molybdenum between Seawater and Ferromanganese Oxides
Geochim. Cosmochim. Acta, **75** (2011) 5762.
- T. Fujimori, Y. Tanino and M. Takaoka
Role of Zinc in MSW Fly Ash during Formation of Chlorinated Aromatics
Environ. Sci. Technol., **45** (2011) 7678.
- L. Cao, H. Park, G. Dodbiba, K. Ono, C. Tokoro and T. Fujita
Keeping Gallium Metal to Liquid State under the Freezing Point by using Silica Nanoparticles
Appl. Phys. Lett., **99** (2011) 143120.
- M. Tada, N. Ishiguro, T. Uruga, H. Tanida, Y. Terada, S. Nagamatsu, Y. Iwasawae and S. Ohkoshi
 μ -XAFS of Single Particle of a Practical NiO_x/Ce₂Zr₂O_y Catalyst
Phys. Chem. Chem. Phys., **13** (2011) 14910.
- Y. Onodera, K. Mori, T. Otomo, A. C. Hannon, M. Sugiyama and T. Fukunaga
Reverse Monte Carlo Modeling of Atomic Configuration for Li₂S-P₂S₅ Superionic Glasses
IOP Conf. Ser.: Mater. Sci. Eng., **18** (2011) 022012.
- S. Takenaka, T. Iguchi, E. Tanabe, H. Matsune and M. Kishida
Catalytic Performance of Pt Metal Particles at the Tips of Carbon Nanotubes
Catal. Lett., **141** (2011) 821.
- L. Wang, A. Yoshiasa, M. Okube and T. Takeda
Titanium Local Structure in Tektite Probed by X-Ray Absorption Fine Structure Spectroscopy
J. Synchrotron Rad., **18** (2011) 885.
- W. J. Chun, K. Miyazaki, N. Watanabe, Y. Koike, S. Takakusagi, K. Fujikawa, M. Nomura and K. Asakura
Angle Resolved Total Reflection Fluorescence XAFS and its Application to Au Clusters on TiO₂ (110) (1 × 1)
J. Ceram. Soc. Jpn., **119** (2011) 890.
- Y. S. Shimamoto, Y. Takahashi and Y. Terada
Formation of Organic Iodine Supplied as Iodide in a Soil-Water System in Chiba, Japan
Environ. Sci. Technol., **45** (2011) 2086.
- T. Furukawa and Y. Takahashi
Oxalate Metal Complexes in Aerosol Particles: Implications for the Hygroscopicity of Oxalate-Containing Particles
Atom. Chem. Phys., **11** (2011) 4289.
- A. G. Gault, S. Langely, A. Ibrahim, R. Renaud, Y. Takahashi, C. Boothman, J. R. Lloyd, I. D. Clark, F. G. Ferris and D. Fortin
Microbial and Geochemical Features Suggest Iron Redox Cycling within Bacteriogenic Iron Oxide-Rich Sediments
Chem. Geol., **281** (2011) 41.
- S. Emura, S. Kimura, K. Tokuda, H. Tambo, S. Hasegawa, and H. Asahi
Co-ordination Alignments at the Vicinity of the Dopant Cr Ions in AlN
Physica Status Solidi c, **8** (2011) 473.

- S. N. Mohd Tawil, D. Krishnamurthy, R. Kakimi, M. Ishimaru, S. Emura, S. Hasegawa and H. Asahi, Influence of Si-Doping on the Characteristics of InGaGdN/GaN MQWs Grown by MBE *Physical Status Solidi C*, **8** (2011) 491.
- H. Tambo, S. Hasegawa, K. Higashi, R. Kakimi, S. N. M. Tawil, Y. K. Zhou, S. Emura and H. Asahi Structural and Magnetic Properties of Diluted Magnetic Semiconductor GaGdN Nanorods *Physics Status Solidi C*, **8** (2011) 494.
- D. Krishnamurthy, S. N. Mohd Tawil, R. Kakimi, M. Ishimaru, S. Emura, S. Hasegawa and H. Asahi Investigations on the Properties of Intermittently Gd-Doped InGaN Structures Grown by Molecular-Beam Epitaxy *Phys. Status Solidi C*, **8** (2011) 497.
- S. N. M. Tawil, D. Krishnamurthy, R. Kakimi, S. Emura, S. Hasegawa and H. Asahi Studies on the InGaGdN/GaN Magnetic Semiconductor Heterostructures Grown by Plasma-Assisted Molecular-Beam Epitaxy *J. Cryst. Growth*, **323** (2011) 351.
- D. Krishnamurthy, S. N. M. Tawil, R. Kakimi, M. Ishimaru, S. Emura, Y.-K. Zhou, S. Hasegawa and H. Asahi Structural Characterization of MBE Grown InGaGdN/GaN and InGaN/GaGdN Structures *Phys. Status Solidi C*, **8** (2011) 2245.
- S. Emura, K. Higashi, A. Itadani, H. Torigoe, Y. Kuroda, A. Nishikawa, Y. Fujiwara and H. Asahi Photoluminescence X-Ray Excitation Spectra in Eu-doped GaN Grown by Organometallic Vapor Phase Epitaxy *Mater. Res. Soc. Symp. Proc.*, **1342** (2011) 1241.
- P. Blanes, L. Sala, S. Garcia, J. Gonzalez, M. Frascaroli, M. Harada, C. Cong, Y. Niwa, C. Matulewicz, H. Prado, A. Cortadi and M. Gattuso Biosorption of Trivalent Chromium from Aqueous Solution by Red Seaweed *Polysiphonia nigrescens* *J. Water Resource and Protection*, **3** (2011) 832.
- T. Fujimori and M. Takaoka Thermochemical Chlorination of Carbon Indirectly Driven by an Unexpected Sulfide of Copper with Inorganic Chloride *J. Hazard. Mater.*, **197** (2011) 345.
- K. Ikeue, N. Miyoshi, T. Tanaka and M. Machida Ca-Containing Mesoporous Silica as a Solid Base Catalyst for the Knoevenagel Condensation Reaction *Catal. Lett.*, **141** (2011) 877.
- S. Takenaka, H. Matsumori, H. Matsune and M. Kishida Highly Durable Pt Cathode Catalysts for Polymer Electrolyte Fuel Cells; Coverage of Carbon Black-Supported Pt Catalysts with Silica Layers *Appl. Catal. A*, **409** (2011) 248.
- Y. Hyobu, T. Itai, D. Hayase, M. Kumagai and S. Tanabe Mobilization of Manganese and Arsenic under Hypoxia in the Bottom of Lake Biwa *Interdisciplinary Studies on Environ. Chem.*, **6** (2011) 133.
- A. Era, M. Tabuchi, T. Nishitani and Y. Takeda A Study on EXAFS Analysis of Cs/GaAs NEA Surface *J. Phys.: Conf. Ser.*, **298** (2011) 012012.

9C

K. Yamamoto, T. Kondo and E. Ito Aggregation Structure and Surface Properties of Poly(Ethylene Maleimide) Copolymer Thin Film Modified with Fluoroalkyl and Alkyl Side Chains *J. Soc. Mater. Sci. Jpn.*, **60** (2011) 14, (*in Japanese*).

N. Ahmed, Y. Shibata, T. Taniguchi and Y. Izumi Photocatalytic Conversion of Carbon Dioxide into Methanol using Zinc-Copper-M(III) (M = Aluminum, Gallium) Layered Double Hydroxides *J. Catal.*, **279** (2011) 123.

Y. Nakamura, M. Adachi, K. Ito, Y. Kato, S. Fujii, M. Sasaki, Y. Urahama and S. Sakurai Effects of Compatibility between Tackifier and Polymer on Adhesion Property and Phase Structure: Tackifier-Added Polystyrene-Based Triblock/Diblock Copolymer Blend System *J. Appl. Polym. Sci.*, **120** (2011) 2251.

Y. Idemoto, T. Hasegawa, N. Kitamura and Y. Uchimoto Dependence of Thermodynamic Stability, Crystal and Electronic Structures and Battery Characteristic on Synthetic Condition and Li Content for $\text{Li}_x\text{Mn}_{0.5}\text{Ni}_{0.5}\text{O}_2$ as a Cathode Active Material of Li-Ion Battery *Electrochemistry*, **79** (2011) 15, (*in Japanese*).

S. Sakurai X-Ray Scattering Analyses on Deformation Behaviors of Thermoplastic Elastomers *NIPPON GOMU KYOKAISHI*, **84** (2011) 21, (*in Japanese*).

T. Matsutani and K. Yamamoto Solvent Annealing Induced Perpendicular Orientation of Cylindrical Microdomains in Polystyrene-*b*-poly(4-hydroxyl styrene)/PEG Oligomer Blend Thin Film Made by Spin-Coating from Selective Solvent *J. Phys.: Conf. Ser.*, **272** (2011) 012015.

I. Bilecka, L. Luo, I. Djerdj, M. D. Rossell, M. Jagodic, Z. Jaglicic, Y. Masubuchi, S. Kikkawa and M. Niederberger Microwave-Assisted Nonaqueous Sol-Gel Chemistry for Highly Concentrated ZnO-Based Magnetic Semiconductor Nanocrystals *J. Phys. Chem. C*, **115** (2011) 1484.

- M. Hori, K. Shozugawa and M. Matsuo
Improvement of Speciation Analysis for Chromium by X-Ray Absorption Fine Structure and Estimation of the Reduction of Hexavalent Chromium in Soil
Bunseki Kagaku, **60** (2011) 379, (*in Japanese*).
- Y. Masubuchi, T. Hata, T. Motohashi and S. Kikkawa
Crystal Structure of Eu-Doped Magnetoplumbite-Type Lanthanum Aluminum Oxynitride with Emission Site Splitting
J. Solid State Chem., **184** (2011) 2533.
- Y. Horiuchi and H. Yamashita
Design of Mesoporous Silica Thin Films Containing Single-Site Photocatalysts and their Applications to Superhydrophilic Materials
Appl. Catal. A, **400** (2011) 1.
- N. D. Tien, T. P. Hoa, G. Kimura, Y. Yamashiro, H. Fujiwara, M. Mochizuki, S. Sasaki and S. Sakurai
Effects of Blending Poly(D,L-Lactide) with Poly(Ethylene Glycol) on the Higher-Order Crystalline Structures of Poly(Ethylene Glycol) as Revealed by Small-Angle X-Ray Scattering
J. Phys.: Conf. Ser., **272** (2011) 012007.
- L. Wang, D. Li, M. Koike, S. Koso, Y. Nakagawa, Y. Xu and K. Tomishige
Catalytic Performance and Characterization of Ni-Fe Catalysts for the Steam Reforming of Tar from Biomass Pyrolysis to Synthesis Gas
Appl. Catal. A, **392** (2011) 248.
- T. Ohkubo, M. Nishi and Y. Kuroda
Actual Structure of Dissolved Zinc Ion Restricted in Less than 1 Nanometer Micropores of Carbon
J. Phys. Chem. C, **115** (2011) 14954.
- T. Yokoyama and K. Eguchi
Anharmonicity and Quantum Effects in Thermal Expansion of an Invar Alloy
Phys. Rev. Lett., **107** (2011) 065901.
- S. Kageyama, S. Seino, T. Nakagawa, H. Nitani, K. Ueno, H. Daimon and T. A. Yamamoto
Formation of PtRu Alloy Nanoparticle Catalyst by Radiolytic Process Assisted by Addition of DL-Tartaric Acid and its Enhanced Methanol Oxidation Activity
J. Nanoparticle. Res., **13** (2011) 5275.
- J. Kugai, R. Kitagawa, S. Seino, T. Nakagawa, Y. Ohkubo, H. Nitani, H. Daimon and T. A. Yamamoto
 γ -Fe₂O₃-Supported Pt-Cu Nanoparticles Synthesized by Radiolytic Process for Catalytic CO Preferential Oxidation
Appl. Catal. A, **406** (2011) 43.
- Y. Ohkubo, M. Shibata, S. Kageyama, S. Seino, T. Nakagawa, J. Kugai and T. A. Yamamoto
Radiation Induced Synthesis of Au-Pd Nanoparticles of Random Alloy Structure Supported on Carbon Particles using the High Energy Electron Beam
Mater. Lett., **65** (2011) 2165.
- T. A. Yamamoto, S. Kageyama, S. Seino, H. Nitani, T. Nakagawa, R. Horioka, Y. Honda, K. Ueno and H. Daimon
Methanol Oxidation Catalysis and Substructure of PtRu/C Bimetallic Nanoparticles Synthesized by a Radiolytic Process
Appl. Catal. A, **396** (2011) 68.
- Y. Zhang, T. Motohashi, Y. Masubuchi and S. Kikkawa
Local Anionic Ordering and Anisotropic Displacement in Dielectric Perovskite SrTaO₂N
J. Cerm. Soc. Jpn., **119** (2011) 581.
- Y. Ohashi, T. Motohashi, Y. Masubuchi, T. Moriga, K. Murai and S. Kikkawa
Preparation, Crystal Structure and Superconductive Characteristics of New Oxynitrides (Nb_{1-x}M_x)(N_{1-y}O_y) where M=Mg, Si and x \approx y
J. Solid State Chem., **184** (2011) 2061.
- L. Bayes-Garcia, T. Calvet, M. A. Cuevas-Diarte, S. Ueno and K. Sato
In situ Synchrotron Radiation X-Ray Diffraction Study of Crystallization Kinetics of Polymorphs of 1,3-Dioleoyl-2-Palmitoyl Glycerol (OPO)
Cryst. Eng. Comm., **13** (2011) 3592.
- L. Chen, T. Mashimo, E. Omurzak, H. Okudera, C. Iwamoto and A. Yoshiasa
Pure Tetragonal ZrO₂ Nanoparticles Synthesized by Pulsed Plasma in Liquid
J. Phys. Chem. C, **115** (2011) 9370.
- E. Omurzak, T. Mashimo, S. Sulaimankulova, S. Takebe, L. Chen, Z. Abdullaeva, C. Iwamoto, Y. Oishi, H. Ihara, H. Okudera and A. Yoshiasa
Wurtzite-Type ZnS Nanoparticles by Pulsed Electric Discharge
Nanotechnology, **22** (2011) 365602.
- Y. Hyobu, T. Itai, D. Hayase, M. Kumagai and S. Tanabe
Mobilization of Manganese and Arsenic under Hypoxia in the Bottom of Lake Biwa
Interdisciplinary Studies on Environ. Chem., **6** (2011) 133.
- M. Otsuka, T. Itai, K. A. Asante, M. Muto and S. Tanabe
Trace Element Contamination around the E-Waste Recycling Site at Agbogbloshie, Accra City, Ghana
Interdisciplinary Studies on Environ. Chem., **6** (2011) 161.
- Y. Uemura, Y. Inada, K. K. Bando, T. Sasaki, N. Kamiuchi, K. Eguchi, A. Yagishita, M. Nomura, M. Tada and Y. Iwasawa
In situ Time-Resolved XAFS Study on the Structural Transformation and Phase Separation of Pt₃Sn and PtSn Alloy Nanoparticles on Carbon in the Oxidation Process
Phys. Chem. Chem. Phys., **13** (2011) 15833.

Y. Uemura, Y. Inada, K. K. Bando, T. Sasaki, N. Kamiuchi, K. Eguchi, A. Yagishita, M. Nomura, M. Tada and Y. Iwasawa
Core-Shell Phase Separation and Structural Transformation of Pt₃Sn Alloy Nanoparticles Supported on γ -Al₂O₃ in the Reduction and Oxidation Processes Characterized by In Situ Time-Resolved XAFS
J. Phys. Chem. C, **115** (2011) 5823.

K. Maeda, T. Ohno and K. Domen
A Copper and Chromium Based Nanoparticulate Oxide as a Noble-Metal-Free Cocatalyst for Photocatalytic Water Splitting
Chem. Sci., **2** (2011) 1362.

K. Gotoh, T. Kinumoto, E. Fujii, A. Yamamoto, H. Hashimoto, T. Ohkubo, A. Itadani, Y. Kuroda and H. Ishida
Exfoliated Graphene Sheets Decorated with Metal/Metal Oxide Nanoparticles: Simple Preparation from Cation Exchanged Graphite Oxide
Carbon, **49** (2011) 1118.

10A

T. Kuribayashi
Behavior of Hydrogen in Crystal Structures of Slab and Mantle Minerals
J. Cryst. Soc. Jpn., **53** (2011) 19, (*in Japanese*).

A. Yoshiasa, H. Maekawa and K. Sugiyama
Crystal Chemistry of MgAl₂O₄ Spinel Solid Solution: Peculiar Site Preference of Cation Observed under Substitution and Pressure
J. Cryst. Soc. Jpn., **53** (2011) 13, (*in Japanese*).

K. Komatsu
The Role of Hydrogen Bond in the Pressure Induced Phase Transition of a Layered Hydrous Mineral-Gibbsite
J. Cryst. Soc. Jpn., **53** (2011) 25, (*in Japanese*).

N. Togashi, K. Sugiyama, J. Yu, S. Qiu and O. Terasaki
Single Crystal Structure Analysis of the Se-Incorporated Mordenite, Coupled with the Anomalous X-Ray Scattering
Solid State Sciences, **13** (2011) 684.

A. Sano-Furukawa, T. Kuribayashi, K. Komatsu, T. Yagi and E. Ohtani
Investigation of Hydrogen Sites of Wadsleyite: A Neutron Diffraction Study
Physics of the Earth and Planetary Interiors, **189** (2011) 56.

L. Chen, T. Mashimo, E. Omurzak, H. Okudera, C. Iwamoto and A. Yoshiasa
Pure Tetragonal ZrO₂ Nanoparticles Synthesized by Pulsed Plasma in Liquid
J. Phys. Chem. C, **115** (2011) 9370.

E. Omurzak, T. Mashimo, S. Sulaimankulova, S. Takebe, L. Chen, Z. Abdullaeva, C. Iwamoto, Y. Oishi, H. Ihara, H. Okudera and A. Yoshiasa
Wurtzite-Type ZnS Nanoparticles by Pulsed Electric Discharge
Nanotechnology, **22** (2011) 365602.

Former 10B

Y. Suzuki, M. Yamamoto, T. Saito, T. Miyanaga, S. Ohwada, A. Iwakoshi, T. Nanke and T. Kobayashi
Anomalous Infrared and Visible Light Absorption and Local Structure of Ag-Au Core/Shell Nanoparticles
Appl. Phys. A, **103** (2011) 81.

M. Katayama, K. Sugimoto, E. Kato, K. Ozutsumi, S. Funahashi and Y. Inada
Novel Structural Variation of Silver(I)-Pyridine Complexes in Nitromethane as Studied by X-Ray Absorption Spectroscopy
Inorg. Chim. Acta, **378** (2011) 66.

10C

T. Sakurai and S. Nojima
Significant Increase in the Melting Temperature of Poly(ϵ -caprolactone) Blocks Confined in the Crystallized Lamellar Morphology of Poly(ϵ -caprolactone)-Block-Polyethylene Copolymers
Polymer J., **43** (2011) 370.

G. Matsuba, H. Inoue and R. Yamaki
Precise Structure Analysis and Properties for New Adhesive "Intelimer"
Sen'i Gakkaishi, **67** (2011) 112, (*in Japanese*).

S. Sakurai
X-Ray Scattering Analyses on Deformation Behaviors of Thermoplastic Elastomers
NIPPON GOMU KYOKAISHI, **84** (2011) 21, (*in Japanese*).

Y. Zhao, G. Matsuba, K. Nishida, T. Fujiwara, R. Inoue, I. Polec, C. Deng and T. Kanaya
Relaxation of Shish-Kebab Precursor in Isotactic Polystyrene after Short-Term Shear Flow
J. Polym. Sci. Part B: Polym. Phys., **49** (2011) 214.

M. Md. Alam, T. Oka, N. Ohta and M. Yamazaki
Kinetics of Low pH-Induced Lamellar to Bicontinuous Cubic Phase Transition in Dioleoylphosphatidylserine/Monoolein
J. Chem. Phys., **134** (2011) 145102.

T. Higashihara, K. Ohshimizu, Y. Ryo, T. Sakurai, A. Takahashi, S. Nojima, M. Ree and M. Ueda
Synthesis and Characterization of Block Copolythiophene with Hexyl and Triethylene Glycol Side Chains
Polymer, **52** (2011) 3687.

N. D. Tien, T. P. Hoa, G. Kimura, Y. Yamashiro, H. Fujiwara, M. Mochizuki, S. Sasaki and S. Sakurai
Effects of Blending Poly(D,L-Lactide) with Poly(Ethylene Glycol) on the Higher-Order Crystalline Structures of Poly(Ethylene Glycol) as Revealed by Small-Angle X-Ray Scattering
J. Phys.: Conf. Ser., **272** (2011) 012007.

T. Kota, K. Imaizumi, S. Sasaki and S. Sakurai
Spontaneous Enhancement of Packing Regularity of Spherical Microdomains in the Body-Centered Cubic Lattice upon Uniaxial Stretching of Elastomeric Triblock Copolymers
Polymers, **3** (2011) 36.

R. Zhu, T. Hoshi, Y. Chishima, Y. Muroga, T. Hagiwara, S. Yano and T. Sawaguchi
Microstructure and Mechanical Properties of Polypropylene/poly(methyl methacrylate) Nanocomposite Prepared using Supercritical Carbon Dioxide
Macromolecules, **44** (2011) 6103.

N. Igarashi, Y. Watanabe, Y. Shinohara, Y. Inoko, G. Matsuba, H. Okuda, T. Mori and K. Ito
Upgrade of the Small Angle X-Ray Scattering Beamlines at the Photon Factory
J. Phys.: Conf. Ser., **272** (2011) 012026.

J. Katakawa, H. Minami, T. Fujita and Y. Sano
Concentric Nano-Sized Vesicle Formation by Immunosuppressant FTY720 Revealed with Small-Angle X-Ray Scattering using Synchrotron Radiation Source
J. Biol. Macromol., **11** (2011) 15.

C. Zwieb, Y. Nakao, T. Nakashima, H. Takagi, S. Goda, E. S. Andersen, Y. Kakuta and M. Kimura
Structural Modeling of RNase P RNA of the Hyperthermophilic Archaeon *Pyrococcus horikoshii* OT3
Biochem. Biophys. Res. Commun., **414** (2011) 517.

J. Kawabata, G. Matsuba, K. Nishida, R. Inoue and T. Kanaya
Melt Memory Effects on Recrystallization of Polyamide 6 Revealed by Depolarized Light Scattering and Small-Angle X-Ray Scattering
J. Appl. Polym. Sci., **122** (2011) 1913.

11A

K. Amemiya and M. Sakamaki
NiO-Like Single Layer Formed on a Ni/Cu(001) Thin Film Revealed by the Depth-Resolved X-Ray Absorption Spectroscopy
Appl. Phys. Lett., **98** (2011) 012501.

K. Amemiya and M. Sakamaki
Sub-nm Resolution Depth Profiling of the Magnetic Structure of Thin Films by the Depth-Resolved X-Ray Magnetic Circular Dichroism Technique
J. Phys. D, **44** (2011) 064018.

M. A. Mannan, Y. Baba, T. Kida, M. Nagano, I. Shimoyama, N. Hirao and H. Noguchi
Orientation of B-C-N Hybrid Films Deposited on Ni(111) and Polycrystalline Ti Substrates Explored by X-Ray Absorption Spectroscopy
Thin Solid Films, **519** (2011) 1780.

M. Sakamaki, N. Kawai, T. Miki, T. Kaneko, T. Konishi, T. Fujikawa, K. Amemiya, Y. Kitajima, Y. Kato, T. Muro, H. Yamauchi and M. Sakai
Observation of Disorder-Driven Carrier Localization by Auger Resonant Raman Scattering in *n*-Type Doped ZnO
Phys. Rev. B, **83** (2011) 155210.

K. R. Koswattage, I. Shimoyama, Y. Baba, T. Sekiguchi and K. Nakagawa
Selective Adsorption of Atomic Hydrogen on a *h*-BN Thin Film
J. Chem. Phys., **135** (2011) 014706.

K. R. Koswattage, I. Shimoyama, Y. Baba, T. Sekiguchi and K. Nakagawa
Study on Selective Adsorption of Deuterium on Boron Nitride using Photon-Stimulated Ion-Desorption
Appl. Surf. Sci., **258** (2011) 1561.

T. Miyanaga, T. Kanno, Y. Fujine, J. Araaki and M. Yoshizawa
Polarized XAFS Study of Mg *K*-Edge for MgB₂ on ZnO
J. Elec. Spec. Relat. Phenom., **184** (2011) 254.

S. Ueda, K. Hayashida, H. Nakajima, N. Anabuki, H. Uchida, H. Tsunemi, M. Fujikawa, H. Mori, T. Kohmura, T. Watanabe, K. Kawai, S. Ikeda, K. Kaneko, K. Sakata, S. Todoroki, H. Mizuno, N. Yagihashi, T. Dotani, M. Ozaki, T. Go-Tsuru, M. Muramatsu, H. Suzuki and S. Takagi
Development of the X-Ray CCD for SXI on Board ASTRO-H
Proc. SPIE, **8145** (2011) 814504.

11B

O. Endo and M. Nakamura
Cyclic Voltammetry and Near Edge X-Ray Absorption Fine Structure Spectroscopy at the Ag L₃-Edge on Electrochemical Halogenation of Ag Layers on Au(111)
Surf. Sci., **605** (2011) 958.

A. Ito, T. Inoue, K. Takehara, N. Shimizu, Y. Kitajima and K. Shinohara
Application of XANES Profiles to X-Ray Spectromicroscopy for Biomedical Specimens: Part I. Discrimination of Macromolecules with Sulfur Atoms
J. X-ray Sci. Tech., **19** (2011) 249.

T. Inoue, K. Takehara, N. Shimizu, Y. Kitajima, K. Shinohara and A. Ito
Application of XANES Profiles to X-Ray Spectromicroscopy for Biomedical Specimens: Part II. Mapping Oxidation State of Cysteine in Human Hair
J. X-ray Sci. Tech., **19** (2011) 313.

T. Fujimori, Y. Tanino and M. Takaoka
Role of Zinc in MSW Fly Ash during Formation of Chlorinated Aromatics
Environ. Sci. Technol., **45** (2011) 7678.

H. Okuda, K. Takeshita, S. Ochiai, S. Sakurai and Y. Kitajima
Near-Surface Relaxation Structure of Annealed Block Copolymer Film on Si Substrates Examined by Grazing-Incidence Small-Angle Scattering Utilizing Soft X-Rays
J. Appl. Cryst., **44** (2011) 380.

T. Fujimori and M. Takaoka
Thermochemical Chlorination of Carbon Indirectly Driven by an Unexpected Sulfide of Copper with Inorganic Chloride
J. Hazard. Mater., **197** (2011) 345.

11D

K. Ozawa and K. Mase
Comparison of the Surface Electronic Structure of H-Adsorbed ZnO Surfaces: An Angle-Resolved Photoelectron Spectroscopy Study
Phys. Rev. B, **83** (2011) 125406.

12C

M. Hatayama, T. Sato, K. Shinoda and C. Inoue
Effects of Cultivation Conditions on the Uptake of Arsenite and Arsenic Chemical Species Accumulated by *Pteris vittata* in Hydroponics
J. Biosci. Bioeng., **111** (2011) 326.

S. L. L. M. Ramos, M. Oguni, Y. Masuda and Y. Inada
Crossover from Low-Temperature Itinerant to High-Temperature Localized Electron Behavior in the Electron-Doped Rare-Earth Metal Cobaltate Perovskites
Phys. Rev. B, **83** (2011) 085109.

N. Ahmed, Y. Shibata, T. Taniguchi and Y. Izumi
Photocatalytic Conversion of Carbon Dioxide into Methanol using Zinc-Copper-M(III) (M = Aluminum, Gallium) Layered Double Hydroxides
J. Catal., **279** (2011) 123.

H. Wang, S. Hamanaka, T. Yokoyama, H. Yoshikawa and K. Awaga
In-situ XAFS Studies of Mn₁₂ Molecular-Cluster Batteries: Super-Reduced Mn₁₂ Clusters in Solid-State Electrochemistry
Chem. Asian J., **6** (2011) 1074.

T. Wada, K. K. Bando, K. Kawai and K. Asakura
In-situ XAFS for Monitoring the Structure of Catalysts under More Realistic Reaction Conditions
Shokubai, **53** (2011) 150, (*in Japanese*).

C. Yogi, K. Kojima, T. Hashishin, N. Wada, Y. Inada, E. D. Gaspera, M. Bersani, A. Martucci, L. Liu and T.-K. Sham
Size Effect of Au Nanoparticles on TiO₂ Crystalline Phase of Nanocomposite Thin Films and their Photocatalytic Properties
J. Phys. Chem. C, **115** (2011) 6554.

K. R. Priolkar, D. N. Lobo, P. A. Bhobe, S. Emura and A. K. Nigam
Role of Ni-Mn Hybridization in the Magnetism of the Martensitic State of Ni-Mn-In Shape Memory Alloys
EPL, **94** (2011) 38006.

C. Tokoro, H. Koga, Y. Oda, S. Owada and Y. Takahashi
XAFS Investigation for As(V) Co-Precipitation Mechanism with Ferrihydrite
J. Mining and Materials Processing Institute of Jpn., **127** (2011) 213, (*in Japanese*).

N. Yabuuchi, M. Sugano, Y. Yamakawa, I. Nakai, K. Sakamoto, H. Muramatsu and S. Komaba
Effect of Heat-Treatment Process on FeF₃ Nanocomposite Electrodes for Rechargeable Li Batteries
J. Mater. Chem., **21** (2011) 10035.

N. Yamaguchi, T. Nakamura, D. Dong, Y. Takahashi, S. Amachi and T. Makino
Arsenic Release from Flooded Paddy Soils is Influenced by Speciation, Eh, pH, and Iron Dissolution
Chemosphere, **83** (2011) 925.

M. Hori, K. Shozugawa and M. Matsuo
Improvement of Speciation Analysis for Chromium by X-Ray Absorption Fine Structure and Estimation of the Reduction of Hexavalent Chromium in Soil
Bunseki Kagaku, **60** (2011) 379, (*in Japanese*).

N. Yabuuchi, K. Yoshii, S. Myung, I. Nakai and S. Komaba
Detailed Studies of a High-Capacity Electrode Material for Rechargeable Batteries, Li₂MnO₃-LiCo_{1/3}Ni_{1/3}Mn_{1/3}O₂
J. Am. Chem. Soc., **133** (2011) 4404.

H. Yamaguchi, H. Shibata, K. Maejima, H. Tampo, K. Matsubara, A. Yamada and S. Niki
Local Structure around Dopant Site in Ga-Doped ZnO from Extended X-Ray Absorption Fine Structure Measurements
J. Phys. Soc. Jpn., **80** (2011) 074602.

B. Mongkhonsin, W. Nakbanpote, I. Nakai, A. Hokura and N. Jearanaikoon
Distribution and Speciation of Chromium Accumulated in *Gynura pseudochina* (L.) DC
Environmental and Experimental Botany, **74** (2011) 56.

T. Kashiwabara, Y. Takahashi, M. Tanimizu and A. Usui
Molecular-Scale Mechanisms of Distribution and Isotopic Fractionation of Molybdenum between Seawater and Ferromanganese Oxides
Geochim. Cosmochim. Acta, **75** (2011) 5762.

L. Cao, H. Park, G. Dodbiba, K. Ono, C. Tokoro and T. Fujita

Keeping Gallium Metal to Liquid State under the Freezing Point by using Silica Nanoparticles
Appl. Phys. Lett., **99** (2011) 143120.

S. Kageyama, S. Seino, T. Nakagawa, H. Nitani, K. Ueno, H. Daimon and T. A. Yamamoto

Formation of PtRu Alloy Nanoparticle Catalyst by Radiolytic Process Assisted by Addition of DL-Tartaric Acid and its Enhanced Methanol Oxidation Activity
J. Nanoparticle. Res., **13** (2011) 5275.

J. Kugai, R. Kitagawa, S. Seino, T. Nakagawa, Y. Ohkubo, H. Nitani, H. Daimon and T. A. Yamamoto
 γ -Fe₂O₃-Supported Pt-Cu Nanoparticles Synthesized by Radiolytic Process for Catalytic CO Preferential Oxidation
Appl. Cat. A, **406** (2011) 43.

Y. Ohkubo, M. Shibata, S. Kageyama, S. Seino, T. Nakagawa, J. Kugai and T. A. Yamamoto
Radiation Induced Synthesis of Au-Pd Nanoparticles of Random Alloy Structure Supported on Carbon Particles using the High Energy Electron Beam
Mater. Lett., **65** (2011) 2165.

T. A. Yamamoto, S. Kageyama, S. Seino, H. Nitani, T. Nakagawa, R. Horioka, Y. Honda, K. Ueno and H. Daimon
Methanol Oxidation Catalysis and Substructure of PtRu/C Bimetallic Nanoparticles Synthesized by a Radiolytic Process
Appl. Cat. A, **396** (2011) 68.

L. Wang, A. Yoshiasa, M. Okube and T. Takeda
Titanium Local Structure in Tektite Probed by X-Ray Absorption Fine Structure Spectroscopy
J. Synchrotron Rad., **18** (2011) 885.

T. Furukawa and Y. Takahashi
Oxalate Metal Complexes in Aerosol Particles: Implications for the Hygroscopicity of Oxalate-Containing Particles
Atom. Chem. Phys., **11** (2011) 4289.

A. G. Gault, S. Langely, A. Ibrahim, R. Renaud, Y. Takahashi, C. Boothman, J. R. Lloyd, I. D. Clark, F. G. Ferris and D. Fortin
Microbial and Geochemical Features Suggest Iron Redox Cycling within Bacteriogenic Iron Oxide-Rich Sediments
Chem. Geol., **281** (2011) 41.

K. Sasaki, K. Takatsugi and T. Hirajima
Effects of initial Fe²⁺ concentration and pulp density on the bioleaching of Cu from enargite by *Acidianus brierleyi*
Hydrometallurgy, **109** (2011) 153.

A. Ohta, H. Kagi, H. Tsuno, M. Nomura, T. Okai and N. Yanagisawa

IR and XANES Spectroscopic Studies of Humic Acids Reacting with Cr(III) and Cr(VI)
Bulletin of the Geological Survey of Japan, **62** (2011) 347.

S. Mitsunobu, Y. Takahashi, S. Utsunomiya, A. M. Matthew, Y. Terada, T. Iwamura and M. Sakata
Identification and Characterization of Nanosized Tripuhyite in Soil Near Sb Mine Tailing
Am. Mineral., **96** (2011) 1171.

S. Takenaka, H. Miyamoto, N. Susuki, H. Matsune and M. Kishida
Highly Durable Carbon Nanotube-Supported Pd Cathode Catalysts Covered with Silica Layers for Polymer Electrolyte Fuel Cells: Effect of Silica Layer Thickness on the Catalytic Performance
ECS Trans., **41** (2011) 2305.

A. Era, M. Tabuchi, T. Nishitani and Y. Takeda
A Study on EXAFS Analysis of Cs/GaAs NEA Surface
J. Phys. :Conf. Ser., **298** (2011) 012012.

Former 13A

T. Nagai, D. Hamane and K. Fujino
Mechanism of Solid Solution and Crystal Chemistry in MgSiO₃-FeAlO₃ Perovskite
J. Cryst. Soc. Jpn., **53** (2011) 8, (*in Japanese*).

K. Takemura and H. Fujihisa
Na-Au Intermetallic Compounds Formed under High Pressure at Room Temperature
Phys. Rev. B, **84** (2011) 014117.

R. Iizuka, H. Kagi, K. Komatsu, D. Ushijima, S. Nakano, A. Sano-Furukawa, T. Nagai and T. Yagi
Pressure Responses of Portlandite and H-D Isotope Effects on Pressure-Induced Phase Transitions
Phys. Chem. Minerals, **38** (2011) 777.

K. Niwa, D. Nomichi, M. Hasegawa, T. Okada, T. Yagi and T. Kikegawa
Compression Behaviors of Binary Skutterudite CoP₃ in Noble Gases up to 40 GPa at Room Temperature
Inorg. Chem., **50** (2011) 3281.

13A

K. Ozawa, S. Munakata, K. Edamoto and K. Mase
Electron Donor Molecule on Oxide Surface: Influence of Surface Termination of ZnO on Adsorption of Tetrathiafulvalene
J. Phys. Chem. C, **115** (2011) 21843.

H. Tanaka, T. Kikuchi, A. Toyoshima, Y. Nagatani, T. Kosuge, K. Mase, F. Watanabe and H. Nishiguchi
Report on Water-Cooled Movable Masks Made of Forged 0.2% Beryllium Copper Alloy
J. Vac. Soc. Jpn., **54** (2011) 481.

Former 13B

H. Oyanagi and C. J. Xhang
Lattice Anomalies and HTSC in Pnictides and Cuprates Studied by XAS: Polaron Resonance as a Common Clue
J. Supercond. Nov. Magn., **24** (2011) 89.

Former 13C

F. Esaka, H. Yamamoto, H. Uono, N. Matsubayashi, K. Yamaguchi, S. Shamoto, M. Magara and T. Kimura
Spectroscopic Characterization of β -FeSi₂ Single Crystals and Homoepitaxial β -FeSi₂ Films by XPS and XAS
Appl. Surf. Sci., **257** (2011) 2950.

F. Esaka, H. Yamamoto, H. Uono, N. Matsubayashi, K. Yamaguchi, S. Shamoto, M. Magara and T. Kimura
Surface Characterization of Homoepitaxial β -FeSi₂ Film on β -FeSi₂ (111) Substrate by X-Ray Photoelectron and X-Ray Absorption Spectroscopy
Phys. Proc., **11** (2011) 150.

M. Imamura, N. Matsubayashi, J. Fan, I. Kojima and M. Sasaki
The Determination of the Thickness of the Silicon Oxide Film by Synchrotron Radiation X-Ray Photoelectron Spectroscopy (SR-XPS) Analysis
Meas. Sci. Technol., **22** (2011) 024007.

K. R. Koswattage, I. Shimoyama, Y. Baba, T. Sekiguchi and K. Nakagawa
Selective Adsorption of Atomic Hydrogen on a *h*-BN Thin Film
J. Chem. Phys., **135** (2011) 014706.

K. R. Koswattage, I. Shimoyama, Y. Baba, T. Sekiguchi and K. Nakagawa
Study on Selective Adsorption of Deuterium on Boron Nitride using Photon-Stimulated Ion-Desorption
Appl. Surf. Sci., **258** (2011) 1561.

14A

S. Gunji, N. Toukairin, Y. Tanaka, F. Tokanai, H. Sakurai, Y. Kishimoto, T. Mihara, K. Hayashida, N. Anabuki, H. Tsunemi, T. Narita, Y. Saito and S. Kishimoto
Basic Performance of a Polarimeter for Gamma-Ray Bursts Using Segmented Scintillators
IEEE Trans. Nucl. Sci., **58** (2011) 426.

T. Sakakura, K. Tanaka, Y. Takenaka, M. Watanabe, Y. Noda, S. Kishimoto, S. Matsuishi and H. Hosono
Accurate Analysis of the Deformed Structures of Inorganic Electrides, Ca₁₂Al₁₄O_{32+x} by Synchrotron X-Ray and Neutron Diffraction
Radioisotopes, **60** (2011) 131, (*in Japanese*).

T. Sakakura, K. Tanaka, Y. Takenaka, S. Matsuishi, H. Hosono and S. Kishimoto
Determination of the Local Structure of a Cage with an Oxygen Ion in C₁₂Al₁₄O₃₃
Appl. Catal. B, **B67** (2011) 193.

D. Yonetoku, T. Murakami, S. Gunji, T. Mihara, T. Sakashita, Y. Morihara, Y. Kikuchi, T. Takahashi, H. Fujimoto, N. Toukairin, Y. Kodama, S. Kubo and IKAROS Demonstration Team
Gamma-Ray Burst Polarimeter (GAP) Aboard the Small Solar Power Sail Demonstrator IKAROS
Publ. Astron. Soc. Japan, **63** (2011) 625.

S. Kishimoto, S. Adachi, T. Taniguchi, M. Ikeno, S. Shimazaki, M. Tanaka and T. Mitsui
Si-APD Array Detectors with 2 ns Pulse-Pair Resolving Time and Sub-ns Resolution for Synchrotron X-Ray Measurements
Nucl. Instrum. Meth. Phys. Res. A, **A650** (2011) 98.

S. Kishimoto, T. Taniguchi, F. Nishikido and R. Haruki
Timing Measurements with a MSM Photodetector Sensitive to a Single X-Ray Photon
KEK Proc., **2011-8** (2011) 173.

14B

K. Hirano
Application of X-Ray Image Magnifier and Demagnifier to Parallel Beam X-Ray Computed Tomography
J. Phys. D: Appl. Phys., **44** (2011) 055501.

K. Hirano
X-Ray Angle-Resolved Computed Tomography using an Asymmetric Analyzer Crystal
Jpn. J. Appl. Phys., **50** (2011) 026402.

H. Sato, M. Ando and D. Shimao
Investigation of Absorbed Radiation Dose in Refraction-Enhanced Breast Tomosynthesis by a Laue Case Analyser
Radiat. Prot. Dosimetry, **146** (2011) 231.

14C

N. Sunaguchi, T. Yuasa, Q. Huo and M. Ando
Convolution Reconstruction Algorithm for Refraction-Contrast Computed Tomography using a Laue-Case Analyzer for Dark-Field Imaging
Optics Letters, **36** (2011) 391.

A. Momose, W. Yashiro, S. Harasse and H. Kuwabara
Four-Dimensional X-Ray Phase Tomography with Talbot Interferometry and White Synchrotron Radiation: Dynamic Observation of a Living Worm
Optics Express, **19** (2011) 8423.

W. Yashiro, S. Harasse, K. Kawabata, H. Kuwabara, T. Yamazaki and A. Momose
Distribution of Unresolvable Anisotropic Microstructures Revealed in Visibility-Contrast Images using X-Ray Talbot Interferometry
Phys. Rev. B, **84** (2011) 094106.

S. Takeya, A. Yoneyama, K. Ueda, K. Hyodo, T. Takeda, H. Mimachi, M. Takahashi, T. Iwasaki, K. Sano, H. Yamawaki and Y. Gotoh
Nondestructive Imaging of Anomalously Preserved Methane Clathrate Hydrate by Phase Contrast X-Ray Imaging
J. Phys. Chem. C, **115** (2011) 16193.

N. Sunaguchi, T. Yuasa, Q. Huo and M. Ando
Refraction-Contrast Tomosynthesis Imaging using Dark-Field Imaging Optics
Appl. Phys. Lett., **99** (2011) 103704.

C. Suzuki, T. Abe, T. Imoto and T. Kosako
Energy Response of an Imaging Plate to Low-Energy Photons for Use in Dosimetry
Jpn. J. Health Phys., **46** (2011) 158.

Y. Suzuki, Y. Chikaura and M. Ando
Computer Simulation on Spatial Resolution of X-Ray Bright-Field Imaging by Dynamical Diffraction Theory for a Laue-Case Crystal Analyzer
J. Appl. Phys., **110** (2011) 084902-1.

E. Takada, A. Takada, A. Inoue, H. Imai, H. Okada, S. Naka, J. Kawarabayashi, T. Nakamura and Y. Namito
Application of Organic Photodiodes to X-Ray Measurements - A Feasibility Study
J. Nucl. Sci. Tech., **48** (2011) 1140.

N. Sunaguchi, T. Yuasa, M. Ando, S. Ichihara, D. Shimao, Q. Huo, M. Sakai, Y. Wu, A. Omi and H. Awane
Refraction-Contrast Computed Tomography using X-Ray Dark Field Imaging
International Forum on Medical Imaging in Asia (IFMIA) 2011, (2011) 360.

T. Yuasa, N. Sunaguchi, Q. Huo and M. Ando
Reconstruction Algorithm of Refraction-Based Computed Tomography: From Viewpoint of X-Ray Optics
International Forum on Medical Imaging in Asia (IFMIA) 2011, (2011) 1.

M. Ando, T. Endo, S. Ichihara, T. Yuasa, K. Mori, D. Shimao, H. Sato, Q. Huo, N. Sunaguchi, M. Sakai, A. Omi and H. Awane
2-Dimensional and 3-Dimensional View of Breast Cancer using Dark-Field Imaging
International Forum on Medical Imaging in Asia (IFMIA) 2011, (2011) 45.

Q. Huo, N. Sunaguchi, M. Sakai, H. Awane, A. Omi, T. Yuasa, K. Hyodo, S. Ichihara and M. Ando
Application of X-Ray Dark Field Imaging to Liver Tissue Specimen
International Forum on Medical Imaging in Asia (IFMIA) 2011, (2011) 363.

H. Sato, M. Ando and D. Shimao
Investigation of Absorbed Radiation Dose in Refraction-Enhanced Breast Tomosynthesis by a Laue Case Analyser
Radiat. Prot. Dosimetry, **146** (2011) 231.

Former 14C2

R. Tateyama, E. Ohtani, H. Terasaki, K. Nishida, Y. Shibasaki, A. Suzuki and T. Kikegawa
Density Measurements of Liquid Fe-Si Alloys at High Pressure using the Sink-Float Method
Phys. Chem. Minerals, **38** (2011) 801.

15A

Y. Takenaka, H. Kitahata, N. L. Yamada, H. Seto and M. Hara
Growth of Gold Nanorods in Gelled Surfactant Solutions
J. Colloid Interface Sci., **356** (2011) 111.

K. Oshima, Y. Sugimoto and K. Wakabayashi
Deduction of the Single-Myosin-Filament Transforms from Partially Sampled Layer Lines in the X-Ray Diffraction Pattern from Vertebrate Striated Muscle
J. Appl. Cryst., **44** (2011) 398.

M. Hishida and K. Tanaka
Long-Range Hydration Effect of Lipid Membrane Studied by Terahertz Time-Domain Spectroscopy
Phys. Rev. Lett., **106** (2011) 158102.

M. Hishida and H. Seto
Lamellar-Lamellar Phase Separation of Phospholipid Bilayers Induced by Salting-in/-out Effects
J. Phys.: Conf. Ser., **272** (2011) 012008.

G. Matsuba, H. Inoue and R. Yamaki
Precise Structure Analysis and Properties for New Adhesive "Intelimer"
Sen'i Gakkaishi, **67** (2011) 112, (*in Japanese*).

S. Sakurai
X-Ray Scattering Analyses on Deformation Behaviors of Thermoplastic Elastomers
NIPPON GOMU KYOKAISHI, **84** (2011) 21, (*in Japanese*).

S. S. A. Rahman, D. Kawaguchi and Y. Matsushita
Microphase-Separated Structures of Poly(4-*tert*-butylstyrene-*block*-4-*tert*-butoxystyrene) upon Gradual Changes in Segregation Strength through Hydrolysis Reaction
Macromolecules, **44** (2011) 2799.

Y. Zhao, G. Matsuba, K. Nishida, T. Fujiwara, R. Inoue, I. Polec, C. Deng and T. Kanaya
Relaxation of Shish-Kebab Precursor in Isotactic Polystyrene after Short-Term Shear Flow
J. Polym. Sci. Part B: Polym. Phys., **49** (2011) 214.

- T. Matsutani and K. Yamamoto
Solvent Annealing Induced Perpendicular Orientation of Cylindrical Microdomains in Polystyrene-*b*-poly(4-hydroxyl styrene)/PEG Oligomer Blend Thin Film Made by Spin-Coating from Selective Solvent
J. Phys.: Conf. Ser., **272** (2011) 012015.
- H. Takeno, K. Obuchi, Y. Maki, S. Kondo and T. Dobashi
A Structural Study of Polyelectrolyte Gels in a Unidirectionally Swollen State
Polymer, **52** (2011) 2685.
- M. Md. Alam, T. Oka, N. Ohta and M. Yamazaki
Kinetics of Low pH-Induced Lamellar to Bicontinuous Cubic Phase Transition in Dioleoylphosphatidylserine/Monoolein
J. Chem. Phys., **134** (2011) 145102.
- Y. Nozue, Y. Kawashima, S. Seno, T. Nagamatsu, S. Hosoda, E. B. Berda, G. Rojas, T. W. Baughman and K. B. Wagener
Unusual Crystallization Behavior of Polyethylene Having Precisely Spaced Branches
Macromolecules, **44** (2011) 4030.
- R. Zhang, C. Dutriez, K. Sugiyama, T. Ishizone and H. Yokoyama
Thermally Robust Nanocellular Thin Films of High- T_g Semifluorinated Block Copolymers Foamed with Supercritical Carbon Dioxide
Soft Matter, **7** (2011) 4032.
- A. Noro, K. Ishihara and Y. Matsushita
Nanophase-Separated Supramolecular Assemblies of Two Functionalized Polymers via Acid-Base Complexation
Macromolecules, **44** (2011) 6241.
- T. Kota, K. Imaizumi, S. Sasaki and S. Sakurai
Spontaneous Enhancement of Packing Regularity of Spherical Microdomains in the Body-Centered Cubic Lattice upon Uniaxial Stretching of Elastomeric Triblock Copolymers
Polymers, **3** (2011) 36.
- Y. Maki, K. Ito, N. Hosoya, C. Yoneyama, K. Furusawa, T. Yamamoto, T. Dobashi, Y. Sugimoto and K. Wakabayashi
Anisotropic Structure of Calcium-Induced Alginate Gels by Optical and Small-Angle X-Ray Scattering Measurements
Biomacromolecules, **12** (2011) 2145.
- Y. Sakai, K. Ueda, N. Katsuyama, K. Shimizu, S. Sato, J. Kuroiwa, J. Araki, A. Teramoto, K. Abe, H. Yokoyama and K. Ito
Fabrication and Structural Analysis of Polyrotaxane Fibers and Films
J. Phys.: Condens. Matter, **23** (2011) 284108.
- H. Okuda, K. Takeshita, S. Ochiai, S. Sakurai and Y. Kitajima
Near-Surface Relaxation Structure of Annealed Block Copolymer Film on Si Substrates Examined by Grazing-Incidence Small-Angle Scattering Utilizing Soft X-Rays
J. Appl. Cryst., **44** (2011) 380.
- N. Igarashi, Y. Watanabe, Y. Shinohara, Y. Inoko, G. Matsuba, H. Okuda, T. Mori and K. Ito
Upgrade of the Small Angle X-Ray Scattering Beamlines at the Photon Factory
J. Phys.: Conf. Ser., **272** (2011) 012026.
- Y. Kawabata, T. Shinoda and T. Kato
Vesicle Growth and Deformation in a Surfactant Solution below the Krafft Temperature
Phys. Chem. Chem. Phys., **13** (2011) 3484.
- L. Bayes-Garcia, T. Calvet, M. A. Cuevas-Diarte, S. Ueno and K. Sato
In situ Synchrotron Radiation X-Ray Diffraction Study of Crystallization Kinetics of Polymorphs of 1,3-Dioleoyl-2-Palmitoyl Glycerol (OPO)
Cryst. Eng. Comm., **13** (2011) 3592.
- Y. Morimoto, T. Nakagawa and M. Kojima
Computational Analyses of Protein Structures by Solution X-Ray Scattering
Seibutsu Butsuri, **51** (2011) 88, (*in Japanese*).
- J. Kawabata, G. Matsuba, K. Nishida, R. Inoue and T. Kanaya
Melt Memory Effects on Recrystallization of Polyamide 6 Revealed by Depolarized Light Scattering and Small-Angle X-Ray Scattering
J. Appl. Polym. Sci., **122** (2011) 1913.
- R. Homma, S. Sato and S. Ichikawa
Molecular Aggregation of Aqueous Carboxybetaines with Bulky Alkyl Chains: Formation of Vesicles and Lamellar Liquid Crystalline Aggregates
Membrane, **36** (2011) 326.

15B1

- H. Sato, H. Maso, Y. Utsumi, H. Kurihara, Y. Mukaegawa, Y. Tezuka, T. Iwazumi, F. Iga, M. Tsubota, H. Namatame and M. Taniguchi
Polarization-Dependent Ti K X-Ray Absorption and Emission Studies of Ti₂O₃ Single Crystal
J. Elec. Spec. Relat. Phenom., **184** (2011) 184.

- Y. Isohama, N. Nakajima, H. Maruyama, Y. Tezuka and T. Iwazumi
Tetragonal-Cubic Phase Transition in BaTiO₃ Probed by Resonant X-Ray Emission Spectroscopy
J. Elec. Spec. Relat. Phenom., **184** (2011) 207.

15B2

- T. Shirasawa, M. Ohyama, W. Voegeli and T. Takahashi
Interface of a Bi(001) Film on Si(111)-7 × 7 Imaged by Surface X-Ray Diffraction
Phys. Rev. B, **84** (2011) 075411.

15C

K. Hirano

Application of X-Ray Image Magnifier and Demagnifier to Parallel Beam X-Ray Computed Tomography
J. Phys. D: Appl. Phys., **44** (2011) 055501.

K. Hirano

X-Ray Angle-Resolved Computed Tomography using an Asymmetric Analyzer Crystal
Jpn. J. Appl. Phys., **50** (2011) 026402.

H. Yamaguchi, H. Shibata, K. Maejima, H. Tampo, K. Matsubara, A. Yamada and S. Niki
 Local Structure around Dopant Site in Ga-Doped ZnO from Extended X-Ray Absorption Fine Structure Measurements
J. Phys. Soc. Jpn., **80** (2011) 074602.

Y. Kato, H. Umezawa, H. Yamaguchi, T. Teraji and S. Shikata

CVD Diamond Dislocations Observed by X-Ray Topography, Birefringence Image and Cathodoluminescence Mapping
Mater. Res. Soc. Symp. Proc., **1282** (2011) 73.

T. Fukamachi, K. Hirano, R. Negishi, Y. Kanematsu, S. Jongsuksawat, K. Hirano and T. Kawamura
 Interference Fringes in Multiple Bragg-Laue Mode
Acta Cryst. A, **67** (2011) 154.

T. Fukamachi, S. Jongsuksawat, Y. Kanematsu, K. Hirano, R. Negishi, M. Shimojo, D. Ju, K. Hirano and T. Kawamura
 X-Ray Interference Fringes from Weakly Bent Crystal
J. Phys. Soc. Jpn., **80** (2011) 083002.

T. Fukamachi, S. Jongsuksawat, Y. Kanematsu, K. Hirano, R. Negishi, M. Shimojo, D. Ju, K. Hirano and T. Kawamura
 Two-Beam X-Ray Interferometer using Diffraction in Multiple Bragg-Laue Mode
J. Phys. Soc. Jpn., **80** (2011) 083001.

H. Umezawa, Y. Kato, H. Watanabe, A. M. M. Omer, H. Yamaguchi and S. Shikata
 Characterization of Crystallographic Defects in Homoepitaxial Diamond Films by Synchrotron X-Ray Topography and Cathodoluminescence
Diamond and Related Materials, **20** (2011) 523.

T. Matsushita, T. Takahashi, T. Shirasawa, E. Arakawa, H. Toyokawa and H. Tajiri
 Quick Measurement of Crystal Truncation Rod Profiles in the Simultaneous Multi-Wavelength Dispersive Mode
J. Appl. Phys., **110** (2011) 102209.

R. Negishi, T. Fukamachi, M. Yoshizawa, Kenji. Hirano, Keiichi. Hirano and T. Kawamura
 Phase Determination of Crystal Structure Factor using Measured Rocking-Curves
Phys. Status Solidi A, **208** (2011) 2567.

K. Seki, Alexander, S. Kozawa, T. Ujihara, P. Chaudouët, D. Chaussende and Y. Takeda
 Formation Process of 3C-SiC on 6H-SiC (0001) by Low-Temperature Solution Growth in Si-Sc-C System
J. Cryst. Growth, **335** (2011) 94.

S. Kozawa, K. Seki, Alexander, Y. Yamamoto, T. Ujihara and Y. Takeda
 Defect Evaluation of SiC Crystal Grown by Solution Method: The Study by Synchrotron X-Ray Topography and Etching Method
Materials Science Forum, **679-680** (2011) 28.

16A

K. Amemiya and M. Sakamaki
 NiO-Like Single Layer Formed on a Ni/Cu(001) Thin Film Revealed by the Depth-Resolved X-Ray Absorption Spectroscopy
Appl. Phys. Lett., **98** (2011) 012501.

K. Amemiya and M. Sakamaki
 Sub-nm Resolution Depth Profiling of the Magnetic Structure of Thin Films by the Depth-Resolved X-Ray Magnetic Circular Dichroism Technique
J. Phys. D, **44** (2011) 064018.

P. Lablanquie, F. Penent, J. Palaudoux, L. Andric, P. Selles, S. Carniato, K. Bucar, M. Zitnik, M. Huttula, J. H. D. Eland, E. Shigemasa, K. Soejima, Y. Hikosaka, I. H. Suzuki, M. Nakano and K. Ito
 Properties of Hollow Molecules Probed by Single-Photon Double Ionization
Phys. Rev. Lett., **106** (2011) 063003.

I. H. Suzuki, Y. Hikosaka, E. Shigemasa, P. Lablanquie, F. Penent, K. Soejima, M. Nakano, N. Kouchi and K. Ito
 Decay Pathways after Xe 3d Inner Shell Ionization using a Multi-Electron Coincidence Technique
J. Phys. B, **44** (2011) 075003.

M. Sakamaki and K. Amemiya
 Element Specific Magnetic Anisotropy Energy of Alternately Layered FeNi Thin Films
Appl. Phys. Express, **4** (2011) 073002.

M. Sakamaki and K. Amemiya
 Effect of Surface Roughness on Magnetism of Ultrathin Co Films
J. Phys.: Conf. Ser., **266** (2011) 012020.

K. Amemiya, Y. Kousa, S. Nakamoto, T. Harada, S. Kozai, M. Yoshida, H. Abe, R. Sumii, M. Sakamaki and H. Kondoh
 Real-Time Observation of CO Oxidation Reaction on Ir(111) Surface at 33 ms Resolution by Means of Wavelength-Dispersive Near-Edge X-Ray Absorption Fine Structure Spectroscopy
Appl. Phys. Lett., **99** (2011) 074104.

Y. Hikosaka, P. Lablanquie, F. Penet, J. Palaudoux, L. Andric, K. Soejima, E. Shigemasa, I. H. Suzuki, M. Nakano and K. Ito
Energy Correlation among Three Photoelectrons Emitted in Core-Valence-Valence Triple Photoionization of Ne
Phys. Rev. Lett., **107** (2011) 113005.

J. Okamoto, K. Horigane, H. Nakao, K. Amemiya, M. Kubota, Y. Murakami and K. Yamada
Resonant Soft X-Ray Magnetic Scattering Study of Magnetic Structures in $\text{La}_{1.5}\text{Ca}_{0.5}\text{CoO}_4$
J. Elec. Spec. Relat. Phenom., **184** (2011) 224.

S. Toyoda, Y. Nakamura, K. Horiba, H. Kumigashira, M. Oshima and K. Amemiya
Nano-Scale Characterization of Poly-Si Gate on High-k Gate Stack Structures by Scanning Photoemission Microscopy
e-J. Surf. Sci. Nanotechnology, **9** (2011) 224.

P. Lablanquie, T. P. Grozdanov, M. Zitnik, S. Carniato, P. Selles, L. Andric, J. Palaudoux, F. Penet, H. Iwayama, E. Shigemasa, Y. Hikosaka, K. Soejima, M. Nakano, I. H. Suzuki and K. Ito
Evidence of Single-Photon Two-Site Core Double Ionization of C_2H_2 Molecules
Phys. Rev. Lett., **107** (2011) 193004.

J. Ishikawa, T. Miyahara, Y. Hirato, H. Ishii, T. Kodama, K. Kikuchi, T. Nakamura, K. Kodama, D. Asakura and T. Koide
MCD Study on $\text{Ce}@C_{82}$ and $\text{Ce}_2@C_{80}$ in the Soft-X-Ray Region
J. Elec. Spec. Relat. Phenom., **184** (2011) 284.

K. Horiba, Y. Nakamura, N. Nagamura, S. Toyoda, H. Kumigashira, M. Oshima, K. Amemiya, Y. Senba and H. Ohashi
Scanning Photoelectron Microscope for Nanoscale Three-Dimensional Spatial-Resolved Electron Spectroscopy for Chemical Analysis
Rev. Sci. Instrum., **82** (2011) 113701.

17A

Y. Toh, D. Takeshita, T. Nagaike, T. Numata and K. Tomita
Mechanism for the Alteration of the Substrate Specificities of Template-Independent RNA Polymerases Structure, **19** (2011) 232.

Z. Nakata, M. Nagae, N. Yasui, H. Bujo, T. Nogi and J. Takagi
Crystallization and Preliminary Crystallographic Analysis of Human LR11 Vps10p Domain
Acta Cryst. F, **67** (2011) 129.

L. M. G. Chavas, Y. Yamada, M. Hiraki, N. Igarashi, N. Matsugaki and S. Wakatsuki
UV LED lighting for Automated Crystal Centring
J. Synchron Rad., **18** (2011) 11.

D. Sasaki, M. Fujihashi, N. Okuyama, Y. Kobayashi, M. Noike, T. Koyama and K. Miki
Crystal Structure of Heterodimeric Hexaprenyl Diphosphate Synthase from *Micrococcus luteus* B-P 26 Reveals that the Small Subunit is Directly Involved in the Product Chain Length Regulation
J. Biol. Chem., **286** (2011) 3729.

X. Pan, M. Li, T. Wan, L. Wang, C. Jia, Z. Hou, X. Zhao, J. Zhang and W. Chang
Structural Insights into Energy Regulation of Light-Harvesting Complex CP29 from Spinach
Nature Structural Molecular Biology, **18** (2011) 309.

K. Nishi, T. Ono, T. Nakamura, N. Fukunaga, M. Izumi, H. Watanabe, A. Suenaga, T. Maruyama, Y. Yamagata, S. Curry and M. Otagiri
Structural Insights into Differences in Drug-Binding Selectivity between Two Forms of Human α_1 -Acid Glycoprotein Genetic Variants, the A and F1*S Forms
J. Biol. Chem., **286** (2011) 14427.

T. Yoshizawa, H. Hashimoto, T. Shimizu, M. Yamabe, N. Shichijo, K. Hanada, H. Hirano and M. Sato
Purification, Crystallization and X-Ray Diffraction Study of Basic 7S Globulin from Soybean
Acta Cryst. F, **67** (2011) 87.

Y. Sato, R. Natsume, Z. Prokop, J. Brezovsky, R. Chaloupkova, J. Damborsky, Y. Nagata and T. Senda
Molecular Bases of Enantioselectivity of Haloalkane Dehalogenase DbjA
Kessyogakkaishi, **53** (2011) 124, (*in Japanese*).

M. Senda, H. Tanaka, T. Ishida, K. Horiike and T. Senda
Crystallization and Preliminary Crystallographic Analysis of D-Serine Dehydratase from Chicken Kidney
Acta Cryst. F, **67** (2011) 147.

J.-H. Shin, H. J. Jung, Y. J. An, Y.-B. Cho, S.-S. Cha and J.-H. Roe
Graded Expression of Zinc-Responsive Genes through Two Regulatory Zinc-Binding Sites in Zur
Proc. Natl. Acad. Sci. USA, **108** (2011) 5045.

T. Hatakeyama, T. Kamiya, M. Kusunoki, S. Nakamura-Tsuruta, J. Hirabayashi, S. Goda and H. Unno
Galactose Recognition by A Tetrameric C-Type Lectin, CEL-IV, Containing the EPN Carbohydrate-Recognition Motif
J. Biol. Chem., **286** (2011) 10305.

S. J. Lee, H. S. Kim, D. J. Kim, H. J. Yoon, K. H. Kim, J. Y. Yoon and S. W. Suh
Crystal Structures of LacD from *Staphylococcus aureus* and LacD. 1 from *Streptococcus pyogenes*: Insights into Substrate Specificity and Virulence Gene Regulation
FEBS Lett., **585** (2011) 307.

- T. Ohnuma, T. Numata, T. Osawa, M. Mizuhara, K. M. Varum and T. Fukamizo
Crystal Structure and Mode of Action of a Class V Chitinase from *Nicotiana tabacum*
Plant Mol. Biol., **75** (2011) 291.
- M. Unno, M. Shinohara, K. Takayama, H. Tanaka, K. Teruya, K. Doh-ura, R. Sakai, M. Sasaki and M. Ikeda-Saito
Binding and Selectivity of the Marine Toxin Neodysiherbaine A and its Synthetic Analogues to GluK1 and GluK2 Kainate Receptors
J. Mol. Biol., **413** (2011) 667.
- Y. Y. Chen, T. P. Ko, C. H. Lin, W. H. Chen and A. H. J. Wang
Conformational Change upon Product Binding to *Klebsiella pneumoniae* UDP-Glucose Dehydrogenase: A Possible Inhibition Mechanism for the Key Enzyme in Polymyxin Resistance
J. Structural Biol., **175** (2011) 300.
- T. Saitoh, M. Igura, Y. Miyazaki, T. Ose, N. Maita and D. Kohda
Crystallographic Snapshots of Tom20-Mitochondrial Presequence Interactions with Disulfide-Stabilized Peptides
Biochemistry, **50** (2011) 5487.
- Q. Chen, Q. Wang, L. Xiong and Z. Lou
A Structural View of the Conserved Domain of Rice Stress-Responsive NAC1
Proteins, **2** (2011) 55.
- M. Unno, T. Matsui and M. Ikeda-Saito
X-Ray Crystallography of a Metalloprotein: a Reaction Intermediate of Heme Oxygenase
J. Cryst. Soc. Jpn, **53** (2011) 213, (*in Japanese*).
- J. Jung, J.-K. Kim, S.-J. Yeom, Y.-J. Ahn, D.-K. Oh and L.-W. Kang
Crystal Structure of *Clostridium thermocellum* Ribose-5-Phosphate Isomerase B Reveals Properties Critical for Fast Enzyme Kinetics
Applied Microbiology and Biotechnology, **90** (2011) 517.
- S. Fushinobu, M. Hidaka, A. M. Hayashi, T. Wakagi, H. Shoun and M. Kitaoka
Interactions between Glycoside Hydrolase Family 94 Cellobiose Phosphorylase and Glucosidase Inhibitors
J. Appl. Glycosci., **58** (2011) 91.
- M. Okuda, T. Shiba, D.-K. Inaoka, K. Kita, G. Kurisu, S. Mineki, S. Harada, Y. Watanabe and S. Yoshinari
A Conserved Lysine Residue in the Crenarchaea-Specific Loop is Important for the Crenarchaeal Splicing Endonuclease Activity
J. Mol. Biol., **405** (2011) 92.
- Y. Uchida, J. Hasegawa, D. Chinnapen, T. Inoue, S. Okazaki, R. Kato, S. Wakatsuki, R. Misaki, M. Koike, Y. Uchiyama, S. Iemura, T. Natsume, R. Kuwahara, T. Nakagawa, K. Nishikawa, K. Mukai, E. Miyoshi, N. Taniguchi, D. Sheff, W. I. Lencer, T. Taguchi and H. Arai
Intracellular Phosphatidylserine is Essential for Retrograde Membrane Traffic through Endosomes
Proc. Natl. Acad. Sci. USA, **108** (2011) 15846.
- D.-F. Li, N. Zhang, Y.-J. Hou, Y. Huang, Y. Hu, Y. Zhang, S.-J. Liu and D.-C. Wang
Crystal Structures of the Transcriptional Repressor RolR Reveals a Novel Recognition Mechanism between Inducer and Regulator
PLoS ONE, **6** (2011) e19529.
- H. S. Kim, S. J. Lee, H. J. Yoon, D. R. An, D. J. Kim, S.-J. Kim and S. W. Suh
Crystal Structures of YwqE from *Bacillus subtilis* and CpsB from *Streptococcus pneumoniae*, Unique Metal-Dependent Tyrosine Phosphatases
J. Struct. Biol., **175** (2011) 442.
- Q. Zhou, Y. Zhai, J. Lou, M. Liu, X. Pang and F. Sun
Thiabendazole Inhibits Ubiquinone Reduction Activity of Mitochondrial Respiratory Complex II via a Water Molecule Mediated Binding Feature
Protein and Cell, **2** (2011) 531.
- A. Zheng, R. Yamamoto, M. Sokabe, I. Tanaka and M. Yao
Crystallization and Preliminary X-Ray Crystallographic Analysis of eIF5B Δ N and the eIF5B Δ N-eIF1A Δ N Complex
Acta Cryst. F, **67** (2011) 730.
- T. Kinoshita, Y. Sekiguchi, H. Fukada, T. Nakaniwa, T. Tada, S. Nakamura, K. Kitaura, H. Ohno, Y. Suzuki, A. Hirasawa, I. Nakanishi and G. Tsujimoto
A Detailed Thermodynamic Profile of Cyclopentyl and Isopropyl Derivatives Binding to CK2 Kinase
Mol. Cell. Biochem., **356** (2011) 97.
- H. Tanaka, M. Senda, N. Venugopalan, A. Yamamoto, T. Senda, T. Ishida and K. Horiike
Crystal Structure of a Zinc-Dependent D-Serine Dehydratase from Chicken Kidney
J. Biol. Chem., **286** (2011) 27548.
- X. Zheng, J. Guo, L. Xu, H. Li, D. Zhang, K. Zhang, F. Sun, T. Wen, S. Liu and H. Pang
Crystal Structure of a Novel Esterase Rv0045c from *Mycobacterium tuberculosis*
PLoS One, **6** (2011)
- K.-J. Lee, C.-S. Jeong, Y. J. An, H.-J. Lee, S.-J. Park, Y.-J. Seok, P. Kim, J.-H. Lee, K.-H. Lee and S.-S. Cha
FrsA Functions as a Cofactor-Independent Decarboxylase to Control Metabolic Flux
Nature Chemical Biology, **7** (2011) 434.

- R. Suzuki, Z. Fujimoto, T. Shiotsuki, M. Momma, A. Tase, M. Miyazawa and T. Yamazaki
Structural Mechanism of JH Delivery in Hemolymph by JHBP of silkworm, *Bombyx mori*
Sci. Rep., **1** (2011) 133.
- T. Arimori, H. Tamaoki, T. Nakamura, H. Kamiya, S. Ikemizu, Y. Takagi, T. Ishibashi, H. Harashima, M. Sekiguchi and Y. Yamagata
Diverse Substrate Recognition and Hydrolysis Mechanisms of Human NUDT5
Nucleic Acids Res., **39** (2011) 8972.
- T. Osawa, S. Kimura, N. Terasaka, H. Inanaga, T. Suzuki and T. Numata
Structural Basis of tRNA Agmatinylation Essential for AUA Codon Decoding
Nature Structural Molecular Biology, **18** (2011) 1275.
- T. Osawa, H. Inanaga, S. Kimura, N. Terasaka, T. Suzuki and T. Numata
Crystallization and Preliminary X-Ray Diffraction Analysis of an Archaeal tRNA-Modification Enzyme, TiaS, Complexed with tRNA^{Ile2} and ATP
Acta Cryst. F, **67** (2011) 1414.
- K. Miyazono, N. Tabei, K. Marushima, Y. Ohnishi, S. Horinouchi and M. Tanokura
Purification, Crystallization and Preliminary X-Ray Analysis of Qlucokinase from *Streptomyces griseus* in Complex with Glucose
Acta Cryst. F, **67** (2011) 914.
- M. Maki, H. Suzuki and H. Shibata
Structure and Function of ALG-2, a Penta-EF-Hand Calcium-Dependent Adaptor Protein
Sci. China Life Sci., **54** (2011) 770.
- N. Suzuki, Y.-M. Kim, Z. Fujimoto, M. Momma, H.-K. Kang, K. Funane, M. Okuyama, H. Mori and A. Kimura
Crystallization and Preliminary Crystallographic Analysis of Dextranase from *Streptococcus mutans*
Acta Cryst. F, **67** (2011) 1542.
- T. Umeda, N. Tanaka, Y. Kusakabe, M. Nakanishi, Y. Kitade and K. T. Nakamura
Molecular Basis of Fosmidomycin's Action on the Human Malaria Parasite *Plasmodium falciparum*
Sci. Rep., **1** (2011) 9.
- H. Yoshida, M. Teraoka, A. Yoshihara, K. Izumori and S. Kamitori
Overexpression, Crystallization, and Preliminary X-Ray Diffraction Analysis of L-Ribose Isomerase from *Acinetobacter* sp. Strain DL-28
Acta Cryst. F, **67** (2011) 1281.
- T. T. N. Doan, J.-K. Kim, Q.-K. Mac, C. Chung, N. Sampath, J.-G. Kim, Y.-J. Ahn and L.-W. Kang
Crystallization and Preliminary X-Ray Crystallographic Analysis of β -ketoacyl-ACP Synthase I (XoFabB) from *Xanthomonas oryzae* pv. *Oryzae*
Acta Cryst. F, **67** (2011) 1548.
- M. Wang, J. Qi, Y. Liu, C. Vavricka, Y. Wu, Q. Li and G. Gao
Influenza A Virus N5 Neuraminidase Has an Extended 150 Cavity
J. Virology, **85** (2011) 8431.
- G. Lu, J. Qi, Z. Chen, X. Xu, F. Gao, D. Lin, W. Qian, H. Liu, H. Jiang, J. Yan and G. Gao
Enterovirus 71 and Coxsackievirus A16 3C Proteases: Binding to Rupintrivir and their Substrate, and Anti-HFMD Drug Design
J. Virology, **85** (2011) 10319.
- C. Vavricka, Q. Li, Y. Wu, J. Qi, M. Wang, Y. Liu, F. Gao, J. Liu, E. Feng, J. He, J. Wang, H. Liu, H. Jiang and G. Gao
Structural and Functional Analysis of Laninamivir and its Octanoate Prodrug Reveals Group Specific Mechanisms for Influenza NA Inhibition
PLoS Pathogens, **7** (2011) e1002249.
- H. Tanaka, T. Nogi, N. Yasui, K. Iwasaki and J. Takagi
Structural Basis for Variant-Specific Neuroigin-Binding by α -Neurexin
PLoS One, **6** (2011) e19411.
- S. Yuzawa, S. Kamakura, Y. Iwakiri, J. Hayase and H. Sumimoto
Structural Basis for Interaction between the Conserved Cell Polarity Proteins Inscuteable and Leu-Gly-Asn Repeat-Enriched Protein (LGN)
Proc. Natl. Acad. Sci. USA, **108** (2011) 19210.
- J. Y. Yoon, J. Kim, S. J. Lee, H. S. Kim, H. N. Im, H.-J. Yoon, K. H. Kim, S.-J. Kim, B. W. Han and S. W. Suh
Structural and Functional Characterization of *Helicobacter pylori* DsbG
FEBS Lett., **585** (2011) 3862.
- C. Cai, Y. Zhao, X. Tong, S. Fu, Y. Li, Y. Wu, X. Li and Z. Lou
Crystallization and Preliminary X-Ray Analysis of the vWA Domain of Human Anthrax Toxin Receptor 1
Acta Cryst., **67** (2011) 64.
- H. Xiang, M. Niyama, S. Sugiyama, H. Adachi, K. Takano, S. Murakami, T. Inoue, Y. Mori, M. Ishikawa, H. Matsumura and E. Katoh
Crystallization and Preliminary X-Ray Crystallographic Analysis of a Helicase-Like Domain from a Tomato Mosaic Virus Replication Protein
Acta Cryst. F, **67** (2011) 1649.

E. Matsuoka, Y. Tanaka, M. Kuroda, Y. Shouji, T. Ohta, I. Tanaka and M. Yao

Crystal Structure of the Functional Region of Uro-Adherence Factor A from *Staphylococcus saprophyticus* Reveals Participation of the B Domain in Ligand Binding
Protein Science, **20** (2011) 406.

F. Yu, Y. Tanaka, K. Yamashita, T. Suzuki, A. Nakamura, N. Hirano, T. Suzuki, M. Yao and I. Tanaka

Molecular Basis of Dihydrouridine Formation on tRNA
Proc. Natl. Acad. Sci. USA, **108** (2011) 19593.

F. Yu, Y. Tanaka, S. Yamamoto, A. Nakamura, S. Kita, N. Hirano, I. Tanaka and M. Yao

Crystallization and Preliminary X-Ray Crystallographic Analysis of Dihydrouridine Synthase from *Thermus thermophilus* and its Complex with tRNA
Acta Cryst. F, **67** (2011) 685.

Y. Yasutake and T. Tamura

Efficient Production of Active Form of Vitamin D₃ by Microbial Conversion: Comprehensive Approach from the Molecular to the Cellular Level
Synthesiology, **4** (2011) 222, (*in Japanese*).

Y. Hu, F. Jiang, Y. Guo, Xi. Shen, Y. Zhang, R. Zhang, G. Guo, X. Mao, Q. Zou and D.-C. Wang

Crystal Structure of HugZ, a Novel Heme Oxygenase from *Helicobacter pylori*
J. Biol. Chem., **286** (2011) 1537.

18A

R. Niikura, K. Nakatsuji and F. Komori

Local Atomic and Electronic Structure of Au-Adsorbed Ge(001) Surfaces: Scanning Tunneling Microscopy and X-Ray Photoemission Spectroscopy
Phys. Rev. B, **83** (2011) 035311.

F. Y. Ran, Y. Tsunemaru, T. Hasegawa, Y. Takeichi, A. Harasawa, K. Yaji, S. Kim and A. Kakizaki

Valence Band Structure and Magnetic Properties of Co-Doped Fe₃O₄(100) Films
J. Appl. Phys., **109** (2011) 123919.

S. Ohno, K. Shudo, F. Nakayama, Y. Ichikawa, M. Tanaka, T. Okuda, A. Harasawa, I. Matsuda and A. Kakizaki

Enhanced Silicon Oxidation on Titanium-Covered Si(001)
J. Phys.: Condens. Matter, **23** (2011) 305001.

Former 18B

K. Ninoi, G. Ju, H. Kamiya, S. Fuchi, M. Tabuchi and Y. Takeda

Novel System for X-Ray CTR Scattering Measurement on in-situ Observation of MOVPE Growth of Nitride Semiconductor Heterostructures
J. Cryst. Growth, **318** (2011) 1139.

S. Fushinobu, T. Uno, M. Kitaoka, K. Hayashi, H. Matsuzawa and T. Wakagi

Mutational Analysis of Fungal Family 11 Xylanases on pH Optimum Determination
J. Appl. Glycosci., **58** (2011) 107.

G. Ju, K. Ninoi, H. Kamiya, S. Fuchi, M. Tabuchi and Y. Takeda

X-Ray Characterization at Growth Temperatures of In_xGa_{1-x}N Growth by MOVPE
Journal of Crystal Growth, **318** (2011) 1143.

18B

M. Sharma, M. K. Sanyal, M. K. Mukhopadhyay, M. K. Bera, B. Saha and P. Chakraborty

Structural and Morphological Characterization of Molecular Beam Epitaxy Grown Si/Ge Multilayer using X-Ray Scattering Techniques
J. Appl. Phys., **110** (2011) 102204.

18C

T. Nagai, D. Hamane and K. Fujino

Mechanism of Solid Solution and Crystal Chemistry in MgSiO₃-FeAlO₃ Perovskite
J. Cryst. Soc. Jpn., **53** (2011) 8, (*in Japanese*).

M. Einaga, A. Ohmura, A. Nakayama, F. Ishikawa, Y. Yamada and S. Nakano

Pressure-Induced Phase Transition of Bi₂Te₃ to a bcc Structure
Phys. Rev. B, **83** (2011) 092102.

T. Watanabe, A. Suzuki, S. Minobe, T. Kawashima, K. Kameo, K. Minoshima, Y. M. Aguilar, R. Wani,

H. Kawahata, K. Sowa, T. Nagai and T. Kase
Permanent El Nino during the Pliocene Warm Period not Supported by Coral Evidence
Nature, **471** (2011) 209.

T. Sato, N. Funamori and T. Yagi

Helium Penetrates into Silica Glass and Reduces its Compressibility
Nature Communications, **2** (2011) 345.

S. Nakano, H. Fujihisa, H. Yamawaki, Y. Gotoh and T. Kikegawa

High-Pressure Transformations and Ionic Conductivity in Low-Z Complex Hydride LiBH₄
The Review of High Pressure Science & Technology, **21** (2011) 213, (*in Japanese*).

R. Iizuka, H. Kagi, K. Komatsu, D. Ushijima, S. Nakano, A. Sano-Furukawa, T. Nagai and T. Yagi

Pressure Responses of Portlandite and H-D Isotope Effects on Pressure-Induced Phase Transitions
Phys. Chem. Minerals, **38** (2011) 777.

K. Matsui, J. Hayashi, S. Mitsuka, H. Nakamura, K. Takeda and C. Sekine

High-Pressure X-Ray Diffraction Study of Unfilled Skutterudite Compound RhAs₃
J. Phys. Soc. Jpn., **80** (2011) SA031.

K. Takeda, K. Ito, J. Hayashi, C. Sekine and T. Yagi
Structural and Electrical Properties of New Filled
Skutterudite Compound BaFe₄As₁₂ Prepared at High
Pressure
J. Phys. Soc. Jpn., **80** (2011) SA029.

K. Matsui, J. Hayashi, K. Akahira, K. Ito, Y. Fukushi,
K. Takeda and C. Sekine
Structural Instability of Unfilled Skutterudite
Compounds TSb₃ (T=Co, Rh and Ir) under High
Pressure
J. Phys.: Conf. Ser., **273** (2011) 012043.

M. Matsushita, S. Nakano, H. Ohfuji, I. Yamada and
T. Kikegawa
Volume and Structural Study of Fe₆₄Mn₃₆ Anti-
Ferromagnetic Invar Alloy under High Pressure
J. Magnetism and Magnetic Materials, **323** (2011) 838.

D. Wakabayashi, N. Funamori, T. Sato and T. Taniguchi
Compression Behavior of Densified SiO₂ Glass
Phys. Rev. B, **84** (2011) 144103.

K. Shirai, H. Dekura, Y. Mori, Y. Fujii, H. Hyodo and
K. Kimura
Structural Study of α -Rhombohedral Boron at High
Pressures
J. Phys. Soc. Jpn., **80** (2011) 084601.

S. Machida, H. Hirai, T. Kawamura, Y. Yamamoto and
T. Yagi
Isotopic Effect and Amorphization of Deuterated
Hydrogen Hydrate under High Pressure
Phys. Rev. B, **83** (2011) 144101.

19A

F. Y. Ran, Y. Tsunemaru, T. Hasegawa, Y. Takeichi,
A. Harasawa, K. Yaji, S. Kim and A. Kakizaki
Valence Band Structure and Magnetic Properties of Co-
Doped Fe₃O₄(100) Films
J. Appl. Phys., **109** (2011) 123919.

19B

Y. Kimoto, T. Matsui and T. Akitsu
Isotope Effect and Lanthanide Contraction for 3d-
4f Cyanide-Bridged Complexes Exhibiting Negative
Thermal Expansion
The Open Crystallogr. J., **4** (2011) 16.

20A

T. Tanabe, T. Odagiri, M. Nakano, Y. Kumagai,
I. H. Suzuki, M. Kitajima and N. Kouchi
Reply to "Comment on 'Effect of Entanglement on the
Decay Dynamics of a Pair of H(2p) Atoms Due to
Spontaneous Emission'"
Phys. Rev. A, **83** (2011) 066102.

T. Odagiri, Y. Kumagai, M. Nakano, T. Tanabe,
I. H. Suzuki, M. Kitajima and N. Kouchi
Formation of Metastable Atomic Hydrogen in the 2s
State from Symmetry-Resolved Doubly Excited States
of Molecular Hydrogen
Phys. Rev. A, **84** (2011) 053401.

M. Kurokawa, M. Kitajima, K. Toyoshima, T. Kishino,
T. Odagiri, H. Kato, M. Hoshino, H. Tanaka and K. Ito
High-Resolution Total-Cross-Section Measurements for
Electron Scattering from Ar, Kr, and Xe Employing a
Threshold-Photoelectron Source
Phys. Rev. A, **84** (2011) 062717.

T. Kohmura, K. Kawai, T. Watanabe, T. Ogawa,
S. Ikeda, K. Ushiyama, K. Kaneko, S. Kitamoto,
H. Murakami, E. Takenaka, K. Nagasaki, K. Higashi,
M. Yoshida, H. Tsunemi, K. Hayasida and N. Anabuki
Measuring the EUV and Optical Transmission of Optical
Blocking Layer for X-Ray CCD Camera
Proc. SPIE, **7732** (2011) 77323.

20B

A. S. Kinsela, R. N. Collins and T. D. Waite
Speciation and Transport of Arsenic in an Acid Sulfate
Soil-Dominated Catchment, Eastern Australia
Chemosphere, **82** (2011) 879.

S. G. Johnston, A. F. Keene, E. D. Burton, R. T. Bush
and L. A. Sullivan
Iron and Arsenic Cycling in Intertidal Surface Sediments
during Wetland Remediation
Environ. Sci. Technol., **45** (2011) 2179.

E. Donner, D. L. Howard, M. D. deJonge, D. Paterson,
M. H. Cheah, R. Naidu and E. Lombi
X-Ray Absorption and Micro X-Ray Fluorescence
Spectroscopy Investigation of Copper and Zinc
Speciation in Biosolids
Environ. Sci. Technol., **45** (2011) 7249.

E. Smith, I. M. Kempson, A. L. Juhasz, J. Weber,
A. Rofe, D. Gancarz, R. Naidu, R. G. McLaren and
M. Grafe
In vivo-in vitro and XANES Spectroscopy Assessments
of Lead Bioavailability in Contaminated Periurban Soils
Environ. Sci. Technol., **45** (2011) 6145.

L. J. Parker, L. C. Italiano, C. J. Morton, N. C. Hancock,
D. B. Ascher, J. B. Aitken, H. H. Harris, P. Campomanes,
U. Rothlisberger, A. D. Luca, M. L. Bello, W. H. Ang,
P. J. Dyson and M. W. Parker
Studies of Glutathione Transferase P1-1 Bound to a
Platinum(IV)-Based Anticancer Compound Reveal the
Molecular Basis of its Activation
Chem. Eur. J., **17** (2011) 7806.

R. Giulian, L. L. Araujo, P. Kluth, D. J. Sprouster,
C. S. Schnohr, A. P. Byrne and M. C. Ridgway
Swift Heavy Ion Irradiation of Pt Nanocrystals:
II. Structural Changes and H Desorption
J. Phys. D : Appl. Phys., **44** (2011) 155402.

- Z. Barnea, C. T. Chantler, J. L. Glover, M. W. Grigg, M. T. Islam, M. D. de Jonge, N. A. Rae and C. Q. Tran
Measuring the Linearity of X-Ray Detectors: Consequences for Absolute Attenuation, Scattering and Absolute Bragg Intensities
J. Appl. Cryst., **44** (2011) 281.
- E. D. Burton, S. G. Johnston and R. T. Bush
Microbial Sulfidogenesis in Ferrihydrite-Rich Environments: Effects on Iron Mineralogy and Arsenic Mobility
Geochim. Cosmochim. Acta, **75** (2011) 3072.
- M. H. Cheah and S. P. Best
XAFS and DFT Characterisation of Protonated Reduced Fe Hydrogenase Analogues and their Implications for Electrocatalytic Proton Reduction
Eur. J. Inorg. Chem, **2011** (2011) 1128.
- N. A. S. Webster, K. J. Hartlieb, P. J. Saines, C. D. Ling and F. J. Lincoln
New Quenched-In Fluorite-Type Materials in the Bi₂O₃-La₂O₃-PbO System: Synthesis and Complex Phase Behaviour up to 750 °C
Mater. Res. Bull., **46** (2011) 538.
- W. Liu, S. J. Borg, D. Testemale, B. Etschmann, J.-L. Hazemann and J. Brugger
Speciation and Thermodynamic Properties for Cobalt Chloride Complexes in Hydrothermal Fluids at 35-440°C and 600 Bar: an in-situ XAS Study
Geochim. Cosmochim. Acta, **75** (2011) 1227.
- D. D. Boland, R. N. Collins, T. E. Payne and T. D. Waite
Effect of Amorphous Fe(III) Oxide Transformation on the Fe(II)-Mediated Reduction of U(VI)
Environ. Sci. Technol., **45** (2011) 1327.
- I. M. Low, W. K. Pang, S. J. Kennedy and R. I. Smith
High-Temperature Thermal Stability of Ti₂AlN and Ti₄AlN₃: A Comparative Diffraction Study
J. Eur. Ceram. Soc., **31** (2011) 159.
- S. J. Mills, P. M. Kartashov, C. Ma, G. R. Rossman, M. I. Novgorodova, A. R. Kampf and M. Raudsepp
Yttriaite-(Y): The Natural Occurrence of Y₂O₃ from the Bol'shaya Pol'ya River, Subpolar Urals, Russia
Am. Mineral., **96** (2011) 1166.
- Q. Zhou, B. J. Kennedy and M. Avdeev
Thermal Expansion Behaviour in the Oxygen Deficient Perovskites Sr₂BSbO_{5.5} (B=Ca, Sr, Ba). Competing Effects of Water and Oxygen Ordering
J. Solid State Chem., **184** (2011) 2559.
- A. C. Monsanto, P. Kappen, Y. Wang, P. J. Pigram, A. J. M. Baker and C. Tang
In vivo Speciation of Zinc in *Noccaea caerulea* in Response to Nitrogen Form and Zinc Exposure
Plant Soil, **348** (2011) 167.
- W. K. Pang, I. M. Low, B. H. O'Connor, V. K. Peterson, A. J. Studer and J. P. Palmquist
In situ Diffraction Study of Thermal Decomposition in Maxthal Ti₂AlC
J. Alloys. and Compounds, **509** (2011) 172.
- P. Kluth, S. M. Kluth, B. Johannessen, C. J. Glover, G. J. Foran and M. C. Ridgway
Extended X-Ray Absorption Fine Structure Study of Porous GaSb Formed by Ion Implantation
J. Appl. Phys., **110** (2011) 113528.
- D. J. Sprouster, R. Giulian, L. L. Araujo, P. Kluth, B. Johannessen, D. J. Cookson and M. C. Ridgway
Swift Heavy-Ion Irradiation-Induced Shape and Structural Transformation in Cobalt Nanoparticles
J. Appl. Phys., **109** (2011) 113504.
- F. Jiao, N. Wijaya, L. Zhang, Y. Ninomiya and R. Hocking
Synchrotron-Based XANES Speciation of Chromium in the Oxy-Fuel Fly Ash Collected from Lab-Scale Drop-Tube Furnace
Environ. Sci. Technol., **45** (2011) 6640.
- D. J. Sprouster, R. Giulian, L. L. Araujo, P. Kluth, B. Johannessen, N. Kirby and M. C. Ridgway
Formation and Structural Characterization of Ni Nanoparticles Embedded in SiO₂
J. Appl. Phys., **109** (2011) 113517.
- R. K. Hocking, R. Brimblecombe, L.-Y. Chang, A. Singh, M. H. Cheah, C. Glover, W. H. Casey and L. Spiccia
Water-Oxidation Catalysis by Manganese in a Geochemical-Like Cycle
Nature Chem., **3** (2011) 461.
- H. L. Daly, M. D. Hall, T. W. Failes, M. Zhang, G. J. Foran and T. W. Hambley
Stabilization of Triam(m)inechloridoplatinum Complexes by Oxidation to Pt(IV)
Aust. J. Chem., **64** (2011) 273.

27A

F. Esaka, H. Yamamoto, H. Udono, N. Matsubayashi, K. Yamaguchi, S. Shamoto, M. Magara and T. Kimura
Spectroscopic Characterization of β -FeSi₂ Single Crystals and Homoepitaxial β -FeSi₂ Films by XPS and XAS
Appl. Surf. Sci., **257** (2011) 2950.

F. Esaka, H. Yamamoto, H. Udono, N. Matsubayashi, K. Yamaguchi, S. Shamoto, M. Magara and T. Kimura
Surface Characterization of Homoepitaxial β -FeSi₂ Film on β -FeSi₂ (111) Substrate by X-Ray Photoelectron and X-Ray Absorption Spectroscopy
Phys. Proc., **11** (2011) 150.

M. A. Mannan, Y. Baba, T. Kida, M. Nagano, I. Shimoyama, N. Hirao and H. Noguchi
Orientation of B-C-N Hybrid Films Deposited on Ni(111) and Polycrystalline Ti Substrates Explored by X-Ray Absorption Spectroscopy
Thin Solid Films, **519** (2011) 1780.

Y. Baba, T. Sekiguchi, I. Shimoyama and N. Hirao
Surface Micro-XAFS and its Application to Real-Time Observation of Organic Thin Films
J. Surf. Anal., **17** (2011) 333.

Y. Baba
Nanostructure Analyses of Organic Thin Films by Photoelectron Emission Microscopy Combined with Synchrotron Soft X-Rays
Catalysts and Catalysis, **53** (2011) 160, (*in Japanese*).

N. Hirao, Y. Baba, T. Sekiguchi and I. Shimoyama
Quick Observation of Photoelectron Emission Microscopy with Focused Soft X-Rays using Poly-Capillary Lens
J. Surf. Anal., **17** (2011) 227.

N. Hirao, Y. Baba, T. Sekiguchi, I. Shimoyama and M. Honda
Microscopic Observation of Lateral Diffusion at Si-SiO₂ Interface by Photoelectron Emission Microscopy Using Synchrotron Radiation
Appl. Surf. Sci., **258** (2011) 987.

27B

M. Nagoshi, T. Kawano, I. Kage and S. Hayakawa
Micro-Beam XRF and Fe-K Edge XAFS on the Cross Section of the Rust Layer Formed on a Weathering Steel
ISIJ International, **1** (2011) 93.

Y. Okamoto, H. Shiwaku, S. Suzuki and T. Yaita
Position Sensitive XAFS Analysis by using Gray Scale Signals of CCD Image
Adv. X-Ray. Chem. Anal., Japan, **42** (2011) 183, (*in Japanese*).

M. Numakura, N. Sato, C. Bessada, Y. Okamoto, H. Akatsuka, A. Nezu, Y. Shimohara, K. Tajima, H. Kawano, T. Nakahagi and H. Matsuura
Structural Investigation of Thorium in Molten Lithium - Calcium Fluoride Mixtures for Salt Treatment Process in Molten Salt Reactor
Prog. Nucl. Energy, **53** (2011) 994.

S. Kosugi, N. Fujita, T. Matsui, F. Hori, Y. Saitoh, N. Ishikawa, Y. Okamoto and A. Iwase
Effect of High Temperature Annealing on Ferromagnetism Induced by Energetic Ion Irradiation in FeRh Alloy
Nucl. Instr. Meth. B, **269** (2011) 869.

Y. Tahara, B. Zhu, S. Kosugi, N. Ishikawa, Y. Okamoto, F. Hori, T. Matsui and A. Iwase
Study on Effects of Swift Heavy Ion Irradiation on the Crystal Structure in CeO₂ Doped with Gd₂O₃
Nucl. Instr. Meth. B, **269** (2011) 886.

T. Nishi, M. Nakada, C. Suzuki, H. Shibata, Y. Okamoto, M. Akabori and M. Hirata
Valence State of Am in (U_{0.95}Am_{0.05})O_{2.0}
J. Nucl. Mat., **418** (2011) 311.

C. N. Sprung, M. Cholewa, N. Usami, K. Kobayashi and J. C. Crosbie
DNA Damage and Repair Kinetics after Microbeam Radiation Therapy Emulation in Living Cells using Monoenergetic Synchrotron X-Ray Microbeams
J. Synchrotron Rad., **18** (2011) 630.

N. Ishikawa, T. Sonoda, Y. Okamoto, Y. Sawabe, K. Takegahara, S. Kosugi and A. Iwase
X-Ray Study of Irradiation Damage in UO₂ Irradiated with High Energy Heavy Ions
J. Nucl. Mater., **419** (2011) 392.

A. Uehara, T. Fujii, H. Matsuura, N. Sato, T. Nagai, K. Minato, H. Yamana and Y. Okamoto
EXAFS Analysis of Uranium(IV) and Thorium(IV) Complexes in Concentrated CaCl₂ Solutions
Proc. Radiochim. Acta, **1** (2011) 161.

O. Pauvert, M. Salanne, D. Zanghi, C. Simon, S. Reguer, D. Thiaudiere, Y. Okamoto, H. Matsuura and C. Bessada
Ion Specific Effects on the Structure of Molten AF-ZrF₄ Systems (A⁺ = Li⁺, and K⁺)
J. Phys. Chem. B, **115** (2011) 9160.

28A

T. Yoshida, I. Nishi, S. Ideta, A. Fujimori, M. Kubota, K. Ono, S. Kasahara, T. Shibauchi, T. Terashima, Y. Matsuda, H. Ikeda and R. Arita
Two-Dimensional and Three-Dimensional Fermi Surfaces of Superconducting BaFe₂(As_{1-x}P_x)₂ and their Nesting Properties Revealed by Angle-Resolved Photoemission Spectroscopy
Phys. Rev. Lett., **106** (2011) 117001.

T. Arakane, T. Sato, T. Takahashi, T. Fujii and A. Asamitsu
Angle-Resolved Photoemission Study of the Doping Evolution of a Three-Dimensional Fermi Surface in Na_xCoO₂
New Journal of Physics, **13** (2011) 043021.

T. Qian, N. Xu, Y.-B. Shi, K. Nakayama, P. Richard, T. Kawahara, T. Sato, T. Takahashi, M. Neupane, Y.-M. Xu, X.-P. Wang, G. Xu, X. Dai, Z. Fang, P. Cheng, H.-H. Wen, and H. Ding
Quasinested Fe Orbitals Versus Mott-Insulating V Orbitals in Superconducting Sr₂VFeAsO₃ as Seen from Angle-Resolved Photoemission
Phys. Rev. B, **83** (2011) 140513.

H. Ding, K. Nakayama, P. Richard, S. Souma, T. Sato, T. Takahashi, M. Neupane, Y.-M. Xu, Z.-H. Pan, A. V. Fedorov, Z. Wang, X. Dai, Z. Fang, G. F. Chen, J. L. Luo and N. L. Wang
Electronic Structure of Optimally Doped Pnictide $\text{Ba}_{0.6}\text{K}_{0.4}\text{Fe}_2\text{As}_2$: A Comprehensive Angle-Resolved Photoemission Spectroscopy Investigation
J. Phys.: Condens. Matter, **23** (2011) 135701.

M. Neupane, P. Richard, Y.-M. Xu, K. Nakayama, T. Sato, T. Takahashi, A. V. Fedorov, G. Xu, X. Dai, Z. Fang, Z. Wang, G.-F. Chen, N.-L. Wang, H.-H. Wen, and H. Ding
Electron-Hole Asymmetry in the Superconductivity of Doped BaFe_2As_2 Seen via the Rigid Chemical-Potential Shift in Photoemission
Phys. Rev. B, **83** (2011) 094522.

T. Saitoh, H. Iwasawa, K. Kurahashi, Y. Nakano, T. Katsufuji, I. Hase, K. Shimada, H. Namatame and M. Taniguchi
Spin-Doping Effect on the Electronic Structure of $\text{Sr}_{1-(x+y)}\text{La}_{x+y}\text{Ti}_{1-x}\text{Cr}_x\text{O}_3$
J. Elec. Spec. Relat. Phenom., **184** (2011) 232.

K. Yoshimatsu, K. Horiba, H. Kumigashira, T. Yoshida, A. Fujimori and M. Oshima
Metallic Quantum Well States in Artificial Structures of Strongly Correlated Oxide
Science, **333** (2011) 319.

T. Yamamoto, R. Yasuhara, I. Ohkubo, H. Kumigashira and M. Oshima
Formation of Transition Layers at Metal/Perovskite Oxide Interfaces Showing Resistive Switching Behaviors
J. Appl. Phys., **110** (2011) 053707.

K. Nakayama, T. Sato, P. Richard, Y.-M. Xu, T. Kawahara, K. Umezawa, T. Qian, M. Neupane, G. F. Chen, H. Ding and T. Takahashi
Universality of Superconducting Gaps in Overdoped $\text{Ba}_{0.3}\text{K}_{0.7}\text{Fe}_2\text{As}_2$ Observed by Angle-Resolved Photoemission Spectroscopy
Phys. Rev. B, **83** (2011) 020501(R).

T. Arakane, T. Sato, T. Takahashi, T. Fujii and A. Asamitsu
Three-Dimensional Electronic Structure in Highly Doped Na_xCoO_2 Studied by Angle-Resolved Photoemission Spectroscopy
J. Phys. Chem. Solids, **72** (2011) 552.

Y.-M. Xu, P. Richard, K. Nakayama, T. Kawahara, Y. Sekiba, T. Qian, M. Neupane, S. Souma, T. Sato, T. Takahashi, H.-Q. Luo, H.-H. Wen, G.-F. Chen, N.-L. Wang, Z. Wang, Z. Fang, X. Dai and H. Ding
Fermi Surface Dichotomy of the Superconducting Gap and Pseudogap in Underdoped Pnictides
Nature Commun., **2** (2011) 392.

I. Nishi, M. Ishikado, S. Ideta, W. Malaeb, T. Yoshida, A. Fujimori, Y. Kotani, M. Kubota, K. Ono, M. Yi, D. H. Lu, R. Moore, Z.-X. Shen, A. Iyo, K. Kihou, H. Kito, H. Eisaki, S. Shamoto and R. Arita
Angle-Resolved Photoemission Spectroscopy Study of $\text{PrFeAsO}_{0.7}$: Comparison with LaFePO
Phys. Rev. B, **84** (2011) 014504.

K. Sugawara, T. Sato, K. Kanetani and T. Takahashi
Semiconductor-Metal Transition and Band-Gap Tuning in Quasi-Free-Standing Epitaxial Bilayer Graphene on SiC
J. Phys. Soc. Jpn., **80** (2011) 024705.

K. Sugawara, K. Kanetani, T. Sato and T. Takahashi
Fabrication of Li-Intercalated Bilayer Graphene
AIP Advances, **1** (2011) 022103.

H. Guo, K. Sugawara, A. Takayama, S. Souma, T. Sato, N. Satoh, A. Ohnishi, M. Kitaura, M. Sasaki, Q.-K. Xue and T. Takahashi
Evolution of Surface States in $\text{Bi}_{1-x}\text{Sb}_x$ Alloys Across the Topological Phase Transition
Phys. Rev. B, **83** (2011) 201104(R).

S. Souma, K. Kosaka, T. Sato, M. Komatsu, A. Takayama, T. Takahashi, M. Kriener, K. Segawa and Y. Ando
Direct Measurement of the Out-of-Plane Spin Texture in the Dirac Cone Surface State of a Topological Insulator
Phys. Rev. Lett., **106** (2011) 216803.

T. Sato, K. Segawa, K. Kosaka, S. Souma, K. Nakayama, K. Eto, T. Minami, Y. Ando and T. Takahashi
Unexpected Mass Acquisition of Dirac Fermions at the Quantum Phase Transition of a Topological Insulator
Nature Physics, **7** (2011)

28B

T. Odagiri, Y. Kumagai, M. Nakano, T. Tanabe, I. H. Suzuki, M. Kitajima and N. Kouchi
Formation of Metastable Atomic Hydrogen in the 2s State from Symmetry-Resolved Doubly Excited States of Molecular Hydrogen
Phys. Rev. A, **84** (2011) 053401.

NE1A

T. Nagai, D. Hamane and K. Fujino
Mechanism of Solid Solution and Crystal Chemistry in $\text{MgSiO}_3\text{-FeAlO}_3$ Perovskite
J. Cryst. Soc. Jpn., **53** (2011) 8, (*in Japanese*).

T. Okada, T. Yagi and D. Nishio-Hamane
High-Pressure Phase Behavior of MnTiO_3 : Decomposition of Perovskite into MnO and MnTi_2O_5
Phys. Chem. Minerals, **38** (2011) 251.

T. Yamamoto, C. Tassel, Y. Kobayashi, T. Kawakami, T. Okada, T. Yagi, H. Yoshida, T. Kamatani, Y. Watanabe, T. Kikegawa, M. Takano, K. Yoshimura and H. Kageyama
Pressure-Induced Structural, Magnetic, and Transport Transitions in the Two-Legged Ladder $\text{Sr}_3\text{Fe}_2\text{O}_5$
J. Am. Chem. Soc., **133** (2011) 6036.

K. Takemura and H. Fujihisa
Na-Au Intermetallic Compounds Formed under High Pressure at Room Temperature
Phys. Rev. B, **84** (2011) 014117.

T. Kawauchi, K. Fukutani, M. Matsumoto, K. Oda, T. Okano, X. W. Zhang and Y. Yoda
Surface Magnetic Canting of Iron Films
Phys. Rev. B, **84** (2011) 020415.

S. Nakano, H. Fujihisa, H. Yamawaki, Y. Gotoh and T. Kikegawa
High-Pressure Transformations and Ionic Conductivity in Low-Z Complex Hydride LiBH_4
The Review of High Pressure Science & Technology, **21** (2011) 213, (*in Japanese*).

T. Yamamoto, Y. Kobayashi, T. Okada, T. Yagi, T. Kawakami, C. Tassel, S. Kawasaki, N. Abe, K. Niwa, T. Kikegawa, N. Hirao, M. Takano and H. Kageyama
B1-to-B2 Structural Transitions in Rock Salt Intergrowth Structures
Inorg. Chem., **50** (2011) 11787.

R. Iizuka, H. Kagi, K. Komatsu, D. Ushijima, S. Nakano, A. Sano-Furukawa, T. Nagai and T. Yagi
Pressure Responses of Portlandite and H-D Isotope Effects on Pressure-Induced Phase Transitions
Phys. Chem. Minerals, **38** (2011) 777.

K. Shirai, H. Dekura, Y. Mori, Y. Fujii, H. Hyodo and K. Kimura
Structural Study of α -Rhombohedral Boron at High Pressures
J. Phys. Soc. Jpn., **80** (2011) 084601.

K. Niwa, T. Yagi and K. Ohgushi
Elasticity of CaIrO_3 with Perovskite and Post-Perovskite Structure
Phys. Chem. Minerals, **38** (2011) 21.

A. K. Arora, T. Sato and T. Yagi
Quenchable High-Density Amorphous Polymorphs of Zirconium Tungstate
J. Phys.: Condens. Matter, **23** (2011) 112207.

M. Sougawa, T. Sumiya, K. Takarabe, Y. Mori, T. Okada, H. Gotou, T. Yagi, D. Yamazaki, N. Tomioka, T. Katsura, H. Kariyazaki, K. Sueoka and S. Kunitsugu
Crystal Structure of New Carbon-Nitride-Related Material $\text{C}_2\text{N}_2(\text{CH}_2)$
Jpn. J. Appl. Phys., **50** (2011) 095503.

Former NE3A

H. Kobayashi, J. Umemura, X. Zhan, Y. Ohishi, Y. Uwatoko, H. Fujii and N. Sakai
Structural and Magnetic Properties of Fe_2P under Pressure at Low Temperature
J. Phys. Soc. Jpn., **80** (2011) 084719.

K. Okitsu, Y. Yoda, Y. Imai and Y. Ueji
Polarization-Dependent X-Ray Six-Beam Pinhole Topographs for a Channel-Cut Silicon Crystal
Acta Cryst. A, **67** (2011) 550.

K. Okitsu
On the Polarization State of X-Rays Generated using a Rotating Four-Quadrant X-Ray Phase Retarder System
Acta Cryst. A, **67** (2011) 557.

K. Okitsu
Computer-Simulated X-Ray Three-Beam Pinhole Topographs for Spherical Silicon Crystals
Acta Cryst. A, **67** (2011) 559.

NE3A

M. Kanagawa, T. Satoh, A. Ikeda, Y. Nakano, H. Yagi, K. Kato, K. Kojima-Aikawa and Y. Yamaguchi
Crystal Structures of Human Secretory Proteins ZG16p and ZG16b Reveal a Jacalin-Related β -Prism Fold
Biochem. Biophys. Res. Commun., **404** (2011) 201.

Y. J. Jeong, B.-C. Jeong and H. K. Song
Crystal Structure of Ubiquitin-Like Small Archaeal Modifier Protein 1 (SAMP1) from *Haloflex volcanii*
Biochem. Biophys. Res. Commun., **405** (2011) 112.

L. M. G. Chavas, Y. Yamada, M. Hiraki, N. Igarashi, N. Matsugaki and S. Wakatsuki
UV LED lighting for Automated Crystal Centring
J. Synchron Rad., **18** (2011) 11.

M. Unno, T. Kawasaki, H. Takahara, C. W. Heizmann and K. Kizawa
Refined Crystal Structures of Human $\text{Ca}^{2+}/\text{Zn}^{2+}$ -Binding S100A3 Protein Characterized by Two Disulfide Bridges
J. Mol. Biol., **408** (2011) 477.

K. Ito, S. Ito, T. Shimamura, T. Kobayashi, K. Abe, A. D. Cameron and S. Iwata
Crystal Structure of Glucansucrase from the Dental Caries Pathogen *Streptococcus mutans*
J. Mol. Biol., **408** (2011) 177.

M. Senda, H. Tanaka, T. Ishida, K. Horiike and T. Senda
Crystallization and Preliminary Crystallographic Analysis of D-Serine Dehydratase from Chicken Kidney
Acta Cryst. F, **67** (2011) 147.

T. Ohnuma, T. Numata, T. Osawa, M. Mizuhara, K. M. Varum and T. Fukamizo
Crystal Structure and Mode of Action of a Class V Chitinase from *Nicotiana tabacum*
Plant Mol. Biol., **75** (2011) 291.

- M. Unno, M. Shinohara, K. Takayama, H. Tanaka, K. Teruya, K. Doh-ura, R. Sakai, M. Sasaki and M. Ikeda-Saito
Binding and Selectivity of the Marine Toxin Neodysiherbaine A and its Synthetic Analogues to GluK1 and GluK2 Kainate Receptors
J. Mol. Biol., **413** (2011) 667.
- T. Yoshida, H. Tsuge, H. Konno, T. Hisabori and Y. Sugano
The Catalytic Mechanism of Dye-Decolorizing Peroxidase DyP May Require the Swinging Movement of an Aspartic Acid Residue
FEBS J., **278** (2011) 2387.
- K. Kubota, K. Nagata, M. Okai, K. Miyazono, W. Soemphol, J. Ohtsuka, A. Yamamura, H. Toyama, K. Matsushita and M. Tanokura
The Crystal Structure of L-Sorbose Reductase from *Gluconobacter frateurii* Complexed with NADPH and L-Sorbose
J. Mol. Biol., **407** (2011) 543.
- D. Fujita, A. Takahashi, S. Sato and M. Fujita
Self-Assembly of Pt(II) Spherical Complexes via Temporary Labilization of the Metal-Ligand Association in 2,2,2-Trifluoroethanol
J. Am. Chem. Soc., **133** (2011) 13317.
- T. Tonozuka, T. Miyazaki and A. Nishikawa
Structural Similarity between a Starch-Hydrolyzing Enzyme and an N-Glycan-Hydrolyzing Enzyme: Exohydrolases Cleaving α -1,X-Glucosidic Linkages to Produce β -Glucose
Trends in Glycoscience and Glycotechnology, **23** (2011) 93.
- Y. Uchida, J. Hasegawa, D. Chinnapen, T. Inoue, S. Okazaki, R. Kato, S. Wakatsuki, R. Misaki, M. Koike, Y. Uchiyama, S. Iemura, T. Natsume, R. Kuwahara, T. Nakagawa, K. Nishikawa, K. Mukai, E. Miyoshi, N. Taniguchi, D. Sheff, W. I. Lencer, T. Taguchi and H. Arai
Intracellular Phosphatidylserine is Essential for Retrograde Membrane Traffic through Endosomes
Proc. Natl. Acad. Sci. USA, **108** (2011) 15846.
- M. Kanagawa, T. Satoh, A. Ikeda, Y. Adachi, N. Ohno and Y. Yamaguchi
Structural Insights into Recognition of Triple-Helical β -Glucans by an Insect Fungal Receptor
J. Biol. Chem., **286** (2011) 29158.
- Z. Fujimoto, H. Ichinose, P. Biely and S. Kaneko
Crystallization and Preliminary Crystallographic Analysis of the Glycoside Hydrolase Family 115 α -Glucuronidase from *Streptomyces pristinaespiralis*
Acta Cryst. F, **67** (2011) 68.
- Y. Yasutake, H. Ota, E. Hino, S. Sakasegawa and T. Tamura
Structures of Burkholderia Thailandensis Nucleoside Kinase: Implications for the Catalytic Mechanism and Nucleoside Selectivity
Acta Cryst. D, **67** (2011) 945.
- H. Tanaka, M. Senda, N. Venugopalan, A. Yamamoto, T. Senda, T. Ishida and K. Horiike
Crystal Structure of a Zinc-Dependent D-Serine Dehydratase from Chicken Kidney
J. Biol. Chem., **286** (2011) 27548.
- R. Suzuki, Z. Fujimoto, T. Shiotsuki, M. Momma, A. Tase, M. Miyazawa and T. Yamazaki
Structural Mechanism of JH Delivery in Hemolymph by JHBP of silkworm, *Bombyx mori*
Sci. Rep., **1** (2011) 133.
- K. Okitsu, Y. Yoda, Y. Imai and Y. Ueji
Polarization-Dependent X-Ray Six-Beam Pinhole Topographs for a Channel-Cut Silicon Crystal
Acta Cryst. A, **67** (2011) 550.
- T. Osawa, S. Kimura, N. Terasaka, H. Inanaga, T. Suzuki and T. Numata
Structural Basis of tRNA Agmatinylation Essential for AUA Codon Decoding
Nature Structural Molecular Biology, **18** (2011) 1275.
- T. Osawa, H. Inanaga, S. Kimura, N. Terasaka, T. Suzuki and T. Numata
Crystallization and Preliminary X-Ray Diffraction Analysis of an Archaeal tRNA-Modification Enzyme, TiaS, Complexed with tRNA^{Ile2} and ATP
Acta Cryst. F, **67** (2011) 1414.
- N. Suzuki, Y.-M. Kim, Z. Fujimoto, M. Momma, H.-K. Kang, K. Funane, M. Okuyama, H. Mori and A. Kimura
Crystallization and Preliminary Crystallographic Analysis of Dextranase from *Streptococcus mutans*
Acta Cryst. F, **67** (2011) 1542.
- S. Saijo, S. Arai, K. M. M. Hossain, I. Yamato, K. Suzuki, Y. Kakinuma, Y. Ishizuka-Katsura, N. Ohsawa, T. Terada, M. Shirouzu, S. Yokoyama, S. Iwata and T. Murata
Crystal Structure of the Central Axis DF Complex of the Prokaryotic V-ATPase
Proc. Natl. Acad. Sci. USA, **108** (2011) 19955.
- Y. Guo, J. Wang, G. Niu, W. Shui, Y. Sun, H. Zhou, Y. Zhang, C. Yang, Z. Lou and Z. Rao
A Structural View of the Antibiotic Degradation Enzyme NDM-1 from a Superbug
Protein Cell, **2** (2011) 384.

H. Yoshida, M. Teraoka, A. Yoshihara, K. Izumori and S. Kamitori
Overexpression, Crystallization, and Preliminary X-Ray Diffraction Analysis of L-Ribose Isomerase from *Acinetobacter* sp. Strain DL-28
Acta Cryst. F, **67** (2011) 1281.

U. Ohto, K. Miyake and T. Shimizu
Crystal Structures of Mouse and Human RP105/MD-1 Complexes Reveal Unique Dimer Organization of the Toll-Like Receptor Family
J. Mol. Biol., **413** (2011) 815.

Y. Shi, J. Qi, A. Iwamoto and G. Gao
Plasticity of Human CD8 $\alpha\alpha$ Binding to Peptide-HLA-A 2402
Molecular Immunology, **48** (2011) 2198.

M. Wang, J. Qi, Y. Liu, C. Vavricka, Y. Wu, Q. Li and G. Gao
Influenza A Virus N5 Neuraminidase Has an Extended 150 Cavity
J. Virology, **85** (2011) 8431.

G. Lu, J. Qi, Z. Chen, X. Xu, F. Gao, D. Lin, W. Qian, H. Liu, H. Jiang, J. Yan and G. Gao
Enterovirus 71 and Coxsackievirus A16 3C Proteases: Binding to Rupintrivir and their Substrate, and Anti-HFMD Drug Design
J. Virology, **85** (2011) 10319.

C. Vavricka, Q. Li, Y. Wu, J. Qi, M. Wang, Y. Liu, F. Gao, J. Liu, E. Feng, J. He, J. Wang, H. Liu, H. Jiang and G. Gao
Structural and Functional Analysis of Laninamivir and its Octanoate Prodrug Reveals Group Specific Mechanisms for Influenza NA Inhibition
PLoS Pathogens, **7** (2011) e1002249.

S. B. Hong, B.-W. Kim, K.-E. Lee, S. W. Kim, H. Jeon, J. Kim and H. K. Song
Insights into Noncanonical E1 Enzyme Activation from the Structure of Autophagic E1 Atg7 with Atg8
Nature Structural Molecular Biology, **18** (2011) 1323.

T. Nagai, H. Unno, M. W. Janczak, T. Yoshimura, CD. Poulter and H. Hemmi
Covalent Modification of Reduced Flavin Mononucleotide in Type-2 Isopentenyl Diphosphate Isomerase by Active-Site-Directed Inhibitors
Proc. Natl. Acad. Sci. USA, **108** (2011) 20461.

Q.-F. Sun, T. Murase, S. Sato and M. Fujita
A Sphere-in-Sphere Complex by Orthogonal Self-Assembly
Angew. Chem. Int. Ed., **50** (2011) 10318.

T. Tomita, T. Kuzuyama and M. Nishiyama
Structural Basis for Leucine-Induced Allosteric Activation of Glutamate Dehydrogenase
J. Biol. Chem., **286** (2011) 37406.

Y. Yasutake and T. Tamura
Efficient Production of Active Form of Vitamin D₃ by Microbial Conversion: Comprehensive Approach from the Molecular to the Cellular Level
Synthesiology, **4** (2011) 222, (*in Japanese*).

Y. Moriwaki, J. M. M. Caaveiro, Y. Tanaka, H. Tsutsumi, I. Hamachi and K. Tsumoto
Molecular Basis of Recognition of Antibacterial Porphyrins by Heme-Transporter IsdH-NEAT3 of *Staphylococcus aureus*
Biochemistry, **50** (2011) 7311.

NE5C

S. Urakawa, R. Matsubara, T. Katsura, T. Watanabe and T. Kikegawa
Stability and Bulk Modulus of Ni₃S, a New Nickel Sulfur Compound, and the Melting Relations of the System Ni-NiS up to 10 GPa
Am. Mineral., **96** (2011) 558.

A. Yamada, T. Inoue, S. Urakawa, K. Funakoshi, N. Funamori, T. Kikegawa and T. Irifune
In situ X-Ray Diffraction Study on Pressure-Induced Structural Changes in Hydrousforsterite and Enstatite Melts
Earth and Planetary Science Letters, **308** (2011) 115.

K. Fuchizaki and N. Hamaya
Equation of State for the Low-Pressure Crystalline Phase of SnI₄
Phys. Rev. B, **84** (2011) 144105.

K. Matsui, J. Hayashi, S. Mitsuka, H. Nakamura, K. Takeda and C. Sekine
High-Pressure X-Ray Diffraction Study of Unfilled Skutterudite Compound RhAs₃
J. Phys. Soc. Jpn., **80** (2011) SA031.

K. Takeda, K. Ito, J. Hayashi, C. Sekine and T. Yagi
Structural and Electrical Properties of New Filled Skutterudite Compound BaFe₄As₁₂ Prepared at High Pressure
J. Phys. Soc. Jpn., **80** (2011) SA029.

K. Matsui, J. Hayashi, K. Akahira, K. Ito, Y. Fukushi, K. Takeda and C. Sekine
Structural Instability of Unfilled Skutterudite Compounds TSb₃ (T=Co, Rh and Ir) under High Pressure
J. Phys.: Conf. Ser., **273** (2011) 012043.

A. Ohumura, K. Fujimaki, F. Ishikawa, Y. Yamada, N. Tsujii and M. Imai
Pressure Effect on Critical Temperature for Superconductivity and Lattice Parameters of AlB₂-Type Ternary Silicide YbGa_{1.1}Si_{0.9}
Phys. Rev. B, **84** (2011) 104520.

NE7A

R. Tateyama, E. Ohtani, H. Terasaki, K. Nishida, Y. Shibazaki, A. Suzuki and T. Kikegawa
Density Measurements of Liquid Fe-Si Alloys at High Pressure using the Sink-Float Method
Phys. Chem. Minerals, **38** (2011) 801.

S. Ono, T. Kikegawa and Y. Higo
In situ Observation of a Garnet/Perovskite Transition in CaGeO_3
Physics and Chemistry of Minerals, **38** (2011) 735.

H. Gotou, T. Yagi, T. Okada, R. Iizuka and T. Kikegawa
A Simple Opposed-Anvil Apparatus for High Pressure and Temperature Experiments above 10 GPa
High Pressure Research, **31** (2011) 592.

R. Shiraishi, E. Ohtani, T. Kubo, N. Doi, A. Suzuki, A. Shimojuku, T. Kato and T. Kikegawa
Deformation Cubic Anvil Press and Stress and Strain Measurements using Monochromatic X-Rays at High Pressure and High Temperature
High Pressure Research, **31** (2011) 399.

NW2A

A. Kobayashi, Y. Suzuki, T. Ohba, S. Noro, H.-C. Chang and M. Kato
Ln-Co-Based Rock-Salt-Type Porous Coordination Polymers: Vapor Response Controlled by Changing the Lanthanide Ion
Inorg. Chem., **50** (2011) 2061.

A. Kobayashi, K. Ohbayashi, R. Aoki, H.-C. Chang and M. Kato
Synthesis, Structure and Photophysical Properties of a Flavin-Based Platinum(II) Complex
Dalton Trans., **40** (2011) 3484.

K. Komori-Orisaku, K. Nakabayashi and S. Ohkoshi
Synthesis of a Chiral-Structured Molecular Magnet Based on a Cyano-Bridged Co-W Bimetal Assembly
Chem. Lett., **40** (2011) 586.

T. Matsushita, T. Takahashi, T. Shirasawa, E. Arakawa, H. Toyokawa and H. Tajiri
Quick Measurement of Crystal Truncation Rod Profiles in the Simultaneous Multi-Wavelength Dispersive Mode
J. Appl. Phys., **110** (2011) 102209.

H. Oyanagi, Z. H. Sun, Y. Jiang, M. Uehara, H. Nakamura, K. Yamashita, L. Zhang, C. Lee, A. Fukano and H. Maeda
In situ XAFS Experiments using a Microfluidic Cell: Application to Initial Growth of CdSe Nanocrystals
J. Synchrotron Rad., **18** (2011) 272.

Y. Uemura, Y. Inada, Y. Niwa, M. Kimura, K. K. Bando, A. Yagishita, Y. Iwasawa and M. Nomura
Formation and Oxidation Mechanism of Pd-Zn Nanoparticles in ZnO Supported Pd Catalyst Studied by *in situ* Time-Resolved QXAFS and DXAFS
Phys. Chem. Chem. Phys., **14** (2011) 2152.

Y. Uemura, Y. Inada, K. K. Bando, T. Sasaki, N. Kamiuchi, K. Eguchi, A. Yagishita, M. Nomura, M. Tada and Y. Iwasawa
In situ Time-Resolved XAFS Study on the Structural Transformation and Phase Separation of Pt_3Sn and PtSn Alloy Nanoparticles on Carbon in the Oxidation Process
Phys. Chem. Chem. Phys., **13** (2011) 15833.

Y. Uemura, Y. Inada, K. K. Bando, T. Sasaki, N. Kamiuchi, K. Eguchi, A. Yagishita, M. Nomura, M. Tada and Y. Iwasawa
Core-Shell Phase Separation and Structural Transformation of Pt_3Sn Alloy Nanoparticles Supported on $\gamma\text{-Al}_2\text{O}_3$ in the Reduction and Oxidation Processes Characterized by In Situ Time-Resolved XAFS
J. Phys. Chem. C, **115** (2011) 5823.

NW10A

H. Takahashi, N. Konishi, H. Ohno, K. Takahashi, Y. Koike, K. Asakura and A. Muramatsu
Preparation of Well-Crystallized $\text{Pd}_{20}\text{Te}_7$ Alloy Nanoparticulate Catalysts with Uniform Structure and Composition in Liquid-Phase
Appl. Catal. A, **392** (2011) 80.

N. Ahmed, Y. Shibata, T. Taniguchi and Y. Izumi
Photocatalytic Conversion of Carbon Dioxide into Methanol using Zinc-Copper-M(III) (M = Aluminum, Gallium) Layered Double Hydroxides
J. Catal., **279** (2011) 123.

N. Kawasaki, H. Wang, R. Nakanishi, S. Hamanaka, R. Kitaura, H. Shinohara, T. Yokoyama, H. Yoshikawa and K. Awaga
Nanohybridization of Polyoxometalate Clusters and Single-Wall Carbon Nanotubes: Applications in Molecular Cluster Batteries
Angew. Chem. Int. Ed., **50** (2011) 3471.

H. Ikemoto, A. Goyo and T. Miyayama
Size Dependence of the Local Structure and Atomic Correlations in Tellurium Nanoparticles
J. Phys. Chem. C, **115** (2011) 2931.

T. Wada, K. K. Bando, K. Kawai and K. Asakura
In-situ XAFS for Monitoring the Structure of Catalysts under More Realistic Reaction Conditions
Shokubai, **53** (2011) 150, (*in Japanese*).

S. Takenaka, N. Susuki, H. Miyamoto, E. Tanabe, H. Matsune and M. Kishida
Highly Durable Carbon Nanotube-Supported Pd Catalysts Covered with Silica Layers for the Oxygen Reduction Reaction
J. Catal., **279** (2011) 381.

Z. Weng, S. Muratsugu, N. Ishiguro, S. Ohkoshi and M. Tada
Preparation of Surface Molecularly Imprinted Ru-Complex Catalysts for Asymmetric Transfer Hydrogenation in Water Media
Dalton Trans., **40** (2011) 2338.

- K. Shimura, K. Maeda and H. Yoshida
Thermal Acceleration of Electron Migration in Gallium Oxide Photocatalysts
J. Phys. Chem. C, **115** (2011) 9041.
- J. Gaudet, K. K. Bando, Z. Song, T. Fujitani, W. Zhang, D. S. Sue and S. T. Oyama
Effect of Gold Oxidation State on the Epoxidation and Hydrogenation of Propylene on Au/Ts-1
J. Catal., **280** (2011) 40.
- K. K. Bando, Y. Koike, T. Kawai, G. Tateno, S. T. Oyama, Y. Inada, M. Nomura and K. Asakura
Quick X-Ray Absorption Fine Structure Studies on the Activation Process of Ni₂P Supported on K-USY
J. Phys. Chem. C, **115** (2011) 7466.
- J. Ohyama, A. Yamamoto, K. Teramura, T. Shishido and T. Tanaka
Modification of Metal Nanoparticles with TiO₂ and Metal-Support Interaction in Photodeposition
ACS Catal., **1** (2011) 187.
- Y. Cheng, H. Kajiro, H. Noguchi, A. Kondo, T. Ohba, Y. Hattori, K. Kaneko and H. Kanoh
Tuning of Gate Opening of an Elastic Layered Structure MOF in CO₂ Sorption with a Trace of Alcohol Molecules
Langmuir, **27** (2011) 6905.
- T. Ohkubo, M. Nishi and Y. Kuroda
Actual Structure of Dissolved Zinc Ion Restricted in Less than 1 Nanometer Micropores of Carbon
J. Phys. Chem. C, **115** (2011) 14954.
- N. Fukaya, M. Ueda, S. Onozawa, K. K. Bando, T. Miyaji, Y. Takagi, T. Sakakura and H. Yasuda
Palladium Complex Catalysts Immobilized on Silica via a Tripodal Linker Unit with Amino Groups: Preparation, Characterization, and Application to the Suzuki-Miyaura Coupling
J. Mol. Catal. A: Chemical, **342-343** (2011) 58.
- M. Katayama, K. Sugimoto, E. Kato, K. Ozutsumi, S. Funahashi and Y. Inada
Novel Structural Variation of Silver(I)-Pyridine Complexes in Nitromethane as Studied by X-Ray Absorption Spectroscopy
Inorg. Chim. Acta, **378** (2011) 66.
- R. Muraio, K. Sugiyama, Y. Kashiwagi, S. Kameoka and A. P. Tsai
Atomic Pair Distribution Function (PDF) Analysis of Raney Pd and Rh Fine Particles
Philosophical Magazine, **91** (2011) 2954.
- T. Komanoya, H. Kobayashi, K. Hara, W.-J. Chun and A. Fukuoka
Catalysis and Characterization of Carbon-Supported Ruthenium for Cellulose Hydrolysis
Appl. Catal. A, **407** (2011) 188.
- H. Kobayashi and A. Fukuoka
Saccharification of Cellulose by Solid Catalysts
J. Jpn. Inst. Energy, **90** (2011) 512, (*in Japanese*).
- S. Kageyama, S. Seino, T. Nakagawa, H. Nitani, K. Ueno, H. Daimon and T. A. Yamamoto
Formation of PtRu Alloy Nanoparticle Catalyst by Radiolytic Process Assisted by Addition of DL-Tartaric Acid and its Enhanced Methanol Oxidation Activity
J. Nanoparticle. Res., **13** (2011) 5275.
- J. Kugai, R. Kitagawa, S. Seino, T. Nakagawa, Y. Ohkubo, H. Nitani, H. Daimon and T. A. Yamamoto
 γ -Fe₂O₃-Supported Pt-Cu Nanoparticles Synthesized by Radiolytic Process for Catalytic CO Preferential Oxidation
Appl. Catal. A, **406** (2011) 43.
- Y. Ohkubo, M. Shibata, S. Kageyama, S. Seino, T. Nakagawa, J. Kugai and T. A. Yamamoto
Radiation Induced Synthesis of Au-Pd Nanoparticles of Random Alloy Structure Supported on Carbon Particles using the High Energy Electron Beam
Mater. Lett., **65** (2011) 2165.
- T. A. Yamamoto, S. Kageyama, S. Seino, H. Nitani, T. Nakagawa, R. Horioka, Y. Honda, K. Ueno and H. Daimon
Methanol Oxidation Catalysis and Substructure of PtRu/C Bimetallic Nanoparticles Synthesized by a Radiolytic Process
Appl. Catal. A, **396** (2011) 68.
- S. Muratsugu, K. Sodeyama, F. Kitamura, S. Tsukada, M. Tada, S. Tsuneyuki and H. Nishihara
Normal and Inverted Redox Potentials and Structural Changes Tuned by Medium Effects in [M₂Mo(η ⁵-C₅Me₅)₂(S₂C₆H₄)₂(CO)₂] (M: Co, Rh)
Chemical Science, **2** (2011) 1960.
- S. Sugiyama, T. Bando, H. Tanaka, K. Nakagawa, K.-I. Sotowa, Y. Katou, T. Mori, T. Yasukawa and W. Ninomiya
Direct Oxidative Esterification of Propionaldehyde to Methyl Propionate using Heavy-Metal-Free Palladium Catalysts under Pressurized Oxygen
J. Jpn. Petrol. Inst., **54** (2011) 380.
- H. Einaga, Y. Teraoka and A. Ogata
Benzene Oxidation with Ozone over Manganese Oxide Supported on Zeolite Catalysts
Catal. Today, **164** (2011) 571.
- K. Shimura, H. Kawai, T. Yoshida and H. Yoshida
Simultaneously Photodeposited Rhodium Metal and Oxide Nanoparticles Promoting Photocatalytic Hydrogen Production
Chem. Comm., **47** (2011) 8958.

S. Hinokuma, M. Okamoto, E. Ando, K. Ikeue and M. Machida

Structure and Catalytic Property of Supported Rhodium Catalysts Prepared using Arc-Plasma
Catal. Today, **175** (2011) 593.

Y. Masubuchi, C. Yamakami, T. Motohashi and S. Kikkawa

Ammonolysis of HTiNbO₅-*n*-Propylamine Intercalation Compound
Chem. Lett., **40** (2011) 1238.

Y. Uemura, Y. Inada, Y. Niwa, M. Kimura, K. K. Bando, A. Yagishita, Y. Iwasawa and M. Nomura

Formation and Oxidation Mechanism of Pd-Zn Nanoparticles in ZnO Supported Pd Catalyst Studied by *in situ* Time-Resolved QXAFS and DXAFS
Phys. Chem. Chem. Phys., **14** (2011) 2152.

K. Motokura, N. Hashimoto, T. Hara, T. Mitsudome, T. Mizugaki, K. Jitsukawa and K. Kaneda

Rhodium-Grafted Hydrotalcite Catalyst for Heterogeneous 1,4-Addition Reaction of Organoboron Reagents to Electron Deficient Olefins
Green Chem., **13** (2011) 2416.

D. Tsukamoto, M. Ikeda, Y. Shiraishi, T. Hara, N. Ichikuni, S. Tanaka and T. Hirai

Selective Photocatalytic Oxidation of Alcohols to Aldehydes in Water by TiO₂ Partially Coated with WO₃
Chem. Eur. J., **17** (2011) 9816.

S. Takenaka, H. Miyamoto, N. Susuki, H. Matsune and M. Kishida

Highly Durable Carbon Nanotube-Supported Pd Cathode Catalysts Covered with Silica Layers for Polymer Electrolyte Fuel Cells: Effect of Silica Layer Thickness on the Catalytic Performance
ECS Trans., **41** (2011) 2305.

T. Hara, J. Sawada, Y. Nakamura, N. Ichikuni and S. Shimazu

An Anionic D-Valine-Palladium (II) Complex Supported on a Hydroxy Double Salt with a Bronsted Basic Phosphate Anion: Application for a Heterogeneous Catalyst toward Aerobic Alcohol Oxidation
Catalysis Science & Technology, **1** (2011) 1376.

Y. Uemura, Y. Inada, K. K. Bando, T. Sasaki, N. Kamiuchi, K. Eguchi, A. Yagishita, M. Nomura, M. Tada and Y. Iwasawa

In situ Time-Resolved XAFS Study on the Structural Transformation and Phase Separation of Pt₃Sn and PtSn Alloy Nanoparticles on Carbon in the Oxidation Process
Phys. Chem. Chem. Phys., **13** (2011) 15833.

Y. Uemura, Y. Inada, K. K. Bando, T. Sasaki, N. Kamiuchi, K. Eguchi, A. Yagishita, M. Nomura, M. Tada and Y. Iwasawa

Core-Shell Phase Separation and Structural Transformation of Pt₃Sn Alloy Nanoparticles Supported on γ -Al₂O₃ in the Reduction and Oxidation Processes Characterized by *In Situ* Time-Resolved XAFS
J. Phys. Chem. C, **115** (2011) 5823.

K. Maeda, R. Abe and K. Domen

Role and Function of Ruthenium Species as Promoters with TaON-Based Photocatalysts for Oxygen Evolution in Two-Step Water Splitting under Visible Light
J. Phys. Chem. C, **115** (2011) 3057.

K. Gotoh, T. Kinumoto, E. Fujii, A. Yamamoto, H. Hashimoto, T. Ohkubo, A. Itadani, Y. Kuroda and H. Ishida

Exfoliated Graphene Sheets Decorated with Metal/Metal Oxide Nanoparticles: Simple Preparation from Cation Exchanged Graphite Oxide
Carbon, **49** (2011) 1118.

NW12A

M. Kanagawa, T. Satoh, A. Ikeda, Y. Nakano, H. Yagi, K. Kato, K. Kojima-Aikawa and Y. Yamaguchi

Crystal Structures of Human Secretory Proteins ZG16p and ZG16b Reveal a Jacalin-Related β -Prism Fold
Biochem. Biophys. Res. Commun., **404** (2011) 201.

K. Matsumoto, K. Okamoto, N. Ashizawa and T. Nishino
FYX-051: A Novel and Potent Hybrid-Type Inhibitor of Xanthine Oxidoreductase

J. Pharmacology and Experimental Therapeutics, **336** (2011) 95.

J. Ohwada, H. Ebiike, H. Kawada, M. Tsukazaki, M. Nakamura, T. Miyazaki, K. Morikami, K. Yoshinari, M. Yoshida, O. Kondoh, S. Kuramoto, K. Ogawa, Y. Aoki and N. Shimma

Discovery and Biological Activity of a Novel Class I PI3K Inhibitor, CH5132799
Bioorg. Med. Chem. Lett., **21** (2011) 1767.

L. Deng, K. Endo, M. Kato, G. Cheng, S. Yajima and Y. Song

Structures of 1-Deoxy-D-Xylulose-5-Phosphate Reductoisomerase/Lipophilic Phosphonate Complexes
ACS Med. Chem. Lett., **2** (2011) 165.

T. Hashiguchi, T. Ose, M. Kubota, N. Maita, J. Kamishikiryo, K. Maenaka and Y. Yanagi

Structure of the Measles Virus Hemagglutinin Bound to its Cellular Receptor SLAM
Nature Structural Molecular Biology, **18** (2011) 135.

L. M. G. Chavas, Y. Yamada, M. Hiraki, N. Igarashi, N. Matsugaki and S. Wakatsuki

UV LED lighting for Automated Crystal Centring
J. Synchron Rad., **18** (2011) 11.

- D. Sasaki, M. Fujihashi, N. Okuyama, Y. Kobayashi, M. Noike, T. Koyama and K. Miki
Crystal Structure of Heterodimeric Hexaprenyl Diphosphate Synthase from *Micrococcus luteus* B-P 26 Reveals that the Small Subunit is Directly Involved in the Product Chain Length Regulation
J. Biol. Chem., **286** (2011) 3729.
- M. Unno, T. Kawasaki, H. Takahara, C. W. Heizmann and K. Kizawa
Refined Crystal Structures of Human Ca²⁺/Zn²⁺-Binding S100A3 Protein Characterized by Two Disulfide Bridges
J. Mol. Biol., **408** (2011) 477.
- N. Okazaki, T. Arimori, M. Nakazawa, K. Miyatake, M. Ueda and T. Tamada
Crystallization and Preliminary X-Ray Diffraction Studies of the Catalytic Domain of a Novel Chitinase, a Member of GH Family 23, from the Moderately Thermophilic Bacterium *Ralstonia* sp. A-471
Acta Cryst. F, **67** (2011) 494.
- S. Mori, K. Shibayama, J. Wachino and Y. Arakawa
Structural Insights into the Novel Diadenosine 5',5''-P¹,P⁴-Tetraphosphate Phosphorylase from *Mycobacterium tuberculosis* H37Rv
J. Mol. Biol., **410** (2011) 93.
- K. Nishi, T. Ono, T. Nakamura, N. Fukunaga, M. Izumi, H. Watanabe, A. Suenaga, T. Maruyama, Y. Yamagata, S. Curry and M. Otagiri
Structural Insights into Differences in Drug-Binding Selectivity between Two Forms of Human α_1 -Acid Glycoprotein Genetic Variants, the A and F1*S Forms
J. Biol. Chem., **286** (2011) 14427.
- T. Yoshizawa, H. Hashimoto, T. Shimizu, M. Yamabe, N. Shichijo, K. Hanada, H. Hirano and M. Sato
Purification, Crystallization and X-Ray Diffraction Study of Basic 7S Globulin from Soybean
Acta Cryst. F, **67** (2011) 87.
- Y. Sato, R. Natsume, Z. Prokop, J. Brezovsky, R. Chaloupkova, J. Damborsky, Y. Nagata and T. Senda
Molecular Bases of Enantioselectivity of Haloalkane Dehalogenase DbjA
Kessyogakkaishi, **53** (2011) 124, (*in Japanese*).
- M. Senda, H. Tanaka, T. Ishida, K. Horiike and T. Senda
Crystallization and Preliminary Crystallographic Analysis of D-Serine Dehydratase from Chicken Kidney
Acta Cryst. F, **67** (2011) 147.
- T. Hatakeyama, T. Kamiya, M. Kusunoki, S. Nakamura-Tsuruta, J. Hirabayashi, S. Goda and H. Unno
Galactose Recognition by A Tetrameric C-Type Lectin, CEL-IV, Containing the EPN Carbohydrate-Recognition Motif
J. Biol. Chem., **286** (2011) 10305.
- S. J. Lee, H. S. Kim, D. J. Kim, H. J. Yoon, K. H. Kim, J. Y. Yoon and S. W. Suh
Crystal Structures of LacD from *Staphylococcus aureus* and LacD. 1 from *Streptococcus pyogenes*: Insights into Substrate Specificity and Virulence Gene Regulation
FEBS Lett., **585** (2011) 307.
- J. H. Lee, H. Park, S. J. Park, H. J. Kim and S. H. Eom
The Structural Flexibility of the Shank1 PDZ Domain is Important for Its Binding to Different Ligands
Biochem. Biophys. Res. Commun., **407** (2011) 207.
- T. Ohnuma, T. Numata, T. Osawa, M. Mizuhara, K. M. Varum and T. Fukamizo
Crystal Structure and Mode of Action of a Class V Chitinase from *Nicotiana tabacum*
Plant Mol. Biol., **75** (2011) 291.
- M. Unno, M. Shinohara, K. Takayama, H. Tanaka, K. Teruya, K. Doh-ura, R. Sakai, M. Sasaki and M. Ikeda-Saito
Binding and Selectivity of the Marine Toxin Neodysiherbaine A and its Synthetic Analogues to GluK1 and GluK2 Kainate Receptors
J. Mol. Biol., **413** (2011) 667.
- T. Yoshida, H. Tsuge, H. Konno, T. Hisabori and Y. Sugano
The Catalytic Mechanism of Dye-Decolorizing Peroxidase DyP May Require the Swinging Movement of an Aspartic Acid Residue
FEBS J., **278** (2011) 2387.
- Y. Y. Chen, T. P. Ko, C. H. Lin, W. H. Chen and A. H. J. Wang
Conformational Change upon Product Binding to *Klebsiella pneumoniae* UDP-Glucose Dehydrogenase: A Possible Inhibition Mechanism for the Key Enzyme in Polymyxin Resistance
J. Structural Biol., **175** (2011) 300.
- T. Saitoh, M. Igura, Y. Miyazaki, T. Ose, N. Maita and D. Kohda
Crystallographic Snapshots of Tom20-Mitochondrial Presequence Interactions with Disulfide-Stabilized Peptides
Biochemistry, **50** (2011) 5487.
- T. Tsukazaki, H. Mori, Y. Echizen, R. Ishitani, S. Fukai, T. Tanaka, A. Perederina, D. G. Vassilyev, T. Kohno, A. D. Maturana, K. Ito and O. Nureki
Structure and Function of a Membrane Component SecDF That Enhances Protein Export
Nature, **474** (2011) 235.
- K. Miyazono, J. Um, F. L. Imai, Y. Katsuyama, Y. Ohnishi, S. Horinouchi and M. Tanokura
Crystal Structure of Curcuminoid Synthase CUS from *Oryza sativa*
Proteins, **79** (2011) 669.

- Y. Katsuyama, K. Miyazono, M. Tanokura, Y. Ohnishi and S. Horinouchi
Structural and Biochemical Elucidation of Mechanism for Decarboxylative Condensation of β -Keto Acid by Curcumin Synthase
J. Biol. Chem., **286** (2011) 6659.
- H. Sakuraba, K. Koga, K. Yoneda, Y. Kashima and T. Ohshima
Structure of a Multicopper Oxidase from the Hyperthermophilic Archaeon *Pyrobaculum Aerophilum*
Acta Cryst. F, **67** (2011) 753.
- H. Sakuraba, T. Kawai, K. Yoneda and T. Ohshima
Crystal Structure of UDP-Galactose 4-Epimerase from the Hyperthermophilic Archaeon *Pyrobaculum calidifontis*
Arch. Biochem. Biophys., **512** (2011) 126.
- T. Tonzuka, T. Miyazaki and A. Nishikawa
Structural Similarity between a Starch-Hydrolyzing Enzyme and an N-Glycan-Hydrolyzing Enzyme: Exohydrolases Cleaving α -1,X-Glucosidic Linkages to Produce β -Glucose
Trends in Glycoscience and Glycotechnology, **23** (2011) 93.
- T. Nakamura, T. Tonzuka, S. Ito, Y. Takeda, R. Sato, I. Matsuo, Y. Ito, K. Oguma and A. Nishikawa
Molecular Diversity of the Two Sugar-Binding Sites of the β -Trefoil Lectin HA33/C (HA1) from *Clostridium botulinum* Type C Neurotoxin
Arch. Biochem. Biophys., **512** (2011) 69.
- K. Taoka, I. Ohki, H. Tsuji, K. Furuita, K. Hayashi, T. Yanase, M. Yamaguchi, C. Nakashima, Y. A. Purwestri, S. Tamaki, Y. Ogaki, C. Shimada, A. Nakagawa, C. Kojima and K. Shimamoto
14-3-3 Proteins Act as Intracellular Receptors for Rice Hd3a Florigen
Nature, **476** (2011) 332.
- S. Fushinobu, M. Hidaka, A. M. Hayashi, T. Wakagi, H. Shoun and M. Kitaoka
Interactions between Glycoside Hydrolase Family 94 Cellobiose Phosphorylase and Glucosidase Inhibitors
J. Appl. Glycosci., **58** (2011) 91.
- S. Fushinobu, T. Uno, M. Kitaoka, K. Hayashi, H. Matsuzawa and T. Wakagi
Mutational Analysis of Fungal Family 11 Xylanases on pH Optimum Determination
J. Appl. Glycosci., **58** (2011) 107.
- M. Okuda, T. Shiba, D-K. Inaoka, K. Kita, G. Kurisu, S. Mineki, S. Harada, Y. Watanabe and S. Yoshinari
A Conserved Lysine Residue in the Crenarchaea-Specific Loop is Important for the Crenarchaeal Splicing Endonuclease Activity
J. Mol. Biol., **405** (2011) 92.
- Y. Uchida, J. Hasegawa, D. Chinnapen, T. Inoue, S. Okazaki, R. Kato, S. Wakatsuki, R. Misaki, M. Koike, Y. Uchiyama, S. Iemura, T. Natsume, R. Kuwahara, T. Nakagawa, K. Nishikawa, K. Mukai, E. Miyoshi, N. Taniguchi, D. Sheff, W. I. Lencer, T. Taguchi and H. Arai
Intracellular Phosphatidylserine is Essential for Retrograde Membrane Traffic through Endosomes
Proc. Natl. Acad. Sci. USA, **108** (2011) 15846.
- M. Kanagawa, T. Satoh, A. Ikeda, Y. Adachi, N. Ohno and Y. Yamaguchi
Structural Insights into Recognition of Triple-Helical β -Glucans by an Insect Fungal Receptor
J. Biol. Chem., **286** (2011) 29158.
- H. S. Kim, S. J. Lee, H. J. Yoon, D. R. An, D. J. Kim, S.-J. Kim and S. W. Suh
Crystal Structures of YwqE from *Bacillus subtilis* and CpsB from *Streptococcus pneumoniae*, Unique Metal-Dependent Tyrosine Phosphatases
J. Struct. Biol., **175** (2011) 442.
- Y. Echizen, T. Tsukazaki, N. Dohmae, R. Ishitani and O. Nureki
Crystallization and Preliminary X-Ray Diffraction of the First Periplasmic Domain of SecDF, a Translocon-Associated Membrane Protein, from *Thermus thermophilus*
Acta Cryst. F, **67** (2011) 1367.
- A. Zheng, R. Yamamoto, M. Sokabe, I. Tanaka and M. Yao
Crystallization and Preliminary X-Ray Crystallographic Analysis of eIF5B Δ N and the eIF5B Δ N-eIF1A Δ N Complex
Acta Cryst. F, **67** (2011) 730.
- Y. J. An, J. H. Lee, H. I. Jung, S. G. Sohn, J. J. Lee, K. S. Park, X. Wu, B. C. Jeong, C. M. Kang, S. S. Cha and S. H. Lee
Crystallization and Preliminary X-Ray Crystallographic Analysis of CTX-M-15, an Extended-Spectrum β -Lactamase Conferring Worldwide Emerging Antibiotic Resistance
Protein and Peptide Letters, **18** (2011) 858.
- Y. Yasutake, H. Ota, E. Hino, S. Sakasegawa and T. Tamura
Structures of Burkholderia Thailandensis Nucleoside Kinase: Implications for the Catalytic Mechanism and Nucleoside Selectivity
Acta Cryst. D, **67** (2011) 945.
- T. Shibahara, T. Satomura, R. Kawakami, T. Ohshima and H. Sakuraba
Crystallization and Preliminary X-Ray Analysis of a Dye-Linked D-Lactate Dehydrogenase from the Aerobic Hyperthermophilic Archaeon *Aeropyrum pernix*
Acta Cryst. F, **67** (2011) 1425.

- Y. Katsuyama, K. Miyazono, M. Tanokura, Y. Ohnishi and S. Horinouchi
Structural and Biochemical Elucidation of Mechanism for Decarboxylative Condensation of β -Keto Acid by Curcumin Synthase
J. Biol. Chem., **286** (2011) 6659.
- H. Sakuraba, K. Koga, K. Yoneda, Y. Kashima and T. Ohshima
Structure of a Multicopper Oxidase from the Hyperthermophilic Archaeon *Pyrobaculum Aerophilum*
Acta Cryst. F, **67** (2011) 753.
- H. Sakuraba, T. Kawai, K. Yoneda and T. Ohshima
Crystal Structure of UDP-Galactose 4-Epimerase from the Hyperthermophilic Archaeon *Pyrobaculum calidifontis*
Arch. Biochem. Biophys., **512** (2011) 126.
- T. Tonozuka, T. Miyazaki and A. Nishikawa
Structural Similarity between a Starch-Hydrolyzing Enzyme and an N-Glycan-Hydrolyzing Enzyme: Exohydrolases Cleaving α -1,X-Glucosidic Linkages to Produce β -Glucose
Trends in Glycoscience and Glycotechnology, **23** (2011) 93.
- T. Nakamura, T. Tonozuka, S. Ito, Y. Takeda, R. Sato, I. Matsuo, Y. Ito, K. Oguma and A. Nishikawa
Molecular Diversity of the Two Sugar-Binding Sites of the β -Trefoil Lectin HA33/C (HA1) from *Clostridium botulinum* Type C Neurotoxin
Arch. Biochem. Biophys., **512** (2011) 69.
- K. Taoka, I. Ohki, H. Tsuji, K. Furuita, K. Hayashi, T. Yanase, M. Yamaguchi, C. Nakashima, Y. A. Purwestri, S. Tamaki, Y. Ogaki, C. Shimada, A. Nakagawa, C. Kojima and K. Shimamoto
14-3-3 Proteins Act as Intracellular Receptors for Rice Hd3a Florigen
Nature, **476** (2011) 332.
- S. Fushinobu, M. Hidaka, A. M. Hayashi, T. Wakagi, H. Shoun and M. Kitaoka
Interactions between Glycoside Hydrolase Family 94 Cellobiose Phosphorylase and Glucosidase Inhibitors
J. Appl. Glycosci., **58** (2011) 91.
- S. Fushinobu, T. Uno, M. Kitaoka, K. Hayashi, H. Matsuzawa and T. Wakagi
Mutational Analysis of Fungal Family 11 Xylanases on pH Optimum Determination
J. Appl. Glycosci., **58** (2011) 107.
- M. Okuda, T. Shiba, D-K. Inaoka, K. Kita, G. Kurisu, S. Mineki, S. Harada, Y. Watanabe and S. Yoshinari
A Conserved Lysine Residue in the Crenarchaea-Specific Loop is Important for the Crenarchaeal Splicing Endonuclease Activity
J. Mol. Biol., **405** (2011) 92.
- Y. Uchida, J. Hasegawa, D. Chinnapen, T. Inoue, S. Okazaki, R. Kato, S. Wakatsuki, R. Misaki, M. Koike, Y. Uchiyama, S. Iemura, T. Natsume, R. Kuwahara, T. Nakagawa, K. Nishikawa, K. Mukai, E. Miyoshi, N. Taniguchi, D. Sheff, W. I. Lencer, T. Taguchi and H. Arai
Intracellular Phosphatidylserine is Essential for Retrograde Membrane Traffic through Endosomes
Proc. Natl. Acad. Sci. USA, **108** (2011) 15846.
- M. Kanagawa, T. Satoh, A. Ikeda, Y. Adachi, N. Ohno and Y. Yamaguchi
Structural Insights into Recognition of Triple-Helical β -Glucans by an Insect Fungal Receptor
J. Biol. Chem., **286** (2011) 29158.
- H. S. Kim, S. J. Lee, H. J. Yoon, D. R. An, D. J. Kim, S.-J. Kim and S. W. Suh
Crystal Structures of YwqE from *Bacillus subtilis* and CpsB from *Streptococcus pneumoniae*, Unique Metal-Dependent Tyrosine Phosphatases
J. Struct. Biol., **175** (2011) 442.
- Y. Echizen, T. Tsukazaki, N. Dohmae, R. Ishitani and O. Nureki
Crystallization and Preliminary X-Ray Diffraction of the First Periplasmic Domain of SecDF, a Translocon-Associated Membrane Protein, from *Thermus thermophilus*
Acta Cryst. F, **67** (2011) 1367.
- A. Zheng, R. Yamamoto, M. Sokabe, I. Tanaka and M. Yao
Crystallization and Preliminary X-Ray Crystallographic Analysis of eIF5B Δ N and the eIF5B Δ N-eIF1A Δ N Complex
Acta Cryst. F, **67** (2011) 730.
- Y. J. An, J. H. Lee, H. I. Jung, S. G. Sohn, J. J. Lee, K. S. Park, X. Wu, B. C. Jeong, C. M. Kang, S. S. Cha and S. H. Lee
Crystallization and Preliminary X-Ray Crystallographic Analysis of CTX-M-15, an Extended-Spectrum β -Lactamase Conferring Worldwide Emerging Antibiotic Resistance
Protein and Peptide Letters, **18** (2011) 858.
- Y. Yasutake, H. Ota, E. Hino, S. Sakasegawa and T. Tamura
Structures of Burkholderia Thailandensis Nucleoside Kinase: Implications for the Catalytic Mechanism and Nucleoside Selectivity
Acta Cryst. D, **67** (2011) 945.
- T. Shibahara, T. Satomura, R. Kawakami, T. Ohshima and H. Sakuraba
Crystallization and Preliminary X-Ray Analysis of a Dye-Linked D-Lactate Dehydrogenase from the Aerobic Hyperthermophilic Archaeon *Aeropyrum pernix*
Acta Cryst. F, **67** (2011) 1425.

Z. Fujimoto and K. Kimura
Crystal Structure of Bacteriophage Φ NIT1 Zinc Peptidase PghP that Hydrolyzes γ -Glutamyl Linkage of Bacterial Poly- γ -Glutamate Proteins, **80** (2011) 722.

T. Tomita, T. Kuzuyama and M. Nishiyama
Structural Basis for Leucine-Induced Allosteric Activation of Glutamate Dehydrogenase
J. Biol. Chem., **286** (2011) 37406.

A. Kawaguchi, T. Ose, M. Yao and I. Tanaka
Crystallization and Preliminary X-Ray Structure Analysis of Human Ribosomal Protein L30e
Acta Cryst. F, **67** (2011) 1516.

E. Matsuoka, Y. Tanaka, M. Kuroda, Y. Shouji, T. Ohta, I. Tanaka and M. Yao
Crystal Structure of the Functional Region of Uro-Adherence Factor A from *Staphylococcus saprophyticus* Reveals Participation of the B Domain in Ligand Binding
Protein Science, **20** (2011) 406.

Y. Yasutake and T. Tamura
Efficient Production of Active Form of Vitamin D₃ by Microbial Conversion: Comprehensive Approach from the Molecular to the Cellular Level
Synthesiology, **4** (2011) 222, (*in Japanese*).

Y. Moriwaki, J. M. M. Caaveiro, Y. Tanaka, H. Tsutsumi, I. Hamachi and K. Tsumoto
Molecular Basis of Recognition of Antibacterial Porphyrins by Heme-Transporter IsdH-NEAT3 of *Staphylococcus aureus*
Biochemistry, **50** (2011) 7311.

NW14A

H. Ichikawa, S. Nozawa, T. Sato, A. Tomita, K. Ichianagi, M. Chollet, L. Guerin, N. Dean, A. Cavalleri, S. Adachi, T. Arima, H. Sawa, Y. Ogimoto, M. Nakamura, R. Tamaki, K. Miyano and S. Koshihara
Transient Photoinduced 'Hidden' Phase in a Manganite
Nature Materials, **10** (2011) 101.

S. Nozawa and S. Koshihara
Dynamical Analysis of Transient Molecular Magnetism and Structural Change by Time-Resolved X-Ray Absorption Fine Structure
Kogaku, **40** (2011) 222, (*in Japanese*).

K. Ichianagi, H. Sekiguchi, S. Nozawa, T. Sato, S. Adachi and Y. C. Sasaki
Laser-Induced Picosecond Lattice Oscillations in Submicron Gold Crystals
Phys. Rev. B, **84** (2011) 024110.

M. Hoshino, T. Sato, A. Tomita, S. Nozawa, S. Adachi and S. Koshihara
Time-Resolved Structure Analysis of Photo-Induced Molecular Dynamics in TTF-CA
Acta Cryst. A, **67** (2011) C520.

S. Nozawa, T. Sato, A. Tomita, M. Hoshino, H. Tokoro, S. Ohkoshi, S. Adachi and S. Koshihara
Dynamic Investigation of Photoinduced Phase Transition in Prussian Blue Analogs by Picosecond Time-Resolved XAFS
Acta Cryst. A, **67** (2011) C109.

T. Sato, S. Nozawa, A. Tomita, M. Hoshino, S. Koshihara, M. Iwamura and S. Adachi
Observation of the Photo-Excited State of [Co^{III}(en)₃]³⁺ by Picosecond Time-Resolved XAFS
Acta Cryst. A, **67** (2011) C521.

L. Guerin, E. Collet, J. Hebert, M. B.-L. Cointe, S. Adachi, S. Koshihara and H. Cailleau
Evidence of One-Dimensional Precursors in the Photoinduced Transformation in TTF-CA
Acta Cryst. A, **67** (2011) C522.

M. Murakami and T. Kouyama
Crystallographic Analysis of the Primary Photochemical Reaction of Squid Rhodopsin
J. Mol. Biol., **413** (2011) 615.

SPF

K. Michishio, T. Tachibana, H. Terabe, A. Igarashi, K. Wada, T. Kuga, A. Yagishita, T. Hyodo and Y. Nagashima
Photodetachment of Positronium Negative Ions
Phys. Rev. Lett., **106** (2011) 153401.

Y. Nagashima, K. Michishio, T. Tachibana and H. Terabe
Towards the Production of an Energy-Tunable Positronium Beam using Ps⁻ Photodetachment Technique
J. Phys.: Conf. Ser., **262** (2011) 012041.

T. Hyodo, K. Wada, A. Yagishita, T. Kosuge, Y. Saito, T. Kurihara, T. Kikuchi, A. Shirakawa, T. Sanami, M. Ikeda, S. Ohsawa, K. Kakihara and T. Shidara
KEK-IMSS Slow Positron Facility
J. Phys.: Conf. Ser., **262** (2011) 012026.

T. Hyodo and K. Wada
The Slow Positron Facility at KEK
J. Particle Accel. Soc. Jpn., **8** (2011) 3, (*in Japanese*).

Synchrotron Radiation Science Division

K. Ohwada, J. Mizuki, K. Namikawa, M. Matsushita, S. Shimomura, H. Nakao and K. Hirota
Contribution of Intermediate Submicrometer Structures to Physical Properties Near T_c in Pb(Zn_{1/3}Nb_{2/3})O₃-9%PbTiO₃
Phys. Rev. B, **83** (2011) 224115.

K. Iwasa, R. Igarashi, K. Saito, C. Laulhe, T. Orihara, S. Kunii, K. Kuwahara, H. Nakao, Y. Murakami, F. Iga, M. Sera, S. Tsutsui, H. Uchiyama and A. Q. Baron
Motion of the Guest Ion as Precursor to the First-Order Phase Transition in the Cage System GdB₆
Phys. Rev. B, **84** (2011) 214308.

H. Yamaoka, I. Jarrige, N. Tsujii, A. Kotani, J.-F. Lin, F. Honda, R. Settai, Y. Onuki, N. Hiraoka, H. Ishii and K.-D. Tsue

Pressure and Temperature Dependences of the Electronic Structure of CeIrSi₃ Probed by Resonant X-ray Emission Spectroscopy
J. Phys. Soc. Jpn., **80** (2011) 124701.

A. Kotani

Crystal Field Effect on X-Ray Magnetic Circular Dichroism Spectra at the L_{2,3} Absorption Edges of Mixed-Valence Ce and Yb Compounds in High Magnetic Fields
Eur. Phys. J. B, **81** (2011) 49.

A. Kotani

Theory of Low Energy Excitations in Resonant Inelastic X-Ray Scattering for Rare-Earth Systems: Yb Compounds as Typical Examples
Phys. Rev. B, **83** (2011) 165126.

A. Kotani, K. O. Kvashnina, S. M. Butorin and P. Glatzel
A New Method of Directly Determining the Core-Hole Effect in the Ce L₃ XAS of Mixed Valence Ce Compounds — An Application of Resonant X-Ray Emission Spectroscopy
J. Elec. Spec. Relat. Phenom., **184** (2011) 210.

K. Ohwada, S. Shimomura, H. Nakao, M. Matsushita, K. Namikawa and J. Mizuki
X-Ray Photon Correlation Spectroscopy of Structural Fluctuations in Relaxor Ferroelectrics PZN-9%PT
J. Phys.: Conf. Series, **320** (2011) 012086.

H. Yamaoka, A. Kotani, Y. Kubozono, A. M. Vlaicu, H. Oohashi, T. Tochio, Y. Ito and H. Yoshikawa
Charge-Transfer Satellite in Ce@C₈₂ Probed by Resonant X-Ray Emission Spectroscopy
J. Phys. Soc. Jpn., **80** (2011) 014702.

S. Kishimoto and Y. Tanaka

Detector Guide for Synchrotron Radiation Users
Kodansha, (2011) (*in Japanese*).

Light Source Division

T. Ozaki, S. Nagahashi, K. Harada, T. Obina, T. Honda and Y. Kobayashi
Status of Magnets and Power Supplies at PF-AR
Proc. 8th Annual Meeting of Particle Accelerator Society of Japan, (2011) 396, (*in Japanese*).

H. Takaki, K. Harada, T. Honda, Y. Kobayashi, T. Miyajima, S. Nagahashi, N. Nakamura, T. Obina, K. Onoue, T. Shibuya, M. Shimada, R. Takai and A. Ueda
Status of Pulsed Sextupole Injection at the PF Ring
Proc. 8th Meeting of Particle Accelerator Society of Japan, (2011) 994, (*in Japanese*).

M. Yamamoto, H. Yoshida, H. Kurisu, T. Honda, Y. Tanimoto, T. Uchiyama, T. Nogami and M. Kobayashi

Development of Extreme High Vacuum System for High Brightness Electron Source of ERL
Proc. 8th Annual Meeting of Particle Accelerator Society of Japan, (2011) 1374, (*in Japanese*).

H. Takaki, A. Ueda, T. Obina, Y. Kobayashi, M. Shimada, R. Takai, S. Nagahashi, N. Nakamura, K. Harada, T. Honda and T. Miyajima
Beam Injection with a Pulsed Multi-Pole Magnet in an Electron Storage Ring
J. Particle Accelerator Society of Japan, **8** (2011) 218, (*in Japanese*).

T. Honda, T. Aoto, S. Asaoka, K. Endo, K. Haga, K. Harada, Y. Honda, M. Izawa, Y. Kobayashi, A. Mishina, T. Miyajima, H. Miyauchi, S. Nagahashi, N. Nakamura, T. Nogami, T. Obina, T. Ozaki, C. O. Pak, H. Sakai, S. Sakanaka, H. Sasaki, Y. Sato, K. Satoh, M. Shimada, T. Shioya, M. Tadano, T. Tahara, T. Takahashi, R. Takai, Y. Yamamoto, K. Tsuchiya, T. Uchiyama, A. Ueda, K. Umemori and M. Yamamoto
Post-Earthquake Recovery of PF Ring and PF-AR
Proc. IPAC2011, San Sebastian, Spain, (2011) 2984.

R. Takai, T. Obina, A. Ueda, S. Nagahashi, K. Harada, T. Honda, N. Nakamura and Y. Kobayashi
Beam Profile Measurement during Top-up Injection with a Pulsed Sextupole Magnet
Proc. DIPAC2011, Hamburg, Germany, (2011) 305.

M. Shimada, T. Miyajima, N. Nakamura, Y. Kobayashi, K. Harada and S. Sakanaka,
Approach to a Start-to-End Simulation of 2-Loop Compact Energy Recovery Linac
Proc. IPAC2011, San Sebastian, Spain, (2011) 1909.

The articles of the experiments utilizing multiple beamlines are simultaneously printed here in each section.